Effects of Carbonation and Calcium Leaching
on Microstructure and Transport Properties of Cement Pastes

Quoc Tri Phung

Promotoren: prof. dr. ir. G. De Schutter, prof. dr. ir. G. Ye
Proefschrift ingediend tot het behalen van de graad van
Doctor in de Ingenieurswetenschappen: Bouwkunde

Vakgroep Bouwkundige Constructies
Voorzitter: prof. dr. ir. L. Taerwe
Faculteit Ingenieurswetenschappen en Architectuur
Academiejaar 2014 - 2015

UNIVERSITEIT
GENT

ISBN 978-90-8578-783-9
NUR 956
Wettelijk depot: D/2015/10.500/27

Supervisors

Prof. Geert De Schutter

Faculty of Engineering and Architecture – Ghent University

Prof. Guang Ye

Faculty of Civil Engineering & Geosciences - Delft University of Technology

Mentors

Dr. Norbert Maes

Institute of Health, Environment and Safety - Belgian Nuclear Research Centre (SCK•CEN)

Dr. Diederik Jacques

Institute of Health, Environment and Safety - Belgian Nuclear Research Centre (SCK•CEN)

Doctoral committee

Prof. Luc Taerwe
Ghent University, Belgium
(chairman)

Dr. Elke Gruyaert
Ghent University, Belgium
(secretary)

Prof. Geert De Schutter
Ghent University, Belgium
(supervisor)

Prof. Guang Ye
Delft University of Technology, The Netherlands
(supervisor)

Dr. Norbert Maes
Belgian Nuclear Research Centre, Belgium

Prof. Klaas Van Breugel
Delft University of Technology, The Netherlands

Prof. Luc Courard
University of Liège, Belgium

Prof. Veerle Boel
Ghent University, Belgium

"The measure of greatness in a scientific idea is the extent to which it stimulates thought and opens up new lines of research."

Paul A.M. Dirac (1902 – 1984)

ABSTRACT

During the past decades, a significant progress has been made in the development of concrete materials. With the development of high performance and self-compacting concrete, the design of concrete structures for hundred-year service life becomes possible. In recent years, concrete has been considered as a useful material for facilities with extremely long-term service life such as radioactive waste repositories. Therefore, the assessment of the long-term performance of such concrete structures is of utmost importance. Within its service environment, these structures undergo chemical degradation processes which are very slow but they significantly change the physical integrity (e.g. transport and mechanical properties) and the chemical condition (e.g. pH) of the structures in the long-term. Chemical degradation is typically the result of alteration of the cement matrix mineralogy caused by interaction with environmental conditions. The interaction disturbs the equilibrium between the pore solution of the cementitious materials and the solid phases of the cement matrix which results in dissolution and/or precipitation of minerals. The chemical degradation of cementitious materials is mostly followed by alteration of the microstructure and, thereby, transport properties. The transport properties such as permeability and diffusivity are the key parameters to evaluate whether the concrete still retains its function as a barrier against the transport of radionuclides and other hazardous products out of the disposal system. Although a lot of effort has been spent on studies concerning the use of cement-based materials in such structures, the evolution of the microstructure and transport properties under chemical degradation over long time periods (up to thousands of years) is still unclear due to the limited experimental timeframe available to capture these processes. This thesis presents a comprehensive study of the consequences of exposure of cementitious materials to carbonation and calcium leaching.

Due to the extremely slow nature of these degradation processes, accelerated methods are needed to reach a certain degradation stage in order to study the behaviour of concrete representative for the long-term. In the present work, an ammonium nitrate solution was used to accelerate the Ca-leaching degradation kinetics, while pure CO_2 at high pressure was applied to speed up the carbonation. The changes in permeability and diffusivity of the degraded materials were measured by novel methods. Microstructural and mineralogical alterations were qualitatively and quantitatively examined by a variety of complementary techniques including SEM/SEM-EDX, MIP, TGA, N_2-adsorption, XRD/QXRD and ion

chromatography. The experiments were performed on cement pastes with different water/powder ratios and limestone filler replacement. In parallel, phenomenological models were also developed to better understand the transient state of degradation and to predict the evolution of the cementitious materials during the degrading processes, which is difficult to capture with experiments.

By using the accelerated techniques, it was able to obtain degraded materials which are representative for long-term degradation states and as such it allowed for studying the microstructure and hence its relation to the transport properties. The novel methods to measure transport properties proposed in this study are promising in terms of the required experimental time, the control of parameters (pressure, flow, concentration) and reliability. More importantly, the techniques allowed for a convenient capturing of the changes in transport properties of the degraded materials, thanks to their high compatibility with the accelerated degradation techniques.

Results showed that leaching and carbonation significantly changed the microstructure and transport properties of cementitious materials but in different manners. The leaching significantly altered the microstructure of the cement paste to a material with a higher specific surface area, increased total porosity and a shift to larger pore sizes resulting in a significant increase in transport properties depending on the degradation state. In contrast, carbonation led to a porosity reduction, shift of pore size distribution to smaller ranges and lower permeability and diffusivity. However, both leaching and carbonation processes induced a lower pH with possible loss of beneficial condition for waste package integrity (e.g. rebar corrosion).

The phenomenological models developed enabled us to simulate and predict the evolution of the microstructure and related transport properties (permeability, diffusivity). In combination with accelerated experiments, it provides us the possibility to assess the long-term performance of cement-based materials used in disposal systems.

Keywords: leaching; carbonation; acceleration; permeability; diffusivity; microstructure; mineralogy; cement paste; limestone filler; modelling

SAMENVATTING

Tijdens de laatste decennia werd een enorme stap voorwaarts gezet betreffende beton als materiaal. Met de ontwikkeling van hogesterktebeton en zelfverdichtend beton wordt het ontwerp van betonconstructies met een gebruiksduur van honderd jaar steeds realistischer. Sinds enkele jaren wordt beton ook beschouwd als een nuttig materiaal voor installaties met een extreem hoge gebruiksduur, zoals constructies voor de opslag van radioactief afval. In het licht hiervan is de studie van het langeduurgedrag van dergelijke constructies van bijzonder belang. Binnen hun gebruiksomgeving ondergaan deze constructies chemische aantastingsprocessen die zeer traag verlopen doch die op lange termijn zeer significante wijzigingen veroorzaken aan de fysische integriteit (bv. transporteigenschappen) en aan de chemische condities (bv. pH). Chemische aantasting is typisch het resultaat van een wijziging aan de mineralogie van de cementmatrix, veroorzaakt door de interactie met de gebruiksomgeving. De omgeving verstoort het evenwicht tussen de poriënoplossing van het cementgebonden materiaal, en de vaste fases van de cementmatrix, resulterend in oplossing en/of afzetting van mineralen. De chemische aantasting van cementgebonden materiaal gaat meestal gepaard met een wijziging van de microstructuur, en dus van de transporteigenschappen. Transporteigenschappen zoals permeabiliteit en diffusiviteit zijn belangrijke parameters voor de evaluatie van de performantie van beton als barrière tegen het transport van radionucliden en andere gevaarlijke producten uit het radioactief afval. Alhoewel reeds vele onderzoeksinspanningen geleverd werden inzake het gebruik van cementgebonden materialen voor dergelijke constructies, blijft de evolutie van de microstructuur en van de transporteigenschappen door chemische aantasting op zeer lange termijn (tot duizenden jaren) onduidelijk. Een probleem hierbij is het beperkte experimentele tijdskader dat beschikbaar is om dergelijke processen te bevatten. Deze thesis presenteert een gedetailleerde studie van de gevolgen van de blootstelling van cementgebonden materialen aan carbonatatie en kalkuitloging.

Door het bijzonder trage karakter van deze aantastingsprocessen zijn versnelde proefmethoden vereist om een zekere aantastingstoestand te bereiken, teneinde een representatieve studie te kunnen uitvoeren voor het gedrag op lange termijn. In voorliggend onderzoek werd een ammoniumnitraatoplossing aangewend om de kalkuitloging te versnellen. Zuiver CO_2 op hoge druk werk toegepast voor de versnelling van het carbonatatieproces. De wijzigingen in permeabiliteit en diffusiviteit van de aangetaste

materialen werden opgemeten met innovatieve methoden. Microstructurele en mineralogische wijzigingen werden kwalitatief en kwantitatief bepaald door middel van een combinatie van complementaire technieken, met inbegrip van SEM/SEM-EDX, MIP, TGA, N_2-adsorptie, XRD/QXRD en ionenchromatografie. De experimenten werden uitgevoerd op cementpasta met verschillende water/poeder-factor, en met variabele vervanging van cement door kalksteenmeel. Fenomenologische modellen werden ontwikkeld om een beter begrip te krijgen van de evoluerende degradatietoestand, en om een voorspelling te kunnen maken van de evolutie van de aantasting in de tijd, wat moeilijk waar te nemen is met experimenten.

Door het gebruik van versnelde methoden konden aangetaste materialen bekomen worden die representatief zijn voor de lange termijn. Dit maakte het mogelijk om de microstructuur te bestuderen, en de relatie met de transporteigenschappen. De voorgestelde nieuwe methoden om transporteigenschappen te bepalen zijn veelbelovend met het oog op de benodigde beproevingstijd en de praktische controle van belangrijke parameters (druk, debiet, concentratie), en zijn tevens betrouwbaar. Daarenboven bieden deze proefmethoden een gepaste mogelijkheid om wijzigingen in transporteigenschappen te bestuderen dank zij de compatibiliteit met de versnelde aantastingstechnieken.

De resultaten tonen aan dat kalkuitloging en carbonatatie de microstructuur en transporteigenschappen van cementgebonden materialen significant wijzigen, zij het op verschillende wijzen. Kalkuitloging verandert op significante wijze de microstructuur van de cementpasta, zodat een materiaal bekomen wordt met een hogere specifieke oppervlakte en een verhoogde totale porositeit. Hierbij worden grotere poriënafmetingen bekomen, wat resulteert in een verhoogd transport, afhankelijk van de aantastingsgraad. In tegenstelling hiermee leidt carbonatatie tot een vermindering van de porositeit, een verschuiving naar kleinere poriënafmetingen, en een verminderde permeabiliteit en porositeit. Nochtans leiden zowel kalkuitloging als carbonatatie tot een lagere pH, met een mogelijk verlies van de gunstige condities met het oog op de integriteit van de verpakking van het radioactief afval (bv. wapeningscorrosie).

De fenomenologische modellen maakten het mogelijk de evolutie van de microstructuur en transporteigenschappen (permeabiliteit, diffusiviteit) te simuleren en te voorspellen. Gecombineerd met de versnelde proefmethoden biedt dit de mogelijkheid om het langeduurgedrag van cementgebonden materialen aangewend voor de opslag van radioactief afval te beoordelen.

Sleutelwoorden: uitloging; carbonatatie; versnelde proeven; permeabiliteit; diffusiviteit; microstructuur; mineralogie; cement pasta; kalksteenmeel; modellering

ACKNOWLEDGEMENTS

This research, which resulted in a doctoral thesis, was one of the three outcomes of a general project to assess the long-term durability of concrete which was funded by the Belgian Nuclear Research Centre (SCK•CEN). The project was a cooperation between SCK•CEN, Ghent University and Technical University of Delft.

I wish to express my sincere gratitude to my supervisor, Professor Geert De Schutter, for his guidance and support throughout the duration of this research. His supervision, suggestions, and critical comments on scientific publications are very much appreciated. I would like to thank my co-supervisor, Professor Guang Ye for his fruitful discussions and valuable advices during the project meetings.

I would like to express my special thanks to SCK•CEN mentors. Norbert Maes provided many inspiring and helpful discussions, practical-oriented support and valuable suggestions from the design of experiments to the evaluation and analysis of experimental results. Thanks are extended to Diederik Jacques who always gave very detailed and critical comments on the manuscripts which significantly improved the quality of the papers.

I have to thank the other members involved in concrete durability project for their discussions, questions and suggestions: Professor Klaas Van Breugel, Janez Perko and Suresh Seetharam. Special thanks go to Patel Ravi, one of the PhD students in the project, who shared his great expertise on modelling with me and raised several tough problems in concrete material science on which our discussions never end!

The experimental support provided by the technicians and other colleagues at SCK•CEN is appreciatively recognized. I would like to mention in particular Elke Jacobs and Arno Grade for their assistance in diffusion experiments; Miroslav Honty and Wim Verwimp for their help in XRD and N_2-adsorption experiments; Ben Gielen for his help in polishing the samples for SEM examinations; Jean Wannijn for his help in ion chromatography; Jef Sannen, Jurgen Verlinden and Roger Mertens for their excellent work in manufacturing the multi-purpose cells and sawing a large amount of samples; Tom Maes, Frank Vandervoort; Louis Van Ravestyn and Marc Van Gompel for their daily assistance in the laboratory.

Thanks are also extended to PhD students at Magnel Laboratory for Concrete Research, Ghent University for sharing their expertise on numerous research topics during the Concrete Technology group meetings over the last four years.

Thanks to all of my friends in the “Boeretang Kingdom” without whom I would not have many happy days in Belgium. I would like to extend my very sincere thanks to the colleagues at the University of Da Nang, Vietnam for their encouragement and support during my study.

I would like to express my deepest gratitude to my family members for their love, support and encouragement while I was thousands of miles away from home. Finally, I wish to give heartfelt thanks to my wife, Hoang Mai, and my lovely daughter, Mai Khanh, with whom I have spent all happy and hard moments throughout these years. Without their love, support, sympathy and patience, the completion of this thesis would not be possible.

Quoc Tri Phung, January 2015

CONTENTS

LIST OF ABBREVIATIONS

w/c	Water to cement ratio
w/p	Water to powder ratio
ACI	American Concrete Institute
ASTM	American Society for Testing and Materials
BET	Brunauer-Emmett-Teller
BFS	Ground granulated blast-furnace slag
BJH	Barrett-Joyner-Halenda
BSE	Backscattered electron
CEM I→ V	Types of cement according to European Committee for Standardization
C-S-H	Calcium silicate hydrates
CH	Calcium hydroxides
C_3S	Tricalcium silicate $3CaO \cdot SiO_2$
C_2S	Dicalcium silicate $2CaO \cdot SiO_2$
C_3A	Tricalcium aluminate $3CaO \cdot Al_2O_3$
C_4AF	Calcium ferroaluminate $4CaO \cdot Al_2O_3 \cdot Fe_2O_3$
DTA	Differential thermal analysis
DTG	Derivative thermo-gravimetry
EDX	Energy dispersive X-ray microanalysis
FIB-SEM	Focus ion beam - Scanning electron microscopy
GC	Gas chromatography
IC	Ion chromatography
ITZ	Interfacial transition zone
KC	Kozeny-Carman
LS	Limestone fillers

ls/p	Limestone fillers to powder ratio
MIP	Mercury intrusion porosimetry
NRVB	Nirex reference vault backfill
N_2-adsorption	Nitrogen adsorption
OPC	Ordinary Portland cement
PFA	Pulverised fuel ash
PVC	Polyvinyl chloride
RILEM	International Union of Laboratories and Experts in Construction Materials
RH	Relative humidity
SE	Secondary electron
S1	Sample with w/p = 0.325; ls/p = 0
S1C-S	Carbonated sample S1 under saturated condition
S1L	Leached sample S1
S2	Sample with w/p = 0.425; ls/p = 0.2
S2C	Continuously-carbonated sample S2 at RH of 65%
S2L	Leached sample S2
S3	Sample with w/p = 0.425; ls/p = 0
S3C	Continuously-carbonated sample S3 at RH of 65%
S3L	Leached sample S3
S4	Sample with w/p = 0.375; ls/p = 0.1
S4C	Continuously-carbonated sample S4 at RH of 65%
S4C-C	Cyclic-carbonated sample S4
S4L	Leached sample S4
S5	Sample with w/p = 0.325; ls/p = 0.2
S5C	Continuously-carbonated sample S5 at RH of 65%
S5C-C	Cyclic-carbonated sample S5

S5L	Leached sample S5
SEM	Scanning electronic microscopy
SP	Superplasticizer
TGA	Thermo-gravimetric analysis
TG	Thermo-gravimetry
XRD	X-ray diffraction
QXRD	Quantitative X-ray diffraction

This page is intentionally left blank!

CHAPTER 1: INTRODUCTION

1.1. Background

Cementitious materials (concrete, mortar, cement paste, grout) are omnipresent in civil and infrastructure constructions, from small components to huge buildings. Despite the development of novel/advanced materials, cement-based materials are now by far the most widely used materials in construction over the world. Besides their classical use in construction, these materials are envisaged for use both as encapsulation of radioactive waste and as engineered barriers for disposal of radioactive waste, both in near-surface repositories for low/intermediate active waste and geological/deep repositories for high level long-lived radioactive waste (see Figure 1.1). The role of cement-based materials in these applications is not only focused on the retention of radionuclides (attributed to its low transport properties) but also in helping creating beneficial conditions for the waste package integrity (steel corrosion) because of its high-pH buffering capacity for a very long period.

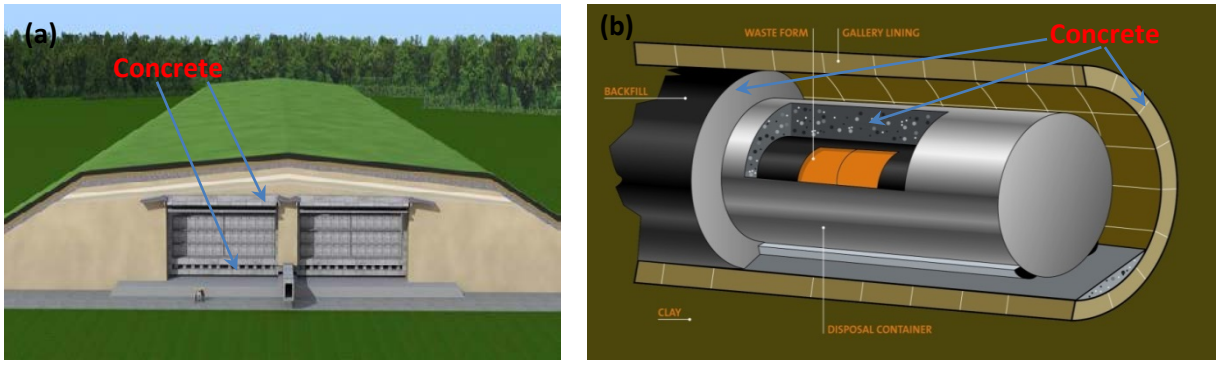

Figure 1.1. Concrete used for encapsulation, backfill and construction in low level waste facility (a) and disposal gallery lining, buffer within Supercontainer, end-plug of gallery and backfill in high level waste facility – Supercontainer concept (b) [adapted from NIRAS' reports [1] and [2]]

Under its service environment, these concrete structures undergo chemical degradation processes which are very slow but important for the long-term durability assessment. Chemical degradation is typically the result of alteration of the cement matrix mineralogy caused by interaction with its environment. The interaction disturbs the equilibrium between the pore solution of the cementitious materials and the solid phases of the cement matrix which results in dissolution and/or precipitation of minerals. The chemical degradation of

cementitious materials is mostly followed by alteration of microstructure and, thereby, its transport properties. The most common chemical degradation processes include chloride ingress, sulphate attack, alkali-silica reactions, carbonation and Ca-leaching [3]. The latter two are extremely slow processes but highly relevant for radioactive waste facilities because the long-term durability of concrete (hundreds up to thousands of years) is a key requirement [4-7] for these applications. The service life of these structures is directly related to the time necessary for the waste's radioactivity to reach its natural level, which typically exceeds hundreds or even thousands of years. It is therefore necessary to explain how concrete will degrade, and how the properties evolve in the long-term.

1.2. Research motivation

The possibility to assess the service life of structures made of cement-based materials for radioactive waste facilities is of great practical importance but raises new challenges. Unlike classical structures, the durability of waste disposal facilities needs to be predicted over hundreds up to thousands of years because of the long-lived activity of radioactive waste. Under service conditions, the disposal facility is attacked by aggressive water, which will induce chemical disequilibrium and dissolution of cementitious solid phases by processes such as Ca-leaching and carbonation (Figure 1.2). Moreover, the heat generated during the repository life may accelerate the chemical processes. The alteration of chemical properties will in turn induce changes in the cement microstructure and consequently changes in mechanical performance and transport properties (permeability, diffusion) of concrete structures. Therefore, a systematic approach is needed to establish the relationship between multiple processes at multiple scales, which would provide knowledge of long-term safety of radioactive waste disposal and suggestions on how safety functions of the repository components can be improved in terms of material and structure designs. Despite advances in this area, a significant amount of work is still needed due to limited experimental timeframe available to capture these long-term processes.

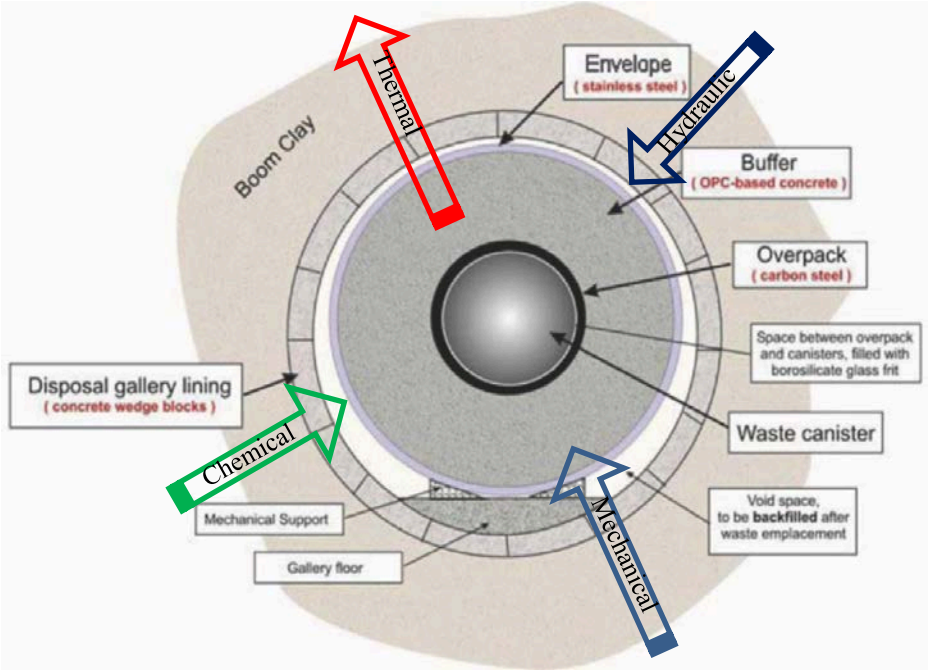

Figure 1.2. Illustration of Belgian repository concrete structure under coupled effects by chemical, physical and mechanical degradation processes [adapted from NIRAS' report [8]]

1.2.1. Research objectives

The objective of this research is a phenomenological study of the relationship between chemical degradation and transport properties of cement-based materials from sub-micro to macro level. Transport properties are often considered as fundamental parameters for characterizing concrete durability because they govern the penetration of aggressive substances responsible for degradation and, thereby, have an important effect on the durability of cement-based materials as illustrated in Figure 1.3. As already stated, chemical degradation will alter the concrete mineralogy, and thus the microstructural properties such as total porosity, pore size distribution, connectivity and tortuosity, which are the most important factors influencing transport properties. This study focused on Ca-leaching and carbonation that are highly relevant in terms of influence on the long-term performance of concrete with respect to the service environment. Permeability and diffusion are chosen as the main transport properties in this study.

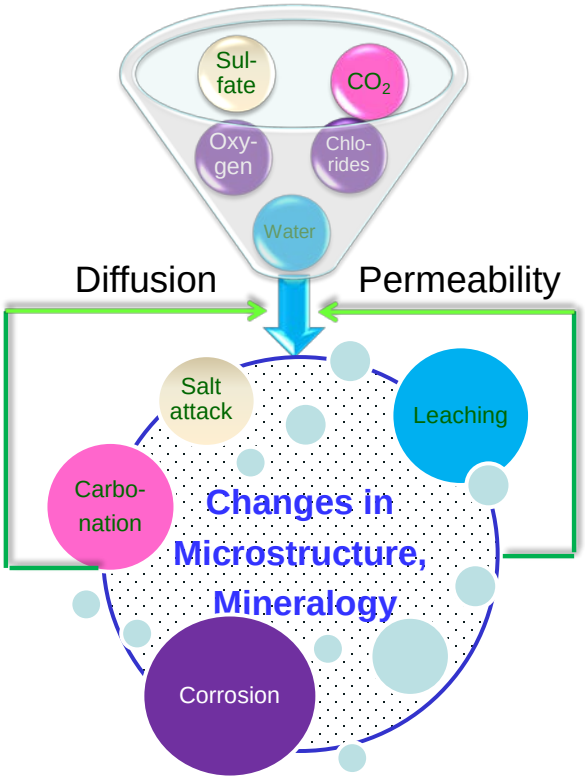

Figure 1.3. Transport properties have an important effect on the durability of cement-based materials. Chemical degradation processes will in turn change the transport properties by microstructural and mineralogical alterations.

A comprehensive research has been carried out focusing on the following four objectives:

- Development of experimental techniques/methodologies to induce degradation and determine transport properties of cement paste. Note that due to the extremely slow nature of the degradation processes, accelerated methods are needed to reach a certain degradation stage to study the behaviour of concrete in the degraded state (relevant for the long-term). Methods to determine transport properties have to be relatively fast; and the setups should be compatible with the accelerated degradation setups to capture the changes in transport properties due to chemical degradation.
- Propose a complementary methodology to examine the changes in mineralogy and microstructure due to carbonation and Ca-leaching.
- Qualitatively and quantitatively study the relationship between the changes in mineralogy, microstructure and transport properties.
- Develop phenomenological models to simulate the degradation of cement paste under the studied conditions and better understand the transient state of the degradation and predict

the evolution of cementitious materials as a function of degradation state, which is difficult to observe with experiments.

1.2.2. Research significance

Scientific community agrees that carbonation/leaching change the transport properties of cement-based materials, but to what extent is still a question. This study allows a better understanding of the alteration degree of transport properties due to the chemical degradation, because it attempts to carry out an in depth investigation concerning the modifications of mineralogy and microstructure and its link to the transport properties. The improved understanding would help to better assess the long-term durability of cement-based materials subjected to chemical degradation. Furthermore, accelerated carbonation and Ca-leaching experiments in combination with phenomenological modelling provides us insights into the evolution of the microstructure and related transport properties of cementitious materials in the long-term.

Additionally, the durability with respect to Ca-leaching is of concern in some immediate/short-term applications such as water tanks, dams, water pipes, bridge foots and tunnels. Carbonation has attracted a great deal of research attention because it significantly reduces the lifespan of reinforced concrete structures as a result of increase in temperature due to global climate change [9] and the increase of global CO_2 emissions. Although a great number of studies has been done on the carbonation and leaching of cementitious materials, the knowledge on how materials are degraded is still incomplete. This study will provide additional knowledge to fill uncertainties in quantifying the carbonation and leaching of cement-based materials with a systematic approach.

1.3. Thesis outline

The PhD thesis composes of 3 main parts: (i) development of test methods, (ii) integrated experimental program, and (iii) interpretation of test results as schematically presented in Figure 1.4. Apart from Chapter 1, which provides a general introduction of the PhD study, the thesis is divided into 8 chapters.

Chapter 2 presents a literature review on permeability and diffusion of cement-based materials. The existing methods, influencing factors and prediction of transport properties are introduced. This review stresses the importance of transport properties with respect to durability of concrete and provides a fundamental basis for developing new testing methods suitable for the goals of this research. Chapter 3 reviews the existing knowledge on leaching

and carbonation of cementitious materials. The mechanism, influencing factors and available methods to study leaching and carbonation are discussed. Furthermore, the influence of carbonation and leaching on microstructure and transport properties are highlighted. Chapter 4 describes in detail the materials, mix design and experimental methods. A novel method to determine water permeability using controlled constant flow is introduced. An adapted method to measure diffusivities of two dissolved gases in a single experiment is also presented. Methods to accelerate the leaching using ammonium nitrate solution and carbonate cement paste under controlled CO_2 pressure gradient are shown. An integrated methodology to characterize degraded and sound cementitious materials is described in detail.

In Chapter 5, the experimental results of the permeability and diffusivity for sound materials are shown. The effects of w/p ratio and limestone filler replacement on transport properties (mainly permeability) is investigated by a factorial experimental analysis. Chapter 6 and Chapter 7 present the changes in microstructure and transport properties due to carbonation and leaching, respectively. Chapter 8 focuses on the modelling aspects. Phenomenological models of carbonation and leaching under studied conditions are developed. The models enable to predict a wide range of parameters related to changes in the microstructure, mineralogy and transport properties of cement-based materials due to carbonation and leaching. Chapter 9 summarizes the most important findings. The key parameters governing changes in transport properties due to chemical degradation and relevance of accelerated degradation experiments to long-term durability assessments of cementitious materials are discussed. Suggestions for future research are given in this concluding chapter.

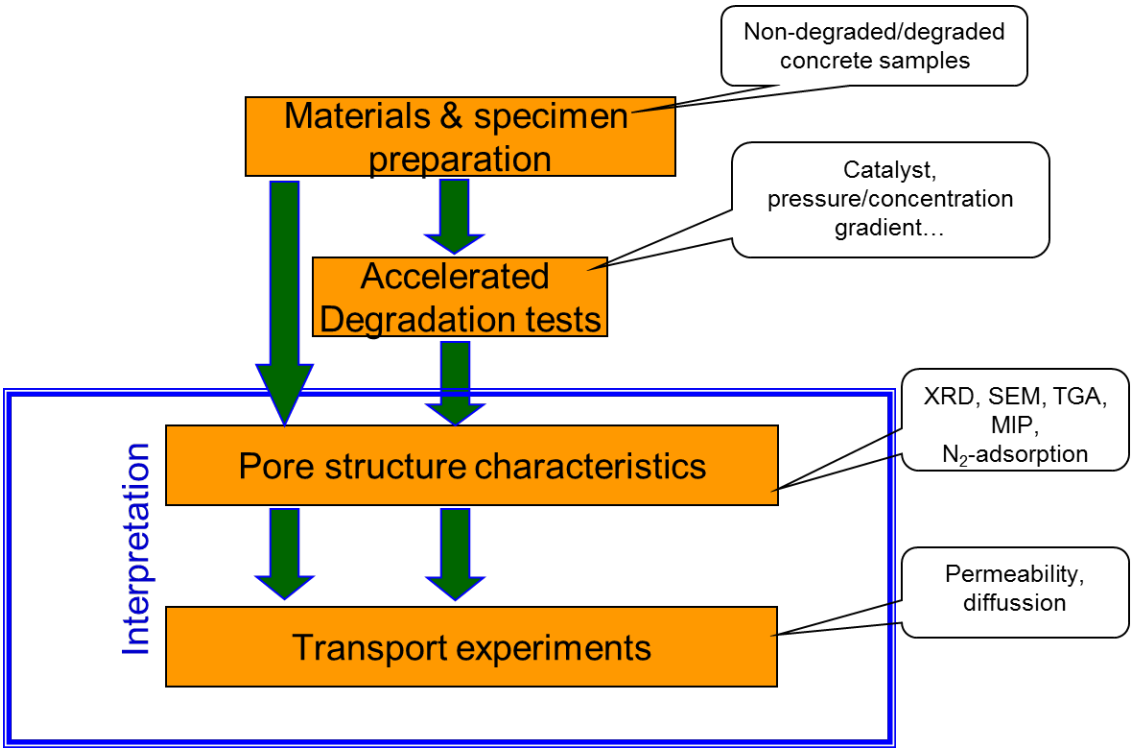

Figure 1.4. Overview of research methodology including development of test methods, experimental program and interpretation of test results

The work presented in this PhD thesis is based on the following papers.

- Q.T. Phung, G.D. Schutter, N. Maes, D. Jacques, G. Ye, **Measuring permeability of cementitious materials**, in: M.G. Alexander, H.-D. Beushausen, F. Dehn, P. Moyo (Eds.) Concrete Repair, Rehabilitation and Retrofitting III, CRC Press, 2012, pp. 287-295.
- D. Jacques, N. Maes, J. Perko, S.C. Seetharam, Q.T. Phung, R. Patel, A. Soto, S. Liu, L. Wang, G.D. Schutter, G. Ye, K.v. Breugel, **Concrete in engineered barriers for radioactive waste disposal facilities - phenomenological study and assessment of long term performance**, in: 15th International Conference on Environmental Remediation and Radioactive Waste Management - ICEM2013, Brussels, Belgium, 2013, pp. 1-10.
- Q.T. Phung, N. Maes, G. De Schutter, D. Jacques, G. Ye, **A methodology to study carbonation of cement paste and its effect on permeability**, in: 4th International Conference on Accelerated Carbonation for Environmental and Materials Engineering (ACEME-2013), 2013, pp. 459-463.
- Q.T. Phung, N. Maes, G. De Schutter, D. Jacques, G. Ye, **Determination of water permeability of cementitious materials using a controlled constant flow method**, Construction & Building Materials, 47 (2013) 1488-1496.

- Q.T. Phung, N. Maes, D. Jacques, G.D. Schutter, G. Ye, **Decalcification of cement paste in NH_4NO_3 solution: Microstructural alterations and its influence on the transport properties**, in: J. Bastien, N. Rouleau, M. Fiset, M. Thomassin (Eds.) 10th fib International PhD Symposium in Civil Engineering, Québec, Canada., 2014 pp. 179-187.
- Q.T. Phung, N. Maes, D. Jacques, G.D. Schutter, G. Ye, **Microstructural and permeability changes due to accelerated Ca leaching in ammonium nitrate solution**, in: M. Grantham, P.A.M. Basheer, B. Magee, M. Soutsos (Eds.) Concrete Solutions - 5th International Conference on Concrete Repair, CRC Press, 2014 pp. 431-438.
- Q.T. Phung, N. Maes, D. Jacques, J. Perko, G.D. Schutter, G. Ye, **Modeling the decalcification of cement paste in ammonium nitrate solution**, in: 3rd internatinal conference on Service Life design for Infrastructure: Keynote speech, Zhuhai, China, 2014 pp. 27-40.
- Q.T. Phung, N. Maes, D. Jacques, E. Bruneel, I.V. Driessche, G. Ye, G.D. Schutter, **Effect of limestone fillers on microstructure and permeability due to carbonation of cement pastes under controlled CO_2 pressure conditions**, Construction & Building Materials, (DOI: 10.1016/j.conbuildmat.2015.02.093).
- Q.T. Phung, N. Maes, D. Jacques, E. Jacop, A. Grade, G.D. Schutter, G. Ye, **Determination of diffusivities of dissolved gases in saturated cement-based materials**, in: International Conference on Concrete Repair, Rehabilitation and Retrofitting, ICCRRR 2015, Leipzig, Germany, (submitted).

CHAPTER 2: REVIEW OF TRANSPORT PROPERTIES OF CEMENTITIOUS MATERIALS

2.1. General introduction

Durability and performance of concrete are affected by a number of chemical degradation phenomena such as carbonation, calcium leaching, sulphate attack, chloride attack, and corrosion of the reinforcement bars [10, 11]. Diffusivity and permeability as macroscopic properties of concrete determine how fast aggressive substances penetrate into concrete, thereby influencing almost all mentioned degradation mechanisms. Therefore, these are fundamental parameters for characterizing long-term performance of concrete rather than the standard compressive/tensile strengths. In this chapter, a critical review on permeability and diffusion of cement-based materials is presented. The existing methods, influencing factors and prediction of transport properties are introduced. The advantages and disadvantages of different techniques are discussed and served as fundamental basics for developing new testing methods suitable for the goals of this research.

2.2. Permeability

2.2.1. Introduction

The intrinsic permeability is the capacity of a porous material to transfer liquids through a fully saturated pore network under a pressure gradient, ∇p [Pa/m], and is determined by Darcy's law [12]:

$$J = -\frac{k}{\eta}\nabla p \tag{2.1}$$

Within the field of engineering, water permeability is normally expressed by the hydraulic conductivity, k_w, which is related to the intrinsic permeability, k, as:

$$k_w = \frac{\rho g}{\eta}k \tag{2.2}$$

where ρ is the density of water [kg/m^3]; η is the dynamic viscosity for water [kg/m.s]; and g is the gravitation constant [m/s^2]. The unit of the hydraulic conductivity (also called as permeability coefficient) is [m/s], while the SI unit of intrinsic permeability is [m^2].

Permeability generally depends on the features of the pore network of cementitious materials which are quantified by variables as porosity, size distribution, tortuosity, connectivity,

specific surface and also micro cracks. These parameters are, amongst others, controlled by the water/cement (w/c) ratio, the particle size distribution, the age of hardened cementitious materials and the ingress of aggressive substances. Due to the importance of permeability, many methods to determine permeability have been proposed [13-20] but none of them seems fully accepted worldwide.

2.2.2. Review of existing water permeability measurement techniques

A variety of methods has been proposed to measure permeability of cementitious materials but a lot of arguments/problems/issues still remain. One of the main challenges is to cope with the continuous change in microstructure as a result of hydration of early age cementitious materials. Therefore, an appropriate method for measuring permeability requires a short measurement time. In general, permeability measurements can be classified in two categories: direct and indirect methods.

2.2.2.1. Direct methods

Most direct methods for determining the permeability of porous materials rely on Darcy's law. In its basic form, the water flux through a disk-shaped sample is measured under a pressure gradient by having a water head at one side of the sample, while maintaining the other side at atmospheric pressure [21]. Based on the geometry of the sample, the permeability is calculated directly from Darcy's law. Although these methods are relatively simple, it can take a long time to reach steady state flow conditions (in the order of several weeks for k_w of 10^{-11} m/s). Unfortunately, hydration during such long testing time can change the pore structure which could lead to changes in permeability (usually decreasing the permeability). To reduce the required measurement time, researchers propose to apply an additional pressure (e.g. 15 bar in [14]) rather than self-gravity of a water head [14, 16, 22]. Nevertheless, due to the higher applied pressure, the probability of leakage at the interface of the sample and the testing cell might be larger.

El-Dieb and Hooton [23, 24] introduced a triaxial cell that can measure permeability as low as 10^{-15} m/s which is a typical value for extremely low-permeable materials such as high performance concrete or high strength concrete. A confining pressure is applied to a cylindrical sample through a rubber sleeve to prevent leakage around the sides. The ratio of confining pressure to driving pressure is recommended to be approximately 4 in order to increase the stability of the measurement. The high-confining pressure condition raises the question whether it may modify the pore structure due to the compression of pores or due to creation of artificial micro cracks, thereby, leading to unrepresentative permeability values.

Instead of imposing longitudinal flow, a radial flow through the sample is created by applying a hydrostatic pressure to the outer surface of a hollow cylindrical sample resulting water to move from the outer to the inner surface of a sample [16, 22]. By measuring the out-flow rate with a linear variable differential transformer [22] or with an out-flow measurement device [16], the permeability is calculated by a modified form of Darcy's law. There are several advantages by using the radial flow method. Firstly, because of a larger contact area of the fluid compared to a longitudinal flow setup, flow rates are higher and, thus, the accuracy of the measurements increases. Secondly, the area which needs to be sealed is minimized; as a result the potential of leakage is decreased. Finally, a hollow cylindrical sample may be easier to saturate than an equivalent solid sample. However, it is quite difficult to prepare a hollow sample, especially, in the case of in-situ concrete.

Another promising method is the centrifuge technique which was first applied on soil materials by Nimmo *et al*. [25, 26]. This method was recently standardized in the ASTM standard D6527 which covers permeability measurements of any porous material [27]. A cylinder-shaped sample is put in a centrifuge with a centrifuge radius of r [m], and a rotation speed of ω [rad/s]. The centripetal force per unit volume, $-\rho r\omega^2$, is the main fluid driving force. The permeability can be calculated as follows (the Equation (1a) is probably wrongly written in reference [28] due to missing term ρg which leads to unit for permeability [m^3.s/kg]):

$$k = -\frac{q\rho g}{\mathrm{d}\psi/\mathrm{d}r - \rho r\omega^2} \tag{2.3}$$

where q is the flux [m/s] and $\mathrm{d}\psi/\mathrm{d}r$ [kg/m^2.s^2] is the matric potential gradient which is negligible if rotation speed is above 400 rotations per minute [28]. An important advantage of the centrifuge technique is that the centrifugal force is a body force which acts, similar to gravity, independently of other driving forces over the entire porous material [28]. The magnitude of centrifugal force per unit volume can be increased by increasing the rotation speed such that it dominates any matric potential gradients. However, if the rotation speed is too large, the sample can be compacted under equivalent pressure exerted by centrifugal acceleration. Additionally, this method can be used to determine out-flow of unsaturated porous materials because it can fix the water content to achieve hydraulic steady state which cannot be done by pressure driven techniques [28]. The centrifuge technique is normally applied for materials of which permeability is not too low as stated in ASTM standard D6527 (10^{-6} – 10^{-13} m/s) [27].

In general, direct methods are quite simple and easy to setup. No additional parameters are needed to interpret the results when using Darcy's law directly. On the other hand, it takes a long time to reach the steady state flow conditions needed to apply Darcy's formula. Therefore, concrete samples are more susceptible to microstructural changes as a consequence of hydration, especially at early hydration stage. Potential for leaks around the sample is high if seal and/or confining pressure are not sufficient. Because of these limitations, the direct methods can only be applied to materials of which the permeability is not too low.

2.2.2.2. Indirect methods

Indirect methods involve either the application of a transient pressure pulse technique or the application of poromechanical techniques.

In 1968, Brace *et al*. [29] introduced a transient pressure method for determining the permeability of granite. The principle of this method is to measure the decay characteristics of pressure, which depend on permeability, after a sudden change of applied pressure. This method can measure permeability coefficient as low as 4×10^{-14} m/s. This method, already applied to cement-based materials [13, 30], needs only measured time series of pressure instead of the extremely low flow rate measurement in the direct methods.

Alternatively, poromechanical techniques measure the strain-time history, which depends on the fluid movement in a pore network, of a sample under an applied pressure or heating. Especially the beam bending method, proposed by Scherer *et al*. [31], is of great interest since it is extremely fast (several minutes to hours compared to days of conventional methods for permeability of the same order of magnitude), and thus suitable for low-permeable materials, and provides also viscoelastic properties (i.e. shear modulus, Young's modulus). This method was originally developed for silica gels [32] and then extended for glass [33] and cementitious materials [15, 34]. However, it is difficult to apply the beam bending method for concrete because the sample must be long and slender enough to avoid micro cracking. For example, the concrete sample should be more than one meter long if it is 10 cm thick [19].

Thermopermeametry and dynamic pressurization are other examples of applying poromechanics to measure permeability. Thermopermeametry was also first introduced for gels [35, 36] and afterwards applied for cementitious materials [37, 38]. The main principle of this method is based on the difference in expansion of liquid and solid phase when heated. This method requires a complete saturation of the sample because water will first fill the pores before flowing out when air is still entrapped. This leads to an underestimation of the

permeability. Therefore, this method may not work well for mortar or concrete for which full saturation state is not easy to obtain within a short time. Dynamic pressurization involves applying a sudden hydrostatic pressure on a cylindrical sample in a closed system. By measuring the history of the re-expansion, the permeability of the sample can be obtained in a relative short time. The sample can be a solid cylinder [17, 18] or a hollow cylinder [22]. The permeability measured by the hollow dynamic pressurization method seems to agree well with the one measured by the solid dynamic pressurization method [39]. However, the hollow dynamic pressurization method probably measures a wider range of concrete permeability because it can also be tested as a radial flow through method.

In general, the indirect methods for measuring permeability are much faster than direct methods because they are based on measurements obtained during non-steady state flow conditions. Potential of leakage is actually eliminated. These techniques can determine very low permeability. However, a full saturation of the sample, which is extremely difficult to obtain for low-permeable materials such as high performance concrete, is absolutely required because the degree of saturation hugely affects test result. With direct methods, the sample saturates during the test until steady state is reached, which also can take a long experimental time. Application of heating or high pressure may also change the microstructure of the cementitious materials. Another disadvantage of these methods is that the experimental setup and the interpretation or analysis are quite complex.

2.2.3. Factors influencing water permeability

There are many factors influencing the permeability of cement-based materials. Several factors are classified as extrinsic related to experimental conditions such as applied pressure, size of sample [40] and confining pressure [16]. Variation of these factors can cause a change of several orders of magnitude in permeability. Another factor which can significantly affect the permeability is the fluid-cement matrix interactions during measurement. In the case of using water as a testing fluid, the time dependent reduction of permeability is mainly due to continuing hydration, autogenous healing and the self-sealing effects [14, 41, 42]. However, these phenomena likely occur in cracked [43, 44] and/or early aged cement-based materials rather than virgin and/or mature materials. Unreactive fluids such as ethanol [14], glycol [45] or 2-propanol [15] may be used instead of water to eliminate the fluid-cement matrix interactions. However, the replacement of water by unreactive fluid may require longer experimental time and especially the fluid exchange would create micro cracks which hugely

increase the permeability. In some cases, the permeability can increase 2 orders of magnitude [15].

Intrinsic factors are related to material properties such as pore network characteristics of the cementitious material which include porosity, pore size distribution, tortuosity, specific surface and micro cracks. These parameters are basically controlled by the water to cement ratio, particle size distribution (cement + aggregate), age of sample and type of constituent materials. Concrete with larger pore size has higher permeability than concrete with smaller pore size despite the same total porosity. This effect is normally reflected through the critical pore size (which is the most frequently occurring pore size in interconnected pores). It is obvious that pore connectivity is one of the most critical factors influencing the permeability. Pores which are blocked cannot transport any fluid. The type of constituent materials mainly affects permeability through hydration degree, especially at early ages. As shown in many studies [15, 46-49], the permeability increases with increasing w/c ratio because of a higher porosity at higher w/c ratio. However, to the knowledge of the author, no direct connection between water to cement ratio and permeability has been proposed. A direct relation between porosity and permeability has been introduced by some researchers [50-54]. Nevertheless, porosity alone should not be a unique factor influencing the permeability, i.e. samples with same porosity may have different permeability.

2.2.4. Prediction of water permeability

In addition to permeability measurements, one can also predict permeability based on other properties of cement-based materials. Katz and Thompson proposed the following equation to predict permeability of saturated rocks [51]:

$$k = c d_o^2 \frac{\sigma}{\sigma_o} \tag{2.4}$$

where c is a constant suggested to be equal to 1/226 [-], d_o is the critical pore diameter which can be estimated by mercury intrusion porosimetry [m], σ denotes the electrical conductivity of the sample [S/m] and σ_o denotes electrical conductivity of fluid used to saturate the sample, [S/m]. The ratio σ_o/σ is also known as the formation factor and is related to diffusion by the Nernst-Einstein relation [55, 56] as: $\sigma_o/\sigma = D_o/D$ where D_o is the diffusivity of ions in the fluid [m^2/s] and D is the diffusivity of ions in the saturated porous medium [m^2/s]. The appropriateness of the Katz and Thompson equation for cementitious materials is not univocal: Garboczi [57] found good correspondence between prediction and measurements,

whereas El-Dieb and Hooton [58] concluded that the theory was not successful due to the hydration and chemical effects in cementitious materials.

Another approach to estimate permeability is based on the pore structure [52, 59] using following relation:

$$k(\theta) = \frac{\phi r_{0.5} \rho g}{12\eta\tau^2 \left(1+{}^{1}/_{\alpha^2}\right)} \tag{2.5}$$

where θ is water content [-], ϕ is porosity [-], $r_{0.5}$ is mean distribution radius [m], τ is tortuosity [-] defined as the ratio between the actual length of flow path to the straight length of a sample, and α is aspect ratio [-]. In the case of saturation, $k(\theta)$ is referred to water permeability. The strength of this relation is the link between pore structural parameters and the permeability. However, these parameters are not easy to determine, especially tortuosity and aspect ratio.

A well-known relationship between permeability and porosity was proposed by Kozeny [54] and later modified by Carman [53] known as Kozeny-Carman (KC) equation. The KC equation is actually derived by comparing Poiseuille's law and Darcy's law.

$$k = C\frac{\phi^3}{(1-\phi)^2} \tag{2.6}$$

where C [m^2] is KC coefficient and may be expressed in several forms [60-62], among them the following form relates C with critical pore diameter and tortuosity [60]:

$$C = \frac{d_{cr}^2}{k_c\tau^2} \tag{2.7}$$

where d_{cr} is the critical pore diameter [m] and k_c is a constant and taken to be 90 [-] for beds packed with spherical particles. The KC relation works well for relatively homogeneous porous media. For more complex materials, the relation has some drawbacks because of the complicated microstructure of hydrates and non-uniform size of the pores as stated elsewhere [63, 64]. Nevertheless, the KC equation is commonly used in concrete literature [20, 65, 66].

In recent years, computer simulations have been intensively used to predict the permeability (also diffusivity) of cement-based materials. The computer-based models enable to simulate the microstructure features using network or digital-analysis, which are served as fundamental information for the prediction of transport properties. Ye *et al.* [67] proposed a network model which takes into account the fluid channel and the critical link, to predict the permeability based on simulated microstructure of cement pastes. A 3D lattice Boltzmann model to calculate the gas and water permeability of cement pastes has been developed by Zalzale *et al.*

[68]. The model enables to predict the transport properties of cement pastes at different water saturation degree and takes into account the transport through C-S-H. The estimation of permeability using SEM image analysis was proposed by Wong *et al.* [49]. The pore structure obtained from 2D backscattered electron images is idealised as a network of tubes arranged in a simple cubic lattice and served as the starting point to predict the permeability. The method is successfully applied on both cement pastes and mortars with a wide range of permeability values.

2.3. Gas permeability

It is well-known that the intrinsic gas permeability is higher than the intrinsic water permeability of cement based-materials (around 2 orders of magnitude) despite the fact that permeability is an intrinsic property of the material [14]. In addition, lower viscosity of gas results in higher fluxes in gas permeability measurement than water permeability measurement. As such, measuring the gas permeability and converting it to the water permeability would be easier because gas permeability determination is less time consuming. Unfortunately, the intrinsic permeability cannot be derived directly from the measured gas permeability because of gas slippage or the so-called Klinkenberg effect [69] which increases the amount of gas passing through the capillaries of porous media compared to prediction from a physical law. Some studies established a statistical, thus empirical, log-log linear correlation between air and water permeability using a huge amount of experimental data [70, 71].

2.4. Diffusion

2.4.1. Introduction

Diffusion of chemical substances plays an important role in many degradation processes (e.g. corrosion of steel bars; chloride, sulphate attacks). Knowledge of diffusion coefficients helps to better design and evaluate concrete structures. Diffusion is a mass transport induced by the random Brownian motion of substance. The diffusion coefficient (diffusivity) is the capacity of a medium to transfer substances (gases, dissolved gases, ions) under a concentration gradient expressed by Fick's first law (1D):

$$J = -D\frac{\partial C}{\partial x} \tag{2.8}$$

where J is the substance flux [kg/m^2.s]; $\frac{\partial C}{\partial x}$ is the concentration gradient [kg/m^4]; and D is the diffusion coefficient [m^2/s]. In porous materials, diffusion is affected by the characteristics of pore network (porosity ϕ [-], tortuosity τ [-], constrictivity δ [-]) which leads to the need to define different diffusion coefficients for practical application [72]. The pore diffusivity, D_p, is smaller than the diffusivity in free water or ideal solutions D_0, which takes into account the effects of tortuosity and constrictivity (a dimensionless parameter depending on the ratio of the size of diffusion species and pore size) and is expressed as:

$$D_p = D_0 \frac{\delta}{\tau^2} \tag{2.9}$$

The effective diffusivity, D_e, takes into account the volume of porous media available for diffusion and is defined as:

$$D_e = \phi D_p = D_0 \frac{\phi\delta}{\tau^2} \tag{2.10}$$

The apparent diffusivity, D_a, takes into account the sorption/binding which retards the diffusion and is linked to the pore diffusivity through a retardation factor ($\geq$1), R_e as follows:

$$D_a = \frac{D_p}{R_e} = D_0 \frac{\delta}{R_e \tau^2} \tag{2.11}$$

As permeability, diffusion generally depends on the pore network characteristics of the cementitious materials, mainly controlled by water/cement ratio, cement type, admixtures, and the age of hardened cementitious materials. Due to the importance of diffusion, many methods to determine diffusivity have been proposed. The diffusion coefficients can be obtained under steady state or transient state conditions. The steady state method requires a long-time experiment compared to the transient method, but it might be accelerated by some means such as using an electrical gradient.

2.4.2. Review of diffusion measurement techniques use for different species and its application on cement-based materials

2.4.2.1. Gas/dissolved gas diffusion

The diffusion of gases is normally determined by through-diffusion technique. The setup is quite simple: a thin sample is located in between two compartments. The setup usually allows measuring the diffusivity of only one gas [73] by injecting the testing gas to the upstream compartment and the sweep gas to the downstream compartment. The sweep gas is needed to

balance the pressure in two compartments which prevents the advective transport. Gas concentrations are determined regularly (by gas chromatography) until steady state is reached.

Figure 2.1 shows a typical concentration profile of a diffusing gas over time. When steady state condition is reached, the concentration profile becomes a straight line which means the diffusive flux across the sample is constant. Therefore, Fick's first law can be applied to calculate the cumulative quantity $Q(t)$ [kg] of testing gas passed through a sample with a cross-sectional area A [m^2]:

$$Q(t) = \int_0^t -D_e A \frac{\partial c}{\partial x} dt' = D_e A \frac{C_0}{L} t \tag{2.12}$$

where L [m] is the length of sample; C_0 [kg/m^3] is the concentration of testing gas in the upstream compartment. Note that the concentration of testing gas is neglected compared to C_0. The effective diffusivity is then easy to compute from the slope of $Q(t)$ curve. In case of no sorption/binding (R_e = 1), the accessible porosity of the sample can be determined from the time-lag t_{lag} [s] which is the intercept of the straight line with the x axis in Figure 2.1. However, it is found that the porosity determined from time-lag is less precise [72].

$$\phi = \frac{6 D_e t_{lag}}{L^2} \tag{2.13}$$

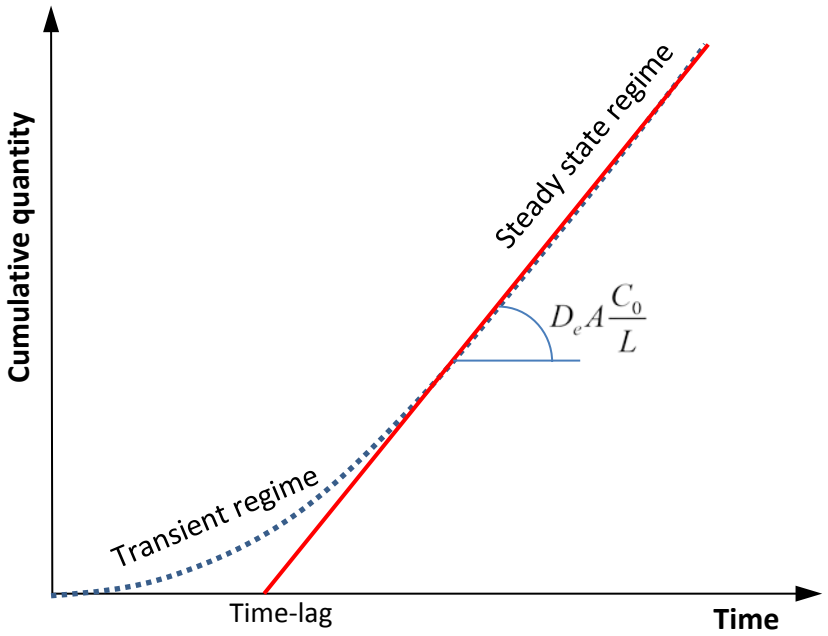

Figure 2.1. Cumulative quantity in the upstream compartment

Keeping the concentration gradient constant is difficult because of sampling which decreases the pressure (thereby concentration) of the testing gas. However, a small variation in the concentration gradient can be permitted [72]. If the pressure in the compartments is dropping too large, a numerical approach is needed to fit the effective diffusion coefficient.

In general, there are three possible gas diffusion mechanisms in porous media: molecular diffusion, Knudsen diffusion, and surface diffusion. The latter, which is contributable for materials with very high surface area, is thought to be less common for cement-based materials. However, whether molecular or Knudsen diffusion is the dominant diffusion mechanism in concrete is still questionable. Generally, it depends on gas pressure and the pore diameters of concrete [73, 74]. Published data on the diffusion of gases in cementitious materials are scarce. Daimon *et al*. [75] used a through-diffusion method to measure the diffusion of hydrogen and nitrogen in dried OPC mortars with different curing time and w/c ratios. The diffusion coefficients obtained are decreasing with curing time and increasing with w/c ratio. After 28-day curing, the diffusion coefficients are 4.8×10^{-7} and 1.9×10^{-7} m^2/s for w/c ratios of 0.65 and 0.5, respectively. Sercombe *et al*. [73] studied the diffusion of hydrogen and xenon in cement paste at different relative humidity, w/c ratios and cement types. Results show that gas diffusion decreases with the increase of RH, especially when RH is higher than 55%. The hydrogen diffusion coefficient is found to decrease 4 orders of magnitude when RH is increased from 3% to 93%. The diffusivity also increases with w/c ratio. While with the same w/c ratio, CEM V paste results in a lower diffusivity compared to CEM I paste. The diffusion coefficient of xenon is found to be lower than hydrogen due to its higher molecular weight. The authors also concluded that gas transport at atmospheric pressure takes place in the transient regime between bulk diffusion and Knudsen diffusion. Chou Chen *et al*. [76] investigated the diffusion of methane in dry and water saturated concretes. The diffusion coefficients for dry material are reported in the range of 3.6×10^{-8} to 3.1×10^{-7} m^2/s. The diffusion coefficients for wet concretes are also found to be lower compared to dry concretes like the study of Sercombe, but only about 20 times lower.

Papadakis *et al*. [77] predicted the diffusion coefficients of CO_2 and O_2 by measuring the diffusivities of He and N_2. The prediction is based on the assumption that Knudsen diffusion is the dominant diffusion mechanism in concrete; thus, the effective diffusivity of a gas can be used to calculate the effective diffusivity of certain gas by dividing it with square root of its molar weight ratio. Note that CO_2 is a reactive gas for concrete (if water is available) and O_2 diffusivity is experimentally difficult to measure. The authors were able to establish a

relationship between the effective diffusivity, porosity and relative humidity. In general, diffusivity exponentially increases with the increase of porosity and it exponentially decreases with the increase of relative humidity. The CO_2 diffusivities are in order of 10^{-8} m^2/s for concretes with porosity of 0.23 – 0.44 and RH of 40 – 80%, while those of O_2 are slightly higher due to its lower molar weight. In an attempt to evaluate the possibility to use hardened cement pastes as gas separation membranes, Gluth *et al*. [74] were able to measure the diffusivity of CO_2 directly (in oven dried samples). The authors showed a relatively lower diffusivity of CO_2 compared to H_2 which allows obtaining a separation factor up to 3.43. The effective diffusivities of CO_2, N_2 and H_2 are found to be increased with the increase of temperature up to 350^{o}C. The authors also made the same conclusion about the contribution of Knudsen diffusion as stated by Sercombe. In the case of samples with the small threshold radii, Knudsen diffusion prevails.

The data on diffusion of dissolved gases in saturated cement-based materials are even scarcer in literature. The measurements are extremely time consuming as the diffusion of dissolved gas in saturated media is much slower than of gas (in gaseous phase) in unsaturated media. However, knowledge of the diffusion of specific dissolved gases is very important, especially for dissolved oxygen which is involved in the corrosion process of steel bars in reinforced concrete. The effective diffusion coefficients of dissolved oxygen are usually determined by an electrochemical method involving cathodic consumption of the diffused oxygen. This technique is much quicker to obtain steady state compared to through-diffusion. Tittarelli [78] studied oxygen diffusion through hydrophobic and normal cement-based materials which were fully immersed in water. It is reported that the effective diffusion coefficient of hydrophobic concrete with w/c of 0.8 is 5×10^{-8} m^2/s which is almost 3 orders of magnitude faster than concrete without hydrophobic admixture (7×10^{-11} m^2/s). The author attributed this difference to that dissolved oxygen directly diffuses as a gaseous phase through the empty pores of a hydrophobic cement matrix. In a comparative study of chloride and oxygen diffusion in saturated cement pastes, Yu *et al*. [79] reported that dissolved oxygen diffuses faster than chloride due to surface charge effect of chloride diffusion, even though the two species have very similar diffusivities in an infinitely dilute solution. The retardation increases with decrease of water/binder ratio, at water/binder ratio of 0.5 the diffusion coefficient of oxygen is about 1×10^{-11} m^2/s which is 2 times faster than one of chloride. Castellote *et al*. [80] have drawn the same conclusion in a study on cement paste with w/c of 0.4. The effective diffusion coefficient of dissolved oxygen determined by electrochemical method is 9.5×10^{-12}

m^2/s which is also about 2.5 times faster than one of chloride determined by either electrochemical or migration tests.

2.4.2.2. Ionic diffusion

Diffusion of ionic species is probably the most significant transport process which affects the chemical degradation of cementitious materials because most degradation occurs in the presence of water in which ionic species can migrate through concrete driven by concentration gradients. The diffusion of ions is more complex than dissolved gases due to its possibility to interact with solid phases of the porous medium (charge repulsion/attraction) and effects of the presence of other ionic species. In general, the effective diffusion coefficients of ionic species can be measured by through-diffusion (as discussed above), in-diffusion or electro-migration methods (often referred to as "migration" tests).

Instead of waiting until steady state like through-diffusion, in-diffusion is a transient method which is less time consuming. The technique is based on the measurement of concentration profile of the testing ion by cutting the sample into small slices at a given time. Experiments are usually designed in such a way that the source concentration of testing ionic species is kept constant and the sample is long enough to be considered as a semi-infinite medium. The apparent diffusion coefficient is then obtained by fitting the concentration profile with solution of the Fick's second law [81]:

$$C(x,t) - C_0 = (C_s - C_0)erfc\left(\frac{x}{2\sqrt{D_a t}}\right) \tag{2.14}$$

where $C(x,t)$ is concentration at depth x [m] and time t [s]; C_0 and C_s are the initial and source concentrations, respectively [mol/m^3]; and *erfc* is the complementary error function.

Electro-migration tests have been developed to accelerate the ionic transport by applying an electrical field. The setup is quite simple. A thin sample is located between two electrodes. A testing ionic species is added to the upstream compartment. A constant electrical potential difference is applied across the sample. In steady-state migration tests, the evolution of the concentration of a given ionic species in the downstream compartment is monitored until steady state is reached. In non-steady state migration tests, the concentration profile of ionic species within the sample is measured after a given period. The calculation of the diffusion coefficient is based on the Nernst–Planck equation [82].

$$J(x) = -D\frac{\partial C}{\partial x} - DC\frac{zF}{RT}\frac{\partial \Psi}{\partial x} + CV(x) \tag{2.15}$$

where C is the concentration [mol/m^3]; D is the diffusion coefficient [m^2/s]; z is the valence number [-]; F is the Faraday constant [coulomb/mol]; R is the ideal gas constant [J/mol.K]; T is the absolute temperature of the liquid [K]; Ψ is the electrical potential [V], and $V(x)$ is the bulk velocity of the fluid along x direction [m/s]. On the right side of Equation (2.15), the first term stands for diffusion, the second term stands for (electro)migration and the last term stands for convection. Note that chemical activity effects are neglected in this expression. Under steady state flow and with assumption that migration is the dominant transport process, it is possible to calculate the effective diffusion coefficient as follows:

$$D_e = \frac{J(x)RTL}{zFC_s\Delta\Psi} \tag{2.16}$$

where C_s is the source (boundary) concentration [mol/m^3]; L is the length of sample [m]; and $\Delta\Psi$ is the potential difference [V]. The flux $J(x)$ can be calculated from the concentration evolution in the downstream compartment. In non-steady state regime, the concentration of ion in the sample changes with time. Fick's second law is applied to solve the problem:

$$\frac{\partial C}{\partial t} = -\frac{\partial}{\partial x}\left(-D\frac{\partial C}{\partial x} - DC\frac{zF}{RT}\frac{\partial \Psi}{\partial x} + CV(x)\right) \tag{2.17}$$

If the convection term is negligible, for semi-infinite media an analytical solution of Equation (2.17) can be obtained by [83]

$$C = \frac{C_s}{2}\left[e^{ax}erfc\left(\frac{x + aDt}{2\sqrt{Dt}}\right) + erfc\left(\frac{x - aDt}{2\sqrt{Dt}}\right)\right] \tag{2.18}$$

where $a = \frac{zF\Delta\Psi}{RTL}$. Note that D in Equation (2.18) is referred as apparent diffusion coefficient because in transient state the physical/chemical interactions have not been completed. The diffusion coefficient is obtained by fitting the calculated to the measured concentration profile.

For concrete materials, the main concern with ionic diffusion is chloride ion migration, because of the extent of reinforcement corrosion damage due to de-icing and exposing to marine environment. A large number of methodologies have been proposed to determine chloride diffusion coefficients. Currently, chloride diffusion tests are classified into two

categories: long-term immersion tests and electro-migration tests. The long-term immersion tests are based on either through-diffusion [84, 85] or in-diffusion methods which have been standardized in ASTM Test Method for Determining the Apparent Chloride Diffusion Coefficient of Cementitious Mixtures by Bulk Diffusion (C1556-04) [86] and Nordtest NT Build 443 [87]. However, a long-term immersion test requires such a long time to determine the diffusion coefficient which may reduce due to the continuous hydration and the retarding effect resulting from chloride binding [88]. The electro-migration tests offer a possibility to significantly shorten the measurement time [83, 89-91]. The method was also standardized in ASTM C1202-97 [92] and Nordtest NT Build 492 [93]. Nevertheless, the migration test has also been criticized because the diffusion coefficients obtained by the migration tests are quite scattered and not the same as the actual values resulting from the difference in penetration mechanism simulated in the electrical migration test and the one occurring in real concrete. An excellent review on this issue was done by Andrade *et al*. [94].

Most of the methods have been applied for saturated materials, few studies focused on partially saturated concretes [95, 96]. The measured chloride ion apparent diffusion coefficients are of the order of 10^{-11} m^2/s for saturated materials while the apparent diffusion coefficients are significantly decreased with the decrease of saturation degree. At a saturation degree of 50%, the apparent diffusion coefficient drops about one order of magnitude compared to saturated material [96].

Besides chloride ions, sulphate ions can also be of relevance for ionic diffusion, as sulphate attack is one of the coherent durability problems in coastal concrete structures. The diffusion coefficient of sulphate ions is normally measured by in-diffusion method in which the sample is located between sodium sulphate solution (5%) at one side and pure water at the other side [97]. A similar migration test protocol for chloride can also be applied for the determination of sulphate diffusion coefficient [98, 99]. The measured chloride ion diffusion coefficients are of the order of 10^{-12} m^2/s [98, 100].

2.4.3. Factors influencing diffusion

One may expect that the intrinsic factors (e.g. porosity, size distribution, tortuosity, specific surface area) would affect diffusion in the same way as for permeability. However, as permeability transport mainly occurs in meso and macro pore sizes, while diffusive transport could also occur in micro (gel) pore sizes (and dead-end pores), the impacts would be different at different ranges of pore sizes. In micropore level, Knudsen diffusion is the main mechanism, while molecular diffusion is the dominant process in larger pore size ranges.

Different methods might result in inconsistent effective diffusion coefficients. The difference is sometimes not only because of the setup itself but also because of the way to interpret experimental data. In order to obtain the diffusion coefficients, a number of assumptions (e.g. constant source concentration, dominant transport mechanisms, multi/single species transport) have to be made. If the experiments do not fulfil these assumptions, results will significantly differ. In case of ionic diffusion determined by the migration methods, a higher applied potential results in higher diffusion coefficients [101]. The source concentration significantly affects the interpretation of diffusion coefficients in non-steady state; but not in steady state [102]. The non-steady state migration method results in a higher chloride diffusivity compared to the diffusivity obtained from the steady state migration test [84, 103].

2.4.4. Prediction of diffusion

In addition to measurements, one can also predict diffusivity based on the pore structure of cement-based materials. Garboczi and Bentz [55] simulated diffusion in cement pastes by means of digital image-based microstructural modelling. The simulation considered diffusion in both capillary and gel pores (C-S-H). The following relationship was proposed:

$$D_e = D_0\left[0.001 + 0.07\phi_{c0}^2 + 1.8H\left(\phi_c - 0.18\right)\left(\phi_c - 0.18\right)^2\right] \tag{2.19}$$

where D_e and D_0 are the effective diffusivity of porous medium and diffusivity in water, respectively [m^2/s]; $H()$ is the Heaviside function; and ϕ_c [-] is capillary porosity (excluded gel pores).

Archie's law [104] empirically relates the porosity and conductivity, thereby diffusivity. This expression was initially suggested for rocks but has been intensively applied for cement-based materials [105, 106].

$$D_e = D_0 k_A \phi^n \tag{2.20}$$

where ϕ is open porosity [-]; n and k_A are constant factors. Furthermore, some researchers [59, 107-109] proposed a correlation of the diffusion coefficient with the pore structure parameters of cement-based materials such as critical radius of pores, average radius of pores, tortuosity, and constrictivity which are difficult to determine experimentally. In additional, computer-based approaches have been used to predict the diffusivity of cementitious materials. The microstructure is either generated by numerical hydration models [110, 111] or image analysis [112].

2.5. Concluding remarks

Since its importance and hard measurement, a variety of test methods have been developed to measure transport properties of cement-based materials and in this chapter available test methods for the determination of permeability and diffusion in the laboratory have been reviewed. It becomes clear that different methods do not always lead to consistent results. For permeability measurements, the variation of measured values is sometimes up to 2 orders of magnitude. For diffusion measurements, the values obtained by different methods are less scattered. Most of the test procedures are applicable for a specific purpose or to certain testing species. The straightforward comparison of observed experimental data may not give a true indication of the relative properties of different materials unless they are determined using the same or at least similar test methods.

Traditional experimental methods require steady state conditions to be reached, which is very time consuming but normally results in reliable results due to its simple interpretation and fewer (or no) assumptions to be made. However, to reduce the measurement time, many methods have been proposed to accelerate the transport by applying a high pressure/concentration gradient or applying an electrical field. These accelerated methods are usually accompanied by many practical problems (e.g. cracking, heating). Furthermore, many assumptions are made to simplify the problem allowing the application of conventional physical/chemical laws to interpret the experimental data.

Prediction of transport properties is of great interest since it saves time and is needed for most degradation models. A variety of models have been proposed from simple to complex models. The complex models require the knowledge of the pore structure of which some parameters are difficult (or impossible) to determine experimentally, such as tortuosity and constrictivity. The extreme complexity of the pore structure complicates the modelling of transport properties for cement-based materials. Most models originate from soil science and direct application for cement-based materials is not straightforward. The combination of analytical and numerical microstructural modelling coupled with image analysis may improve the predictive potential of models.

To conclude, the measurement methods for the determination of transport properties are, to some extent, not accepted worldwide, which leads to a difficulty in comparison of the values obtained from different methods. There is still a need to develop methods which meet some key requirements such as high repeatability, short measurement time, high accuracy, easy application and fewer assumptions made.

This page is intentionally left blank!

CHAPTER 3: REVIEW OF CARBONATION AND CALCIUM LEACHING OF CEMENTITIOUS MATERIALS

3.1. General introduction

Many environments to which concrete is exposed are highly aggressive due to various chemical components. In such environments, concrete is subjected to processes of chemical degradation. Chemical degradation is typically the result of alteration of the cement matrix mineralogy caused by interacting with severe environment. The interaction disturbs the equilibrium between the pore solution and the solid phases of the cement matrix which results in dissolution and/or precipitation of minerals. The chemical degradation of cementitious materials is mostly followed by a weakening of the material and the alteration of the microstructure. Changes in the microstructure thereby affect the transport properties. In this chapter, the consequences of exposure of cementitious materials to carbon dioxide and calcium leaching are reviewed.

3.2. Carbonation

3.2.1. Introduction

The carbonation process in cement-based materials is a deterioration phenomenon. Carbonation results in a pH decrease. The development of lower alkaline environment accelerates the corrosion of reinforcing bars in concrete because of dissolution of the thin oxide passive layer protecting the steel bars from corrosion [10]. Another effect of carbonation is shrinkage which is less serious and not commonly considered in practice. The mechanism of carbonation shrinkage is not yet fully understood. It is probably caused by reorganization of the microstructure due to carbonation, or by polymerization and dehydration of the hydrous silica product from the carbonation of C-S-H. Further explanations of carbonation shrinkage can be found elsewhere [113, 114]. On the other hand, carbonation also results in beneficial effects. It is generally believed that carbonation decreases transport properties and refines pore structure of Portland cement-based materials. Furthermore, in recent years, there is considerable interest in applying carbonation of cement-based materials for solidification and stabilization of radioactive waste. The technique often used to carbonate radioactive waste-forms is supercritical carbonation by applying a high CO_2 pressure in a reactor to accelerate the carbonation [115].

3.2.2. Mechanism of carbonation

Carbonation is a chemical degradation process through the reaction between Ca^{2+} and CO_3^{2-} ions. However, the carbonation process is a complex physicochemical phenomenon. In most cases, it is believed that the driving force behind the carbonation is diffusion of CO_2 [116-118]. When concrete is exposed to environmental conditions containing carbon dioxide, CO_2 penetrates into the concrete pore network system and dissolve in the pore water.

$$CO_2(g) \rightarrow CO_2(aq) \quad (3.1)$$

$$CO_2(aq) + H_2O \rightarrow H_2CO_3 \quad (3.2)$$

$$H_2CO_3 \rightarrow HCO_3^- + H^+ \quad (3.3)$$

$$HCO_3^- \rightarrow CO_3^{2-} + H^+ \quad (3.4)$$

Bicarbonate ion HCO_3^- is unstable in high alkaline environment (about 12.8 in concrete). Therefore it dissociates and forms carbonate ion CO_3^{2-}. The carbonate ions then react with available Ca^{2+} ions in pore solution to precipitate as $CaCO_3$.

$$Ca^{2+} + CO_3^{2-} \rightarrow CaCO_3 \quad (3.5)$$

Portlandite (solid state) formed during hydration of C_3S and C_2S will start dissolving because of the decrease of the Ca^{2+} concentration in the pore water resulted from the $CaCO_3$ precipitation, sustaining the reaction of portlandite dissolution and calcite precipitation (Equation (3.5)). A schematic representation of the process is presented in Figure 3.1.

$$Ca(OH)_2(s) \rightarrow Ca^{2+} + 2OH^- \quad (3.6)$$

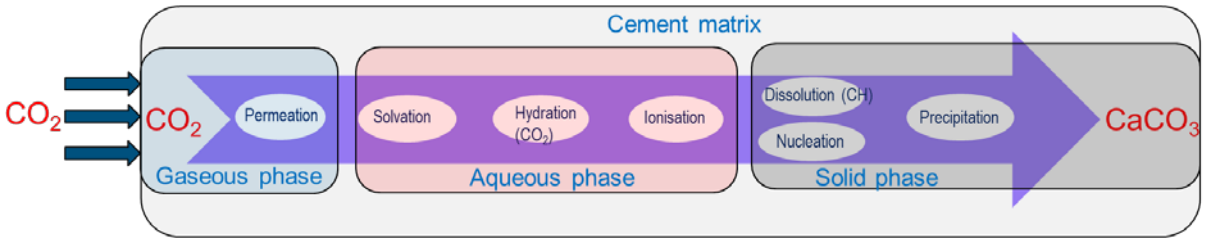

Figure 3.1. Summary of carbonation process in cement-based materials

As long as portlandite is present, the pH is buffered. After depletion of portlandite, the pH drops by approximately 3 units [119] when not buffered by other cement minerals. Thus, other solid hydration products (Calcium-silicate-hydrate (C-S-H), Monosulphate (AFm), Ettringite (AFt))

become unstable. C-S-H starts dissolving at pH of 12.5, AFm at pH of 11.6, while AFt decomposes at pH of below 10.6 [120, 121]. Carbonation will reduce the Ca/Si ratio of C-S-H. The carbonation reactions of C-S-H, AFm and AFt are summarized in Equations (3.7) to (3.10), respectively [122, 123].

$$C\text{-}S\text{-}H_1 + CO_2 \rightarrow C\text{-}S\text{-}H_2 + CaCO_3 + H_2O \quad (3.7)$$

where Ca/Si in $C\text{-}S\text{-}H_1$ is higher than in $C\text{-}S\text{-}H_2$. If CO_2 still remains, the carbonation reaction continues until the $C–S–H_1$ is completely decalcified and finally forms calcium carbonate.

$$3CaO.2SiO_2.3H_2O + 3CO_2 \rightarrow 3CaCO_3 + 2SiO_2 + 3H_2O \quad (3.8)$$

$$4CaO.Al_2O_3.SO_3.12H_2O + 3CO_2 \rightarrow 3CaCO_3 + CaO.SO_3.2H_2O + Al_2O_3.3H_2O + 7H_2O \quad (3.9)$$

$$6CaO\cdot Al_2O_3\cdot 3SO_3\cdot 32H_2O + 3CO_2 \rightarrow 3CaCO_3 + 3CaO\cdot SO_3\cdot 2H_2O + Al_2O_3\cdot 3H_2O + 23H_2O \quad (3.10)$$

Carbonation also occurs with unhydrated products (e.g. C_3S, C_2S) of hardened cementitious materials as shown in reactions (3.11) to (3.14). Actually, C_3S and C_2S may slowly hydrate to release $Ca(OH)_2$, and carbonate ions will react with calcium ions to form calcium carbonate afterwards. These processes can occur in the carbonated zone.

$$2(3CaO.SiO_2) + 6H_2O \rightarrow 3CaO.2SiO_2.3H_2O + 3Ca(OH)_2 \quad (3.11)$$

$$2(2CaO.SiO_2) + 4H_2O \rightarrow 3CaO.2SiO_2.3H_2O + Ca(OH)_2 \quad (3.12)$$

$$3CaO.SiO_2 + 3CO_2 + xH_2O \rightarrow 3CaCO_3 + SiO_2.xH_2O \quad (3.13)$$

$$2CaO.SiO_2 + 2CO_2 + xH_2O \rightarrow 2CaCO_3 + SiO_2.xH_2O \quad (3.14)$$

Calcium carbonate exists in three crystallographic forms: the stable form of calcite and two metastable forms of aragonite and vaterite [124].

In general, it is thought that the carbonation mechanism is determined by the inward diffusion of CO_2 [116-118] in normal conditions. However, it depends on the conditions of carbonation: whether the concrete is fully or partially saturated; the CO_2 concentration, the relative humidity; and the CO_2 pressure gradient. In the case of carbonation of unsaturated materials, CO_2 gas will diffuse in the concrete through the connected pore network. The CO_2 gas then dissolves into the aqueous phase and precipitates with Ca^{2+} ions. Because the rates of dissolution and reaction are much faster than the rate of diffusion, the diffusion of CO_2 gas becomes the rate-limiting process of carbonation. Nevertheless, in the case of concrete used

for underground waste disposal purposes, concrete is almost fully saturated and subjected to a high hydrostatic pressure and the surrounding environment may contain a high bicarbonate concentration, for example clay rock in Callovo-Oxfordian formation [125] or Boom clay in Mol site [126]. Therefore, a combination of diffusion and advection should be taken into account when one considers the carbonation mechanism. This is also the case in accelerated carbonation by applying a high gradient pressure in which advection has a significant contribution to the carbonation process. However, so far as the author is aware, none of published studies considers the contribution of advection to carbonation of cementitious materials.

3.2.3. Factors influencing carbonation

There are many factors influencing carbonation: chemistry of hydration products, free water content, internal relative humidity (RH), pore structure, CO_2 partial pressure and external conditions where carbonation occurs (e.g. ambient relative humidity, temperature, CO_2 concentration and applied pressure).

In general, the higher the CO_2 concentration, the quicker the carbonation proceeds. However, up to a certain concentration, the carbonation may not increase because the retention process resulting from porosity reduction and releasing water overwhelms the effect of higher concentration. Increasing temperature will speed up the carbonation process because the reaction and penetration of CO_2 occurs faster. The core reaction in carbonation is the reaction between CO_2 and portlandite. Therefore, the more portlandite present in the hydration products, the higher the degree of carbonation [127]. Note that a higher carbonation degree is not necessarily synonymous with larger carbonation depth. As an example, the depth of carbonation in concrete produced by cement with a certain replacement of other pozzolanic materials (fly ash, silicafume) may be greater than one produced by ordinary Portland cement (OPC) [120]. However, the carbonation degree may be lower because the amount of portlandite in pozzolanic materials is less than those in OPC due to pozzolanic reaction consuming $Ca(OH)_2$. CO_2 still remains after carbonation at outer layer and it can penetrate more deeply to inner layer of concrete. Also, CO_2 can diffuse more easily through less dense carbonated layer in this case.

Water plays an important role in the carbonation process. Carbonation does not occur without water. It is a catalyst in carbonation reaction even though this reaction releases water. However, water can fill the pores and prevent CO_2 gas to penetrate into the concrete pore network. In fact, carbonation reaches the highest efficiency at an internal relative humidity

between 50-70% [120]. It is worth noting the difference between relative humidity and degree of saturation when carbonation is considered. The degree of saturation is the fraction of the pore volume filled with water while internal RH is the fraction of the ambient vapour pressure to the saturation vapour pressure in pore system. The effect of the former on carbonation is more significant than the latter.

3.2.4. Methods to carbonate cement-based materials and examine its carbonation products

To some extent, the main goal of a carbonation study is to predict the rate of carbonation depth propagation and the service lifetime of reinforced concrete structures. However, carbonation of concrete under atmospheric conditions (low CO_2 concentration) is extremely slow because it is a diffusion-controlled process. The reaction conditions (temperature, RH) may vary due to climate change during carbonation process. Due to the long duration, it is very difficult to study the carbonation and a comparative study is almost impossible to perform due to the inconsistency in carbonation conditions. Therefore, in order to study carbonation a number of accelerated carbonation methods have been proposed.

A standard way is to put concrete samples in a controlled chamber with a specific CO_2 concentration and optimized relative humidity to speed up carbonation [127-129]. This method takes weeks or months to get a carbonation front of several millimetres depending on the CO_2 concentration. A common range of partial pressure of carbon dioxide is from 1% to 10% [130-132]. However, a higher CO_2 concentration [133-135] has been extensively applied to accelerate the carbonation despite the criticism that phenomena would be different from natural carbonation [136, 137] in terms of the chemical composition and the microstructure of carbonated cement-based materials. In order to conclude whether carbonation at different CO_2 concentrations results in different changes in microstructure and mineralogy, one should perform the carbonation experiments until a stable endpoint at which the carbonation process is completely finished. This condition is difficult to reach for natural carbonation in a limited experimental timeframe or even with low CO_2 concentration. Therefore it still needs more quantitative experiments to answer the question about difference in natural and accelerated carbonation with high CO_2 concentration. Nevertheless, it is widely accepted that the moisture evolution during carbonation plays a key role. In accelerated conditions, a large amount of released water due to the fast reaction may not have sufficient time to leave the sample which reduces the carbonation rate. In contrast, less water is released and it has enough time to

diffuse and leave the sample in natural carbonation. For this reason, accelerated carbonation with high CO_2 concentration might not be suggested for kinetic studies.

An alternative method is based on applying a high pressure gradient (tens to hundreds of bar). Concrete samples can reach full carbonation in few hours or even in few minutes. However, the samples can be damaged by micro cracks (elevated pressure) and heat generation (exothermic reaction). The method is mostly applied for CO_2 sequestration or heavy metal immobilization [138-142]. Additionally, accelerated carbonation during curing is found to have great benefits in terms of increasing the mechanical properties and reducing transport properties [143, 144].

In order to characterize the carbonation products, a number of experimental techniques can be used, including methods of mass gain, Thermo-gravimetric analysis (TGA), X-ray diffraction (XRD), chemical analysis, and infrared spectroscopy. Mass gain is a simple method by determining the percentage of mass change of specimen due to carbonation [118, 145]. However, the most common method consists of determining the carbonation depth by phenolphthalein indicator. By observing the colour change of phenolphthalein (pink changes to colourless in carbonated zone because of change in pH), one can quantitatively determine the carbonation depth. Nevertheless, it is not always easy to define clearly where the border is in the case of a non-sharp front. This method cannot detect carbonated area with pH values of higher than 9 [146, 147]. To overcome this problem TGA, gammadensimetry [148], XRD and infrared spectroscopy [147] are more suitable methods. However, these methods are quite complex and time consuming, and require specialized equipment. The principle of TGA is to determine changes in weight of a sample according to temperature changes while gammadensimetry is based on measuring density variations due to the evolution of the water content gradient over time. With the assumption that no water moves out by drying during the carbonation process, the CO_2 profile can be drawn based on the density increase. This method also provides water content profiles, which is important input data for modelling [149]. XRD is a destructive technique to identify crystalline phases. This method can detect portlandite and amorphous hydrated products [150]. Infrared (IR) spectrometry is used to identify the different forms of calcium carbonate (calcite, aragonite, vaterite) [151] by its characteristic infrared absorption wavelengths. Optical microscopy or/and scanning electron microscopy (SEM) are other useful approaches to study how the microstructure changes after carbonation.

3.2.5. Influence of carbonation on microstructure and transport properties

It is generally believed that carbonation decreases transport properties (permeability, diffusivity) [152-154], and refines pore structure (porosity, pore size) [132, 152] of Portland cement-based materials. However the extent of modification in transport properties and microstructure significantly depends on carbonation conditions (RH, CO_2 concentration, etc.) and cement types. The reduction of permeability and diffusivity is the result from the precipitation of carbonation products (mainly calcite) in the pore structure. This leads to a significant reduction of the total porosity (molar volume of portlandite is smaller than molar volume of calcite), and thereby transport properties.

In blended cement systems (containing ground granulated blast-furnace slag – BFS or fly ash – PFA), the carbonation depth propagation can be faster than in OPC system due to lower portlandite content. The modifications in microstructure are also expected to occur in different ways. Kinoshita *et al*. [133] investigated the carbonation of blended cement systems with a very high replacement level of OPC with BFS or PFA in accelerated conditions (15% CO_2, 50–60% RH). It is observed that in the BFS:OPC = 9:1 system, the space of C–S–H gel is occupied by grain-like products after carbonation, leaving a distinctive pore structure of up to several micrometres, while not observed in the microstructure of the OPC and PFA:OPC = 3:1 systems. The porosity increase in BFS/OPC paste was also reported by Borges *et al*. [155] despite accelerated or natural carbonation, and was attributed to the carbonation of C-S-H gel. However, Borges also observed a porosity increase in PFA/OPC pastes but with higher replacement (40-75%).

In lower puzzolanic additive replacement systems (30% PFA, 65% BFS), Ngala *et al*. [156] found that there is not only a reduction in the total porosity in both OPC and blended pastes with carbonation, but also a redistribution of the pore sizes. The proportion of large pores (diameter> 30 nm) is increased slightly for OPC pastes but much more significantly for the BFS and PFA pastes. This is in line with the findings of Pihlajavaara [157] who stated that the carbonation seems to affect more the larger pores (20 – 100 nm) than the smaller ones.

Liwu Mo *et al*. [158] studied the effects of accelerated carbonation on the microstructure of Portland cement pastes containing reactive MgO in accelerated condition with mostly pure CO_2 (99.9%) and high RH (98%). It has been found that the degree of porosity reduction is larger with the increase of reactive MgO content.

Most published studies report a decrease in specific surface area after carbonation [159-162]. The decrease is due to both a decrease in total porosity and a shift in a pore size distribution

towards smaller pore sizes. Houst [160] showed that specific surface area is significantly reduced after carbonation. For cement paste with w/c ratio of 0.3, that specific surface area of carbonated material is 70% of the non-carbonated material. The decrease is higher with an increase in w/c ratio, down to 43% for sample with w/c ratio of 0.8. Pihlajavaara [157] observed the same phenomenon in which cement paste with w/c ratio of 0.3 exhibits a smaller specific surface area decrease (44%) compared to one with w/c ratio of 0.45 (50%). Chen *et al*. [161] also found a decrease in specific surface area of low heat carbonated Portland cement paste, but only for samples with pre-curing in water. The specific surface area sharply decreases by about 50% after 21 day carbonation. For those without pre-curing, the specific surface areas vary in narrow range regardless the carbonation time (up to 70 days). Johannesson *et al*. [162] reported that the specific surface area of OPC paste is slightly decreased after carbonation. The specific surface area of well-carbonated paste is 29.4 m^2/g compared to 31.8 $m^2/$ of non-carbonated paste.

Specific surface area of carbonated cementitious materials is sometimes increased as shown by You *et al*. [163]. The specific surface area of carbonated waste cement (from a recycling process to recover coarse aggregate from waste concrete) increases linearly with the increase of the carbonation degree. The observation is explained due to the formation of highly polymerized silica gel.

Carbonation in OPC systems normally results in a decrease in the transport properties, but carbonation under supercritical conditions (high pressure) or in blended cement systems with high additive replacements could sometimes increase the transport properties. Borges *et al*. [132] showed that permeability increases for composite cement pastes containing high amounts of BFS (BFS:OPC = 3:1 and 9:1) subjected to accelerated carbonation, due to carbonation shrinkage and cracking during testing. Although carbonation has resulted in an overall density increase and overall porosity decrease, OPC pastes, however, do not show a significant change in permeability after carbonation.

For the Nirex reference vault backfill (NRVB) cement pastes (containing 6% Portland cement, 28.6% limestone powder, 9.8% lime, and 35.6% water) which have high porosity, Rochelle *et al*. [164] showed that the carbonation under high pressure (4 and 8 MPa) decreases 3 orders of magnitude for water permeability and 2 orders of magnitude for gas permeability. Even higher permeability decrease has been observed for cement grout as reported by Dewaele *et al*. [165]. The carbonation of cement grouts (w/c ratios of 0.4 and 0.47) under high pressure decreases the permeability in carbonated layer from two to six

orders of magnitude. Carbonated samples exhibit a smaller average pore size and an increased specific surface area compared to non-carbonated samples.

Liteanu *et al*. [153] measured the permeability changes in wet mature Class A wellbore cement exposed to supercritical CO_2 (30 MPa confining pressure, 10 MPa CO_2 pressure, 80°C). Water permeability measurements of unfractured cement show a continuous and significant decrease during exposure to static CO_2 rich-fluids. The intrinsic permeability is decreased from 1.8×10^{-16} m^2 down to 5.2×10^{-17}, 3.8×10^{-17} and 8.3×10^{-18} m^2 after one, two and three months of exposure, respectively. For fractured samples, permeability decrease is not strong despite the fact that the fractured samples showed heavy carbonation in the fracture plane. The permeability is decreased from 3.9×10^{-14} m^2 to 1×10^{-14} m^2 after one month reaction and remained constant afterwards. In case of accelerated carbonation under atmospheric pressure, the degree of permeability reduction is much lower than carbonation under high pressure. Under accelerated carbonation (65% RH, 5% CO_2, 25^{o}C), Song *et al*. [166] showed that the permeability of carbonated concretes are 3.2 and 2.7 times lower compared to reference concretes after 4 month carbonation for w/c ratios of 0.65 and 0.55, respectively. In the same carbonation conditions, Claisse *et al*. [154] showed there is only a small increase in the impermeability index. After 140 days of exposure to CO_2, carbonation leads to an approximately 37 percent and 4 percent increase in the impermeability index (defined as $\log_{10}(1/k)$) for concretes with w/c ratios of 0.6 and 0.45, respectively.

On the other hand, Lesti *et al*. [167] reported a permeability increase of cement-based materials exposed to supercritical CO_2. Most of the samples exhibit gas permeability increases of 2 to 4 orders of magnitude after 6 month exposure, except for the fly ash containing cementing system which shows no increase after one month exposure and only a slight increase in permeability after six month exposure. The authors attributed the increase in permeability to crack formation as a consequence of expansion during $CaCO_3$ crystallization. This statement is in line with the findings of Fabbri *et al*. [168] who showed that micro crack formation during supercritical CO_2 induces not only an increase of its permeability but also a degradation of the mechanical properties of cement-based materials.

Studies on changes in diffusivity due to carbonation are rare, perhaps due to long experimental time needed to measure the diffusion coefficient of carbonated materials. Ngala *et al*. [156] concluded that carbonation of cement pastes has a large effect on diffusion. The effects are more significant for the blended pastes than for plain OPC pastes. It is surprising that the effective chloride diffusion coefficient in blended pastes increases by two orders of

magnitude while oxygen diffusion coefficient increases by one order of magnitude. The reasons could be attributed to larger capillary porosity observed in carbonated sample despite smaller total porosity. The coarsening of the pore structure is attributed to the formation of additional silica gel due to the decomposition of the C-S-H gel.

Portlandite is the main phase to carbonate in most cases, however, under accelerated conditions other phases may be carbonated, especially C-S-H. When C-S-H is carbonated, a decalcification occurs, leading to a C-S-H with a smaller molar volume and a smaller Ca/Si ratio compared to non-carbonated C-S-H as shown by Morandeau *et al*. [130]. If the pore volume created by C-S-H carbonation is not compensated by formed calcium carbonation, the carbonation of C-S-H will result in a porosity increase.

3.3. Calcium leaching

3.3.1. Introduction

Leaching is a process of ion extraction from solid compounds by dissolution. In cement based-materials, leaching of calcium, also called decalcification, is of utmost importance because of the high calcium (Ca) content in cement compared to other potentially leachable ions (Fe^{2+}, Al^{3+}, Mg^{2+}, etc.) and the high solubility of the aqueous Ca-controlling phase portlandite. Ca-leaching is one of the most serious degradation processes in concrete and reinforced concrete structures for the very long-term (nuclear waste disposal system) or in hydro structures (dam, bridge, water tank) but it has only been studied since the 1980s despite the long history of concrete. The reason is that leaching of concrete is an extremely slow process under normal conditions (few mm leaching front in a hundred years [169]). However, the lifetime of civil concrete structures is normally under one hundred years and that is too short to see the effects of leaching degradation. Leaching of cement-based materials changes its properties such as a reduction in pH, an increase in porosity and transport properties and detrimental effects on properties related to long-term durability.

3.3.2. Chemical and physical leaching process

Ca-leaching is a dissolution-diffusion process of dissolved Ca ions in the pore solution. This happens when the cement matrix is in contact with a low pH or low alkaline solution. The typical pH value of the pore solution of concrete is about 12.5-13, therefore, any solution with pH below this range (e.g. water) is considered as an aggressive environment to concrete. During leaching, dissolution is much faster than diffusion; hence the solid-liquid equilibrium curve of calcium has been commonly used for understanding different stages of leaching.

Berner [170] is the first researcher who proposed the solid-liquid equilibrium curve by compiling experimental solubility data available in literature. The curve is composed out of three almost linear parts characteristic for the different leaching stages.

In the first stage, where the Ca concentration in the aqueous phase is higher than 20 mol/m^3, portlandite is quickly dissolved. Portlandite has the highest solubility amongst all calcium containing solid phases in cement matrix. Portlandite is entirely dissolved and does not re-precipitate like C-S-H. In the second stage, where the Ca concentration in aqueous phase is higher than 2 mol/m^3 and lower than 20 mol/m^3, C-S-H is partially dissolved. Sulfoaluminates are also dissolved in this stage [171]. The dissolution of C-S-H is incongruent, in which C-S-H with higher Ca/Si ratio completely dissolves and re-precipitates at a lower Ca/Si ratio C-S-H [172]. In the third stage, where the Ca concentration in the aqueous phase is lower than 2 mol/m^3, the partially leached C-S-H continues dissolving at a faster rate to form silica gel which is the end product of leaching.

When dissolved in pore solution, calcium ions will leach out by advection or diffusion. Advective removal of Ca is governed by the water flow and is the quickest leaching degradation of a concrete structure. However, it is not common in reality except in some special structures like dams or water tanks. Diffusive removal of Ca is much slower but more common and is controlled by the Ca concentration gradient. Both diffusion and advection are governed by the microstructure of concrete which is changed during leaching.

3.3.3. Factors influencing leaching

There are many factors influencing the leaching of cementitious materials. Among them, the main factors are listed below:

- Diffusivity and permeability (in case of flowing water) are the most important factors. These factors determine how easy Ca ions are transported out of the cement matrix.
- Surrounding solution: the lower the pH of the solution, the higher the leaching rate. Leaching in flowing solution is faster than in static solution. Solutions with the ability to increase the solubility of calcium containing solid phases (e.g. ammonium nitrate) can significantly accelerate the leaching process. Leaching in deionized water occurs quicker than in hard water.
- An electrical field could accelerate the leaching process because of the increasing Ca ion movement in the pore solution towards electrode of opposite charge [173].

- Saturation degree: partially saturated concrete can undergo leaching, but with much slower rate compared to saturated concrete.
- Initial amount of Ca in solid phases: the higher the total amount of Ca in concrete (especially the amount of portlandite), the higher the potential of leaching.

3.3.4. Experimental methods to study leaching

Considering the slow degradation process but the need to study long-term durability of concrete, accelerated testing is a relevant approach to better understand the effect of leaching on the alteration of microstructure and transport properties. A variety of accelerated methods have been proposed such as applying an electrical field [173], using deionized water [174, 175], using low pH solutions [176, 177]; applying flow-through conditions [178] or using high concentration ammonium nitrate (NH_4NO_3) solutions [179, 180]. Among them, using an ammonium nitrate solution to accelerate the leaching kinetics is one of the most popular methods because it results in faster degradation compared to other methods under diffusive-transport conditions while it results in the same end-products. The mechanism of acceleration is not only due to the lower pH of NH_4NO_3 solution but primarily because of the increase in the solubility of the leachable phases in cementitious matrix induced by NH_4NO_3.

Many studies quantify the propagation of degraded depth of leached materials and characterize its mechanical behaviour [181, 182]. However, there are only a few studies that discuss the modification of the microstructure after leaching [183, 184] and the effects of leaching on transport properties [185, 186]. The post-analysis techniques used for characterizing carbonated materials (Section 3.2.4) are also applied to study leached materials. However, care must be taken while preparing samples of leached cement-based materials. Due to significant loss in mechanical properties, the samples must be handled in a proper way to preserve the integrity of leached materials.

3.3.5. Influence on microstructure and transport properties

One might intuitively presume that leaching alters the cementitious materials to a material with coarser microstructure and higher transport properties. And this presumption is confirmed by literature. However, to what extent the microstructure and transport properties are modified, is still questionable.

With regard to accelerated leaching in ammonium nitrate solution, most studies report an increase in porosity and coarser pore size distribution. Nevertheless, the level of modifications strongly depends on the compositions of the native materials. In general, cementitious

materials with less portlandite content exhibit a better leaching resistance, and the same trend is observed for materials having pozzolanic activity.

Berra *et al*. [187] showed that adding 3.8% nanosilica could slightly reduce the porosity increase due to accelerated leaching of cement paste CEM I, however, the decrease of compressive strength of the leached specimens is significantly retarded. Porosity even decreases for mortars with cement CEM III (blast-furnace slag) and CEM IV (fly ash +limestone filler) due to precipitation, as reported by Segura *et al*. [188]. However, porosity still increases for long time (more than 2-week leaching). A maximum porosity increase of about 30% has been observed for CEM I mortars after 32-day leaching regardless the w/c ratio. The pore surface area significantly increases, but critical pore diameter and threshold pore diameter (the largest pore size at which pore volume is significantly increased) are almost unchanged for CEM III and CEM IV mortars. However, the critical and threshold pore diameters increases for CEM II and CEM I mortars, respectively. The effect of slag admixture to cement mortar in the reduction of porosity increase was also found by Cheng *et al*. [189]. The porosity increase is a function of degraded depth as pointed out by Poyet *et al*. [184]. A huge porosity increase from 26% to 80% has been reported at the surface directly in contact with ammonium nitrate solution for cement paste with w/c of 0.5 and 18.5% fly ash replacement.

In an attempt to assess the influence of cement type on transport properties and Ca-leaching, Perlot [185] performed accelerated leaching in ammonium nitrate solution on two mortars made from CEM I and CEM V/A (22% fly ash and 22% blast furnace slag). The fly ash and blast furnace slag addition not only improves the microstructure of sound mortar, but also increases the resistance against leaching. Even while having a similar porosity, the chloride diffusivity is 5 times lower for sound CEM V/A mortar. After leaching, the porosity and specific surface area are doubled and tripled, respectively, in both leached mortars. The alterations of transport properties are similar for both mortars regardless its difference in initial transport properties (and microstructure): gas permeability increases more than one order of magnitude while chloride diffusivity increases less than one order of magnitude. Agostini *et al*. [190] confirmed that the degree of gas permeability is the same for CEM II/B-M mortars despite its difference in w/c ratios (0.5 and 0.8). The permeability in the leached zone in which portlandite is completely dissolved and C-S-H is partially leached increases more than two orders of magnitude under ammonium nitrate leaching. However for both

mortars tested, major variations in permeability (and microstructure) are thought to be linked to portlandite leaching, minor alteration is attributed to C-S-H decalcification.

Sometimes, as in the study of Yurtdas *et al*. [191], a reduction in permeability for leached material is observed. The water permeability of the degraded material is lower than that of sound material during triaxial compression tests, although ammonium nitrate leaching leads to significant increase of porosity of cement paste (approximately 50%). This is due to the plastic deformation of the leached material which allows a compaction without cracking. However, under measuring conditions without confining pressure, the permeability of the degraded material is about 2.4 times higher than that of the sound material.

Gallé at el. [186] investigated the leaching behaviour of a CEM I cement paste and of a concrete prepared with almost similar w/c ratios (0.45 and 0.43, respectively). Until the complete dissolution of portlandite, water porosity is doubled for both cement paste and concrete, respectively from 33% to 61% and 10% to 19%. The authors observed that C-S-H is also significantly affected by leaching in ammonium nitrate solution which contributes about 13% porosity increase. A significant increase in water permeability is observed, more than two orders of magnitude for both leached cement paste and concrete in which all the portlandite is completely dissolved. Note that confining pressure was also applied to measure permeability like the case of Yurtdas *et al*. [191], but a decrease in permeability of the leached materials was not observed. The permeability increase is assumed to be related to the newly created porosity which is mainly due to portlandite dissolution.

In order to investigate diffusivity changes at different degradation stages, Bernard *et al*. [116] performed the leaching tests on CEM I cement paste and mortar with the same w/c of 0.4. The authors showed that at the degradation stage at which porlandite, hydrated aluminates and sulfoaluminates disappear, the effective diffusivity of HTO is increased 118 times for either cement paste or mortar. While only portlandite is disappearing, the diffusivity is only increased 31 times for both cement paste and concrete.

Instead of using ammonium nitrate solution, Saito *et al*. [173] applied an electrochemical method to accelerate the leaching. A potential gradient of 10 V/cm is applied on a mortar with and without pozzolanic admixture replacement (blast furnace slag and silica fume). The porosity is increased two times in OPC mortars while it is only increased by 40% to 50% in the pozzolanic admixture replacement mortars. This results in a large difference in water permeability alterations. The water permeability in the degraded region increases by about

two orders of magnitude in the OPC mortars, but only by one order of magnitude in the pozzolanic replacement mortars regardless the same starting permeability.

The number of studies on leaching using deionized water is limited due to long experimental time. Jain *et al*. [175] investigated the leaching of plain paste (CEM I/II), pastes with 10% replacement of cement by fly ash and glass powder, and paste with 6% replacement of cement by silica fume. All pastes have the same w/c of 0.4. The porosity of all the cement pastes increases with leaching duration. The plain pastes show the highest increase, up to 11% after 90 days of leaching. The glass powder modified pastes show the lowest porosity increase, only 5% because the presence of NaOH in its pore solution reduces the solubility of portlandite. The silica fume/fly ash modified pastes show a similar porosity increase of about 8%. Porosity increase is mainly caused by portlandite dissolution, although C–S–H decalcification also contributes to porosity increase for long leaching duration. After 90 days of leaching, C-S-H contributes almost 3%, while portlandite contributes 8% to the total porosity enhancement. Haga *et al*. [192] performed leaching experiments on OPC cement paste with high w/c of 0.7 using ion-exchanged water. The pore size distribution after leaching for 56 weeks shows an increase in the pore volume in the pore size range between 0.05 and 0.5 µm. The total pore volume of the sample is increased 22% after 56 weeks of leaching. C-S-H leaching is also observed and contributes about 6% of the porosity increase which is determined by comparing experimental total porosity results and the calculation of porosity increase resulting from portlandite dissolution.

In a comparison study, Carde *et al*. [179] performed the leaching tests on the same CEM I cement paste with w/c of 0.5 using ammonium nitrate solution and deionized water. The pH of deionized water is lowered to 4.5 by nitric acid addition in order to increase the leaching kinetics. Results show that both environments lead to total portlandite dissolution in the degraded zone and to a progressive decalcification of C-S-H, but the kinetics is much faster when using of ammonium nitrate (2 orders of magnitude). At the same leaching degree, the porosity increase is the same for both conditions.

3.4. Concluding remarks

Leaching and carbonation of cement-based materials are slow processes but relevant for assessment of long-term (reinforced) concrete durability. Many experimental approaches exist to understand the behaviour of degraded materials at different degradation stages. Most of the approaches rely on accelerated techniques by making the environmental conditions more

aggressive. However, there is still on-going discussion regarding whether the degradation mechanism in accelerated conditions is the same to natural conditions. If it is, it is still not generally validated how to extrapolate the accelerated testing conditions to real performance. To answer this key question, one has to validate the accelerated methodologies against natural testing conditions in detail in which the changes in mineralogy and microstructure at certain degradation stages should be identical or mostly similar for both conditions.

One important thing that cannot be captured in accelerated tests is the continuous hydration of cement-based materials. Under natural conditions there is still evolution of the hydrated cement matrix structure, while under accelerated conditions the continuous hydration is not taken into account due to shortened experimental time. It is generally assumed that accelerated tests can be used for the characterization of degraded materials and its resistance to chemical degradation. However, it is not fully recommended to use accelerated testing for the kinetic study in term of predicting the degradation rate under natural conditions.

There is an agreement in literature that carbonation and leaching change the transport properties of cement-based materials, but to what extent is still questionable. The confusion comes from the unclear definition of what exactly is a leached material; whether it concerns complete/partial portlandite dissolution or complete portlandite dissolution + partial C-S-H dissolution. To better understand how far the transport properties are altered due to chemical degradation, changes in mineralogy and microstructure should be intensively examined.

CHAPTER 4: MATERIALS, MIX DESIGN AND EXPERIMENTAL METHODS

4.1. Materials

All experiments were performed on cement pastes made from cement, tap water and limestone filler. Type I ordinary Portland cement (CEM I 52.5 N) was used. The cement has quite high Blaine specific surface of 4350 cm^2/g.

Table 4.1 gives a summary of the chemical properties. Limestone filler (Calcitec 2001S) used has a Blaine specific surface of 3500 cm^2/g and a $CaCO_3$ content of 98.30%. Other chemical and physical properties are shown in Table 4.2. Superplasticizer Glenium 27 was added to the mix with content of 0.5% with respect to mass of cement.

The materials used in this study are simulated (but without coarse aggregates) the one used for Belgian Supercontainer (see Figure 1.1) which is new reference design for disposal of high-level waste and spent fuel [193]. There are some restrictions to the selection of materials of the Portland concrete buffer (self-compacting concrete) [6]. It is recommended that the used cement should have a limited hydration heat generation to avoid/limit thermal cracking. The amount of sulphate and aluminium is as small as better, which reduces the sulphate attack and the ettringite formation resulting in deteriorate hardened concrete structures. Additionally, the cement matrix should offer a high pH environment to prevent the corrosion of steel overpack. For those reasons, the Portland cement CEM I has been chosen and pozzolanic reaction materials (fly ash, silicafume, etc.) are avoided to prevent pH drop.

Limestone has been used as filler and aggregates because it contains low reactive constituents (silicon, aluminium, magnesium), which limits the alkali-aggregate reaction resulting in expansion and cracking [194]. Furthermore, limestone filler can help to increase viscosity and stability of the concrete [195]. The replacement of cement by limestone filler may also reduce the heat generation (at a given w/p ratio). The use of organic admixtures is limited as it results in a H_2 gas pressure buld-up in the concrete buffer under irradiated conditions [194]. Therefore, it is recommended to use as low as possible amount of superplasticizer (polycarboxylate based – such as Glenium 27) in order to increase the workability of the fresh concrete. In general, the chemical compositions of used materials should be as simple as possible and do not make the mineralogy complex after hydration.

Table 4.1. Chemical compositions (wt. %) of the cement (from manufacture fact sheet)

CaO	63.0%	Chromium(VI)	$<2.10^{-4}$%
SiO_2	20.0%	Cl^-	0.06%
Fe_2O_3	3.0%	Na_2O eq.	0.85%
Al_2O_3	5.0%	Loss on ignition	1.60%
Sulphate SO_3	2.9%	Insoluble residue	0.50%

Table 4.2. Chemical and physical properties of limestone filler (from manufacture fact sheet)

Density	2.7 g/cm^3	$CaCO_3$	98.30%
Blaine specific surface	3500 cm^2/g	MgO	0.36%
Particle size distribution:		SiO_2	0.75%
Passing 2mm	100.0%	Al_2O_3	0.25%
Passing 500µm	99.9%	Fe_2O_3	0.10%
Passing 125µm	97.0%	Na_2O eq.	0.05%
Passing 63µm	77.0%	pH	9.5
D_{50} (50% passing)	10.1µm		

4.2. Factorial experimental program

In order to investigate the effects of water/powder (w/p) ratio and the cement replacement by limestone filler (ls/p) on water permeability, diffusion of dissolved gas, carbonation and Ca-leaching, a factorial experimental design has been proposed. In cement industry, Portland limestone cements have been produced by inter-grinding clinker and limestone (and gypsum) in which different limestone/(limestone + clinker) ratios are initially chosen. Therefore, the "water/cementitious material" ratio for Portland limestone cement is actually the "water/powder" ratio. To keep consistence, w/p ratio and limestone filler replacement were chosen in this study instead of w/c ratio and limestone filler replacement. However, dilution effect due to limestone filler addition can be easily investigated by converting w/p ratio to w/c ratio.

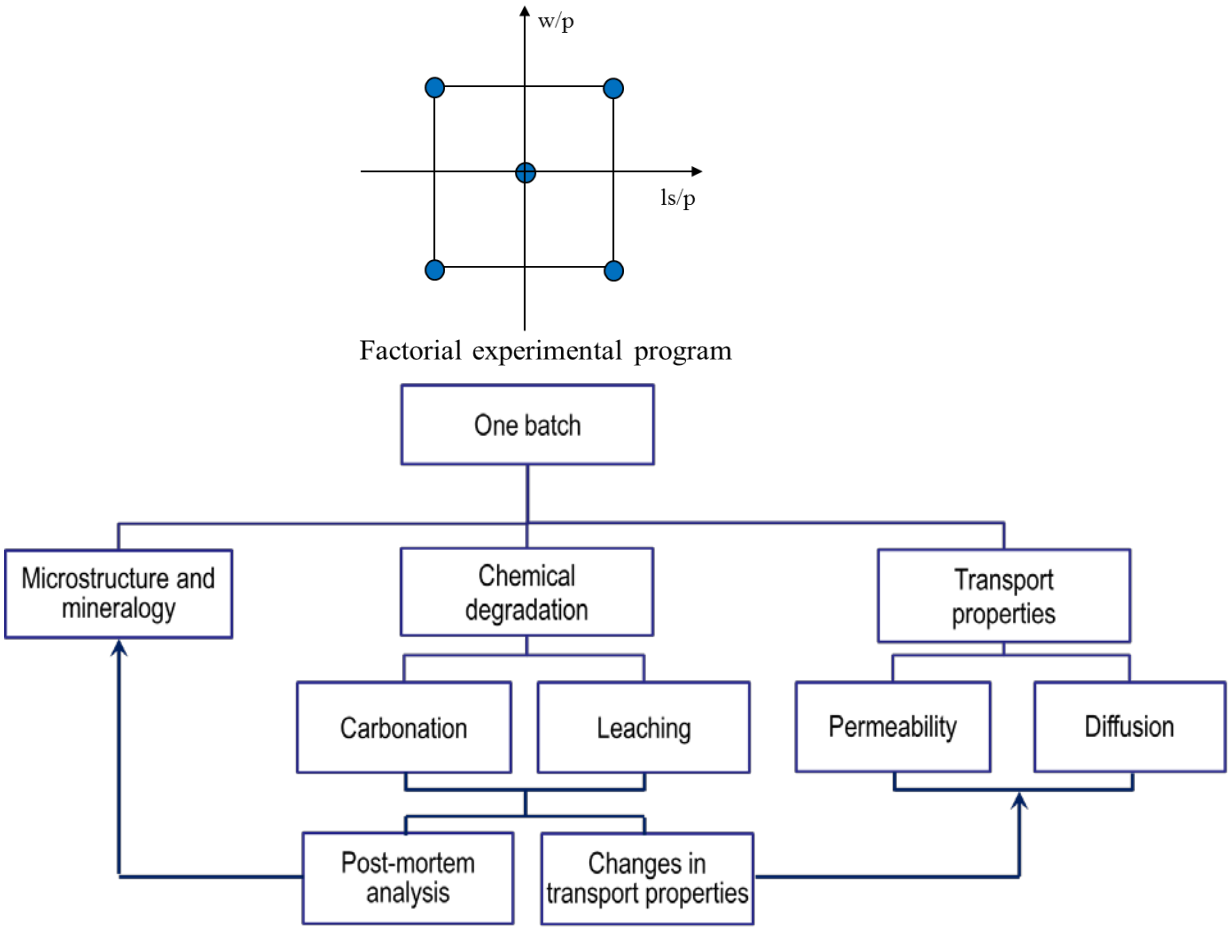

Figure 4.1. General experimental program: 3 sets of samples (for transport property measurements, chemical degradation tests and quantification of initial microstructure and mineralogy) were prepared for each batch to take into account the continuous hydration of cement pastes. The degradation tests were followed by a series of post-mortem analyses and determination of changes in transport properties.

In this design, w/p ratio varied from 0.325 to 0.425; limestone filler replacement ratio varied from 0 to 20%. Those ranges were selected based on one of the real mixtures developed for radioactive waste repository. This design has 2^2 factorial points and 1 centre point. A detail of the design is shown in Table 4.3 and graphically presented in Figure 4.1. The run order was randomly generated to eliminate a bias. It is supposed that this designed experiment can produce significantly more information and requires fewer runs. Note that due to limited time for experiments in the PhD timeframe and long-time needed for diffusion and carbonation experiments, the full factorial experimental program was only applied on water permeability measurements and leaching experiments. For carbonation and diffusion experiments, only few points in the factorial experimental program were chosen for investigation (detailed later in Chapters 5 and 6).

Table 4.3. Detail of factorial experiment design: LS = limestone filler; SP = superplasticizer

Run order	Cement kg	LS kg	Powder kg	Water kg	w/c -	w/p -	ls/p %	SP l	Sample
1	450	0	450	146	0.325	0.325	0	2.3	S1
2	360	90	450	191	0.531	0.425	20	1.8	S2
3	450	0	450	191	0.425	0.425	0	2.3	S3
4	405	45	450	169	0.417	0.375	10	2.0	S4
5	360	90	450	146	0.406	0.325	20	1.8	S5

4.3. Experimental methods to determine transport properties

4.3.1. Determination of water permeability using a controlled constant flow method

4.3.1.1. Research significance and principle

The review of existing methods to measure permeability of porous materials shows that a particular technique is only suitable for specific purposes. There is a need to have a flexible and sensitive method suitable for measuring permeability changes due to chemical degradation of concrete. The technique should meet three requirements: short measurement time; reliability and being simple enough to apply. Because none of the reviewed techniques meets all these requirements, an improved direct method was proposed. The proposed method is very flexible and it is convenient to do further tests on the same sample. The samples can be decoupled after the test and connected to another setup in which the diffusivity can be tested or to perform carbonation tests. After a carbonation test, the samples can again be connected to the permeability setup to study the effect of carbonation on the permeability. The integrated tests also enable for studying the transport properties of leached samples. A sequence of different tests on the same sample is possible by using quick couplings which help to disconnect the permeability cell (embedded sample inside) from the rest of measurement device and recouple it to another setup compatible with the permeability cell.

The proposed technique was based on the technique used to measure permeability of low-permeable clay materials (10^{-12} – 10^{-13} m/s) at the Belgian Nuclear Research Centre [196]. The diameter of the sample was increased while the height was decreased, which helps to obtain higher flow compared to the original method for clayey materials. A specially designed permeability cell allows applying higher pressure gradients. Controlling and measuring of the pressure and flow rate were improved by using Syringe pumps. The principle is quite simple. A pressure gradient of 5 to 10 bar was applied by controlling the pressure at both sides of a saturated cement-based core embedded in a permeability cell. When the flow reaches almost steady state, the constant pressure mode was changed to the constant flow mode. Instead of

measuring the flow rate like existing direct techniques, the pressure was measured, which is much more accurate than measuring flow rate. The pressure and water flow were controlled by precise Syringe pumps. A good contact between the cement-based materials and the permeability cell was obtained by testing different resins.

4.3.1.2. Experimental program and setup

A full factorial experimental program was applied to investigate the effects of limestone filler replacement and w/p ratio on water permeability. In order to check the validity of Darcy's law, permeability measurements were performed on a Ca-leached sample. The leached sample which was degraded in ammonium nitrate solution 6M in 28 days had a w/c ratio of 0.53 and 20% limestone filler replacement (sample S2). The permeability of the leached sample is expected to be considerably high which allows achieving a large flow rate with a relatively low applied gradient pressure. Various flow rates were applied to check whether a linear relationship exists between driving pressure gradient and flow rate.

A schematic view and a picture of the experimental setup are presented in Figure 4.2 and Figure 4.3, respectively. The core of the system is the permeability cell which consists of an outer part of steel and an inner part of polycarbonate (Figure 4.4). The steel part allows applying a high pressure gradient. An outer part made of polycarbonate (e.g. to limit production costs) would stand only low applied pressures. The polycarbonate inner part enables a visual check of the contact between the resin and the sample and is useful in further post-mortem analysis by X-ray. In order to improve the friction between the inner part and the sample, grooves were created on the surface of the inner part. Good fitting of the inner and outer parts was obtained by their conical shapes.

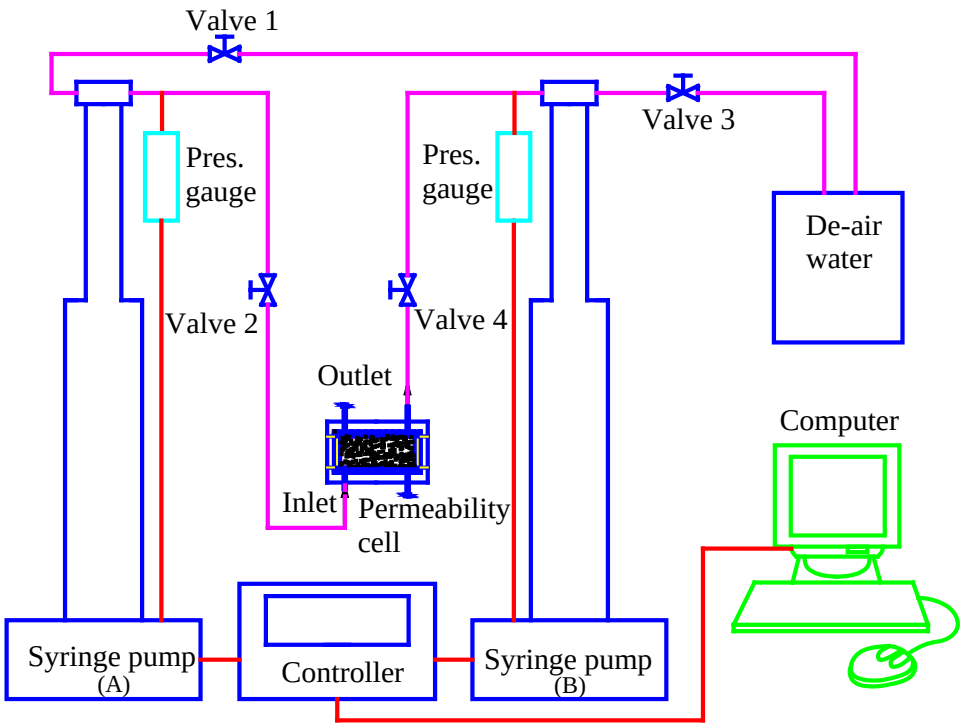

Figure 4.2. Schematic test setup for permeability determination

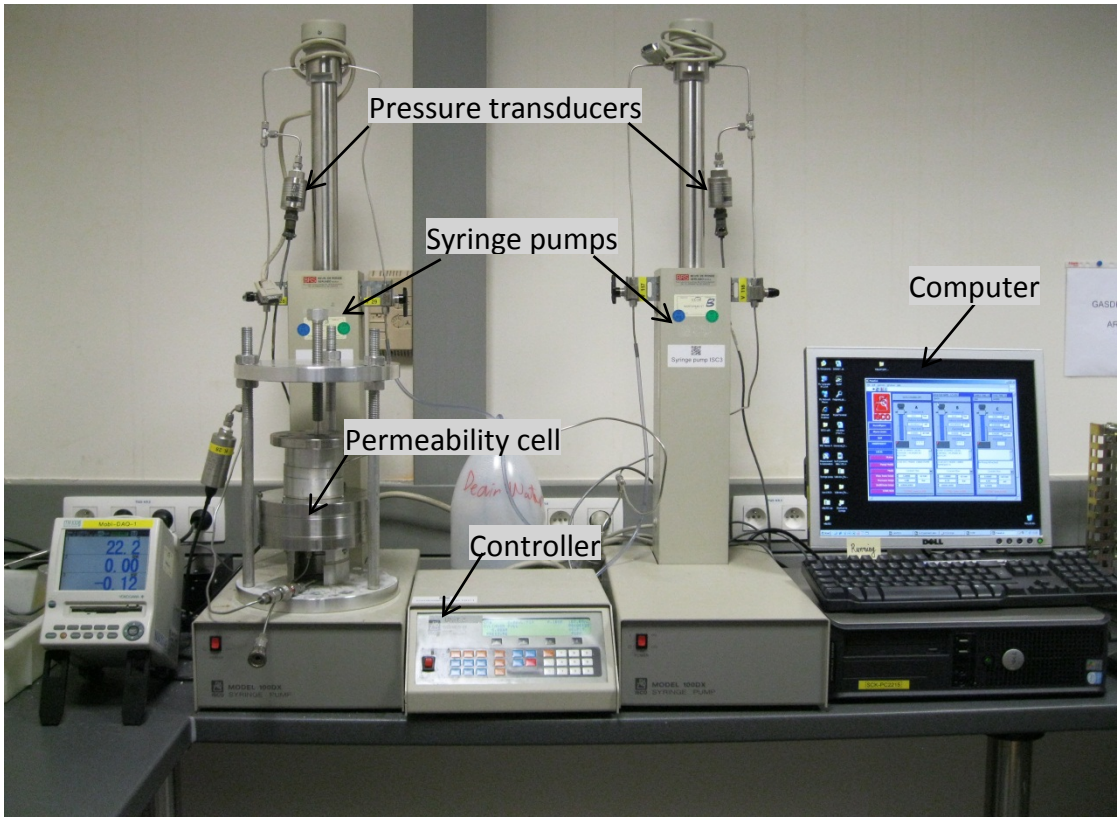

Figure 4.3. Photo of permeability experiment

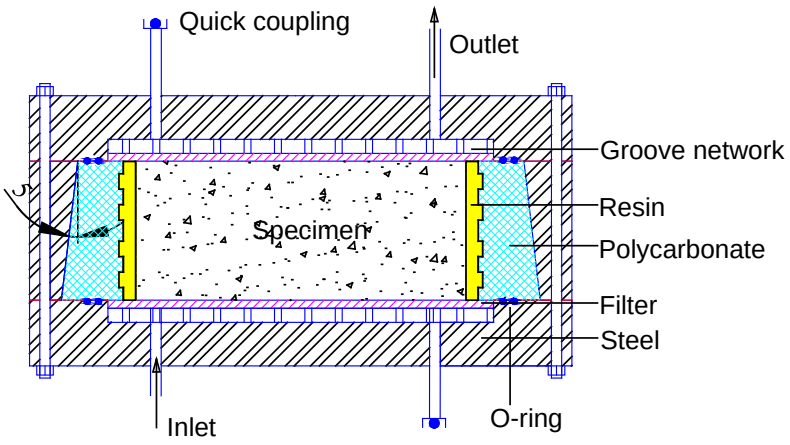

Figure 4.4. Details of permeability cell

The sample disk with a diameter of 97.5 mm and thickness of 25 mm was embedded into the inner part of the cell by a resin. The choice of an efficient resin is crucial to avoid leakage around the side of the sample. The resin should have low viscosity, good contact with polycarbonate and cement paste, high strength, transparency and low heat generation during embedding. From a series of tested resins, Sika® Injection-451 was selected as the most optimal choice.

The top and bottom lids were also made of steel. The inner surfaces of the lids had a special design with a groove network to distribute water evenly on the surface of the sample (see Figure 4.5). Cellulose membrane filters with high water flow rate (30 ml/min at $\Delta p = 1$ bar) were placed between the sample sides and the lids to prevent particle transport and improve the distribution of water. Quick couplings (SWAGELOK, Ohio, USA) helped to expel air and fill all connection tubes before measuring the permeability.

Two Isco Syringe pumps, model 100DX, were used to apply either a pressure gradient or constant flow rate on the permeability cell. These two pumps were connected to one pump controller. The controller was connected to a computer through a RS-232 port. The Syringe pumps were capable of providing stable and accurate flows as low as 0.01 µl/min which is an absolute requirement for measuring the permeability of low-permeable materials. The pumps also provided a stable and precise pressure with the accuracy of 0.5% full scale. Data were recorded and stored on the computer every minute.

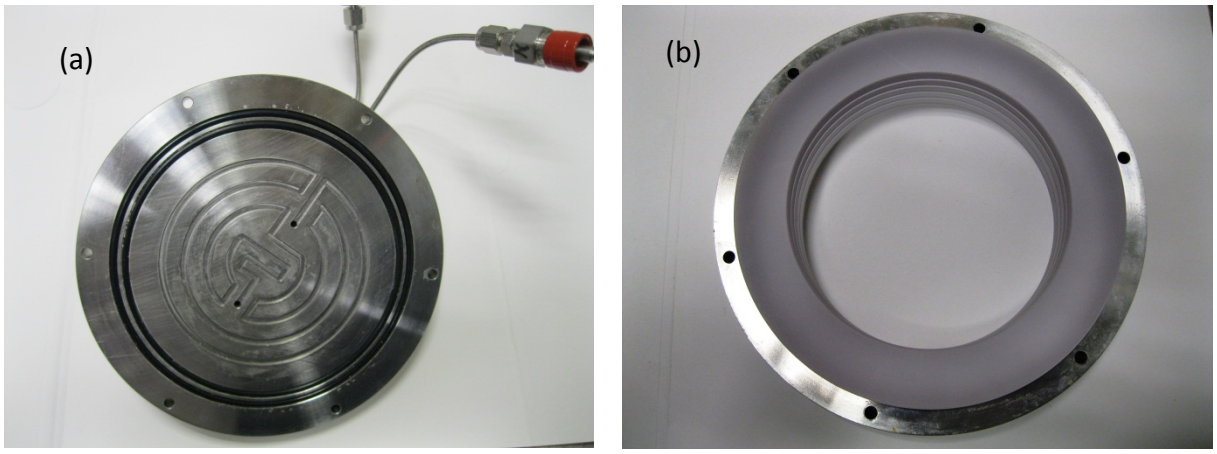

Figure 4.5. Lid (a) and body (b) of permeability cell

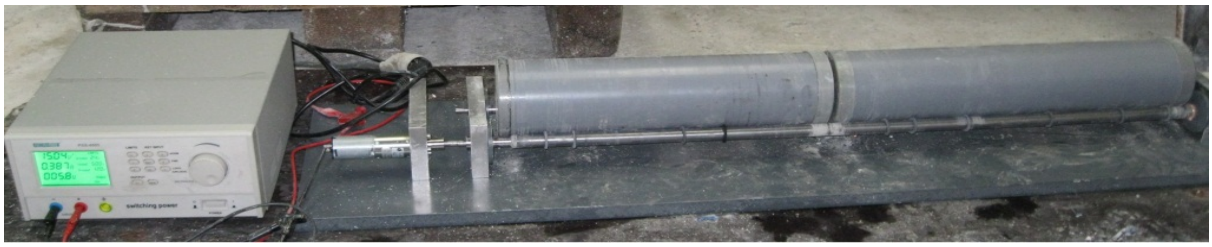

Figure 4.6. Rotation machine to prevent segregation

4.3.1.3. Experimental procedure and data analysis

Cement paste was poured in a cylindrical PVC tube with inner diameter of 97.5 mm. The sample was then rotated during 24 hours at a speed of 3 revolutions per minute to prevent segregation (see Figure 4.6). Afterwards, the sample was cured in a sealed condition in a temperature controlled room (22 ± 2^{o}C) for 27 days. The 28-day-cured cement paste was sawn into 30 mm thick slices. The disks were then embedded into the polycarbonate part of the permeability cells. It took 24 hours for the resin to polymerize before polishing to obtain the final sample thickness of 25 mm. The samples were afterwards saturated under vacuum conditions using following procedure (Figure 4.7):

– Open valves 1, 2 and 3 while keeping valve 4 closed; run vacuum pump for 3 hours to remove air in the samples and lime water.

– Close valve 1 and open valve 4 (valves 2 and 3 are still opened); slightly open the vent on the chamber with lime water to increase somewhat the pressure to make the water flow to the sample chamber. Lime water will be drawn towards the sample chamber due to the vacuum. Close valve 4 when the samples are fully submerged in lime water; keep the

vacuum pump running for one hour.

– Remove the vacuum; leave the samples for soaking for 20 hours at atmospheric pressure.

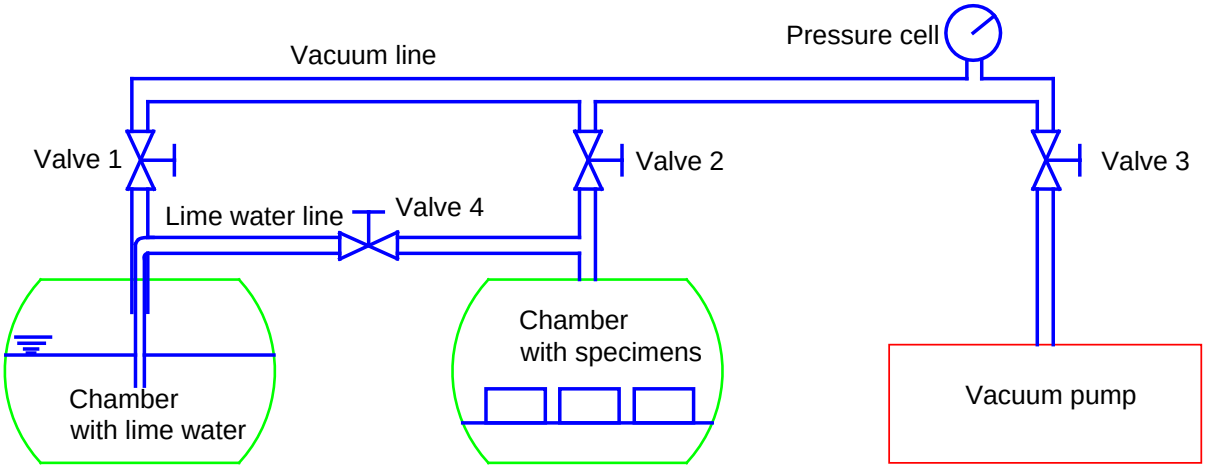

Figure 4.7. Vacuum saturation setup

It is worth mentioning that the samples may not be fully saturated after one day following this procedure (depending on w/c ratio). However, the experimental procedure for the permeability measurement includes further saturation up to full saturation of the sample. After one day of saturating the samples, the embedded samples were fitted in the steel outer part and fitted between the two cell lids by screws. Double O-rings were put between each lid and the embedded sample to prevent leakage. Prior to the permeability measurement, the sealing of the whole system was checked and all tubes and connections were filled up with water. Air in the system was removed thanks to quick couplings. The most critical parameter of the experimental procedure is the pressure gradient: it should not be too high as micro cracks can occur in the sample, but high enough to have a sufficiently high flow rate for accurate flow measurements. The applied pressure gradient selected was dependent on the w/c ratio of the samples and was therefore optimized for each w/c ratio by applying a predefined pressure loading procedure (see Figure 4.8). An important constraint is that the applied pressure remains below 10 bar which is still lower than breakthrough of pore walls. For the cement pastes in this study, the applied pressure was in the range 8 – 10 bar. A typical loading procedure is presented in Figure 4.8. First, a constant back pressure of one bar was applied to the upper side of the cell by Syringe pump A (Figure 4.2). The back pressure played an important role in saturating the sample (in case the sample was not completely saturated) and maintaining the full saturation state. The other side was stepwisely loaded by another Syringe pump B until a sufficiently high out-flow was obtained. There was no out-flow (even negative

flow) at the beginning of the pressure loading because the in-flowing water might still saturate the sample although a strict saturation procedure had been followed (as described earlier). When the in-flow was stabilized (variation less than ± 10% within 24 hours), Syringe pump B was changed from constant pressure mode to constant flow mode. The reason to change to the constant flow mode is that measuring pressure is much more accurate than measuring flow rate. It means that the statistical variation of pressure is lower than the variation in extremely low flow rate which is the case of low permeable cement-based materials. The constant flow rate was defined based on an average of flow rate in 24 hours before changing the mode. Finally, only pressure readings of Syringe pump B were recorded until the difference between out-flow and in-flow rate was less than ± 10%. The time required reaching this condition varied with the permeability coefficient, normally it held about one-third of total experiment time. The permeability was calculated using the average of pressure readings in 12 hours after reaching the condition. The total time needed for one measurement depended on the w/c ratio of the sample but it was less than one week when the permeability coefficient is larger than 10^{-13} m/s.

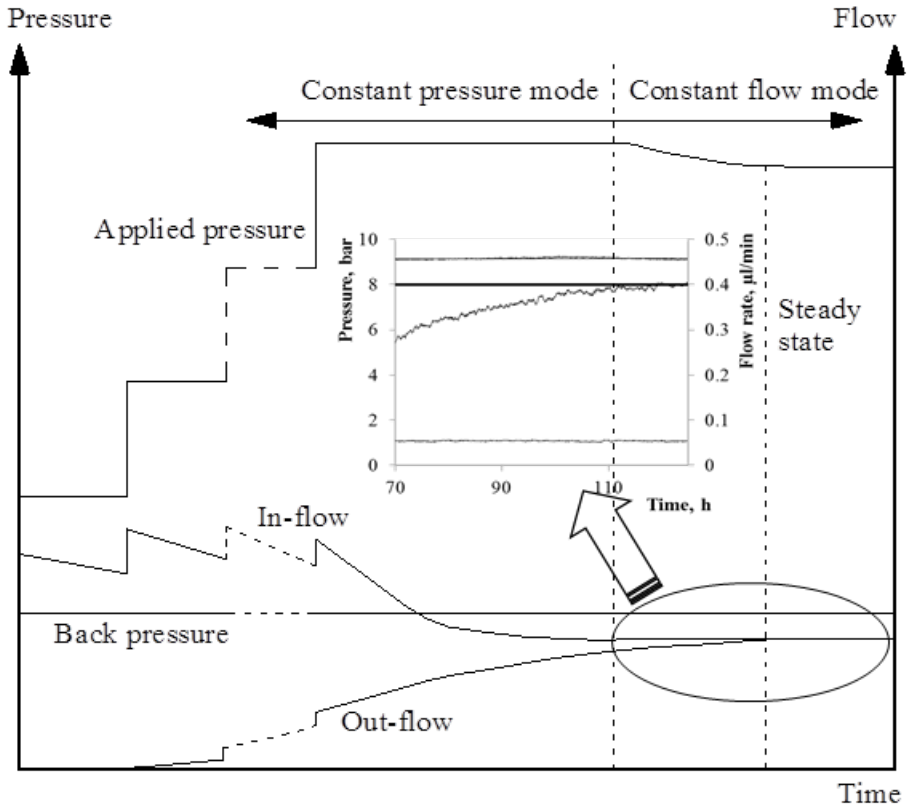

Figure 4.8. Typically applied pressure procedure - back pressure refers to the pressure of Syringe pump A (see Figure 4.2) on the upper side of the permeability cell; applied pressure refers to the pressure of Syringe pump B on the lower side of the permeability cell.

4.3.2. Determination of diffusivities of dissolved gases in saturated cementitious materials

4.3.2.1. Research significance and principle

Diffusion is an important property for characterizing concrete durability because it governs the penetration of aggressive substances (Cl^-, SO_4^{2-}, O_2, CO_2) responsible for degradation. However, data on the diffusion of substances (other than Cl^-) in concrete are scarce due to time and resource consuming measurements. This work describes a method to determine the diffusion coefficients of dissolved gases in saturated cement-based materials in order to study the effects of degradation on the transport properties. The proposed method was adapted from the technique used to determine the diffusivity of clay materials [197]. The method is based on a flow-through diffusion methodology and allows simultaneous determination of diffusivities of two dissolved gases diffusing in opposite directions. A cement plug was mounted between two water reservoirs pressurized by two different gases at equal pressure to avoid advection (~ 10 bar). The changes in the dissolved gas concentration (at the opposite sides) were measured indirectly via the gaseous phase which is in equilibrium with the aqueous phase according to Henry's law. Additionally, a simple 1-D diffusive transport model (based on 1st and 2nd Fick's laws) was developed to interpret the experimental data. The concentrations at outlet and inlet were used as inputs for the model, and the diffusivity was obtained by a fitting procedure.

4.3.2.2. Sample preparation and experimental setup

The diffusion experiments were performed on intact samples S3 (w/p = 0.425, ls/p = 0), S4 (w/p = 0.375, ls/p = 0.1) and carbonated and leached samples S3C and S3L. The gas couple He-Xe was used for all cases. The same sample preparation procedure for permeability measurement was used for diffusion measurement to determine dissolved gas diffusivity. For carbonated sample, the sample needs to be saturated before diffusion test. Thanks to the flexibility of the primary cell, the sample/cell can be easily switched/disconnected from the carbonation setup and mounted/connected to the diffusion setup by means of quick connect couplings. For the leached samples, the leached material was still kept in water to prevent any drying cracks before embedding into diffusion cell. The embedding of the leached materials was done in a closed chamber with relative humidity of 100%. After embedding, the sample was submerged in water for a couple of days to ensure that it is fully saturated before connecting to diffusion testing system.

A schematic view and a picture of the experimental setup are presented in Figure 4.9 and Figure 4.10, respectively. The setup is similar to the one used for clay materials [197] except for the diffusion cell which is exactly the same of the permeability cell. Two precise pressure transducers (TURCK, Plymouth, USA) were used to measure gas pressure in the pressurized water vessels. The water with the dissolved gas was circulated over the contact filter in the cell by means of magnetic coupled gear pumps (ISMATEC, Glattbrugg, Switzerland). The diffusion cell was connected to the system through quick connectors.

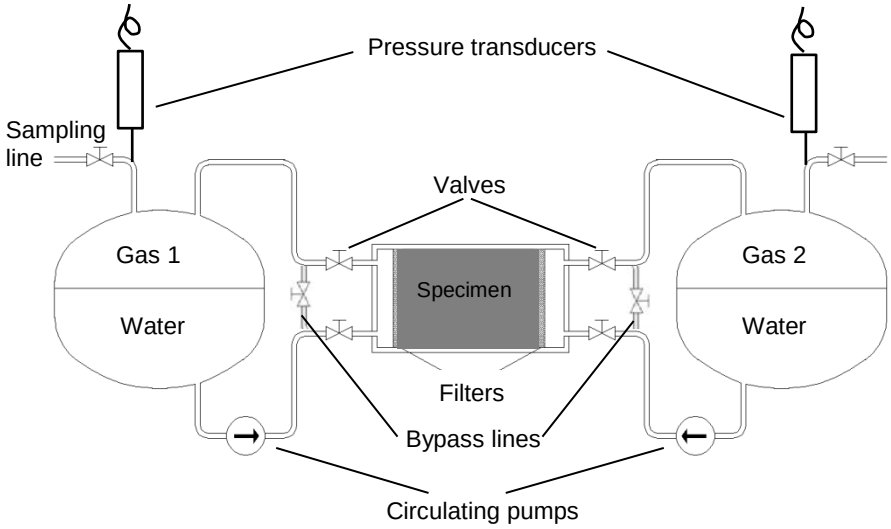

Figure 4.9. Schematic experimental setup of diffusion (adapted from [197])

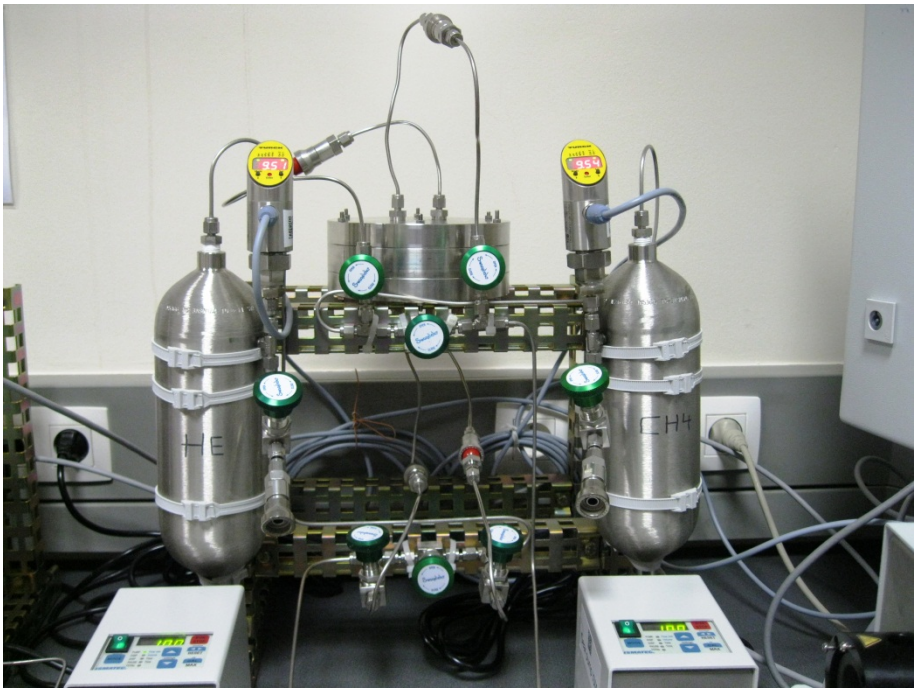

Figure 4.10. Image of the diffusion experiment

4.3.2.3. Experimental procedure

The experiments were performed in a temperature controlled room at 22 ± 2°C. Prior to the diffusion measurements, the sealing of the whole system was checked by applying a gas pressure of 12 bar and following the pressure evaluation over time (few weeks). The entire setup is considered to be gastight if the pressure remains stable. The air or residual gas from previous tests in the system was removed as much as possible by flushing the system with the testing gases. During flushing, bypass lines were opened while all valves connected to the sample were closed to prevent diffusion proceeding at this step. Care must be taken to avoid testing gas contamination of each vessel (i.e. gas 1 present in vessel 2 and vice versa). Subsequently, a volume of 0.5 litre of degassed water was added to each vessel, whereafter they were pressurized by the respective gases to a similar pressure of about 10 bar to prevent advective transport. Prior to the measurement, a sample was taken to determine the initial gas composition of both vessels and referred as the sample at the time zero. In order to start the test, all valves connected to the sample were opened, the bypass lines were closed. At that moment, the pressures in both vessels slightly dropped due to small volume increase of the system, but still in balance. Gas samples were regularly taken (generally every 2 weeks) via sampling lines until enough data points were collected to obtain diffusivity (few months). To avoid a too large pressure drop due to sampling, the sample volumes taken were only 6 ml. The gas composition was analysed with a CP4900 micro gas chromatographer (VARIAN, Palo Alto, USA).

4.3.2.4. Data analysis

In order to interpret the experimental data, a 1-D diffusive transport model was developed [197]. Fick's laws were used to describe the diffusion of the dissolved gases.

$$J_{dg} = -D_e \frac{\partial C_{dg}}{\partial x} \tag{4.1}$$

$$\phi R_e \frac{\partial C_{dg}}{\partial t} = D_e \frac{\partial^2 C_{dg}}{\partial x^2} \tag{4.2}$$

where J_{dg} [mol/m^2.s] is flux of dissolved gas; D_e [m^2/s] is the effective diffusion coefficient; ϕ [-] denotes porosity; R_e denotes the retardation factor which takes into account the interactions of dissolved gas and the medium. Note that in most cases, the retardation factor R_e of inert gas is one. C_{dg} [mol/m^3] denotes concentration of dissolved gas in the porous medium; t [s] denotes time and x [m] denotes length. With constant boundary conditions,

Equation (4.2) can be solved analytically using the inverse Laplace method [81]. However, during sampling the concentration at the upstream was decreased. As such boundary conditions are not easily implemented in analytical solutions, a numerical method was chosen to solve the problem.

At the upstream, the dissolved gas concentration was imposed as a boundary condition. The dissolved gas concentration was calculated from gas pressure above the water, which was regularly measured, by Henry's law.

$$C_{dg}^{u} = K_H P^{u} \tag{4.3}$$

where C_{dg}^{u} [mol/m^3] is concentration of dissolved gas at the upstream; K_H [mol/m^3.atm] is Henry constant; P^u [atm] denotes gas pressure. At the downstream, the concentration was considered to be zero because of extremely small value compared to the concentration at upstream (approved by experimental results). The quantity $Q_{out}(t)$ [mol] of dissolved gas diffused out of the sample was calculated as follows:

$$Q_{out}(t) = A\int_0^t J(L,t')dt' \tag{4.4}$$

where A [m^2] and L are cross section and length of the sample, respectively; $J(L,t')$ is the flux at the downstream boundary. The quantity $Q_{out}(t)$ must be equal to the total amount of testing gas $Q_{mea}(t)$ at the downstream (in water and gas phase) which can be determined by measuring the partial pressure P^d [atm] of the testing gas above the water at the downstream according to Clapeyron equation and Henry's law for ideal gas.

$$Q_{out}(t) = Q_{mea}(t) = K_H P^d V_l + \frac{V_g P^d}{RT} \tag{4.5}$$

where V_l and V_g [L^3] are water and gas volumes at the downstream, respectively; R denotes universal gas constant [J/mol.K] and T [K] denotes temperature. Initially, the concentration of dissolved gas was zero in the sample. The diffusion problem was numerically solved in COMSOL Multiphysics. The effective diffusion coefficient was obtained by using a least squares fitting procedure of the diffused quantity $Q_{out}(t)$ to the measured one $Q_{mea}(t)$ with the MATLAB Optimization Toolbox.

The changes in effective diffusivity of cementitious materials are due to the alterations of porosity, tortuosity and constrictivity resulting from degradation processes. In order to estimate the effects of carbonation/leaching on the changes of effective diffusion coefficients of other substances, a lumped parameter $\tau^2/\phi\delta$ can be calculated as follows:

$$\frac{\tau^2}{\phi\delta} = \frac{D_0}{D_e} \tag{4.6}$$

where D_0 [m^2/s] is the diffusion coefficient of species in pure water; τ [-] is tortuosity; and δ [-] is constrictivity.

4.4. Experimental methods to chemically degrade cementitious materials

4.4.1. Carbonation under controlled CO_2 pressure gradient

4.4.1.1. Research significance and principle

Under normal conditions (i.e. under low CO_2 concentration, no pressure gradient), the diffusion of CO_2 in either saturated or partially saturated conditions is the rate-limiting step in the carbonation process [116-118] because CO_2 dissolution and reaction rates are much faster. Nevertheless, in the case of concrete used for underground waste disposals, concrete is almost fully saturated and subjected to a high hydrostatic pressure and the surrounding environment may contain a high bicarbonate concentration. Furthermore, during the operational period (several decades up to hundreds of years) of repositories, a large hydrostatic pressure gradient is present because the repository is not yet closed. Therefore, a combination of diffusion and advection should be taken into account when one considers the carbonation mechanism. This is also the case in accelerated carbonation by applying a high pressure gradient in which advection in the gas phase has a significant contribution to the carbonation process. However, so far as the author is aware of, none of the published studies considers the contribution of advection to carbonation of cementitious materials.

In this study, a new method was proposed in which an elevated pressure gradient of pure CO_2 was applied to samples at a controlled internal relative humidity to take into account the contribution of gaseous advection. The method also enables to shorten experimental time because under atmospheric conditions carbonation is an extremely slow process. A standard way to study the carbonation is to put concrete samples in a controlled chamber with a given CO_2 concentration and optimized relative humidity (50-70%) to speed up the carbonation [127-129]. The drawbacks of such type of experiments are (i) the difficulty in quantification of the CO_2 uptake during carbonation, (ii) impossible to count for the contribution of pressure

gradient and (iii) poor in controlling the initial hygrothermal conditions of the samples, which are overcome by using the proposed method.

The setup allows for easy connecting to other setups before and after carbonation to measure diffusivity or water permeability. An elevated pure CO_2 pressure gradient was applied on a partially/fully saturated sample which is embedded in a special carbonation cell. The penetration of CO_2 into the cement paste sample (partially saturated) occurs via two ways: i) CO_2 gas transports through connected pores under a pressure and concentration gradient; ii) dissolved CO_2 transports with the movement of water under a pressure driving force (when initial saturation degree of the sample is high). The transport and dissolution of CO_2 in the sample is described in detail in Section 8.1.2.1. The amounts of CO_2 flowing in and out of the carbonation cell were precisely measured with mass flow meters allowing for quantification of the amount of carbon dioxide reacting with cement.

4.4.1.2. Sample preparation and experimental setup

Table 4.4 summarizes the experimental program for the carbonation study. Most of the tests were performed at relative humidity of 65% except for sample S1 which was performed in fully saturated condition. The samples S3, S4 and S5 have different w/p ratios but quite similar w/c ratios (0.425, 0.416 and 0.406, respectively) which allow comparing the effects of limestone filler addition on carbonation. Two carbonation procedures were applied on sample S4 and S5: continuous and cyclic carbonation (detailed later).

Table 4.4. Experimental program for carbonation study

Sample	w/p	Limestone filler, %	Relative humidity		Carbonation procedure	
			65%	Saturated	Continuous	Cyclic
S1	0.325	0		x	x	
S2	0.425	20	x		x	
S3	0.425	0	x		x	
S4	0.375	10	x		x	x
S5	0.325	20	x		x	x

Figure 4.11 shows a schematic view of the experimental setup; and a picture of the testing rig is shown in Figure 4.12. The main part of the system is the carbonation cell which has the same design as the permeability cell described in Section 4.3 but with a different embedding procedure (described below). The amount of carbon dioxide reacting with the cement was derived from measurements with two mass flow meters “red-y smart meter GSM” at each side of the carbonation cell. One had a higher measurement range (0-50 ml/min) to measure flow when carbonation rates were high at early experimental times; the other one had a lower range

(0-10 ml/min) to measure flow when the carbonation rate was decreased. Using two mass flow meters with different ranges improves the measurement accuracy. The mass flow meters measured every minute the mass flow rate, the total amount of CO_2 passing and the temperature. In order to prevent damage of mass flow meters by the high relative humidity conditions, a moisture trap was placed before the outlet mass flow meters. A precise pressure controller (precision of 1/10000 bar) was used to apply a constant pressure at the upstream side. The other side of the sample was balanced to atmospheric pressure.

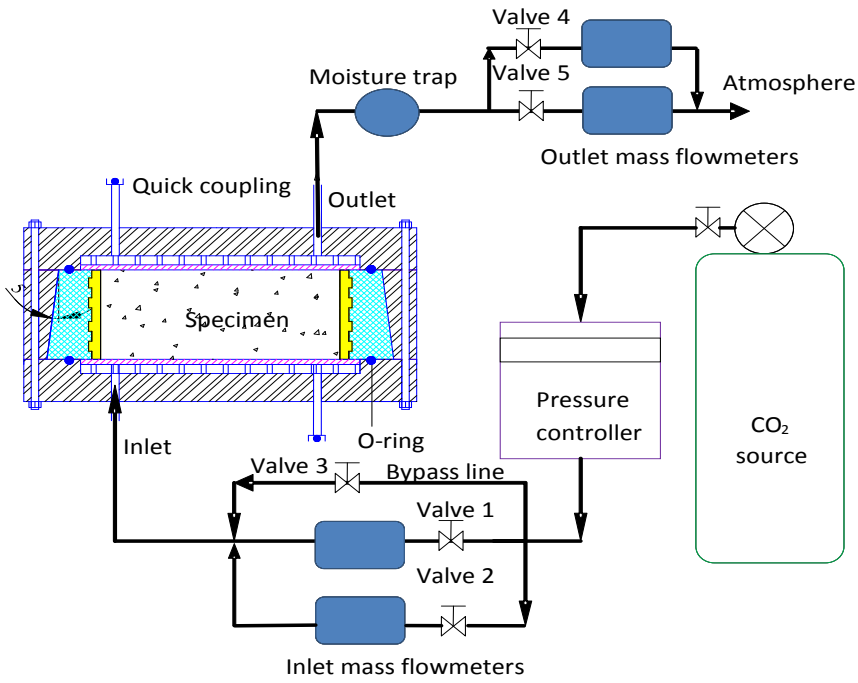

Figure 4.11. Proposed carbonation setup using pressurized CO_2 and recording of the CO_2 in- and out-flows

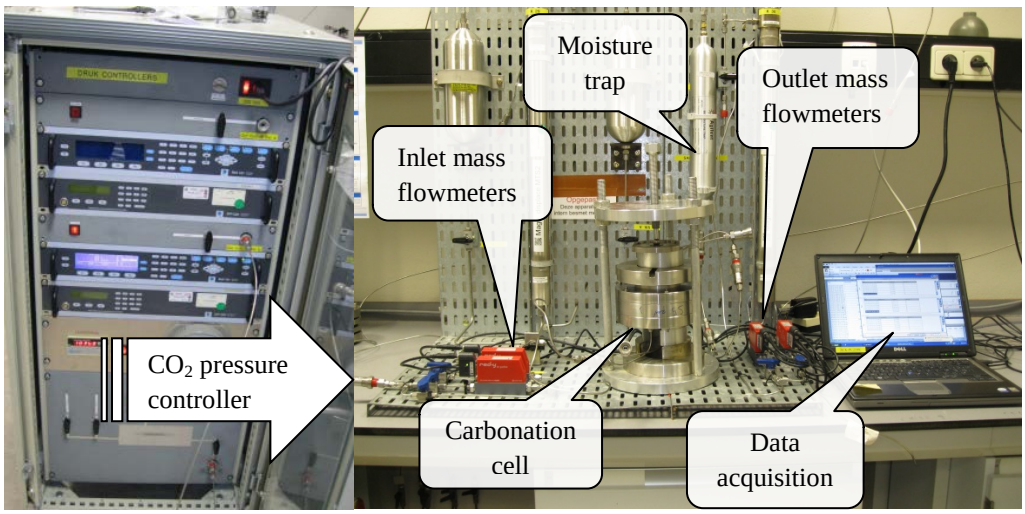

Figure 4.12. A picture of the carbonation setup

4.4.1.3. Experimental procedure

Small cement paste disks of 25 mm thickness were prepared following the same procedure as for the permeability measurement (see Section 4.3.1.3). Prior to the carbonation experiment, the samples were conditioned to a target internal relative humidity of 65% to have optimal conditions for fast carbonation. Sample S1, which was tested under saturated condition, was saturated using the same saturation procedure for permeability measurement. To equilibrate the sample to the target RH, an accelerated conditioning procedure was adopted as follows:

(i) The initial RH of the sample (~ 90%) and open porosity (MIP results) were estimated;

(ii) The relationship between porosity, RH, and saturation degree [198] was used to estimate the required amount of water to be evaporated to reach the target RH;

(iii) The sample was dried in an oven at 35^{o}C until the mass decrease approximated the estimated amount of water in the previous step (4~5 days for RH 65%). An oven temperature of 35^{o}C prevents cracking and possible dehydration of C-S-H;

(iv) The sample was placed into a desiccator containing a certain salt solution ($NaNO_2$ at 22^{o}C) to obtain the target RH until change in mass between two subsequent daily measurements was less than 0.02%. With this procedure, the samples reached the target RH of 65% in a period of less than 1 month.

The sample was then embedded into the inner part of the carbonation cell by a resin within a desiccator at the same RH. It took about 24 hours for the resin to polymerize. The sample was placed in the desiccator for several more days for re-equilibration to the target RH. It is worth noting that embedding before conditioning is not recommended because cracking can occur due to the shrinkage of the restrained sample during the drying shrinkage process.

The carbonation cell was then connected to the CO_2 pressure system at one side while the other side was in contact with air (ambient condition). Prior to the carbonation measurement, the sealing of the whole system was checked to ensure no leakage. All tubes and connections were filled up with CO_2 at the high pressure side. These steps are very important because if moisture still remains in the system, the initial RH of the sample can be changed and the quantification of CO_2 uptake is not accurate. Two procedures to carbonate the sample were proposed. The first procedure was based on applying a continuous constant CO_2 pressure gradient; the second procedure accelerated the carbonation process by alternating CO_2 pressure cycles with drying periods.

- **Continuous carbonation**

CO_2 pressure was increased at one side of the sample, while the other side was balanced to atmospheric pressure. At the beginning, the valves connected to the inlet mass flow meters (valve 1 and 2) were closed, while the valve connected to the bypass line (valve 3) was opened. When pressure reached the target value, valve 1 which was connected to the mass flow meter with high measurement range (up to 50 ml/min) was slowly opened, and then valve 3 was slowly closed. In this way, one avoids damaging the mass flow meter by a sudden increase in flow. The amount of CO_2 going into the system was recorded from the moment valve 1 was opened, which eliminated the amount of gas needed to fill the space in the connections. At the other side of the sample, valve 4 (connected to the low range flow meter) was opened, while valve 5 (connected to the high range flow meter) was closed. In this way, the mass flow meter started measuring the amount of CO_2 leaving the system.

After a few hours of high inlet flow, the inlet flow decreased because the carbonation reaction released water which decreased the air-filled porosity and carbonation products were formed reducing the porosity. When the inlet flow was less than 10 ml/min, the mass flow meter was switched to the low range flow meter.

A constant absolute pressure of 6 bar was applied in order to have at one hand a sufficient high pressure of pure CO_2 to reduce the experimental time, but on the other hand, to reduce the risk for inducing micro cracks in the cement paste by applying a too high pressure. A carbonation test was performed for period of 4 weeks.

- **Cyclic carbonation**

As the carbonation reaction releases water which increases the local saturation degree and significantly reduces the carbonation rate, carbonation periods were alternated with drying cycles as illustrated in Figure 4.13. The sample was first carbonated during time T_1 under the same pressure gradient as applied during the continuous carbonation. Subsequently, it was dried for a time T_1' to remove water and bring the sample back to a RH approximating to the initial RH (65%). Then a new carbonation – drying cycle started, and so on. The carbonation periods T_1, T_2, …, T_n were determined based on the inlet flow rate. When the rate was less than 0.5 ml/min, the carbonation cycle was stopped and the drying cycle started. The drying periods T_1', T_2', …, T_n' were difficult to determine quantitatively because measurement of the RH within the sample is not possible within this experimental setup. However, trial tests indicated that a higher carbonation degree was observed if the drying period increases over

time, i.e. $T_1' < T_2' < \ldots < T_n'$. A longer drying period over time reflects a denser cement paste and a deeper carbonation front, resulting in deeper water production, with increasing carbonation.

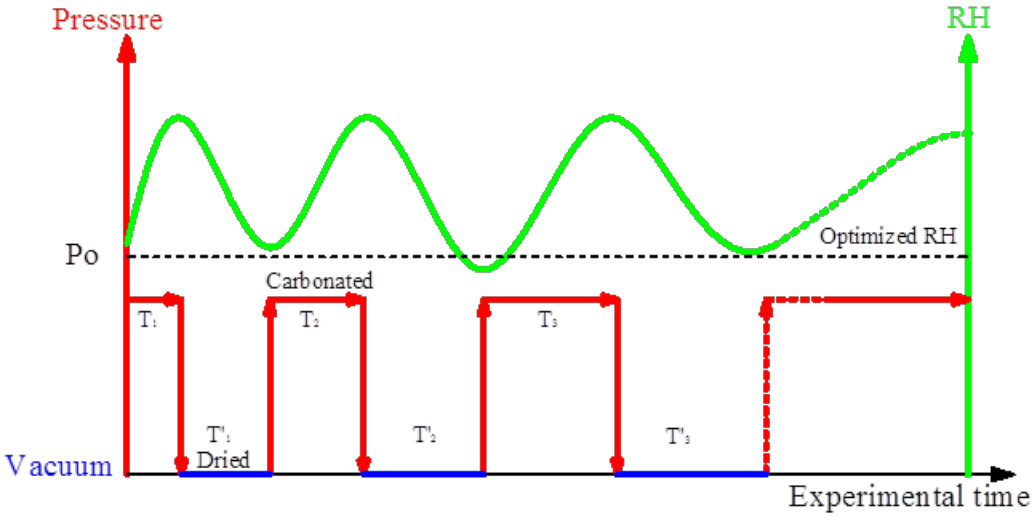

Figure 4.13. A Schematic illustration of cyclic carbonation procedure to accelerate carbonation process

4.4.2. Accelerated leaching using 6M ammonium nitrate solution

4.4.2.1. Need and principle

Considering the slow leaching degradation process but the need to study long-term durability of concrete, accelerated testing is a relevant approach to better understand the leaching phenomenon and the coinciding alteration of microstructure and transport properties. In this study, an ammonium nitrate solution was used to accelerate the leaching kinetics. This is one of the most popular methods because it results in faster degradation compared to other methods under diffusive-transport conditions and has the same end-products. The mechanism of acceleration is not only due to the low pH of NH_4NO_3 solution but mainly due to an increase in the solubility of the leachable phases in cementitious matrix induced by NH_4NO_3. When diffusing into cement-based materials, NH_4NO_3 reacts with most of the main phases in cement paste according to following reactions:

With **portlandite**:

$$Ca(OH)_2 + 2NH_4NO_3 \rightarrow \mathbf{Ca(NO_3)_2} + 2NH_{3(aq)} + 2H_2O \quad (4.7)$$

With **Calcium silica hydrates (C-S-H)**:

$$C_xS_yH_z + 2NH_4NO_3 \rightarrow C_{x-1}S_yH_{z-1} + \mathbf{Ca(NO_3)_2} + 2NH_{3(aq)} + 2H_2O \quad (4.8)$$

$C_{x\text{-}1}S_yH_{z\text{-}1} + 2(x\text{-}1)NH_4NO_3 \rightarrow$

$ySiO_2 + (x\text{-}1)\mathbf{Ca(NO_3)_2} + 2(x\text{-}1)NH_{3(aq)} + (z+x\text{-}2)H_2O$

With **Ettringite (AFt)**:

$2C_6A\dot{S}_3H_{32} + 24NH_4NO_3 \rightarrow$

$3CaSO_4 + 9\mathbf{Ca(NO_3)_2} + Al_2(SO_4)_3 + 2Al(NO_3)_3 + 24NH_{3(aq)} + 76H_2O$ (4.9)

With **Monosulfoaluminate (AFm)**:

$4C_4A\dot{S}H_{12} + 48NH_4NO_3 \rightarrow$

$CaSO_4 + 15\mathbf{Ca(NO_3)_2} + Al_2(SO_4)_3 + 6Al(NO_3)_3 + 48NH_{3(aq)} + 72H_2O$ (4.10)

$NH_{3(aq)} \rightarrow NH_{3(g)}$ (4.11)

Calcium nitrate is a very soluble salt. Therefore, the concentration of Ca ions in pore solution is much higher than in a portlandite-controlled system. Furthermore, aqueous NH_3 converts to gaseous NH_3 which escapes from the system hence it drives the reactions (4.7) to (4.10) to the right side. It helps to prevent the equilibrium of the system, which stops the leaching acceleration.

4.4.2.2. Experimental procedure and test setup

The full experimental program was applied to investigate the effects of limestone filler replacement and w/p ratio on Ca-leaching. Cement pastes were poured and cured with the same procedure as the permeability experiments (see Section 4.3.1.3). Afterwards, the 28-day-cured cement pastes were sawn into 25 mm thick slices. In order to study one dimensional leaching (bottom and top of the slice), the PVC cover in the axial direction remained on the cement paste slice. Additionally, epoxy resin was poured to fill the gap (if available) between PVC cover and cement paste as shown in Figure 4.14a. In such a way radial leaching is prevented.

The same saturation procedure for the permeability measurements was used to saturate the cement slices in saturated lime solution in order to avoid initial leaching. The saturated cement slices were immersed in ammonium nitrate solution chambers. The ratio between NH_4NO_3 solution over the contact surface area of the sample was 8 cm^3/cm^2. Such a factor was chosen to ensure that the pH of the solution was always below 9.25. When a higher pH is reached, the solution needs to be changed to maintain leaching acceleration [199]. The renewal of solution is avoided because the solution is used for quantitative analysis of the Ca-leached amounts.

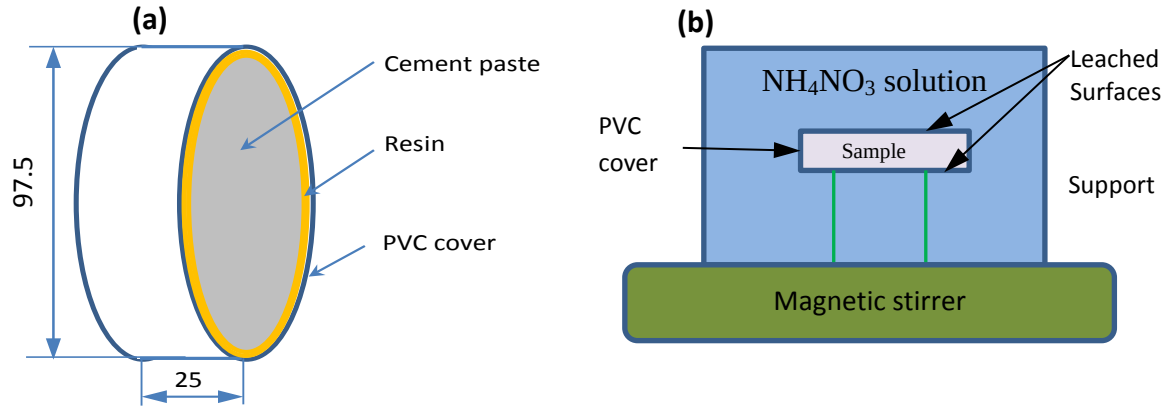

Figure 4.14. Preparation of cement paste slice for accelerated leaching in ammonium nitrate 6 mol/l solution (a) and a schematic setup of leaching experiment (b)

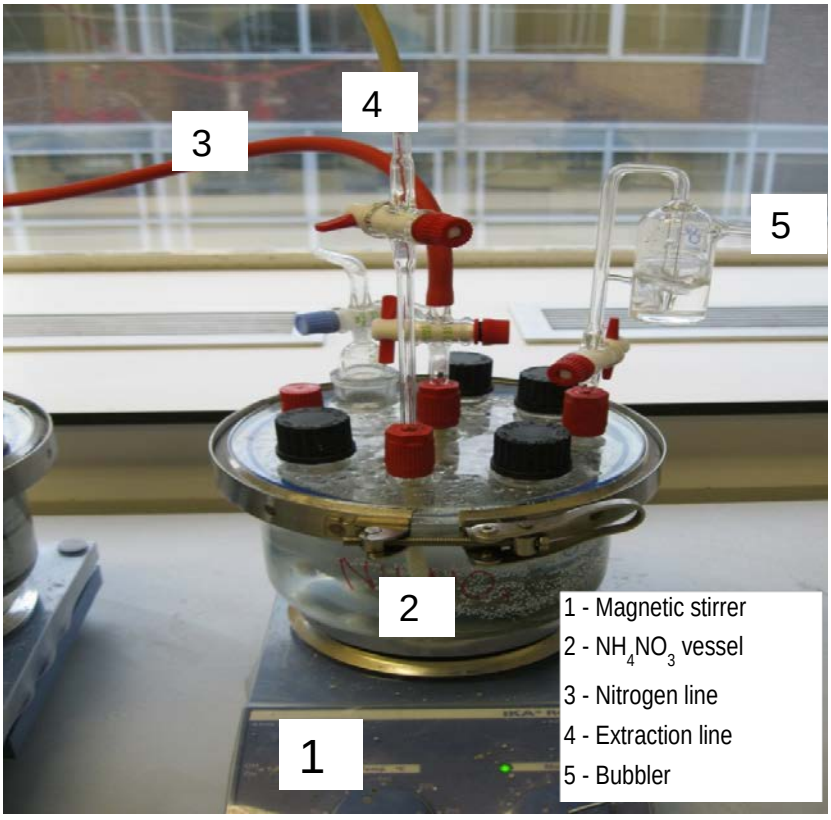

Figure 4.15. Accelerated leaching setup using NH_4NO_3 solution

A schematic setup and a picture of the leaching experiment are given in Figure 4.14b and Figure 4.15, respectively. Nitrogen was bubbled through the system to prevent carbonation during leaching and to remove the formed NH_3 gas via the bubbler (water lock). The solution was homogenized by a magnetic stirrer. There was an extraction line to extract solution for further analysis and follow up the pH of the solution. The setup consisted of 3 NH_4NO_3

chambers which allowed simultaneously leaching of three samples. Reference samples were prepared from the same batch of cement paste and kept under the same conditions except for immersion in ammonium nitrate solution.

4.5. Experimental methods to characterize degraded and sound cementitious materials

The scope of this study is to phenomenologically understand how far transport properties would be altered due to chemical degradation. The strong link between chemical degradation and transport property change is the alterations of microstructure and mineralogy. For those reasons, characterization of the degraded and intact cementitious materials is needed. In order to come to an as much as complete picture of the degradation phenomena, a variety of post-analysis techniques like SEM/SEM-EDX, XRD/QXRD, MIP, TGA, ion chromatography and N_2-adsorption were applied.

4.5.1. Scanning electron microscope and energy dispersive X-ray microanalysis

4.5.1.1. Introduction

The scanning electron microscope (SEM) has been used as a powerful petrographic technique for material characterization since the early 1970's. SEM imaging is basically either in a secondary electron mode or a backscattered electron mode. The secondary electron images are generated by scanning a low energy electron beam over the specimen surface. Therefore, they provide a lot of information about the specimen surface. Whereas, the backscattered electron images (BSE) are generated by a high energy electron beam which provide information of deeper depths (few microns) [200]. One of the most important advantages of BSE images is that its contrast depends on the atomic number of the specimen. The difference in grey level allows phase separation of the cementitious materials (each phase has different mean atomic number: alite > belite > portlandite > tobermorite > ettringite [201]). Pores appear in black colour. For the purposes of this study, BSE images were taken.

In terms of qualitative analysis, BSE imaging in combination with energy dispersive X-ray microanalysis (EDX) is a useful method to identify different cementitious constituents. However, quantitative analysis is only possible with EDX if the specimen is well polished to obtain a flat surface. In this study, EDX was used to produce atomic Ca/Si profiles along the leaching depth and elemental mapping over the transient zone of leached materials. Additionally, it was used in combination with BSE images to better separate the phases of intact/degraded cement pastes.

4.5.1.2. Sample preparation

For the purpose of taking BSE images, polished sections were prepared. Carbonated/leached materials were taken in parallel to the longitudinal axis and the scanning area was within 3 mm from the reactive surface and referred as “carbonated/leached samples”. Samples were also taken on the transition area of leached materials which was qualitatively identified by the changed phenolphthalein colour. Reference samples were taken from intact materials after removing the surface in contact with atmosphere to avoid the effects of atmospheric carbonation.

The sample preparation procedure for SEM measurements is described in Figure 4.16. Drying is an essential step for SEM sample preparation. Resin cannot penetrate into the sample unless the free water in the sample has been removed. The solvent replacement method was chosen to dry the samples. This method is found to be a good technique to preserve the microstructure for SEM analysis [202]. The samples were immersed in 2-propanol 99.5% for 2 weeks, and then placed in a vacuum chamber under 2.5×10^{-2} mbar for 3 days. The dried samples were impregnated in an extremely low viscosity resin before grinding and polishing. The harden resin has a very high strength (80 MPa for compressive strength and 50 MPa for tensile strength). Resin impregnation helps to fill the voids and pores; preserve the original microstructure; enhance contrast between solid phases and pores; and prevent cracking during grinding/polishing. The polished samples were then coated by a thin gold layer (few µm) to prevent charging during SEM examination. Even with gold coating, the samples might be charged because a non-conductive resin was used. Therefore, the top and bottom of sample were connected by a conductive copper tape.

SEM measurements of samples were done using a JEOL JSM 6610 scanning electron microscope. Energy Dispersive X-ray analysis was carried out with the aid of ESPRIT Software. ImageJ software was used for phase separation.

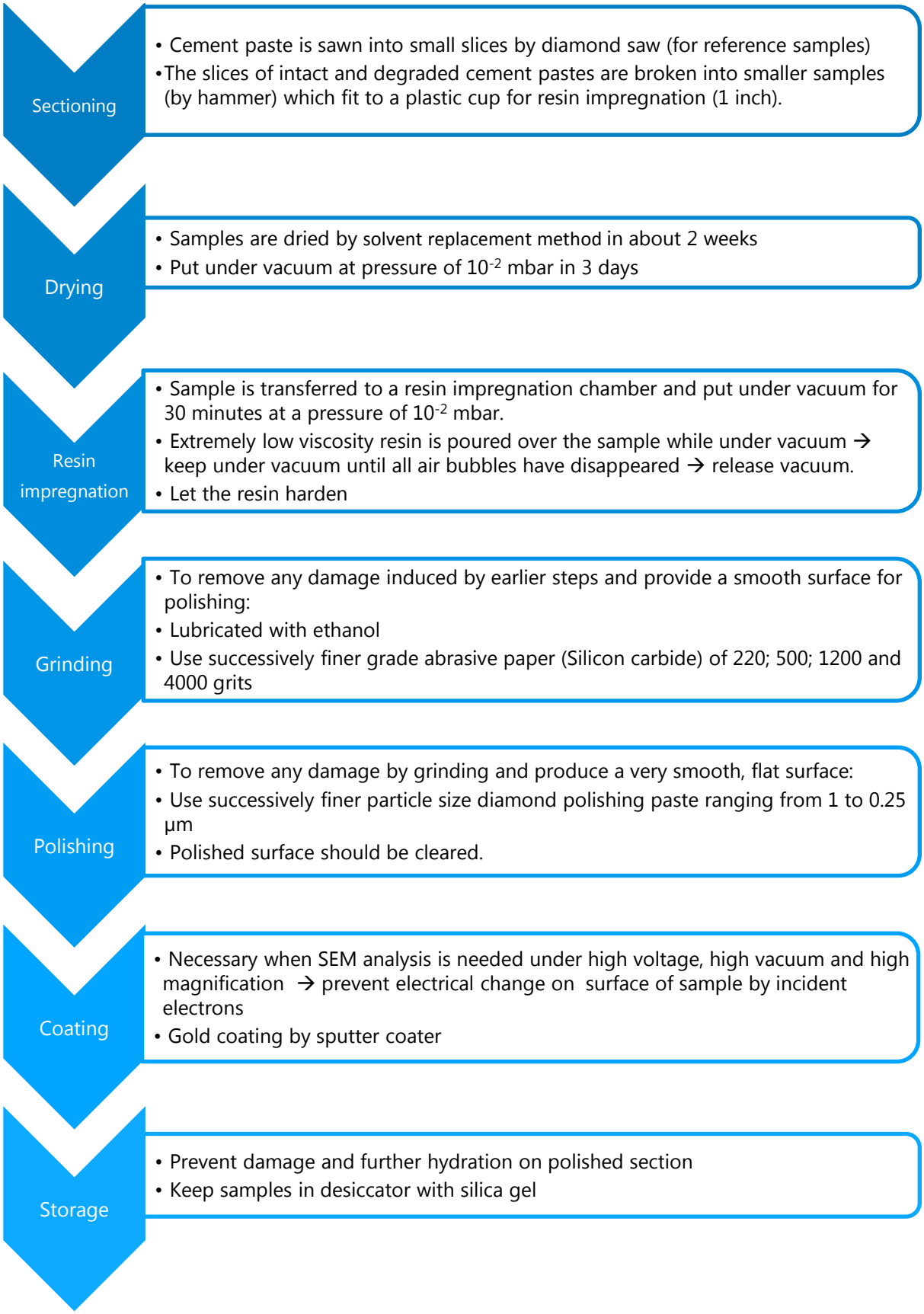

Figure 4.16. Sample preparation procedure for SEM analysis [201, 203]

4.5.2. Mercury intrusion porosimetry

4.5.2.1. Introduction

Despite some limitations, MIP has been considered as a common method to characterize pore structure of cementitious materials because it is simple, fast, reproducible and able to cover a wider range of pore sizes compared to other methods. Mercury as a non-wetting liquid for cementitious materials will not enter into the pore with a certain radius if the intrusion pressure does not reach a corresponding value according to the Washburn equation [204]. In this way, the pore sizes can be calculated from the pressures which force mercury into the pores:

$$r_p = \frac{-2\gamma_m cos\theta}{P_m} \tag{4.12}$$

where r_p is the pore radius [m]; γ_m is the surface tension between mercury and pore wall (0.48 N/m for this study); θ is the contact angle (140^o for this study); and P_m is the applied pressure of mercury [N/m^2]. MIP provides a variety of pore structure information including total porosity, pore size distribution, bulk density, specific surface area, especially critical and threshold pore diameters which are the most important parameters related to transport properties of cement-based materials. The critical pore diameter is defined as the most frequently occurring pore size in interconnected pores, while the threshold pore diameter is the largest pore size at which pore volume is significantly increased (see Figure 4.17). However, one should keep in mind that MIP measures the connected pores rather than real pores existing in the systems [205]. Furthermore, gel pores (nm size) are difficultly measured by MIP for normal applied pressure range (up to 200 MPa), and air voids, cracks are not detected by MIP.

In this study, MIP was used to obtain the changes in pore structural parameters of materials after carbonation and leaching. Those parameters were treated as comparative indexes rather than for characterization of real microstructure. For leached material, because of its high ductility, the maximum applied pressure was limited to about 30 MPa instead of 200 MPa for reference and carbonated materials. The compression of the leached sample was also taken into account in pore structural calculations.

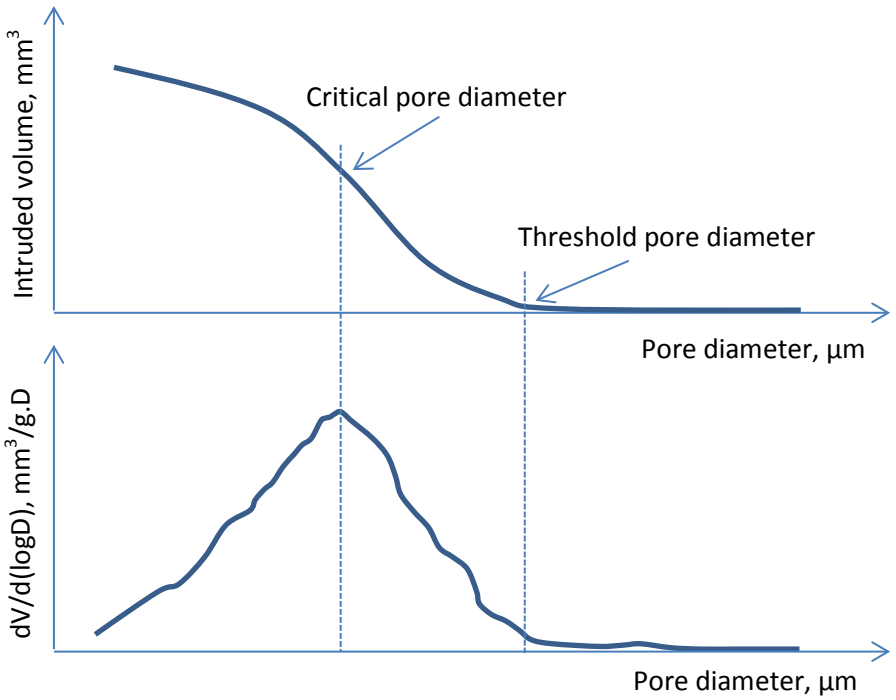

Figure 4.17. Definitions of critical and threshold diameters – adapted from [206]

4.5.2.2. Sample preparation and experimental procedure

Several carbonated/leached paste pieces were taken within 3 mm from the reactive surface and referred as "carbonated/leached samples". The mass of each sample was about 3-4 grams. The procedure to take reference samples was similar to the one for SEM measurements. Freeze drying was chosen to prepare samples for MIP and nitrogen adsorption measurements. By freeze drying, water crystals sublimate which prevents micro crack formation because of capillary stress if drying passes through the liquid state [207]. This method also gives a dried sample in a quite short period. Samples were directly immersed in liquid nitrogen until the escape of gas bubbles stops. Subsequently, the samples were transferred to a vacuum chamber where a vacuum pressure of 2.5×10^{-2} mbar is applied for 24 hours. Dried samples were kept in closed glass bottles until examination.

MIP experiments were performed on PASCAL 140/440 porosimeter. The pressurization was done in low and high pressure parts. In the low pressure part, after evacuation and mercury filling, the pressure was continuously increased up to 0.2 MPa then reduced to atmospheric pressure before moving to the high pressure part. The sample volume was determined from the low pressure part and also information of large pores was provided from this part. In the high pressure part, the pressure of mercury was continuously increased up to a maximum

pressure of 200 MPa for all samples except for leached samples for which maximum applied pressure was 30 MPa.

4.5.3. Nitrogen adsorption

4.5.3.1. Introduction

Gas adsorption has been considered as a useful and popular technique to study micropores and mesopores of porous materials. It was first applied on cement pastes in 1940s [208]. When a gas is in contact with a porous solid surface, it resides on the solid surface by different mechanisms including mono/multi-layer adsorption, or capillary condensation [206]. Gases used as adsorbates include oxygen, krypton, argon, alcohols, and water vapour, but frequently used gas is nitrogen because of its low reactivity with cementitious materials and many published data for comparison. Data obtained from adsorption experiment are adsorbed gas amount and the corresponding relative pressure, which are then used for the determination of specific surface area, pore volume, and pore size distribution by a large number of methods (BJH, Langmuir, BET, etc.). Among them, the BET specific surface area is the most common parameter obtained from gas adsorption experiments.

In this study, nitrogen adsorption was used to obtain the changes in pore structural parameters of materials after carbonation and leaching. N_2-adsorption was able to measure over a pore size range of about 3 – 76 nm. In case of leached materials, the compression of samples was very large at high applied pressure of mercury during MIP experiment, which was not the case for nitrogen adsorption experiment. For this reason, combining MIP and nitrogen adsorption measurements will give a better understanding of the pore structure of cementitious materials, especially for leached paste. The MIP gives reasonable results for larger pore sizes while N_2-adsorption provides information on the smaller pores. In this way, pore structure information is obtained in a broad pore size range.

4.5.3.2. Sample preparation and experimental procedure

Sample treatment was the same to MIP experiments. Nitrogen adsorption measurements were done on a TriStar II 3020 Micromeritics. Dried samples were weighed and degassed under vacuum at 35^{o}C for 24 hours. The amount of nitrogen adsorbed during the test was calculated by using volumetric method (based on gas laws). About 80 equilibrium points were collected during adsorption and desorption. More data points were collected at the low relative pressure part in order to derive the micropore volume.

4.5.4. Thermal gravimetric analysis and differential thermal analysis

4.5.4.1. Introduction

Thermal gravimetric analysis (TGA) measures the changes in the mass of a sample when the sample is subjected to a temperature increase (most often a linear temperature increase with time). The changes that occur on heating include thermal events: melting, phase transition, sublimation, and decomposition. TGA is an extremely powerful quantitative thermal technique, but it gives no direct chemical information. Knowledge of reactions/processes occurring at specific temperature range during heating is required to determine the compositions of the sample. TGA measures mass changes in a material as a function of temperature (or time), while in differential thermal analysis (DTA) the temperature of a sample is compared with that of an inert reference material during heating. The temperature should be the same until a thermal event occurs. It is advantageous to use both DTA and TGA, because DTA events can occur even when there is no involved mass change (e.g. crystallization).

DTA and TGA have been intensively used to quantify phase compositions in hydrated cement-based materials including portlandite, calcite [130, 209, 210], ettringite, gehlenite [211]. The method is thought to obtain a higher accuracy compared to other methods (quantitative XRD, SEM). In this study, DTA and TGA were used to determine the portlandite and calcium carbonate profiles of carbonated and reference samples.

4.5.4.2. Sample preparation

A hole with a diameter of 10 mm was drilled longitudinally in the carbonated sample. Drilling was halted every 3 mm to collect the dust before continuing drilling. To prevent cross contamination, the hole was carefully cleaned by compressed air before continuing the drilling. For the reference sample, the surface layer was removed before collecting the powder. Collected powder was dried under vacuum and kept in sealed conditions. TGA/DTA was performed in a NETZSCH STA 449F3 thermal analyser. A weighed sample, usually between 30 and 40 mg was heated from room temperature up to 1100^{o}C at a heating rate of 10^{o}C per minute under a constant nitrogen flow rate of 120 ml/min. A blank test (without sample) was also performed to correct the buoyancy effect which results in apparent mass increases.

4.5.5. Qualitative and quantitative powder X-ray diffraction

4.5.5.1. Introduction

Powder X-ray diffraction is (XRD) one of the most important tools used to identify the structure of a crystal, in which the crystalline atoms cause a beam of incident X-rays to diffract into many specific directions [212]. When an X-ray beam strikes a powdered sample which has crystals randomly arranged, the X-rays are scattered by atoms which produces a diffraction pattern containing information about the atomic arrangement within the crystal. Note that only crystalline materials, not amorphous materials produce a diffraction pattern. Each crystalline material has a unique diffraction pattern followed Bragg's law.

XRD has been intensively used by many researchers [213-217] in the characterization of Portland cement-based systems in both qualitative and quantitative analyses. The main advantages of XRD are the ease and speed of measurement. However, its accuracy in terms of phase quantification especially for hydrated cement-based materials is questionable. Rietveld method with whole pattern approaches has been considered as a reliable technique to quantify cementitious phases in multi-phase systems but it requires a well-defined crystal structure database and a strict sample preparation.

In this study, the main purpose of using XRD is to see the changes in phases after degradation. For leached materials, TGA could not be applied because the decomposition of $Ca(NO_3)_2$ coincides with decomposition of other phases. Therefore, the use of quantitative XRD is needed. Furthermore, XRD provides information on more phases compared to TGA (mainly portlandite and calcite).

4.5.5.2. Sample preparation

Similar to the preparation of samples for TGA, powder was collected from reference and degraded samples by drilling longitudinally in the samples and collection of dust at regular intervals. Prior to analysis, the samples were dried (vacuum). For samples on which a quantitative analysis was performed, 10% of ZnO internal standard material was added to the mixture. The classical grinding procedure (by hand with pestle and porcelain mortar) was used to reduce the size of the grains. This method is time consuming compared to using Micronizing mill but avoids reaction of portlandite with alcohol (needed in the Micronizing mill) forming a carbonate-like product ($Ca(OCH_3)_2$) [218]. Powder XRD measurements were done using a Philips X'Pert Pro Diffractometer. The samples were scanned over the 2θ range of $5 – 70^o$ using Cu-Kα radiation at 45 kV and 40 mA.

4.5.5.3. Rietveld refinement

The Rietveld method is used to refine the crystal structure model of a material, allowing determination of the mass fraction at different phases. The method uses full profile fitting procedure to iteratively compare the experimental pattern with calculated pattern which is generated by a model phase. The difference between observed and calculated patterns is minimized by adjusting parameters in the model through a least square fitting. In this study, Rietveld refinement was performed using X'Pert Highscore Plus software. Crystal structure database was downloaded from the American Mineralogist Crystal Structure Database [219]. Refined parameters included background, scale factor, zero shift, lattice cell, Caglioti parameters (W, U, V), peak shape, asymmetry and preferred orientation. Semi-automatic mode was used to refine the following parameters step by step (i.e. refined one parameter at a time, and then added one additional parameter at a time for next refinement step to avoid divergence).

a. Scale factor
b. Background
c. Zero shift
d. Cell
e. W
f. W+V
g. W+V+U
h. W+V+U + Peak Shape 1
i. W+V+U + Peak Shape 1 + Asymmetry/ preferred orientation

In order to evaluate the refinements, X'Pert Highscore Plus gives many agreement indices to judge the refinement including residual of least-squares refinement (R_p), weighted residual (R_{wp}) and goodness of fit (GOF):

$$R_P = \frac{\sum |y_{io} - y_{ic}|}{\sum y_{io}} \tag{4.13}$$

$$R_{wp} = \left[\frac{\sum w_i \left(y_{io} - y_{ic} \right)^2}{\sum w_i y_{io}^2} \right]^{-1/2} \tag{4.14}$$

$$R_{\exp} = \left[\frac{N - P}{\sum w_i y_{io}^2} \right]^{1/2} \tag{4.15}$$

$$GOF = \left[\frac{R_{wp}}{R_{\exp}} \right]^2 \tag{4.16}$$

where R_p residual quantifies the difference between the observed (y_{io}) and calculated (y_{ic}) data points on a point-by-point basis; R_{wp} weights the residual so that higher intensity data points are more important than low intensity data points; R_{exp} evaluates the quality of the data; and *GOF* compares R_{wp} to R_{exp}. N is the number of observations; P is the number of least-squares parameters being estimated; and w_i is the weight fraction of phase i. Generally, a good refinement is obtained if R_{wp} or R_p is as small as possible, while *GOF* tends to be one. In this research, Rietveld refinements were required to obtain appropriate pattern fitting in which R_{wp} or R_p was smaller than 10% and *GOF* was less than 5.

Rietveld analysis always normalizes all phase fractions to 100%. Due to the presence of amorphous phases and uncounted crystalline phases, the mass fractions given by Rietveld analysis are overestimated. However, the amount of internal standard addition is known (10% ZnO in this study) allowing calculating the real percentage of each phase in the mixture:

$$[X_i] = [X_i]_c \frac{[ZnO]_{add}}{[ZnO]_c} \left(\frac{100}{100 - [ZnO]_{add}} \right)\% \tag{4.17}$$

where $[X_i]$ and $[X_i]_c$ are the real and calculated mass fraction of phase i, respectively; $[ZnO]_{add}$ and $[ZnO]_c$ are the real and calculated mass fraction of ZnO, respectively. Furthermore, amorphous mass fraction (related to C-S-H), $[Am]$ is obtained as follows:

$$[Am] = 100 \left(1 - \frac{[ZnO]_{add}}{[ZnO]_c} \right) \left(\frac{100}{100 - [ZnO]_{add}} \right)\% \tag{4.18}$$

4.5.6. Ion chromatography

Ion chromatography (IC) was used to quantify the amount of calcium leached out from the samples during the leaching experiments. The surrounding solution was extracted every seven days up to the end of the experiment. Prior to the measurement, the solution was filtered through a 0.45 µm syringe filter, and then diluted with milli-Q water to a (1:1000) solution. The IC analysis was performed using a Dionex CS12A column and a 20 mM MSA isocratic elution. Detection was performed by a Dionex EC50 electro conductivity detector.

4.5.7. Weighing method

The mass of sample before and after leaching was determined under saturated condition by a precise balance (10^{-3} g). This is a direct method to quantify the mass loss due to leaching.

4.5.8. Phenolphthalein spraying

Phenolphthalein spraying is the simplest, cheapest and the most popular method to detect the carbonated zone as recommended by RILEM [146]. This method is also frequently used to detect the Ca-leached zone. However, this method only roughly identifies the zone of carbonation/leaching and cannot detect the partly carbonated/leached area with pH values higher than 9 [146, 147]. As such, it cannot detect the exact portlandite dissolution front in cementitious systems because the pH is buffered at higher values by other cement hydrates [220] resulting in the underestimation of the carbonation depth [221] or leached depth. The phenolphthalein test does not really measure the carbonation of the sample but only its pH.

In this study, phenolphthalein was used to determine the so-called “phenolphthalein degraded depth” by carbonation and leaching. The leaching tests were stopped after 7, 14, 21 and 28 days to examine different leaching grades. The leached samples were cut into hemispherical parts and sprayed by a phenolphthalein solution to determine the phenolphthalein degraded depth. Sawing the sample can result in a smearing effect: the degraded depth can be smeared out due to cross contamination by dust. Alternatively, a freshly exposed surface can be prepared by axially breaking the sample using a hammer. For carbonated materials, the phenolphthalein degraded depth was only determined after 28-day carbonation.

4.6. Concluding remarks

A factorial experimental program was proposed which allowed studying the effects of w/p ratio and limestone filler replacement on transport properties and chemical degradation. A new technique was optimised to measure water permeability of cement-based materials using a controlled constant flow method. A method to measure the diffusivity of dissolved gases was proposed which enabled determination of the effective diffusion coefficients of 2 gases in a single experiment. A new carbonation method has been developed in which a high (pure) CO_2 pressure gradient was applied to accelerate the carbonation process. The method allowed studying the contribution of advection to the carbonation of cement-based materials. The leaching process was accelerated by using ammonium nitrate 6M. The changes in permeability and diffusivity due to chemical degradation could be easily investigated in a testing series thanks to the compatibility of proposed methods.

A variety of complementary post-analysis techniques were used to qualitatively and quantitatively examine the intact and degraded materials. Comprehensive information obtained from these techniques provides a full picture of how transport properties of cement-based materials are changed due to leaching and carbonation via the evolution of the mineralogy and the microstructure.

CHAPTER 5: EFFECTS OF W/P RATIO AND LIMESTONE FILLER ON TRANSPORT PROPERTIES OF INTACT CEMENT PASTES

5.1. Introduction

In this chapter, the effects of w/p ratio and limestone filler replacement on water permeability and diffusivity of dissolved gas using the proposed methods in Section 4.3 are presented. Furthermore, the relationship between microstructure and transport properties is discussed. The experiments were performed on hardened cement paste samples following the factorial experimental design (Section 4.2), under fully saturated condition.

5.2. Water permeability

5.2.1. Validity of Darcy's law

Darcy's law, which was applied to calculate the permeability in the proposed method, was validated on a Ca-leached sample. Figure 5.1 is the plot of flow rate against pressure gradient of leached sample. It can be seen that the flow rate is linearly dependent on the pressure gradient with a relation coefficient of 0.9992. This indicates that the flow through the sample is laminar, which is the most restrictive condition for the validity of Darcy's law. The permeability coefficient (i.e. hydraulic conductivity) was considerably high, 2.59×10^{-10} m/s, for leached sample. It is expected that the validity of Darcy's law is still kept for less permeable cementitious materials because laminar flow can be more easily obtained when the fluid is moving slowly.

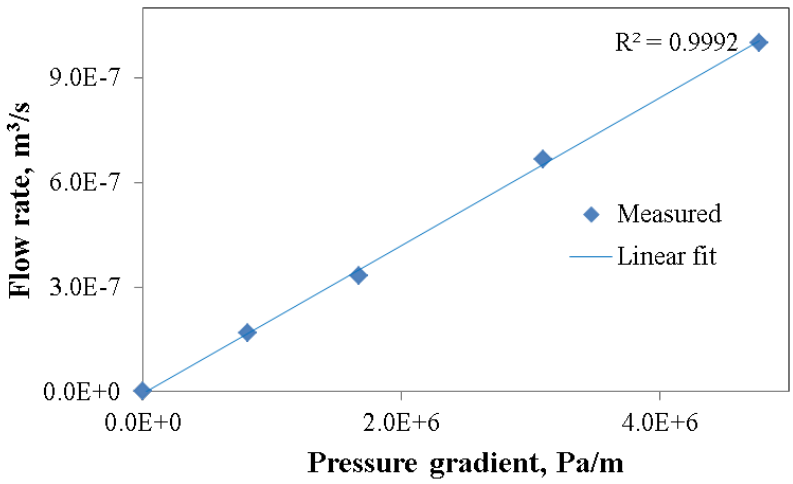

Figure 5.1. Linear relationship between flow rate and pressure gradient

5.2.2. Effects of w/p ratio and limestone filler replacement on water permeability

The determined permeability coefficients of cement pastes with w/p ratios ranging from 0.325 to 0.425 and limestone filler replacement ranging from 0 to 20% (see Table 4.3 for the detail of mix design) are represented by cube and interpolated surface (using Akima's polynomial method [222]) plots in Figure 5.2. It can be seen in the surface plot that, to improve the impermeability, one should choose a mix design with a low w/p ratio and low limestone filler replacement. In order to clearly visualize the effects of w/p ratio and limestone filler replacement on permeability, the main effects and interaction plots were built using statistic software Minitab. The main effects plot (Figure 5.3a) shows that the permeability strongly decreases with decreasing w/p ratio and limestone filler replacement. There does not seem to be a large difference in the magnitude of the effects of w/p ratio and limestone filler replacement as its quite similar slopes (referred to the changes of the response when factorial values vary from low to high levels). The regression equation (first-order) of logarithm of permeability coefficient is obtained as follows:

$$\log_{10}(k) = -17.65 + 12.47\ \text{ls/p} + 11.74\ \text{w/p} - 21.15\ \text{ls/p} \times \text{w/p} \qquad (5.1)$$

where k is the permeability coefficient [m/s]; ls/p is the ratio of limestone filler over powder (cement + limestone filler); w/p is the ratio of water over powder. The correlation coefficient (r^2) is 0.9965 indicating that the predicted model fits the experimental data well.

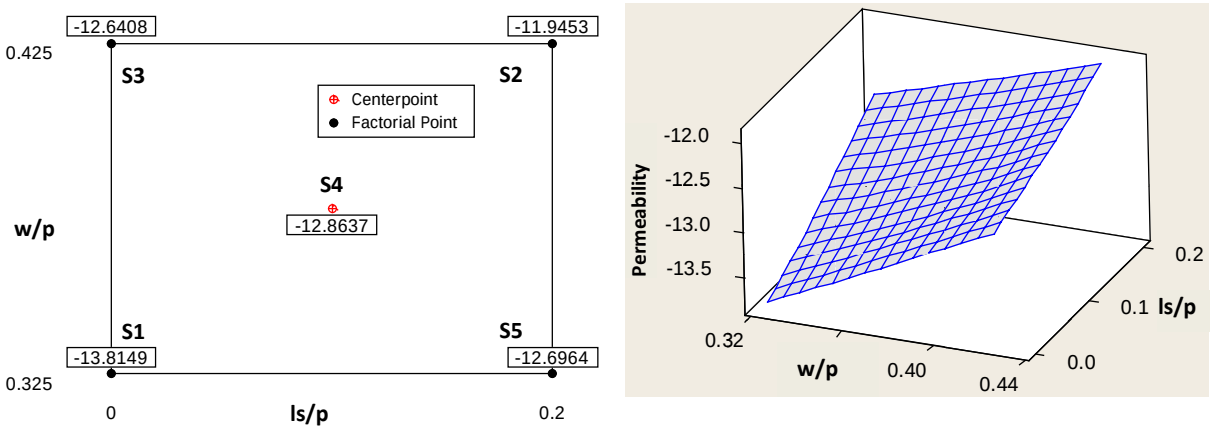

Figure 5.2. Cube plot and interpolated surface plot of permeability (logarithmic transformation) vs. w/p ratio and limestone filler replacement (ls/p)

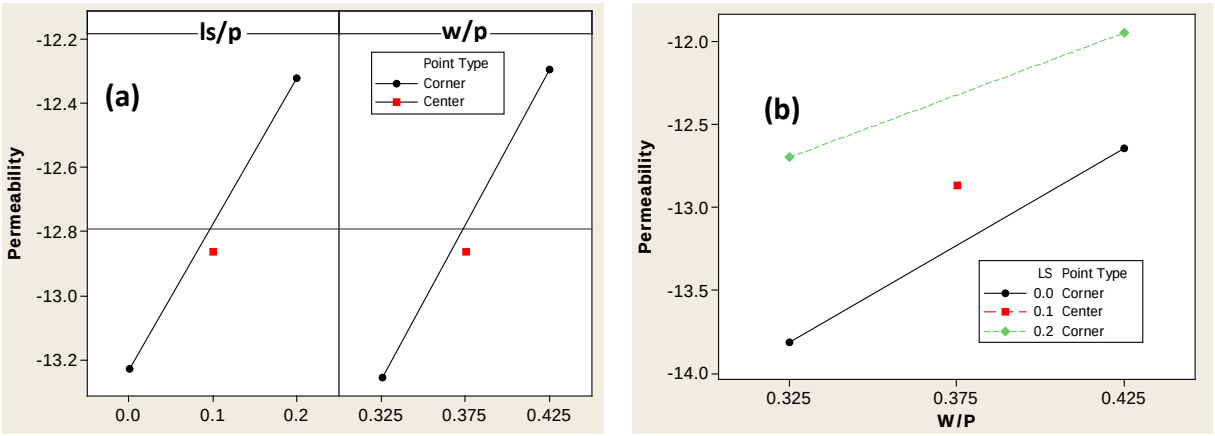

Figure 5.3. Main effects plot (a) and interaction plot (b) for permeability (logarithmic transformation)

The interaction plot (Figure 5.3b) enables us to visualize the interaction effect (i.e. the combined effects of factors on the dependent measure. When an interaction effect is present, the impact of one factor depends on the level of the other factor) of w/p ratio and limestone filler replacement on the permeability. As the connected lines of factor levels are not parallel to each other, there might be interaction. However, the interaction is not significant because the extent of departure is small. The interaction is getting stronger with the increase of w/p ratio and limestone filler replacement.

In general, the total capillary porosity of cement paste is expected to decrease when its w/p (or w/c) ratio is lower [47, 58, 223, 224]. The decrease in capillary porosity (which is composed mainly by large and connected pores) leads to a limitation or a decrease of pathways in hardened cement paste resulting in a reduced permeability. It is worth mentioning that the permeability of cement pastes is lower than the permeability of concretes with the same w/c ratio by around two orders of magnitude. Although concrete consists of aggregates having lower permeability values compared to other components in the mixture, micro cracks present at the interfacial transition zone (ITZ) between hardened cement paste and aggregates increase the permeability of concrete. The micro cracks are generally larger than capillary pores, and the propagation of micro cracks will develop the interconnections that increase the permeability [225]. The permeability measured on cement pastes in this study followed the same trend compared to the permeability of concretes with similar w/c ratios.

Literature on the effects of limestone filler addition on transport properties of cement-based materials is quite scattered. Most studies [226-228] agree that there is no significant change in transport properties as long as limestone filler replacement is less than 10%. Tsivilis *et al*.

[228] measured the gas and water permeability of concretes with different limestone filler replacements (up to 35%). The gas permeability is increased with the increase of limestone filler replacement while the water permeability exhibits an opposite behaviour. However, the change in permeability is not that significant (less than 30%) which might not be different enough to overwhelm the error on permeability measurement. The high w/c ratios (0.62 and 0.7) may result in a minor effect on the permeability characteristics as stated by the authors. On the contrary, Matthews [229] found that oxygen permeability decreases with increasing limestone filler replacement (up to 25%), In this case, the w/c ratio is 0.6 which is a bit lower than one of Tsivilis' study. Moir *et al*. [230] also found that the presence of limestone slightly reduces the oxygen permeability concretes made with 5 or 25 % limestone filler replacement. Ramezanianpour *et al*. [226] measured the water penetration depths of concrete mixtures made with 0, 5%, 10%, 15% and 20% limestone filler replacements. The authors found that the minimum water penetration depth is obtained for the mixture with 10% limestone filler replacement. Adding 20% limestone filler replacement results in the worst water permeability regardless curing ages.

Generally, the reduction of transport properties is attributed to the nucleation effect of fine particles of $CaCO_3$ which refines the pore structure of pastes. The connectivity of the pore structure is reduced. On the other hand, the increase in transport properties normally relies on the hypothesis that fluid transports faster in the interfacial transition zone between bulk cement paste and limestone particles. Furthermore, water demand (for the same hydration degree) is lower for limestone-cement paste if limestone filler is considered as inert filler. Thus, with the same w/p ratio, more water in limestone-cement paste results in more pores after hydration and setting. In order to know which effects are dominant, knowledge on the quality of limestone filler and cement, which is characterized by particle size distribution, and compositions of both cement and limestone filler is needed. The method to incorporate cement/clinker with limestone (blending or inter-grinding) may affect the properties of limestone-cement-based materials as it might produce somehow different particle size distributions. In this study, limestone filler was added to plain cement by blending. The particle size distribution of the limestone filler was coarser than the one of the cement. For these reasons, it might support the finding that water permeability was increased with the increase of limestone filler replacement in this study.

Table 5.1. Summary of MIP results of reference samples

Parameters	**S1**	**S2**	**S3**	**S4**	**S5**
w/p	0.325	0.425	0.425	0.375	0.325
ls/p	0	0.2	0	0.1	0.2
Permeability coefficient, m/s:	$10^{-13.8}$	$10^{-11.9}$	$10^{-12.6}$	$10^{-12.9}$	$10^{-12.7}$
Accessible porosity, %:	10.40	23.65	16.48	13.73	12.92
Average pore diameter (4V/A), nm:	22.67	29.87	26.09	24.24	25.40
Critical pore diameter, nm:	25.74	49.87	32.00	36.41	29.03
Specific surface, m^2/g:	7.77	14.90	10.58	9.44	7.56

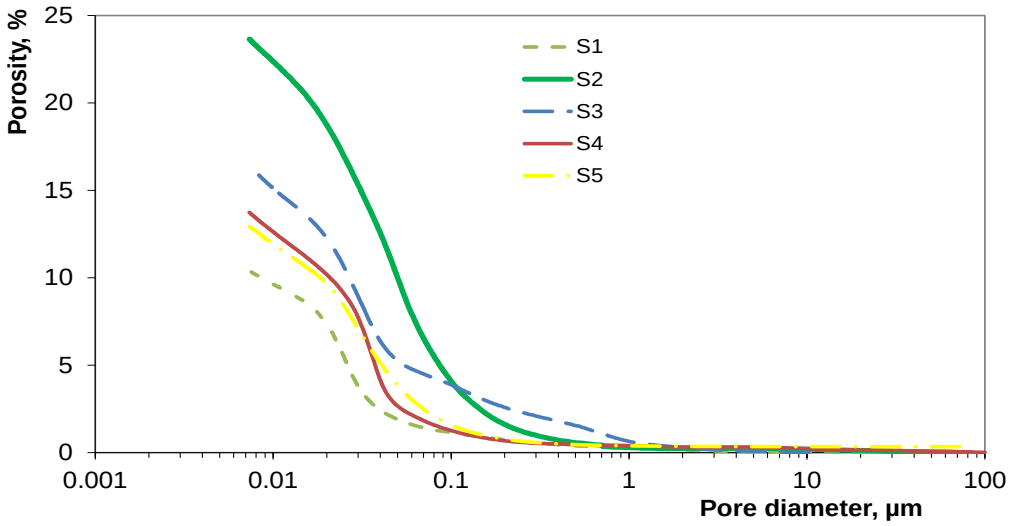

Figure 5.4. Porosity versus pore diameter determined by MIP

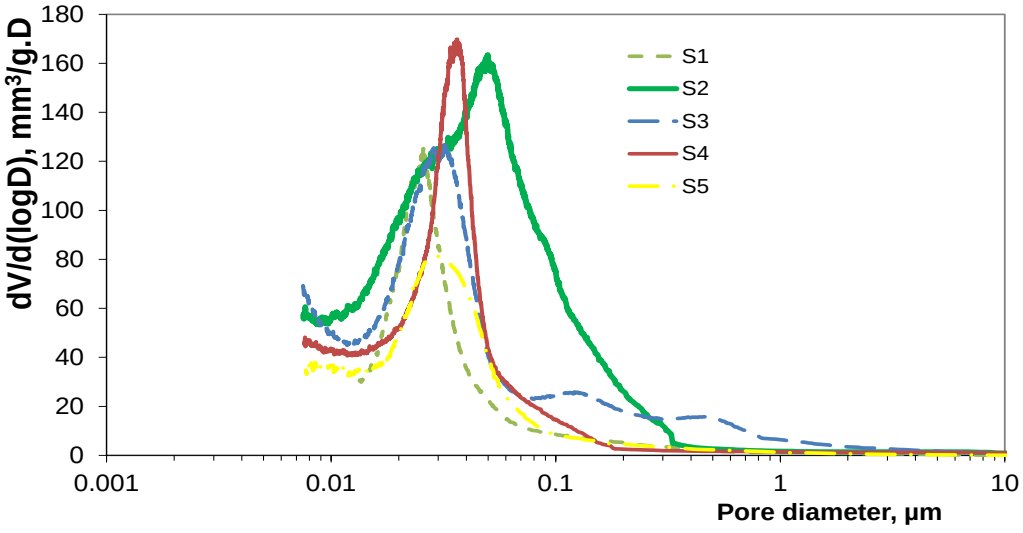

Figure 5.5. Differential pore size distribution determined by MIP

5.2.3. Pore structure and its effect on water permeability

The porosity and pore size distribution are shown in Figure 5.4 and Figure 5.5, respectively. At a given w/p ratio, adding limestone filler made the microstructure coarser, especially for high w/p ratio (i.e. sample S2 vs. sample S3). However, at a given w/c ratio, the limestone filler replacement refined the microstructure of cement pastes. As evidenced in Table 5.1, sample S3 had higher porosity and bigger average pore diameter compared to sample S4 (10% limestone filler replacement) despite its quite similar w/c ratio (0.425 and 0.416). In most cases, the samples with larger porosity and coarser pore size distribution resulted in higher water permeability. However, sample S5 did not follow the general trend as it showed higher water permeability despite smaller porosity and finer pore size distribution compared to sample S4 (see Figure 5.2). This phenomenon might a consequence of different air void content or macro pores in two samples. Unfortunately MIP experiment does not generally enable to detect air voids because air voids are only intruded after threshold pressure is reached, and thus counted for smaller pores. Furthermore, big pores may be intruded by mercury before increasing pressure, and are thereby not counted in total porosity.

Figure 5.6 compares the measured permeability with literature values. Note that only results of the mixtures without limestone filler (S1 and S3) in the factorial experimental program and results in a separate study [231] using the proposed method are shown in Figure 5.6. In general, the results obtained with the tested experimental setup are consistent with published data, especially with the data of [232] based on a traditional method in which a constant hydrostatic pressure of about 3 bar is applied to truncated conical samples until a steady state flow is obtained (approximately 4 weeks). The favourable agreement gives confidence in the validity of the developed method. Permeability coefficients obtained from this study are lower than the results of Ye [233] and Goto *et al*. [47] by one order of magnitude, and higher than the results obtained from beam bending [15] and dynamic pressurization [18] methods although the values from beam bending and dynamic pressurization methods were obtained at earlier curing ages (21 and 14 days, respectively). The differences are attributed to variations in blending of the samples, curing conditions and the fineness of the cement used and especially to differences in the calculation of permeability values between direct and indirect methods. The way to pour and blend cement paste significantly influences the permeability, especially at high w/c ratios in which the cement pastes tend to develop vertical channels [232] if there is no sufficient solution to prevent bleeding. In this study, the bleeding potential

was reduced thanks to short height and wide diameter of the mould besides well vibration during casting and the use of the vibration device.

The studied samples were cured in saturated lime water before testing while Ye only cured samples in sealed condition [233]. The degree of hydration of the lime water saturated curing samples is much higher than sealed curing samples; as such, there are more empty pores in the sample under sealed curing conditions [233, 234]. Additionally, the specific surface area (4350 cm^2/g) of the Portland cement type I used in this study is higher than the ones used in the studies of Ye and Goto *et al* [47] while lower than the Portland cement type III (ASTM) used in the studies of Vichit-Vadakan *et al*. [15] and Grasley *et al*. [18]. It is believed that the degree of hydration is accelerated if the sample is cured in saturated lime solution and/or when the fineness of the cement is higher. Therefore, the porosity significantly reduces [235] and as a consequence the permeability decreases. The work of Banthia *et al*. [236] also showed a lower permeability of cement type III paste compared to cement type I paste.

The interactions between water and cement matrix could be reduced in this proposed method because the continuous hydration of mature cement paste was limited because of the relatively short measurement time in the proposed method. Furthermore, the measurement was conducted on lime water saturated samples in a closed system which could decrease the dissolution of $Ca(OH)_2$ and the carbonation of dissolved $Ca(OH)_2$ – one of the main mechanisms of self-healing property of cement-based materials [42].

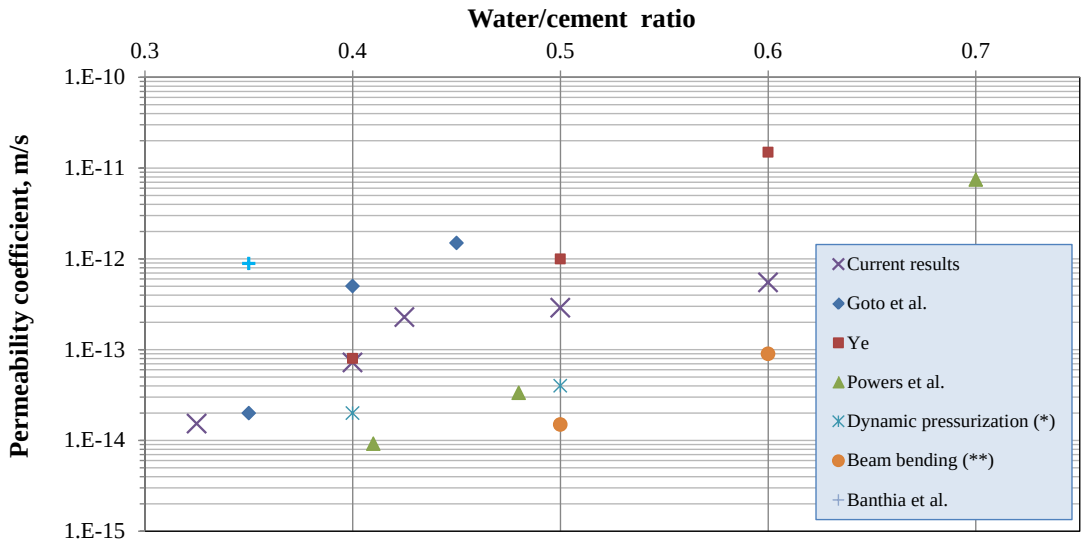

Figure 5.6. Permeability of cement pastes at different w/c ratios and comparison of the current test results versus literature data: (*) measured at 21 days of curing, (**) measured at 14 days of curing, for the rest at 28 days of curing

5.2.4. Correlation between pore structure parameters and water permeability

This section aims at finding how water permeability is correlated to key pore structure parameters which can be determined by MIP. The main parameter influencing permeability is accessible porosity. However, porosity itself is not well correlated with the water permeability as shown in Figure 5.7a. Another factor significantly affecting the water permeability is the pore size distribution which is characterized by several parameters including critical, threshold (the largest pore size at which pore volume is significantly increased) and average pore diameters. Furthermore, water permeability also depends on tortuosity which accounts for the tortuous and reduced transport pathway. However, it is impossible to measure tortuosity directly. The author tried to relate the water permeability with 2 measureable parameters: accessible porosity and critical pore diameter (from MIP experiments) by modifying the Carman-Kozeny relation [62] as follows:

$$k_w = \varsigma d_{cr}^2 \frac{\phi^{2.5}}{(1-\phi)} \tag{5.2}$$

By plotting the intrinsic water permeability (converted from hydraulic conductivity using Equation (2.2)) versus $d_{cr}^2 \frac{\phi^{2.5}}{(1-\phi)}$, the author found a good correlation with correlation coefficient of 0.99 as shown in Figure 5.7b. The slope yields value of $\varsigma = 0.0017$ [-]. The relationship gives an estimation of permeability if the key parameters (determined by MIP) are known.

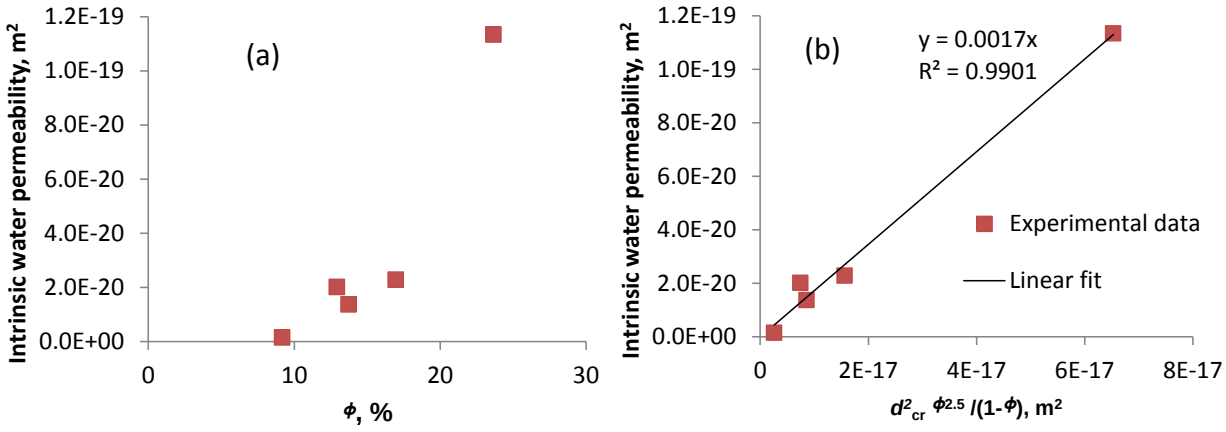

Figure 5.7. Correlation of intrinsic water permeability and accessible porosity (a) and $d_{cr}^2\phi^{2.5}/(1-\phi)$ (b)

5.3. Diffusivity

The diffusion experiments were performed on two reference samples S3 (w/p = 0.425, ls/p = 0) and S4 (w/p = 0.375, ls/p = 0.1). These samples had quite similar w/c ratios, i.e. 0.425 for S3 and 0.416 for S4. In order to obtain the effective diffusion coefficients, the accessible porosity was determined by a combination of MIP and N_2-adsorption experiments. The MIP experiments determined the porosity down to the pores with minimum diameter of 7.35 nm (corresponding to maximum intrusion pressure of 200 MPa). The porosity in pore size range of 3.17 – 7.35 nm was determined by N_2-adsorption experiments. BJH method [206] was used to calculated pore volume. Despite the quite similar w/c ratios, the accessible porosity of sample S4 was 16.8% which is relatively lower than sample S3, 19.7%, due to limestone filler addition (total accessible porosity determined by MIP + N_2-adsorption combination is detailed later in Table 7.3). It is assumed that there is no adsorption for He and Xe due to its inert characteristics as noble gases. Thus the retardation factor R_e was set to one. Due to lower diffusivity of Xe compared to He (5 times lower in free water), the concentration of Xe at the outlet was not high enough to be detected reliably by gas chromatography within the experimental time (4-5 months). Therefore only the data of He diffusion are presented for the reference samples. Figure 5.8 (a) and (b) show the fitted and measured partial pressure profiles of He at the outlet for reference samples S3 and S4, respectively. Good correlation coefficients were obtained for both cases. The effective diffusion coefficients of samples S3 and S4 were 2.32×10^{-11} m^2/s and 1.22×10^{-11} m^2/s, respectively. As for permeability, the limestone filler addition improved the microstructure which resulted in a decrease of diffusivity of about 50%. Ramezanianpour *et al*. [226] also reported a significant decrease in chloride diffusion due to limestone filler addition for the cases of OPC concrete with w/c ratio of 0.45 and concrete with w/p ratio of 0.37 and 20% limestone filler replacement (w/c = 0.46). However, when w/c ratio increases to 0.55, the reduction effect in diffusion is not clear. Note if the comparison is only based on the same w/p ratio, Ramezanianpour showed an increase in diffusion if the limestone filler replacement was higher than 10% which was also observed by Bonavetti *et al*. [237].

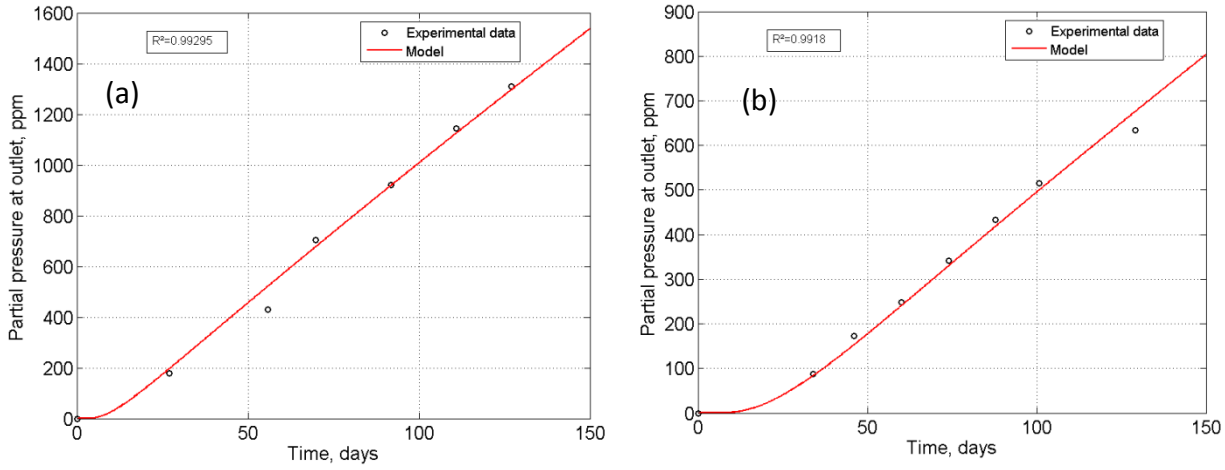

Figure 5.8. Increase in He partial pressure at the downside compartment in the through-diffusion experiment with dissolved gases - Comparison between experiment and model for reference samples S3 (a) and S4 (b)

From the obtained effective diffusion coefficients the square of tortuosity/constrictivity ratios can be calculated by Equation (4.6). Diffusion coefficients for other gases can be calculated if one considers that they exhibit similar τ^2/δ ratio. The author calculated the diffusivities of Xe which were not able to determine by the experiments as shown in Table 5.2. It can be seen that the effective diffusion coefficient of Xe is quite small compared to He (5 times lower). Therefore, the time needed for collecting enough data to extract Xe effective diffusion coefficient is relatively longer for the case of He.

Table 5.2. Estimation of effective diffusion coefficient [m^2/s] for Xe from information of tortuosity and constrictivity obtained from He diffusion experiment

Sample	Dissolved gas	D_e	D_0 [238]	ϕ, %	R_e	τ^2/δ
S3	He	2.32×10^{-11}	7.22×10^{-9}	19.7	1	61.2
	Xe	4.73×10^{-12}	1.47×10^{-9}	19.7	1	61.2
S4	He	1.22×10^{-11}	7.22×10^{-9}	16.8	1	99.1
	Xe	2.49×10^{-12}	1.47×10^{-9}	16.8	1	99.1

5.4. Summary and conclusions

In this chapter, the effects of limestone filler replacement and w/p (w/c) ratio on microstructure, water permeability and dissolved gas diffusion were investigated. Water

permeability measurements were performed following a factorial experimental program, while gas diffusion experiments were carried out on 2 selected samples S3 and S4 (with and without limestone filler, similar w/c ratio) for comparison.

The experimental results showed that the developed methods for the determination of permeability and diffusivity seem promising in terms of the required experimental time and the parameter control (pressure, flow, concentration). The permeability results were comparable with results from studies reported in literature even though there were some variations due to differences in sample preparation and cement type. For dissolved gas diffusion, to the knowledge of the author, this is the first time that data on diffusion of dissolved He (inert gas) in cement-based materials were reported. Oxygen is the only dissolved gas of which diffusion data can be found in literature of cement-based materials [78, 80].

It was observed that both limestone filler and w/p ratio had significant influences on water permeability. Permeability was increased with the increase of w/p ratio and limestone filler replacement. However, there was no interaction effect between w/p ratio and limestone filler replacement in the testing range (w/p = 0.325; 0.375; 0.425 and ls/p = 0; 0.1; 0.2). At a given w/p ratio, adding limestone filler made the microstructure coarser, especially for high w/p ratio. Nevertheless, if the comparison is based on a given w/c ratio instead of w/p ratio, the limestone filler replacement refined the microstructure resulting in permeability decreases of cement pastes.

The water permeability was highly correlated to key pore structure parameters obtained from MIP experiments: accessible porosity and critical pore diameter. A good correlation of intrinsic water permeability and $d_{cr}^2 \frac{\phi^{2.5}}{(1-\phi)}$ was found. However, more experimental data are needed to validate this relation.

The same trend of the effects of w/p ratio and limestone filler replacement was observed for dissolved gas diffusion. However the effects were less significant than for water permeability. The square of tortuosity/constrictivity ratio calculated from the measured gas (He) can be used to estimate the diffusion coefficients for other gases.

This page is intentionally left blank!

CHAPTER 6: EFFECTS OF CARBONATION ON MICROSTRUCTURE AND TRANSPORT PROPERTIES OF CEMENT PASTES

6.1. Introduction

In this chapter, the changes in microstructure, mineralogy and transport properties of cement pastes subjected to carbonation using the proposed method in Section 4.4.1 are presented. Carbonated samples were analysed by a series of methods (see Section 4.5) including SEM, MIP and N_2-adsorption to characterize the microstructural changes; phenolphthalein spraying, XRD, TGA and water permeability, diffusivity measurements to study alterations in chemical compositions and transport properties. The experiments were performed on hardened cement paste samples with different water/powder and limestone filler replacement ratios, under fully/partially-saturated conditions (detailed in Table 4.4).

6.2. CO_2 uptake and carbonation depth

The CO_2 uptake is defined as the mass ratio between the CO_2 which reacted with the sample and the cement in the sample, expressed as:

$$Uptake_{CO_2} = \frac{\left(m_{CO_2}^{inlet} - m_{CO_2}^{outlet}\right)}{cem} 100\% \quad (6.1)$$

where $m_{CO_2}^{inlet}$ and $m_{CO_2}^{outlet}$ [kg] are the mass of CO_2 measured by inlet and outlet mass flow meters, respectively; cem is the cement mass in the sample [kg].

Figure 6.1 shows the CO_2 uptake of sample S3C, S4C and S5C during 28 days of continuous carbonation ("C" denotes continuous carbonation). The CO_2 uptake rate was initially very fast but decreased significantly after a few hours of carbonation. Initially, CO_2 mainly penetrated into the unsaturated (RH = 65%) sample via the gaseous phase. As carbonation proceeds, the released water increased the saturation degree of the sample. At a certain time, the sample was getting saturated close to the inlet which prevented further gaseous transport. Evidence of water saturation was indeed observed at the upstream side of the sample. The porosity reduction (showed later) in this layer also contributed to a slower CO_2 transport. From the moment of saturation of the first thin layer, the carbonation rate dramatically dropped. The longer the experimental time, the lower the carbonation rate because the released water tends to saturate the entire sample, hence slowing down the (gaseous) CO_2 transport.

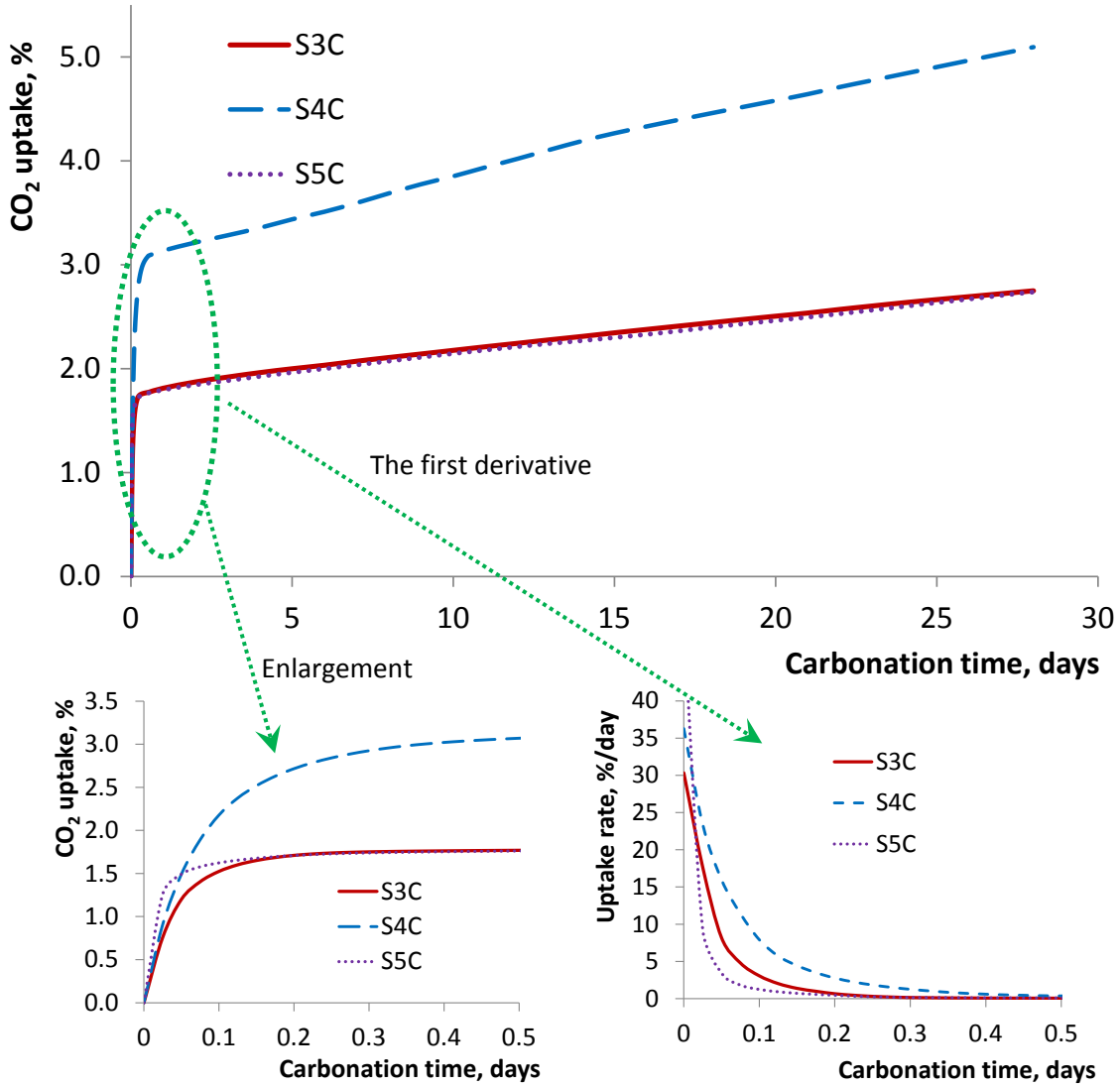

Figure 6.1. CO_2 uptake (in percentage wrt. cement mass in sample) of samples S3C, S4C and S5C as a function of time during continuous carbonation – the first derivative curves (right-bottom) show a decrease in carbonation rate over time.

The total CO_2 uptakes of S3C and S5C were similar despite its different initial uptake rates. Sample S3 had a higher w/p ratio but quite similar water permeability compared to sample S5 which could result in the same residual CO_2 uptake. Both initial and residual CO_2 uptake rates were the highest for the S4C sample, but major difference was found in the initial carbonation stage. This indicates that the CO_2 advection in the gaseous phase during the initial carbonation and diffusion in the aqueous phase after the initial carbonation were the fastest in sample S4C. Note that the transport of CO_2 is not only affected by the pore structure itself which is represented by "intrinsic" permeability and diffusivity, but also by the evolution of hygrothermal conditions (RH, temperature) of the sample. Due to a larger Ca amount and

higher potential for C-S-H carbonation (Section 6.4.2), the reaction rate (between Ca^{2+} and CO_3^{2}) could be faster for S3C. Therefore, the RH (and saturation degree) was getting higher in the first layer of S3C which prevented further CO_2 penetration. Consequently, the initial saturated water permeability of S3C was even higher than S4C (shown later in Table 6.6), the transport of CO_2 of S4C could be faster than S3C because the saturation degree of S3C increased quicker than S4C. Furthermore, gas permeability may not follow the same trend as water permeability due to slip effects [69] which is affected by internal pore surface area. For sample with limestone fillers (S4C), calcite may precipitate preferentially on limestone particles than on portlandite and C-S-H phases (shown later in Figure 6.17), which promotes the CO_2 uptake. Additionally, the dilution effect does contribute to larger CO_2 uptake of S4C compared S3C (i.e. more cement in S3C). However if the limestone filler replacement is increased from 10% (sample S4) to 20% (sample S5), the limestone filler no longer promotes the CO_2 uptake. The CO_2 uptake of S5C was significantly smaller than S4C as a result of higher limestone filler replacement (lower w/p ratio).

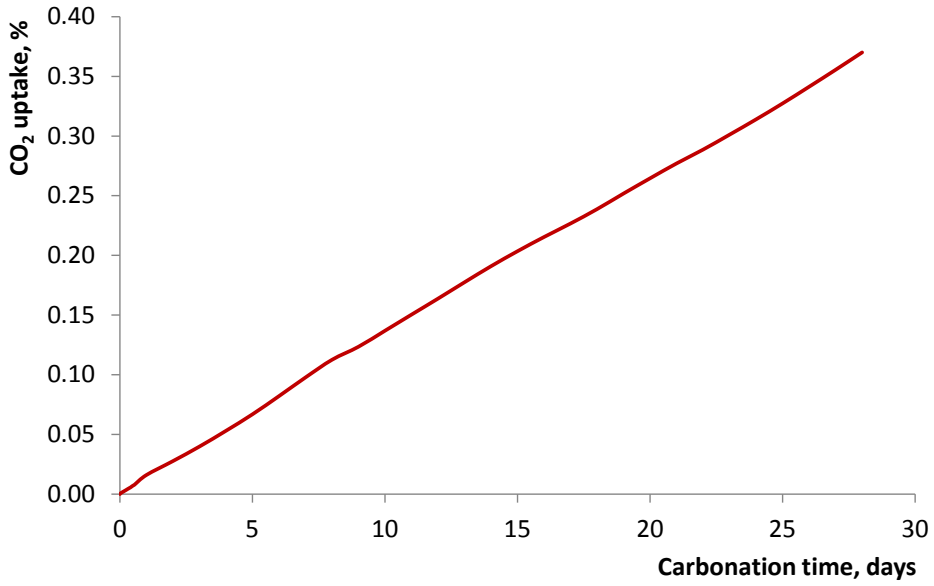

Figure 6.2. CO_2 uptake (in percentage wrt. cement mass in sample) of saturated sample S1C-S as a function of time during continuous carbonation

The carbonation of fully saturated sample showed different characteristics compared to partially saturated samples. The CO_2 uptake of fully saturated sample S1C-S was very small, 0.37% after 28 days of continuous carbonation. More interesting, there was no fast initial uptake as seen in partially saturated samples. The CO_2 uptake was almost linearly increased from the beginning until the end of experiment (Figure 6.2). This phenomenon is explained

due to lacking of transport in gaseous phase of saturated sample. The transport mechanisms of CO_2 were both diffusion and advection in aqueous phase, but the later was the dominated process.

Applying a cyclic carbonation method significantly increased the carbonation degree as shown in Figure 6.3 for S4C-C and S5C-C. After five carbonation-drying cycles within one week, the CO_2 uptake of S4C-C reached 5.1% which is even higher than the CO_2 uptake after 4 weeks of continuous carbonation. The drying time of sample S5C-C was increased which resulted in a higher CO_2 uptake compared to S4C-C. After four carbonation-drying cycles within 19 days, the CO_2 uptake of S5C-C reached 12.5% which was 4.6 times larger than the CO_2 uptake after 4 weeks of continuous carbonation. The cyclic carbonation procedure clearly prevents saturation (see Figure 6.4), re-establishing gaseous CO_2 pathways and, thereby, increasing carbonation rates.

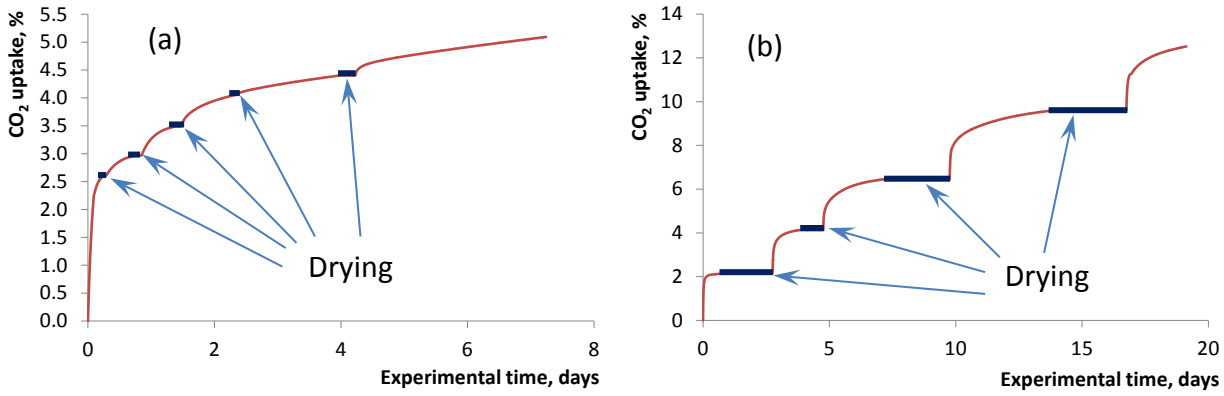

Figure 6.3. CO_2 uptake of samples S4C-C (a) and S5C-C (b) by applying cyclic carbonation method – experimental time referred to the total carbonation and drying time

The carbonation depths determined by phenolphthalein spraying of carbonated samples under different carbonation conditions are presented in Table 6.1. It is important to note that the phenolphthalein test does not really measure the carbonation depth but only its pH. The carbonation front obtained by the proposed carbonation method (high PCO_2 and transport by diffusion and advection) (see Figure 6.5) was not as sharp as the front mostly obtained under natural conditions (low PCO_2, no advection). This observation is supported by TGA results (section 6.3.2) in which the portlandite content gradually decreased with distance from the upstream side. The observation of a gradual front is due to the mass transport rate of CO_2 is not neglected compared to the carbonation reaction rate [134] as it should be under natural

conditions. The contribution of advective transport significantly increased the mobility of CO_2, at least in initial carbonation stage.

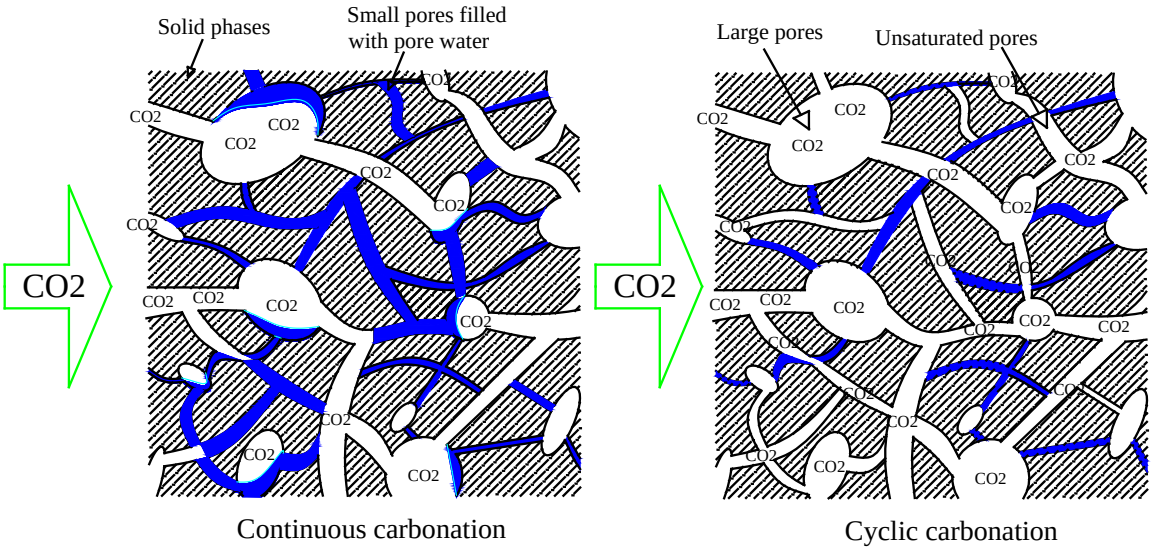

Figure 6.4. Conceptual comparison of aqueous and gaseous phase distribution within the cement pore structure during continuous and cyclic carbonation: saturation degree is significantly increased due to continuous carbonation as small pores are mostly filled with released water as carbonation proceeds; while for cyclic carbonation part of small pores are emptied during drying cycle. Volume of both large and small pores are changed by cyclic carbonation, while mainly large pores for continuous carbonation.

The phenolphthalein method did not detect a carbonation front for sample S1C-S indicating that the pH of pore solution was still higher than 9. The carbonation depth of sample S2C was the highest (3.7 mm) amongst all samples subjected to continuous carbonation due to its highest w/c ratio. The carbonation depths obtained after 28-days of continuous carbonation were quite similar for samples S3C (2.7 mm), S4C (2.5 mm) and S5C (2.3 mm) despite larger CO_2 uptake of S4C compared to S3C and S5C. This observation illustrates that the phenolphthalein indicator itself is not a sufficient indicator for carbonation rate. For sample S3C, portlandite might still be present but covered in the carbonation product layer while other phases (e.g. C-S-H) were carbonating. Therefore, phenolphthalein spraying led to an overestimation of carbonation depth of S3C.

Carbonation depth was more pronounced for cyclic-carbonated samples. The carbonation depth of S4C-C was twice (5.1 mm) than one of S4C, even though the carbonation time for the former was only 7 days. In case of sample S5, cyclic carbonation in 19 days resulted in 3 times deeper carbonated zone compared to continuous carbonation for 28 days.

Table 6.1. Carbonation depth determined by phenolphthalein spraying under different testing conditions

Sample	S1C-S	S2C	S3C	S4C	S4C-C	S5C	S5C-C
w/p	0.325	0.425	0.425	0.375	0.375	0.325	0.325
ls/p	0	0.2	0	0.1	0.1	0.2	0.2
Relative humidity, %	Saturated	65	65	65	65	65	65
Testing time, days	28	28	28	28	7	28	19
Carbonation method	Cont.	Cont.	Cont.	Cont.	Cyclic	Cont.	Cyclic
Carbonation depth, mm	0	3.7	2.7	2.5	5.1	2.3	7.5

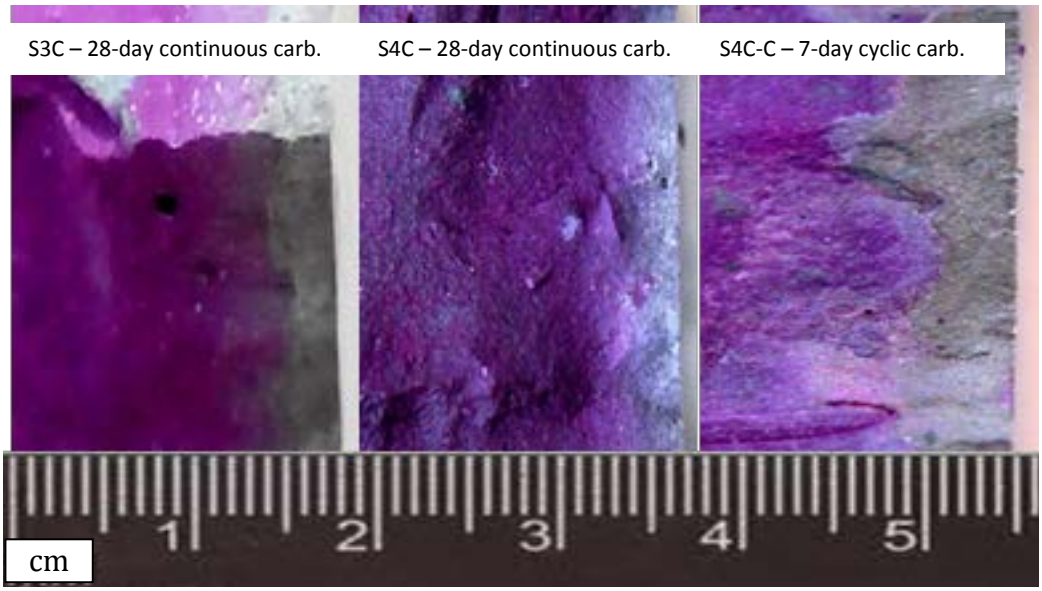

Figure 6.5. Carbonation depths of samples S3C and S4C after 28-day continuous carbonation and of sample S4C-C after 7-day cyclic carbonation (the carbonated zone is grey coloured)

6.3. Phase changes

6.3.1. XRD results

Figure 6.6 presents the XRD patterns for continuously-carbonated and reference samples for the first 3 mm from the inlet. Presence of portlandite is indicated by the peaks at 2θ = 17.9^{o} and 34.2^{o}. There is an intense peak at 29.4^{o} corresponding to calcite which was formed during carbonation in all carbonated samples under 65% RH. For sample S1C-S which was carbonated under saturated condition, the reflection peaks of portlandite are indeed lower and the peaks of calcite are more visible, but the magnitude of alteration is much lower than for samples subjected to carbonation at 65% RH. Note that the intense peak of calcite in reference

samples S2, S4 and S5 is due to the limestone replacement (10% for S4 and 20% for S2, S5). Interesting is the peak of vaterite in all carbonated samples S1C-S, S2C, S3C and S4C even with relatively low intensity. The formation of vaterite is favoured when the system has a low Ca^{2+}/CO_3^{2-} concentration ratio [133, 239] which is the case during accelerated carbonation. Furthermore, the carbonation of ettringite leads to the formation of vaterite crystals [129]. The XRD patterns indicate ettringite dissolution as ettringite peaks are more visible in the reference samples than in the carbonated samples in most cases.

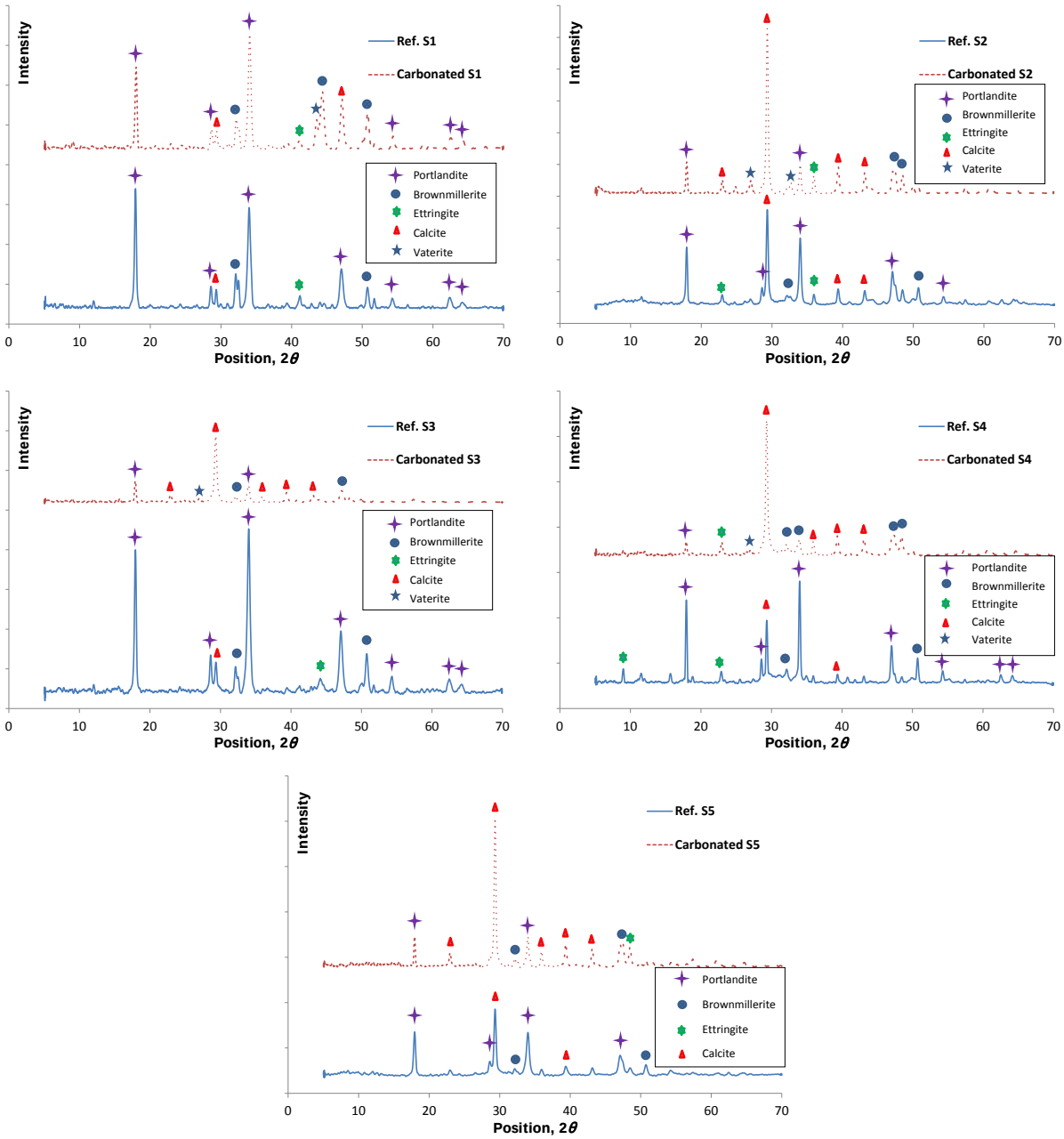

Figure 6.6. XRD patterns of reference and continuously-carbonated samples taken in the first 3 mm depth from the inlet – sample S1 was initially fully saturated, samples S2, S3, S4, and S5 was initially at 65% RH.

6.3.2. TGA results

Typical thermo-gravimetric and derivative thermo-gravimetric (TG/DTG) curves of continuously-carbonated sample S4C are shown in Figure 6.7. The tangent method was used to determine the percentage of portlandite and calcite in the reference and carbonated samples [240] in order to take into account the gradual decomposition of C-S-H. The dehydration of C-S-H mainly occurs in temperature range of 180 – 300°C [210]. However, it partially decomposes in the other temperature ranges, especially 400 – 500°C in which portlandite also decomposes. Two clear steps of portlandite (400 – 500°C) and calcite (560 – 765°C) decomposition were easy to detect in all samples. However, the formation of vaterite (as found in XRD pattern) during carbonation was not clearly identified.

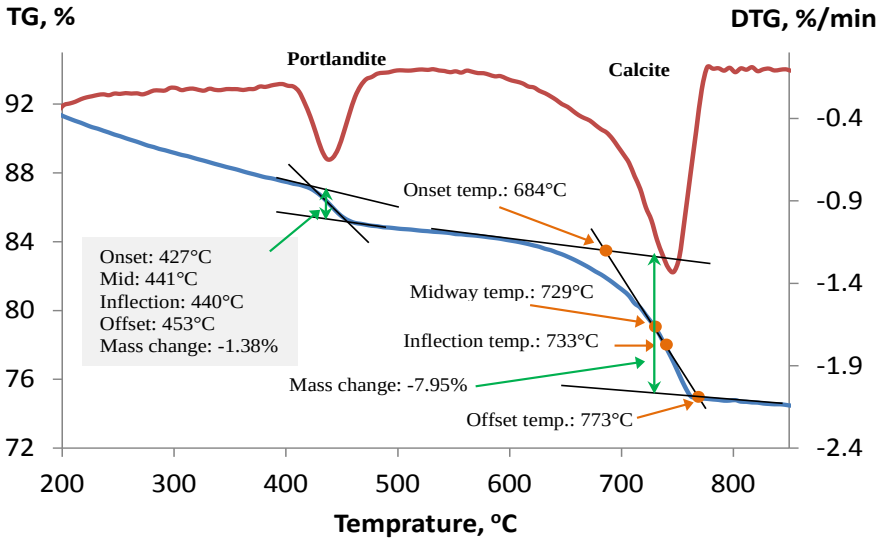

Figure 6.7. Illustration of tangent method to determine portlandite and calcite contents of continuously-carbonated sample S4C, depth 3 – 6 mm: TG curve is in blue, DTG curve is in red.

Figure 6.8 and Figure 6.9 show that in S3C and S4C, portlandite and calcite, respectively, gradually decreases and increases up to a depth of 12 mm. Note that the surface at the downstream side which was not in contact with the pure CO_2 was slightly carbonated by CO_2 originating from the atmosphere (observed at depths above 20 mm). Portlandite was observed in the first sampling interval (0-3 mm) although the phenolphthalein test indicated a pH lower than 9 in that interval (2.7 and 2.5 mm for S3C and S4C, respectively). It is hypothesized here that under accelerated conditions in which the transport of CO_2 is faster than Ca ions, a calcite layer may form around the portlandite (or C-S-H) particles. Two main consequences are that (i) these portlandite particles are not easily accessible for CO_2 and thus further carbonation is

extremely limited (illustrated in Figure 6.18), and (ii) the pH of the pore solution is no longer buffered by portlandite.

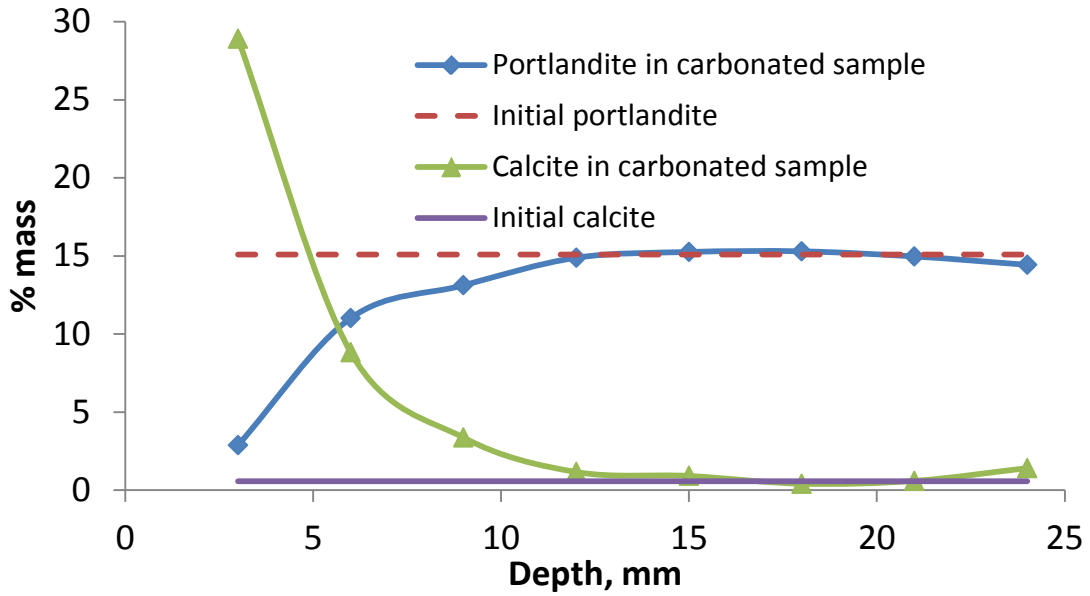

Figure 6.8. Changes in portlandite and calcite contents as a function of depth averaged over 3 mm depth intervals of the carbonated sample S3C under continuous carbonation. The initial portlandite and calcite contents are determined from the reference sample.

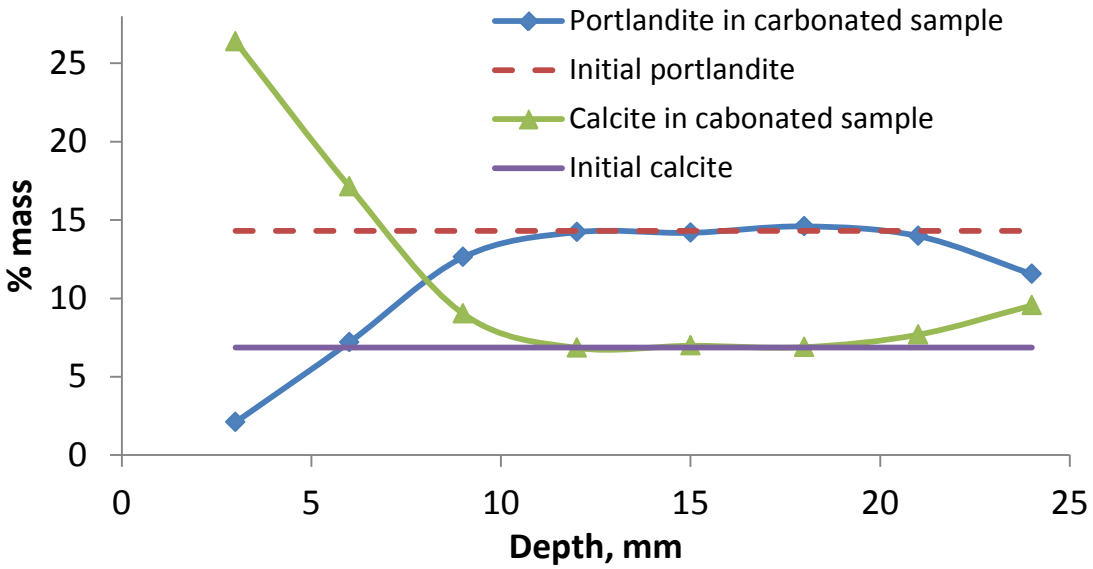

Figure 6.9. Changes in portlandite and calcite contents as a function of depth averaged over 3 mm depth intervals of the carbonated sample S4C under continuous carbonation. The initial portlandite and calcite contents are determined from the reference sample.

The profiles of portlandite and calcite for the carbonated sample under saturated condition S1C-S are presented in Figure 6.10. The same trends in increase of portlandite and decrease of calcite over the depth were observed as for carbonated sample under 65% RH. However, the change in portlandite (and calcite) content of S1C-S was much lower than S3C and S4C.

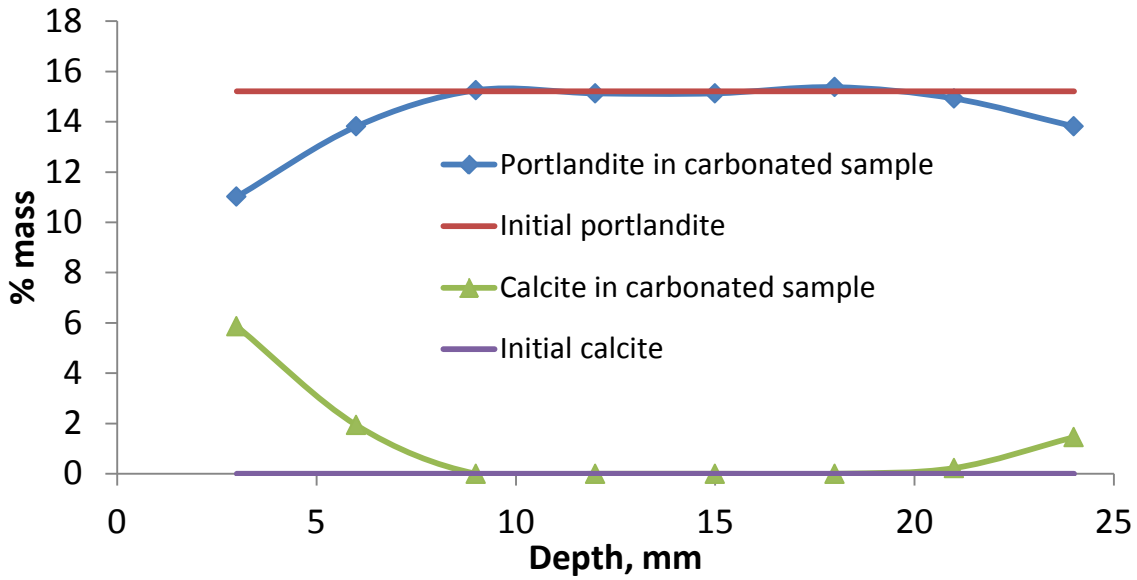

Figure 6.10. Changes in portlandite and calcite contents as a function of depth averaged over 3 mm depth intervals of the carbonated sample S1C-S under continuous carbonation. Sample was saturated before carbonation. The initial portlandite and calcite contents are determined from the reference sample.

In order to identify whether other phases (mainly C-S-H) than portlandite react with CO_2, the calculated amount of calcite formed from portlandite carbonation was compared with the measured calcite content. The amount of reacted portlandite content was calculated from the difference in portlandite content between the carbonated and reference samples. This value was taken as a proxy for the calcite formed from portlandite carbonation. The calcite formed from C-S-H carbonation (with assumption that the carbonation of the minor phases was negligible) was estimated as the difference between the calcite content measured by TGA and the calcite formed from portlandite. The estimation showed that C-S-H carbonation contributes 41.8%, 33.3% and 4.6% to calcite formation in the intervals 0-3, 3-6 and 6-9 mm for S3C, respectively. The carbonation of C-S-H in S4C was limited to 15.5% and 6.4% in the intervals 0-3 and 3-6 mm, respectively (Figure 6.11). There was no C-S-H carbonation observation beyond those depths. Note that the formation of vaterite (as seen in XRD results)

is difficult to quantify by TGA, but quantitative XRD would be a relevant method to study the formation of vaterite.

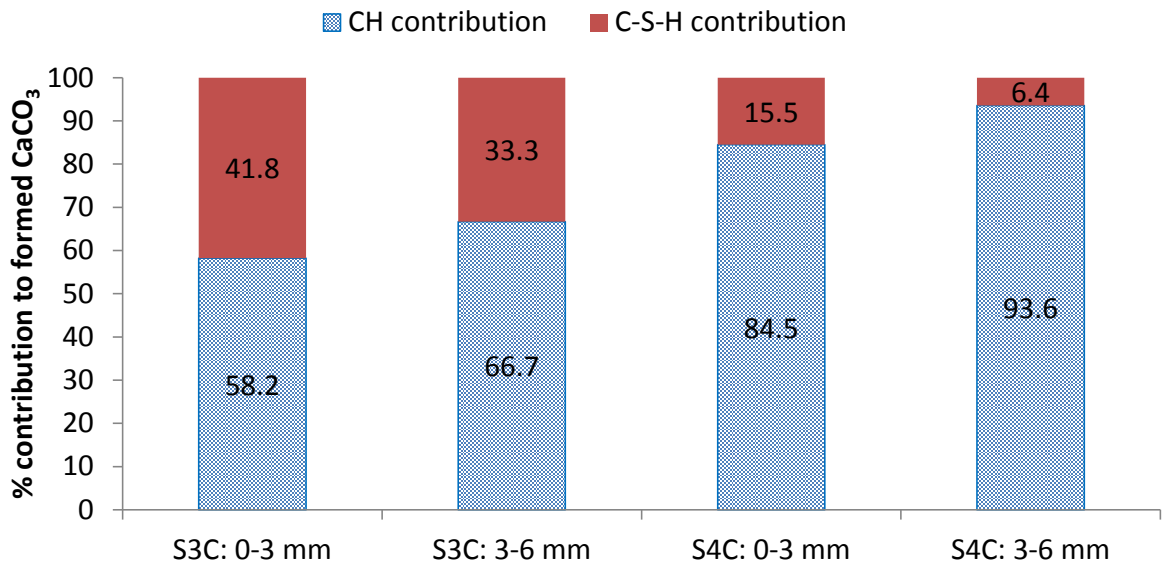

Figure 6.11. Evidences of C-S-H carbonation at the depth which is near reactive surface - the carbonation of the minor phases (e.g. AFm, Aft) was negligible.

6.4. Changes in porosity and pore size distribution

6.4.1. MIP results

Table 6.2 summarizes the MIP results. In most cases, the bulk densities of carbonated samples were slightly increased due to CO_2 uptake. In general, continuous carbonation slightly reduced accessible porosity. The porosity of continuously-carbonated samples (unsaturated) decreased about 2.3 - 2.5%, except for sample S3C which showed a larger porosity reduction from 16.5 to 12.9%. The fully saturated sample S1C-S was also reduced in porosity but much less (1.2%). The average pore diameter was reduced for continuously-carbonated samples, except for sample S2C which exhibited a slight increase despite its porosity reduction after carbonation. However, the decrease in porosity of S2C was mainly situated in the pores less than 0.02 µm (Figure 6.13). The median pore diameter (where 50% porosity) was also decreased, except for samples with 20% limestone filler replacement S2C and S5C. The MIP specific surface area which was calculated based on a cylindrical pore model was decreased for all carbonated samples, among them sample S3C showed the largest reduction.

In contrast to continuously-carbonated sample S4C, the average and median pore diameters of sample S4C-C subjected to cyclic carbonation were slightly increased as shown in Figure

6.15. Cyclic carbonation increased the porosity in the range 0.04 – 0.3 µm, but significantly decreased the number of pores smaller than 0.04 µm. The porosity of cyclic-carbonated sample (S4C-C) was also decreased, but less pronounced than the sample subjected to continuous carbonation (S4C). However, the MIP specific surface area reduced more significantly from 9.4 to 6.8 m^2/g.

Table 6.2. Changes in porosity, critical and threshold pore diameters and bulk density due to carbonation determined by MIP – "C", "C-C" denote continuous and cyclic carbonation, respectively; sample S1C-S was carbonated under saturated condition, the rest was at 65% RH.

Sample	S1	S1C-S	S2	S2C	S3	S3C	S4	S4C	S4C-C	S5	S5C
w/p	0.325	0.325	0.425	0.425	0.425	0.425	0.375	0.375	0.375	0.325	0.325
ls/p	0	0	0.2	0.2	0	0	0.1	0.1	0.1	0.2	0.2
Accessible porosity, %	10.4	9.2	23.7	21.4	16.5	12.9	13.7	11.3	12.8	12.9	10.6
Average pore diam., nm	22.7	20.9	29.9	34.8	26.1	21.8	24.2	21.1	30.2	25.4	24.7
Median pore diam., nm	25.7	22.6	42.8	49.7	32.2	28.7	32.5	26.9	47.7	32.8	36.9
Critical pore diam., nm	25.7	21.9	49.9	67.5	32.0	33.0	36.4	30.0	54.6	29.0	45.1
Threshold pore diam., nm	60	40	300	300	1000	100	200	60	300	300	300
Specific surface, m^2/g	7.8	7.5	14.9	12.9	10.6	7.7	9.4	8.1	6.8	7.6	6.1
Bulk density, g/cm^3	1.89	1.90	1.72	1.70	1.78	2.14	1.85	1.86	1.93	2.06	1.99

The cumulative pore volume and pore size distributions are shown in Figure 6.12 to Figure 6.16, for carbonated sample S1C, S2C, S3C, S4C, and S5C, respectively. When applying continuous carbonation, the threshold pore diameter (at which the intruded volume significantly increases) tended to reduce; in some cases (S2C and S5C) the threshold pore diameter was unchanged. In contrast, the threshold pore diameter of sample subjected to cyclic carbonation (S4C-C) slightly increased, from 0.2 µm to 0.4 µm. The critical pore size, which is the most frequently occurring pore size in interconnected pores, generally varied in a small range: some (S1C-S, S3C, S4C) slightly decreased, some (S2C, S5C) slightly increased. In contrast to the continuously-carbonated sample S4C, the cyclic-carbonated sample S4C-C exhibited a shift of the critical pore diameter to larger pore size. In the case of critical pore diameter increase, the porosity reduction was mainly situated in the pores less than 0.03 µm.

The reference samples exhibited sharp distributions which suggest that most of the pores of the reference samples are mainly distributed in a narrow range. While most carbonated samples (S2C, S3C, S4C, S4C-C) exhibited more rounded peaks (even more than one peak

for S2C and S3C) which indicates a broadening of the pore size distribution [241]. The increase in porosity in pore size range 0.05 – 0.2 µm of S4C-C can be attributed to micro cracking which might occur during process of the cyclic carbonation.

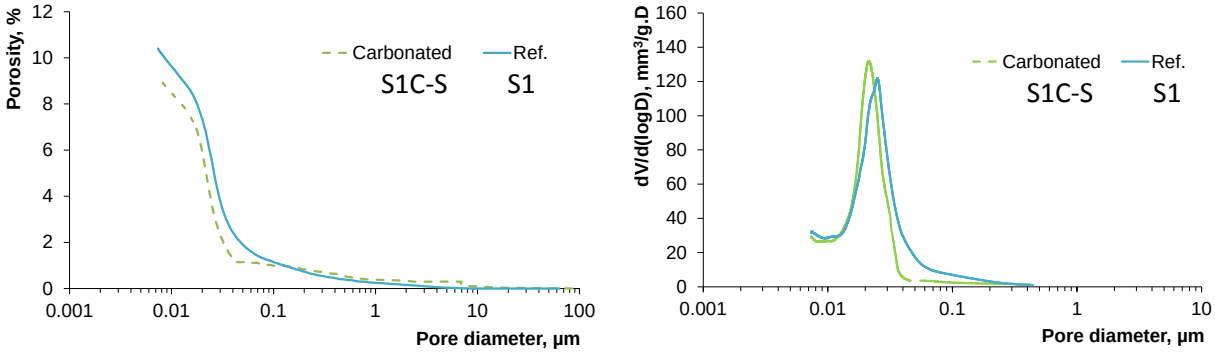

Figure 6.12. Changes in pore structure due to carbonation accessed by MIP: porosity vs. pore diameter (left) and differential pore size distribution (right) of continuously-carbonated and reference samples S1; carbonation under saturated condition

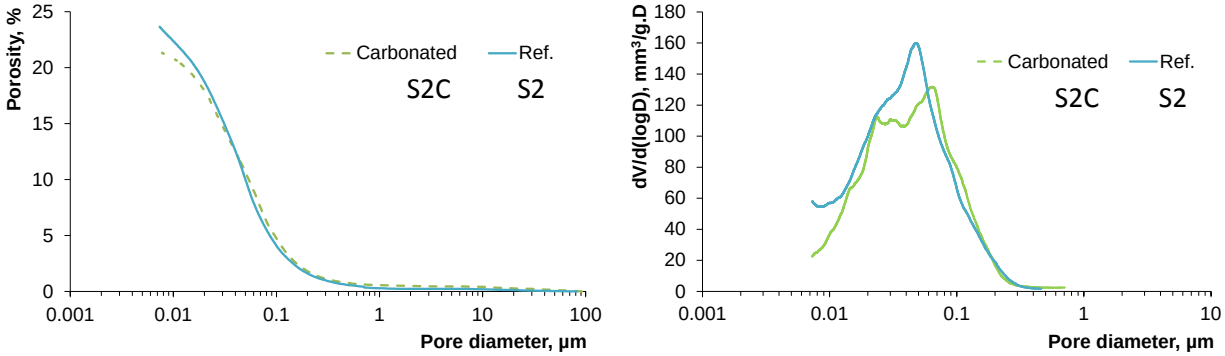

Figure 6.13. Changes in pore structure due to carbonation accessed by MIP: porosity vs. pore diameter (left) and differential pore size distribution (right) of continuously-carbonated and reference samples S2

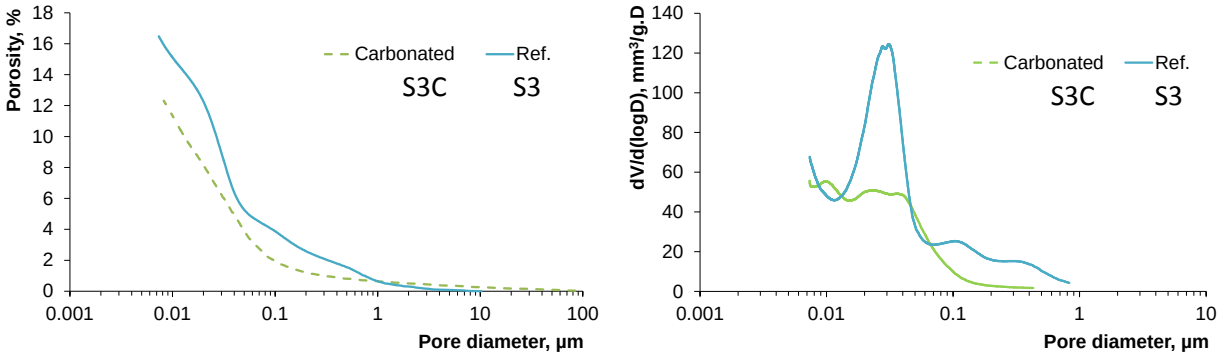

Figure 6.14. Changes in pore structure due to carbonation accessed by MIP: porosity vs. pore diameter (left) and differential pore size distribution (right) of continuously-carbonated and reference samples S3

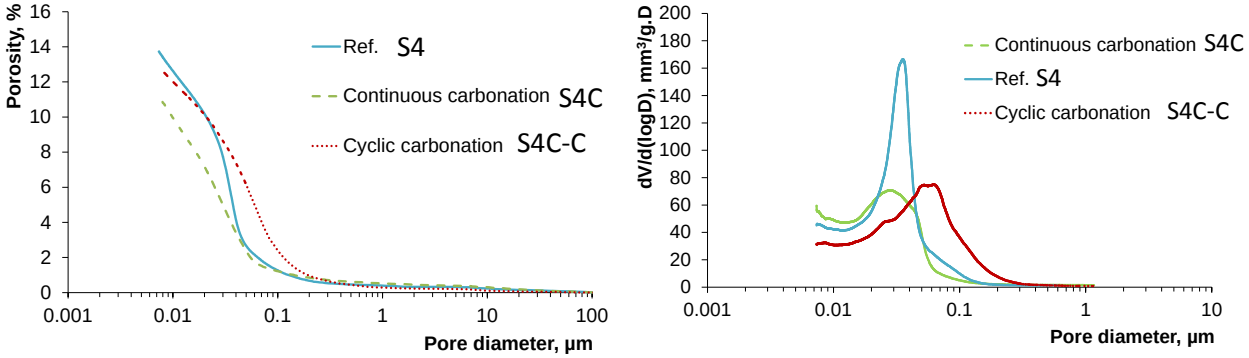

Figure 6.15. Changes in pore structure due to carbonation accessed by MIP: porosity vs. pore diameter (left) and differential pore size distribution (right) of continuously-carbonated, cyclic-carbonated and reference samples S4

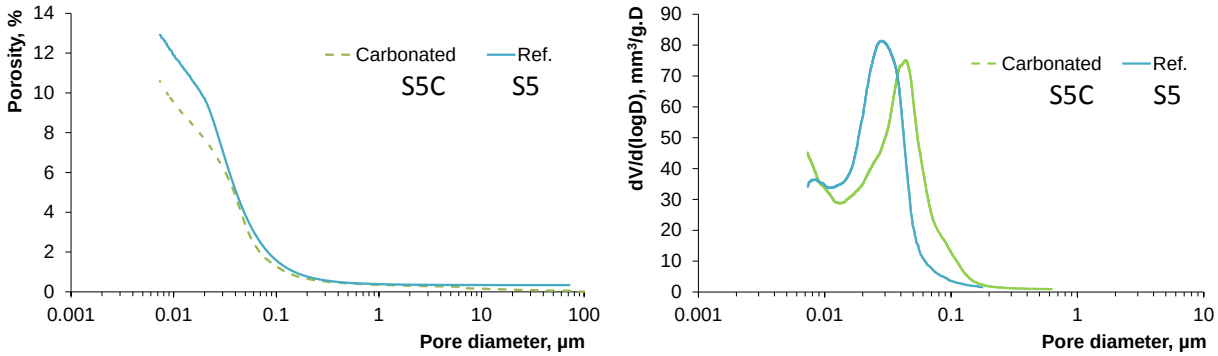

Figure 6.16. Changes in pore structure due to carbonation accessed by MIP: porosity vs. pore diameter (left) and differential pore size distribution (right) of continuously-carbonated and reference samples S5

6.4.2. Nitrogen gas adsorption results

N_2-adsorption provides complementary information on porosity/pore size compared to MIP for the smaller pore size range (micro to mesopores). The same trend in porosity decrease due to carbonation was observed as for the MIP results. Carbonation reduced the porosity in all carbonated samples under partially saturated condition, however, with a larger decrease when cyclic carbonation was applied (at mesopore sizes) as shown in Table 6.3. The average pore diameter determined by BJH method of sample S2C was slightly increased due to carbonation which is similar to MIP result. For the other continuously-carbonated samples, the average pore diameter gently decreased or remained almost unaltered (S4C). A small increase in the average pore diameter was observed for the sample subjected to cyclic carbonation S4C-C.

Table 6.3. Summary of N_2-adsorption results of carbonated and reference samples – "C" and "CC" denote continuous and cyclic carbonation, respectively; sample S1C-S was carbonated under saturated condition, the rest was at 65% RH.

Sample	S1	S1C-S	S2	S2C	S3	S3C	S4	S4C	S4C-C	S5	S5C
w/p	0.325	0.325	0.425	0.425	0.425	0.425	0.375	0.375	0.375	0.325	0.325
ls/p	0	0	0.2	0.2	0	0	0.1	0.1	0.1	0.2	0.2
BET surface area, m^2/g	9.9	18.2	33.3	21.3	30.6	38.0	34.8	23.2	13.5	6.2	7.5
Porosity (BJH), %	5.0	7.2	15.2	10.1	13.0	10.7	9.2	8.4	5.1	5.4	4.0
BJH adsorption average pore diameter (4V/A), nm	13.4	11.7	12.5	15.7	11.6	9.7	9.5	9.8	10.3	15.8	11.4

Table 6.4. Micropore information of carbonated and reference samples determined using Dubinin-Astakhov model [242] – "C" and "CC" denote continuous and cyclic carbonation, respectively; sample S1C-S was carbonated under saturated condition, the rest was at 65% RH.

Sample	S1	S1C-S	S2	S2C	S3	S3C	S4	S4C	S4C-C	S5	S5C
w/p	0.325	0.325	0.425	0.425	0.425	0.425	0.375	0.375	0.375	0.325	0.325
ls/p	0	0	0.2	0.2	0	0	0.1	0.1	0.1	0.2	0.2
µ-pore spec. surface, m^2/g	6.1	13.9	27.6	17.0	23.7	28.8	26.4	17.5	10.7	5.0	5.0
µ-pore volume, mm^3/g	4.0	6.8	13.5	8.0	11.6	14.1	12.8	8.5	5.3	2.6	2.4
Meso/micro volume ratio	6.5	5.6	6.5	7.4	6.9	4.3	3.9	5.3	5.1	10.5	8.3

The micropores (smaller than 2 nm) of sample S4C-C were also strongly affected by cyclic carbonation. Both micropore surface area and micropore volume were significantly decreased during cyclic carbonation, while effects were less for continuous carbonation (Table 6.4). As illustrated in Figure 6.4, part of the small pores can be emptied during the drying process of cyclic carbonation. Thus, CO_2 can access and react to alter the structure of small pores in terms of surface area and volume fraction.

The relations between specific surface area, average pore size and pore size distribution during carbonation deserve some attention. Most published studies report a decrease in specific surface area after carbonation [159-162]. The decrease is due to both a decrease in total porosity and a shift in the pore size distribution towards smaller pore sizes. The carbonated samples S2C, S4C and S4C-C indeed showed a decrease in specific surface area and a decrease in pore volume (Table 6.3). However, the average pore size distribution did not consistently shift towards smaller pore size range. The BJH adsorption average pore diameter (mesopores) was even increased for S2C and remained almost unchanged for S4C

and S4C-C. Therefore, the micropore reduction during carbonation could contribute to the changes in specific surface area instead of only the average mesopore size decrease. As evidences from micropore information, there was a decrease in both pore volume and specific surface area at nanometer scale of S2C, S4C and S4C-C; and the ratio between meso/micropore volumes shows a shift towards higher values after carbonation (Table 6.4).

On the other hand, it is quite surprising that the BET specific surface area for samples without limestone filler addition (S1C-S, S3C) increased after carbonation. One possible explanation is that the decrease in average pore size is faster than the reduction of total pore volume. This is, however, not supported by the measurements: the porosity of S3C decreased 22% and 18% by MIP and N_2-adsorption measurements, respectively, which was similar to the decrease in average pore diameter (27% (MIP) and 16% (N_2-adsorption)). For sample S1C-S, porosity even increased as seen from N_2-adsorption result, while the reduction in porosity and average pore size determined by MIP were quite similar (12% and 8%, respectively). Alternatively, the observation can be explained by the opening of C-S-H gel pores or small necks of ink-bottles pores (narrow entrances but wide bodies) as a consequence of C-S-H carbonation [243]. As indicated by the TGA results, C-S-H carbonation contributed up to 41.8% of calcite formation for sample S3C, which was 2.5 times larger than that of sample S4C. Both micropore volume and specific surface area of S1C-S and S3C were increased as seen in Table 6.4. This means that the opening of gel pores dominates the changes of micropore structure compared to the pore filling by calcium carbonate precipitation. As the C-S-H carbonation results in lower Ca/Si ratio, the structure of C-S-H becomes more porous and accessible by nitrogen (see Figure 6.17). Consequently, the specific surface area is expected to increase [244]. The specific surface area of C-S-H is much higher than that of bulk paste (low density C-S-H has a specific surface area of about 250 m^2/g [245]), but only part of this contributes to the average specific surface area of intact paste due to limitation in accessibility of nitrogen to small gel pores. The carbonated sample S5C also showed a slight increase in BET specific surface area which may be again attributed to C-S-H carbonation. It is not clear in many other studies if the reported specific surface area is for samples with or without C-S-H carbonation. If the latter, the difference in specific surface area of carbonated samples S1C-S, S3C and S5C with findings in literature could be attributed to C-S-H carbonation.

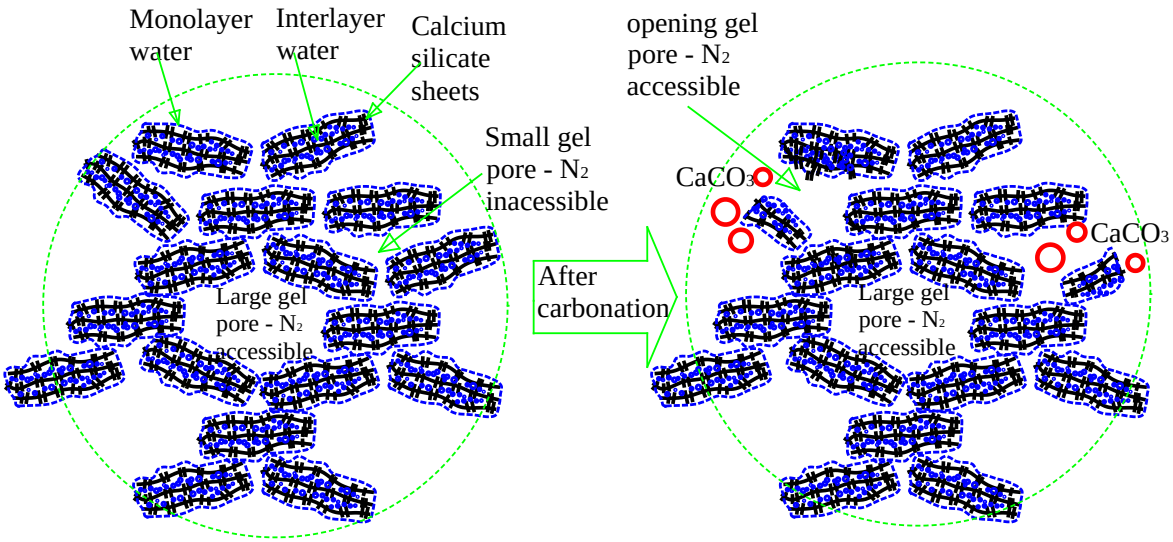

Figure 6.17. Schematic illustration of the opening gel pores of C-S-H due to carbonation – C-S-H colloid model adapted from [246]

The different alteration of the specific surface area of carbonated samples during carbonation is due to differences in composition and w/p (w/c) ratio. For samples with limestone fillers (S2C, S4C), the limestone fillers can act as nucleation sites for calcite precipitation from portlandite carbonation. This process then limits the amount of calcite available for forming protecting layers around portlandite particles as schematically shown in Figure 6.18. Therefore, portlandite carbonation is favoured compared to C-S-H carbonation for samples without limestone fillers. Sample S5C with 20% limestone filler replacement, however, showed a slight increase of BET specific surface area. Probably, a small amount of C-S-H was carbonated in this case. Generally, the samples with lower w/p ratio and with limestone filler replacement result in finer microstructures (compared to samples with the same w/c ratio). The limestone filler may act as a nucleation site for hydration reactions [247] given a denser pore structure with a higher hydration degree. Consequently, the accessibility of CO_2 to gel pores is limited; thereby, lower C-S-H carbonation.

Sample S1C-S which was carbonated under saturated conditions exhibited a large increase in BET specific surface area (50%). Under saturated conditions combined with a pressure gradient, the transport of CO_2 is mainly via advection of the aqueous phase. The water containing dissolved CO_2 contacts either with portlandite or C-S-H. Therefore, the C-S-H carbonation is favoured (more C-S-H fraction) which results in more specific surface area. As

evidenced, the micropore specific surface area of S1C-S was doubled after carbonation (Table 6.4). The mesopore volume was also increased due to carbonation.

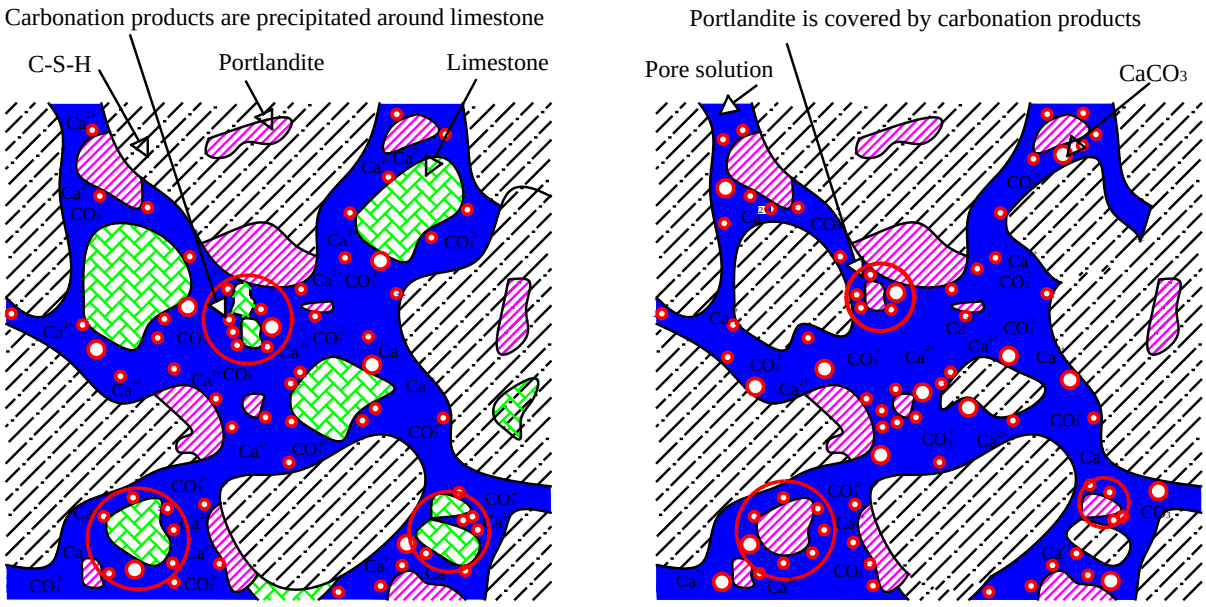

(a) Sample with limestone filler

(b) Sample without limestone filler

Figure 6.18. Effect of limestone fillers on the carbonation – limestone fillers play as nucleation sites for calcium carbonate precipitation.

Figure 6.19 and Figure 6.20 present the pore volume and pore size distribution of carbonated and reference samples determined by the BJH method. Samples S1C-S and S3C showed a steeper slope of cumulative pore volume at pore diameters smaller than 6 nm which indicates a larger porosity beyond this pore size due to C-S-H carbonation compared to reference samples. C-S-H carbonation which results in low density C-S-H might make the carbonated samples S1C-S and S3C more accessible to nitrogen. However, this larger porosity was not observed on the carbonated samples with limestone filler addition S2C, S4C and S4C-C. A significant porosity decrease was observed for sample S4C-C subjected to cyclic carbonation.

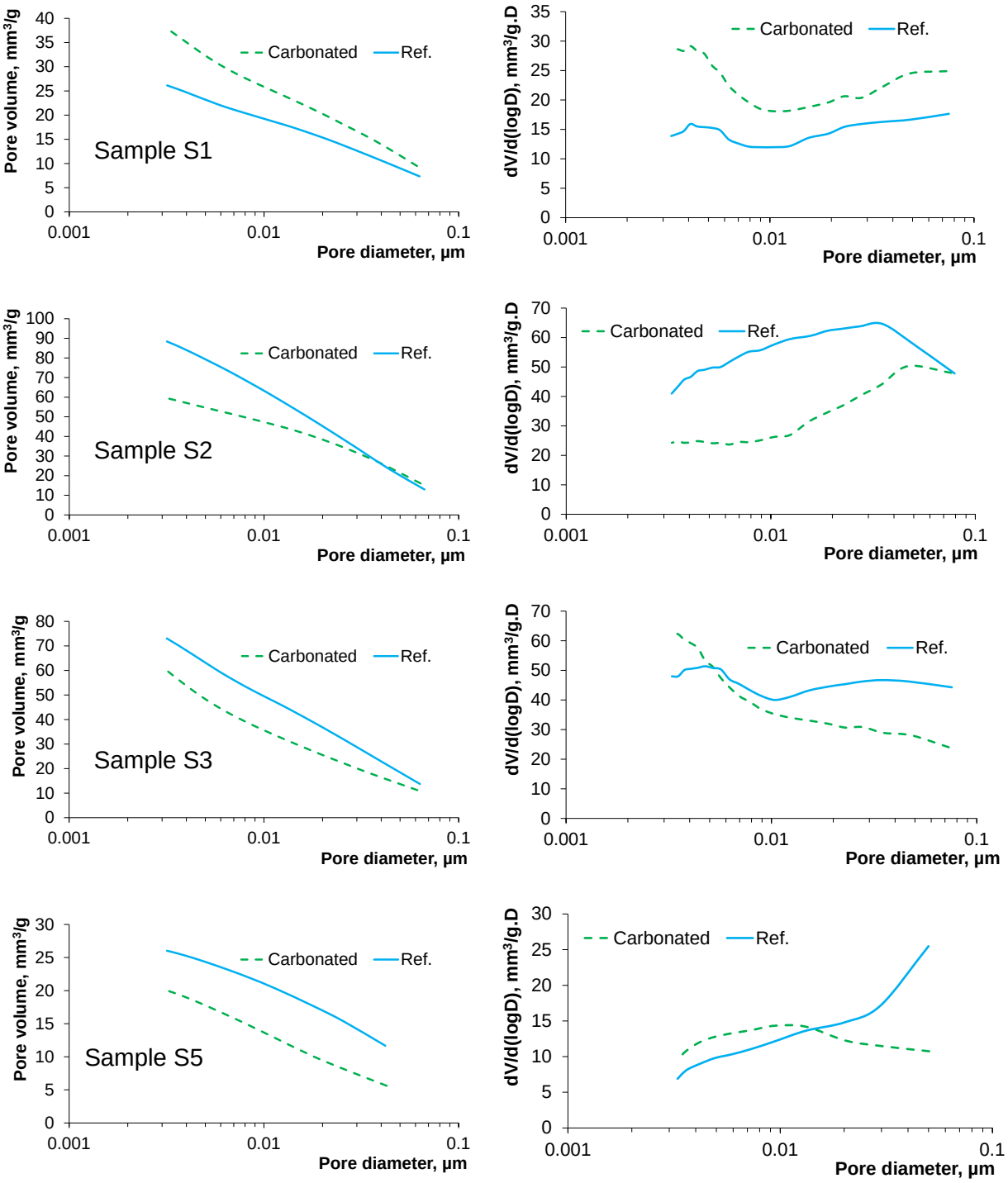

Figure 6.19. Changes in pore structure due to carbonation accessed by N_2-adsorption: intruded volume vs. pore diameter (left) and differential pore size distribution (right) continuously-carbonated and reference samples - sample S1 was carbonated under saturated condition; the rest was at 65%RH.

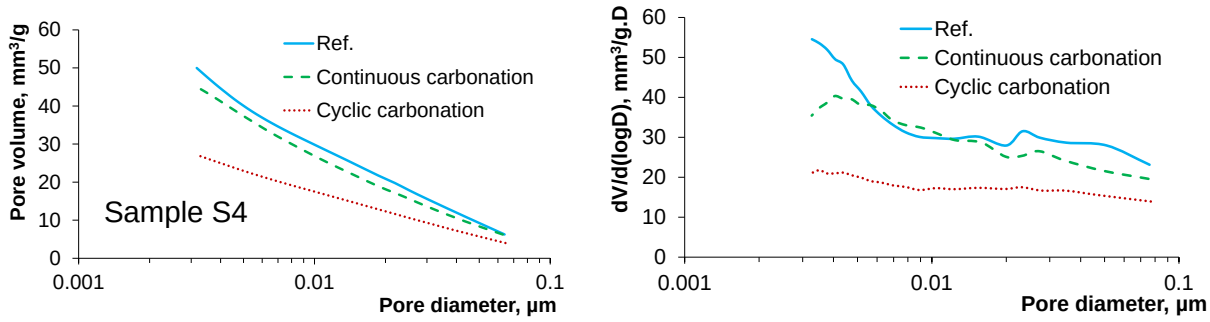

Figure 6.20. Changes in pore structure due to carbonation accessed by N_2-adsorption: intruded volume vs. pore diameter (left) and differential pore size distribution (right) of continuously-carbonated, cyclic-carbonated and reference samples S4

6.5. Microstructural alterations via SEM

The SEM images in Figure 6.21 to Figure 6.24 allow comparing the microstructure of the carbonated samples with the reference samples. Backscattered electron images were segmented to distinguish the distribution of portlandite, pores, C-S-H, calcium carbonate and residual cement clinkers based on a grey level histogram. C-S-H and calcium carbonate are difficult to distinguish because of their similarity in brightness intensity. Therefore, C-S-H and calcium carbonate were grouped together. Other minor phases (e.g. ettringite, thaumasite) were not counted in the phase segmentation. The area fraction (equal to volume fraction for isotropic materials) of each phase was calculated and presented on the right-hand sides of Figure 6.21 to Figure 6.24. Note that the porosity calculated from SEM images might be smaller than the real porosity due to limitation of SEM resolution (magnification of 1000 in these images). The average area fraction which was obtained by the quantification of a set of 8 ± 2 images on the same sample is summarised in Table 6.5. Results showed that carbonation led to a relative decrease in total porosity which was in line with the results obtained by MIP and N_2-adsorption. The pore size of carbonated materials was reduced, especially the amount of big pores (larger than 2 µm) was relatively decreased which was not observed from MIP results because of its limitations at that pore size range.

The portlandite content was significantly reduced in the carbonated samples. The portlandite carbonation by cyclic method was less than that by continuous method (sample S4). This observation indicates that the cyclic carbonation results in larger CO_2 uptake and deeper carbonation depth, but the carbonation of portlandite might be less pronounced compared to continuous carbonation. In this case, a larger amount of portlandite might be covered by carbonation products because of faster carbonation. The remaining portlandite was gathered

in smaller clusters compared to the reference samples. Furthermore, in carbonated samples S3C and S5C, more portlandite remained located near the pores (area A and B in Figure 6.22 and C in Figure 6.24), which supports the hypothesis of carbonation products forming around portlandite particles. Some big limestone filler clusters were found in samples with limestone filler, especially in samples with 20% limestone filler replacement of which the size of limestone filler clusters might be up to 10 µm diameter. The total C-S-H and calcium carbonate content increased after carbonation because calcium carbonate was formed and only a small amount of C-S-H was reacted with CO_2. There was no clear trend for the variation of unhydrated cement content.

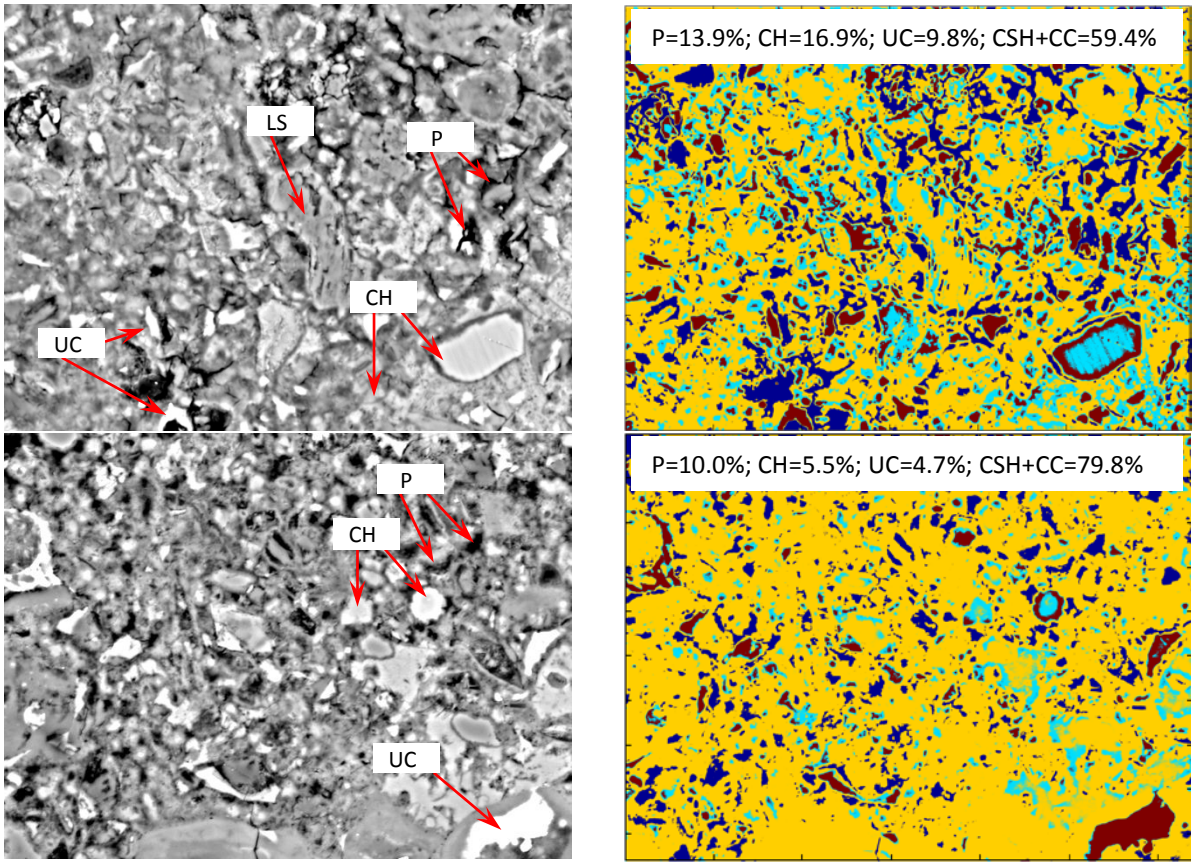

Figure 6.21. SEM images (left) and phase segmentation (right) of reference sample S2 (top) and carbonated sample S2C (bottom): P = pore (blue), CH = portlandite (cyan), UC = unhydrated cement (dark red), combined C-S-H and CC (yellow), LS = limestone filler, CC = calcium carbonate; field width of 128 µm

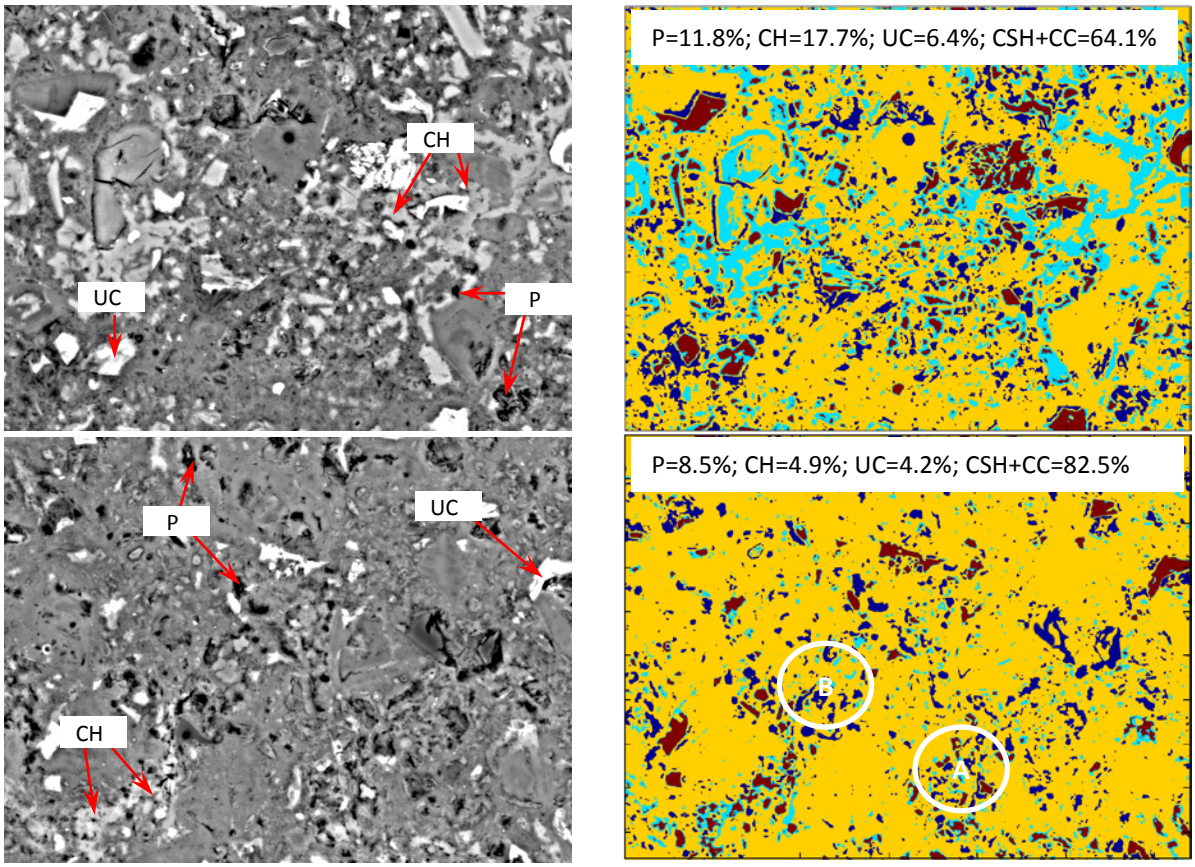

Figure 6.22. SEM images (left) and phase segmentation (right) of reference sample S3 (top) and carbonated sample S3C (bottom): P = pore (blue), CH = portlandite (cyan), UC = unhydrated cement (dark red), combined C-S-H and CC (yellow), CC = calcium carbonate; field width of 128 µm

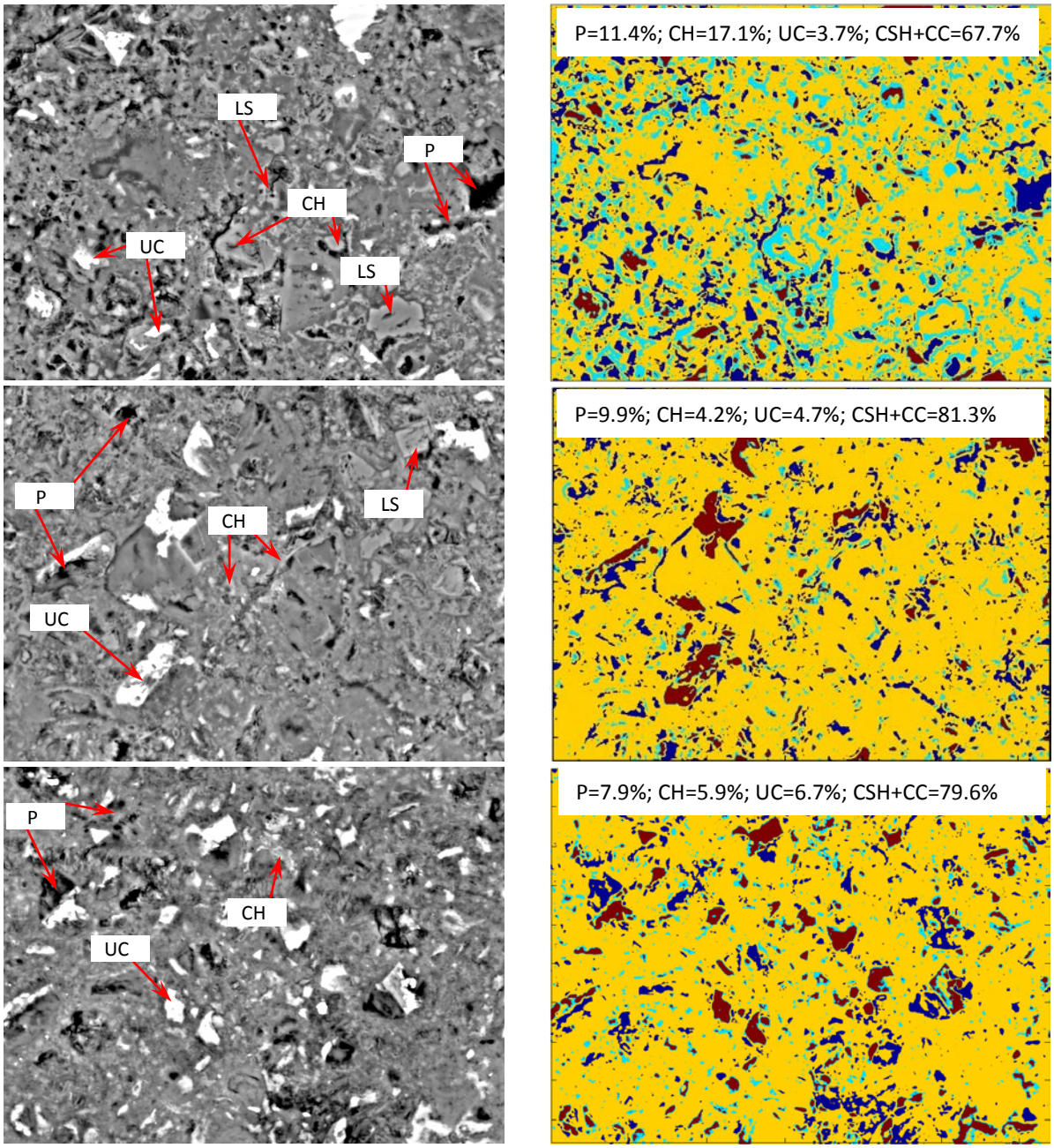

Figure 6.23. Comparison of the microstructure and phase fraction of reference sample S4 (top), continuously-carbonated sample S4C (middle) and cyclic-carbonated sample S4C-C (bottom): P = pore (blue), CH = portlandite (cyan), UC = unhydrated cement (dark red), combined C-S-H and CC (yellow), CC = calcium carbonate, LS = limestone filler; field width of 128 µm

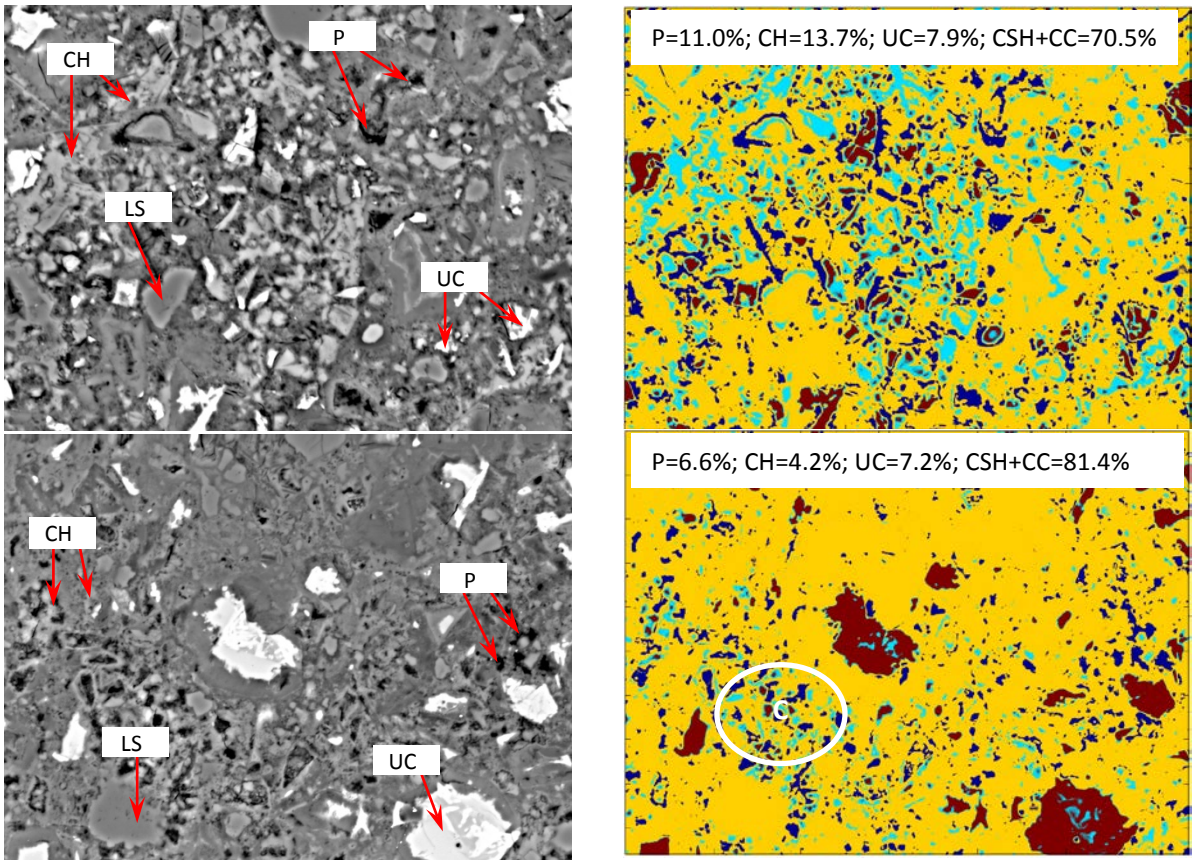

Figure 6.24. SEM images (left) and phase segmentation (right) of reference sample S5 (top) and carbonated sample S5C (bottom): P = pore (blue), CH = portlandite (cyan), UC = unhydrated cement (dark red), combined C-S-H and CC (yellow), CC = calcium carbonate, LS = limestone filler; field width of 128 µm

Table 6.5. Summary of the average area fraction of carbonated and reference samples

Sample	S2	S2C	S3	S3C	S4	S4C	S4C-C	S5	S5C
w/p	0.425	0.425	0.425	0.425	0.375	0.375	0.375	0.325	0.325
ls/p	0.2	0.2	0	0	0.1	0.1	0.1	0.2	0.2
Pore, %	15.3	10.2	11.5	8.7	10.6	8.8	6.9	11.3	7.6
	± 1.1	± 0.9	± 1.2	± 0.9	± 1.1	± 0.6	± 1.0	± 1.0	± 0.9
Portlandite, %	15.9	8.7	16.0	4.8	16.6	4.3	7.1	14.2	4.0
	± 1.6	± 2.6	± 1.2	± 1.1	± 1.2	± 1.5	± 1.0	± 1.4	± 1.2
Calcium carbonate + C-S-H, %	63.3	75.7	65.2	80.8	67.2	81.3	78.9	67.3	81.9
	± 1.9	± 2.7	± 2.1	± 1.4	± 2.4	± 2.8	± 1.6	± 3.2	± 1.6
Unhydrated cement, %	5.5	5.4	7.4	5.7	6.0	5.6	7.1	7.3	6.5
	± 2.0	± 2.0	± 1.5	± 1.1	± 1.6	± 1.8	± 1.4	± 2.2	± 1.4

6.6. Change in water permeability

Permeability was decreased by a factor of 6.4, 2.9 and 2.6 after 4 weeks of continuous carbonation under 65% RH for samples S3C, S4C and S5C, respectively (Table 6.6). It is important to mention that permeability should be interpreted as a composite permeability because the carbonation of the sample was not uniform with depth. The permeability decrease is directly linked to the porosity decrease in the carbonated zone. Furthermore, the pore connectivity is decreased because of calcite precipitation. In general, mass transport properties are mainly affected by capillary and large pores [185] which are changed by portlandite carbonation. However, the carbonation of C-S-H and other phases also contributes to permeability changes. On one hand, C-S-H carbonation results in calcite precipitation leading to a porosity decrease. On the other hand, the molar volume of carbonated C-S-H (lower Ca/Si) would be smaller than uncarbonated C-S-H which increases the porosity [130]. Therefore, in general, the porosity at nanometer scale might slightly decreased due to C-S-H carbonation as partly supported in Figure 6.19, Figure 6.20 and Table 6.4, thereby lowering the permeability.

The degree of porosity and average pore diameter reductions were larger for sample S3C compared to S4C, while sample S3C and S5C had a quite similar reduction as seen from both MIP and N_2-adsorption results. Furthermore, the C-S-H carbonation increased the surface area as shown by N_2-adsorption results, which reduced the permeability by increasing the friction between the fluid and pore wall. These could be the possible explanations for the higher permeability decrease in S3C compared to S4C, while the permeability decreases of S4C and S5C were similar to each other.

Table 6.6. Reduction in intrinsic permeability of cement pastes after 28-day carbonation – $k_{ref.}$ and k are the permeability of sound and carbonated samples, respectively.

Sample	S3	S3C	S4	S4C	S5	S5C
Permeability, m^2	2.3×10^{-20}	3.6×10^{-21}	1.4×10^{-20}	4.8×10^{-21}	2.0×10^{-20}	7.8×10^{-21}
$k_{ref.}$ /k ratio		6.4		2.9		2.6

In order to estimate the average intrinsic permeability of the carbonated zone, a series model (Figure 6.25) was applied in which permeability of carbonated zone and uncarbonated zone were assumed to be constant over the depth within the zone.

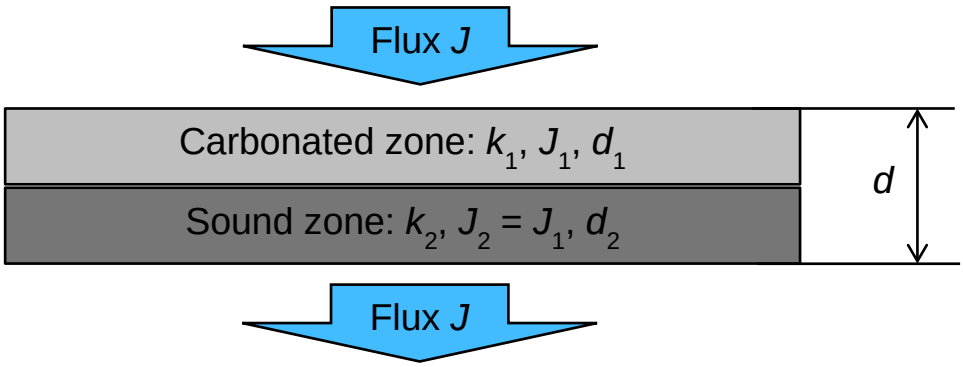

Figure 6.25. Series model to compute permeability of carbonated zone

The fluxes in each zone and the overall flux must be the same because each zone is connected together in series.

$$J_1 = J_2 = J = \frac{k_{car}}{\eta}\frac{\Delta p_{car}}{d_{car}} = \frac{k_{un}}{\eta}\frac{\Delta p_{un}}{d_{un}} = \frac{k}{\eta}\frac{\Delta p}{d} \tag{6.2}$$

where J_1, J_2 and J [kg/m^2.s] denote the fluxes of carbonated, sound zones and overall flux, respectively; Δp_{car} and Δp_{un} [Pa] denote the pressure difference of carbonated and sound zones, respectively; d_{car}, d_{un} and d [m] denote the thicknesses of carbonated, sound zones and thickness of sample, respectively; η [Pa.s] denotes the dynamic viscosity of the fluid; k_{car}, k_{un} and k [m^2] denote the permeability coefficients of carbonated, sound zones and the overall permeability coefficient of sample. Additionally, the sum of pressure drops on each zone must be equal to pressure difference, Δp, applied on the sample:

$$\Delta p_{car} + \Delta p_{un} = \Delta p \tag{6.3}$$

Therefore, the average permeability coefficient of the carbonated zone can be derived as:

$$k_{car} = \frac{dk_{un}k}{d(k_{un} - k) + d_{car}k_{un}} \tag{6.4}$$

The permeability of the sound zone was considered the same as the permeability of the corresponding reference sample (Table 6.6). The calculated permeability of carbonated zone is presented in Table 6.7. It can be seen that the permeability of the carbonated zone decreased up to factor of 51 for carbonated sample S3C which is a much larger reduction compared to the reduction of the overall permeability (6.4 times). Note that the results could be somewhat overestimated because the permeability of the considered sound zone is

probably lower than that of reference sample. The modelling study presented in Chapter 8 will give more details on this issue.

Table 6.7. Estimation of intrinsic permeability of carbonated zone using series model

Parameters	d_{car}, mm	d, mm	k, m^2	k_{un}, m^2	k_{car}, m^2	k_{un}/k_{car}
S3C	2.7	25	3.6×10^{-21}	2.3×10^{-20}	4.5×10^{-22}	51
S4C	2.5	25	4.8×10^{-21}	1.4×10^{-20}	6.9×10^{-22}	20
S5C	2.3	25	7.8×10^{-21}	2.0×10^{-20}	11.1×10^{-22}	18

6.7. Change in diffusivity

The diffusion experiments were performed on carbonated sample S3C. The porosity of the carbonated sample is not the same over the depth of sample. The average porosity of the carbonated sample was calculated by weighted average method as follows:

$$\phi_a = \frac{\phi_{car} d_{car} + \phi_{ref}(d - d_{car})}{d} \tag{6.5}$$

where ϕ_a , ϕ_{car} and ϕ_{ref} [-] denote the average porosity of the carbonated sample, the porosity of the carbonated zone and the porosities of the reference sample, respectively; d_{car} and d [m] denote the thicknesses of carbonated zone and the sample, respectively. Furthermore, the porosity might be decreased due to the continuous hydration of the sample during long time diffusion experiment. However, this effect was not counted in this calculation. The retardation factor R_e was set at one. Figure 6.26 shows the fitted and measured partial pressure profiles of He at the outlet for carbonated sample S3C. A good correlation was obtained (r^2 = 0.9919). The effective diffusion coefficient of S3C was 1.64×10^{-11} m^2/s, which is 30% lower than the effective diffusion coefficient of the reference sample. Thus the reduction in diffusion is much lower than the reduction in permeability due to carbonation.

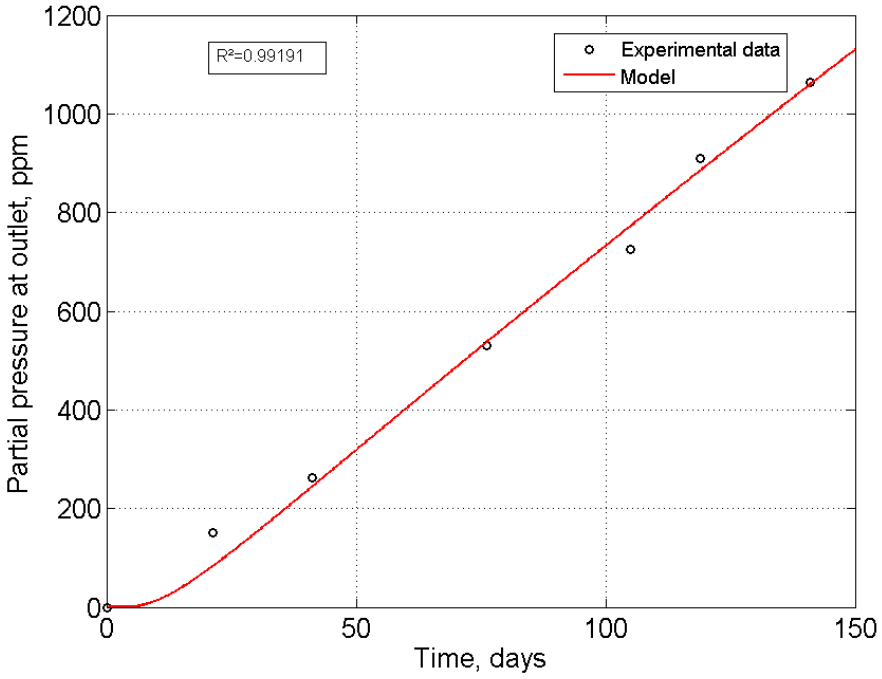

Figure 6.26. Comparison of the He partial pressure at the outlet obtained from experiment and model for carbonated sample S3C after 28 days of continuous carbonation

Like permeability, the effective diffusion coefficient of the carbonated sample should be treated as the composite (overall) effective diffusion coefficient. As for permeability, the series model can also be applied for the calculation of the effective diffusion coefficient of the carbonated zone with an assumption that the effective diffusion coefficient of sound zone equals to the one of the reference sample. Estimation of the effective diffusion coefficient of the carbonated zone resulted in a value of 4.72×10^{-12} m^2/s, which is 5 times lower than the effective diffusion coefficient of reference sample.

Table 6.8. Estimation of effective diffusivity of carbonated zone using series model

Parameters	d_{car}, mm	d, mm	D, m^2/s	D_{un}, m^2/s	D_{car}, m^2/s	D_{un}/D_{car}
S3C	2.7	25	1.64×10^{-11}	2.32×10^{-11}	4.72×10^{-12}	4.92

6.8. Summary and conclusions

In this chapter, a new carbonation method proposed in Section 4.4.1 was used to carbonate partially/fully saturated cement paste samples. The proposed method allows for an accurate quantification of CO_2 uptake, good control of initial conditions and examination of the effect

of carbonation on the permeability and diffusivity changes of carbonated cement-based materials. A variety of post-analysis techniques including XRD, MIP, N_2-adsorption, SEM and TGA were used to characterize the microstructural and mineralogical changes. Integrated post-analysis techniques enable to provide a complete picture of how microstructure and mineralogy change due to carbonation.

Two carbonation procedures were proposed: continuous and cyclic carbonation. The cyclic carbonation seems to be a relevant method to increase the carbonation degree compared to the continuous carbonation, but can potentially results in formation of micro-cracks during drying cycles. The CO_2 uptake during continuous carbonation was extremely fast in the first few hours of carbonation when CO_2 transport through the gaseous phase was still dominant. It was then followed by a strong drop in carbonation rate because the sample gradually saturates by the released water. Continuous or cyclic carbonation resulted in a different mechanism in terms of the transport of CO_2, the propagation of the carbonation front and the contribution of cementitious phases (CH, C-S-H) to the carbonation. The square-root-time law for carbonation was not applicable for the studied conditions due to the contribution of advective transport.

MIP, N_2-adsorption and SEM results confirmed a relative reduction in porosity of the carbonated materials. The pore size distribution of most continuously-carbonated samples was slightly shifted to smaller pore size range, while cyclic carbonation may slightly increase the critical pore diameter. Both continuous and cyclic carbonation resulted in a broadening of the pore size distributions compared to reference samples. Futhermore, SEM image analysis showed a reduction of big capillary pore size which was not seen from MIP results. TGA results showed that portlandite was still present in the carbonated zone detected by phenolphthalein spraying. More importantly, the portlandite content was gradually decreasing over the depth of sample, while calcite content was gradually increasing which indicates that the carbonation front is not sharp under the experimental conditions. Portlandite was the main phase which was carbonated but C-S-H can be carbonated as well under these accelerated conditions, especially in the sample without limestone filler. The carbonation of C-S-H highly increased the specific surface area due to the opening of the gel pores.

Limestone filler replacement showed some interesting results. For samples S3C and S4C (similar w/c ratio), the CO_2 uptake was doubled for sample with limestone fillers (S4C) despite lower initial water permeability. This was partially attributed to a lower rate in increase of the saturation degree resulting from a lower reaction rate and precipitation of

calcite on limestone particles which promotes CO_2 uptake. Note that under the studied conditions the transport rate might not be neglected compared to the reaction rate, at least in the initial carbonation stage. Limestone filler can partially play as nucleation sites for precipitation of calcium carbonates which promotes more portlandite carbonation. The micropore volume and specific surface area were decreased for carbonated samples with limestone fillers, but increased for carbonated samples without limestone fillers as a consequence of C-S-H carbonation.

The carbonation led to a significant decrease in water permeability resulting from the changes in microstructure and mineralogy. Carbonation also resulted in a decrease in diffusion of dissolved gas, but less pronounced. The permeability decrease could be mainly attributed to the portlandite carbonation and partially to the C-S-H carbonation. The changes in diffusion might be mainly affected by C-S-H carbonation which could explain for the less reduction in diffusion compared to permeability. A series model was also proposed to estimate the permeability and diffusivity of the carbonated zone. Estimations showed that the permeability and diffusivity of the carbonated zone were significantly decreased (factor of 51 and 5 for permeability and diffusivity) compared to the composite values.

CHAPTER 7: EFFECTS OF ACCELERATED CALCIUM LEACHING ON MICROSTRUCTURE AND TRANSPORT PROPERTIES OF CEMENT PASTES

7.1. Introduction

In this chapter, the changes in microstructure, mineralogy and transport properties of cement pastes subjected to accelerated leaching using the proposed method in Section 4.4.2 are presented. Leached samples were analysed by a series of methods (see Section 4.5) including SEM, MIP and N_2-adsorption to characterize the microstructural changes; phenolphthalein spraying, XRD, TGA, SEM-EDX, ion chromatography and water permeability, diffusivity measurements to study alterations in chemical compositions and transport properties. The leaching experiments were performed on hardened cement paste samples with different water/powder and limestone filler replacement ratios following the factorial experimental design, under fully saturated conditions.

7.2. pH evolution of surrounding solution

Figure 7.1 shows that the pH of surrounding solution evolves during the experiment. In few experimental days, the pH rapidly increased. It reached the stable values of about 9 after 7 days for all testing samples. The pH of surrounding solution is less than 9.25 to maintain leaching acceleration [199]. The value 9.25 is actually the equilibrium constant of the reaction $NH_4^+ \rightarrow NH_3(aq) + H^+$. If the pH is smaller than 9.25, the solution has more ammonium than ammonia to accelerate the leaching.

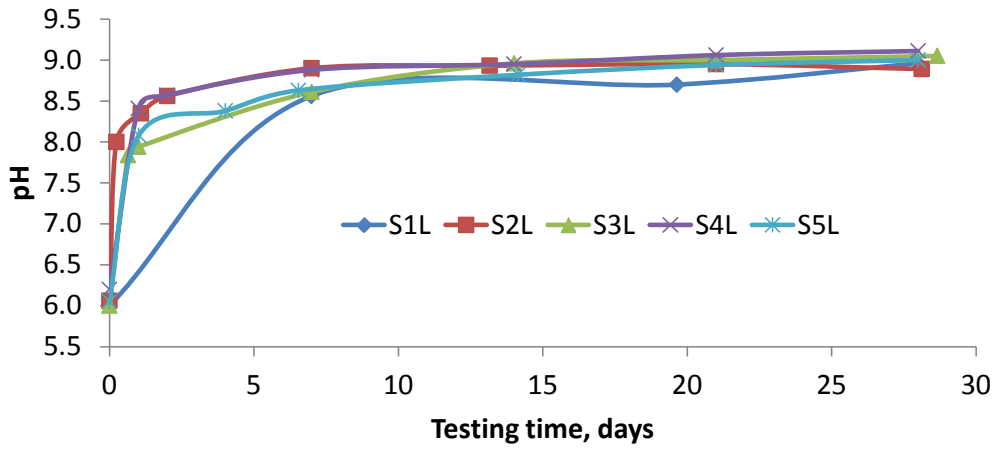

Figure 7.1. pH evolution of surrounding solution over testing time – sample S1 was only measured the pH from 7 testing days; "L" denotes leached sample.

7.3. Degraded depth

Figure 7.2 shows an example of a typical degradation front due to leaching as determined by phenolphthalein. The degraded zone (lowered pH) is grey, while in the intact zone the phenolphthalein colours pink due to the high pH. The degraded depth at the interface with the PVC cover is generally less developed and is considered as an artefact caused by the interface. The degraded depth was determined as the average of 5 locations excluding the interface area.

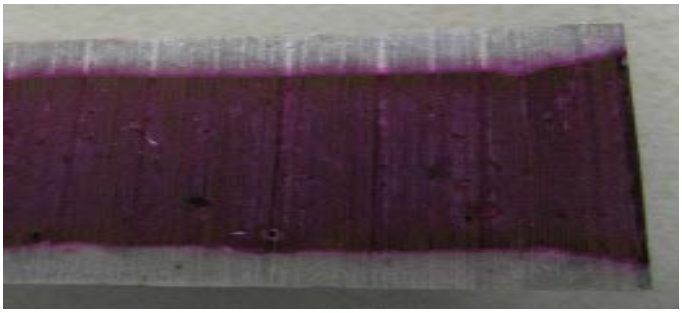

Figure 7.2. An example of the determination of leached depth by phenolphthalein spraying – sample S3L after 7 leaching days

The degraded depth linearly increased with the square root of immersion (reaction) time in NH_4NO_3 as shown in Figure 7.3. This is one of the indicators which illustrates that leaching in ammonium nitrate solution is a diffusion controlled phenomenon. The degradation rates were obtained from the slope of the linear relation between depth and sqrt(*t*) and used as response in the factorial study to investigate the effects of limestone filler replacement and w/p ratio. The degradation rates (in unit $mm/day^{0.5}$) are represented by the cube plot and the interpolated surface plot (using Akima's polynomial method [222]) in Figure 7.4. In the surface plot shows that to improve the resistance to leaching, one should choose a mix design with a low w/p ratio and low limestone filler replacement. The effects of w/p ratio and limestone filler replacement on the propagation of degradation front can be visualized in Figure 7.5a. It is clear that the degradation rate strongly increases with the increase of w/p ratio. The rate was increased by 70% when w/p ratio increased from 0.325 to 0.425. Adding limestone filler also induced a faster degradation rate. However, the effects of limestone filler replacement was much lower than the effects of w/p ratio. The regression equation (first-order) of degradation rate is obtained as follows:

$$Rate_{dep} = -1.397 - 0.538\ ls/p + 7.3\ w/p - 3.5\ ls/p \times w/p \quad (7.1)$$

where $Rate_{dep}$ [mm/day$^{0.5}$] is the degradation rate; ls/p is the ratio of limestone filler over powder (cement + limestone filler); and w/p is the ratio of water over powder. The correlation coefficient (r^2) is 0.999 indicating that the predicted model fits the experimental data well.

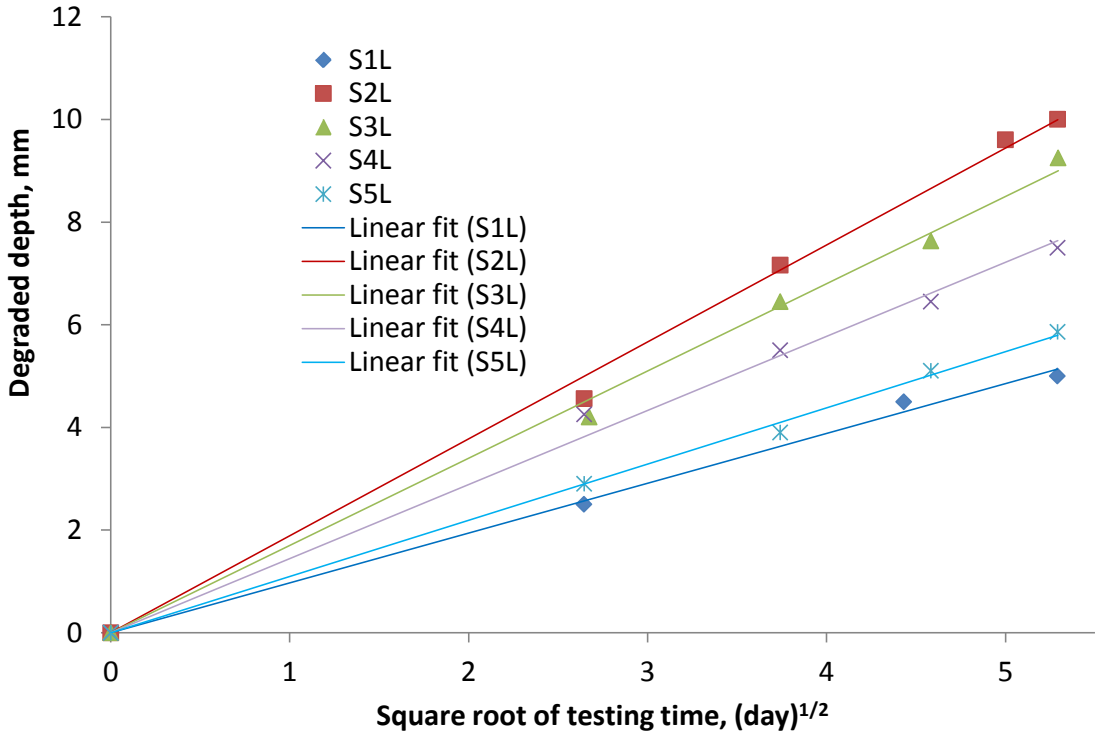

Figure 7.3. Increase of phenolphthalein degraded depth over immersed time

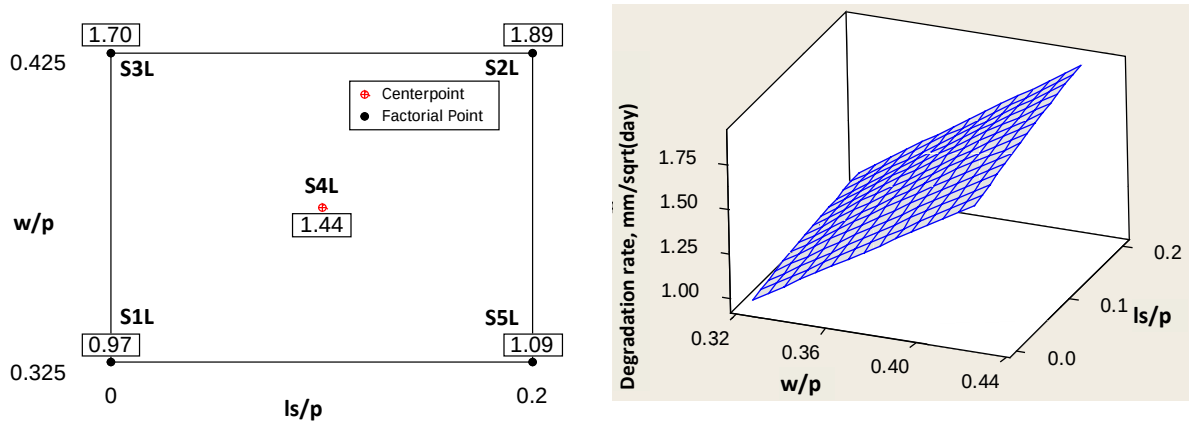

Figure 7.4. Cube plot and interpolated surface plot of degradation rate (mm/day$^{0.5}$) vs. w/p ratio and limestone filler replacement

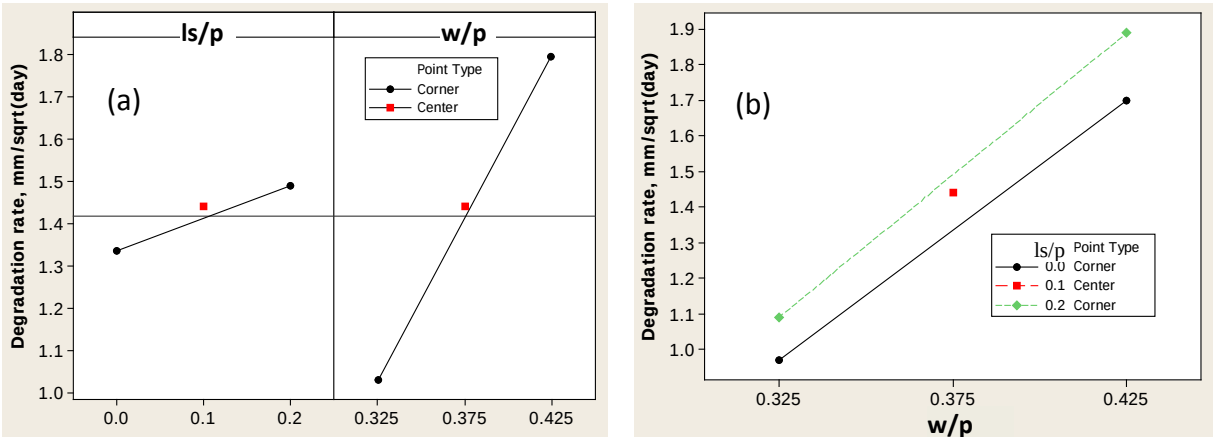

Figure 7.5. Main effects plot (a) and interaction plot (b) for degradation rate

The interaction plot (Figure 7.5b) enables to visualize the interaction effects of w/p ratio and limestone filler replacement on the degradation rate. As the connected lines of factor levels are almost parallel to each other, there might not be interaction present (or minor contribution).

7.4. Amount of leached Ca and mass change

7.4.1. Ca-leached rate

Figure 7.6 presents the amount of calcium in the surrounding solution (determined by ion chromatography) which is linearly related to the amount of calcium leached out from the cement pastes (initial concentration ~ 0) with square root of time. Because the limestone filler is not leached (extremely small solubility), the calculated values shown in Figure 7.6 have been normalized to the cement content of the samples before leaching. Again, a linear relation of leached amount over square root of time was observed similar to the propagation of the degraded depth.

The Ca-leached rates (obtained from the slope of linear fitting line) were used as response in the factorial study to investigate the effects of limestone filler replacement and w/p ratio. The Ca-leached rates (in unit %/day$^{0.5}$) are represented by cube and interpolated surface plots in Figure 7.7. The effects of w/p ratio and limestone filler replacement on the Ca-leached rate can be visualized in Figure 7.8a. It is shown that the Ca-leached rate reaches the highest rate at w/p ratio of 0.375 and 20% limestone filler replacement. The effect of limestone filler replacement was lower than the effect of w/p ratio in the investigated range. The Ca-leached rate was increased by 50% when w/p ratio increased from 0.325 to 0.425, while less than 10%

when ls/p ratio increased from 0 to 0.2. The regression equation (first-order) of Ca-leached rate is obtained as follows:

$$Rate_{Ca} = -0.715 + 0.168\ ls/p + 6.1\ w/p + 1.1\ ls/p \times w/p \quad (7.2)$$

where $Rate_{Ca}$ [%/day$^{0.5}$] is the Ca-leached rate; ls/p is the ratio of limestone filler over powder (cement + limestone filler); and w/p is the ratio of water over powder. The correlation coefficient (r^2) is 0.998 indicating that the predicted model fits the experimental data well.

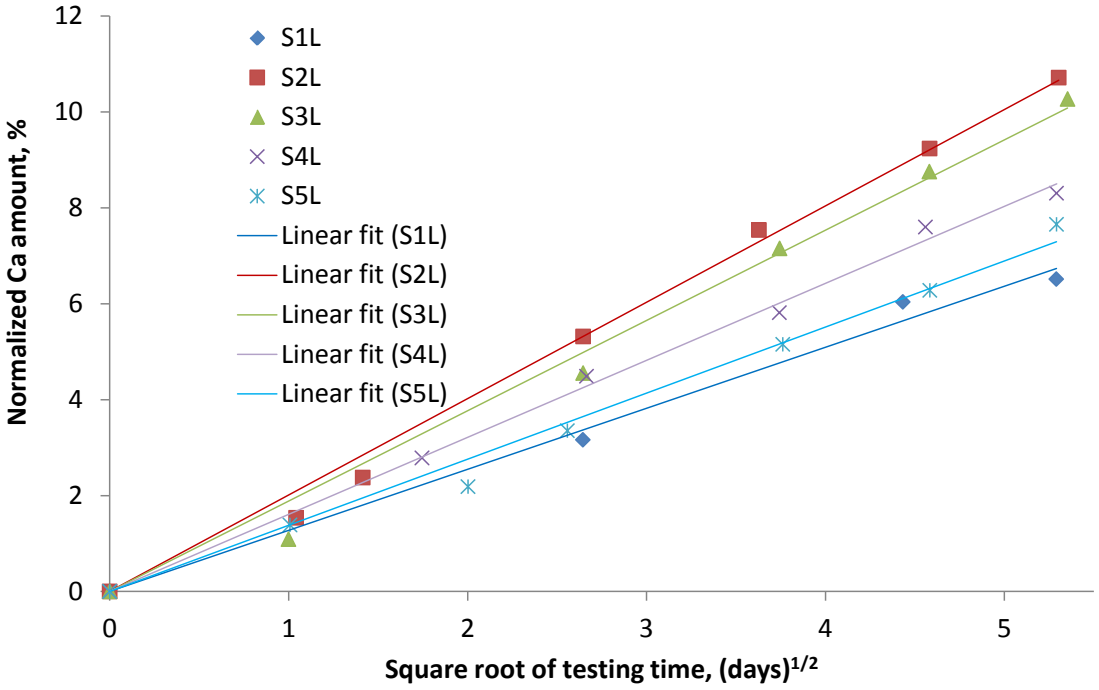

Figure 7.6. Increase of normalized Ca-leached amount to cement over immersed time

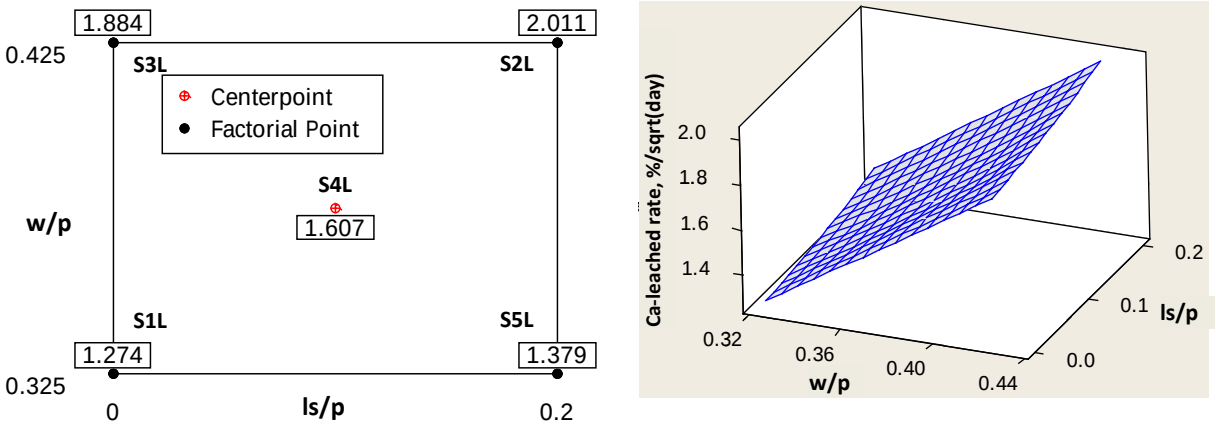

Figure 7.7. Cube plot and interpolated surface plot of Ca-leached rate (%/day$^{0.5}$) vs. w/p ratio and limestone filler replacement

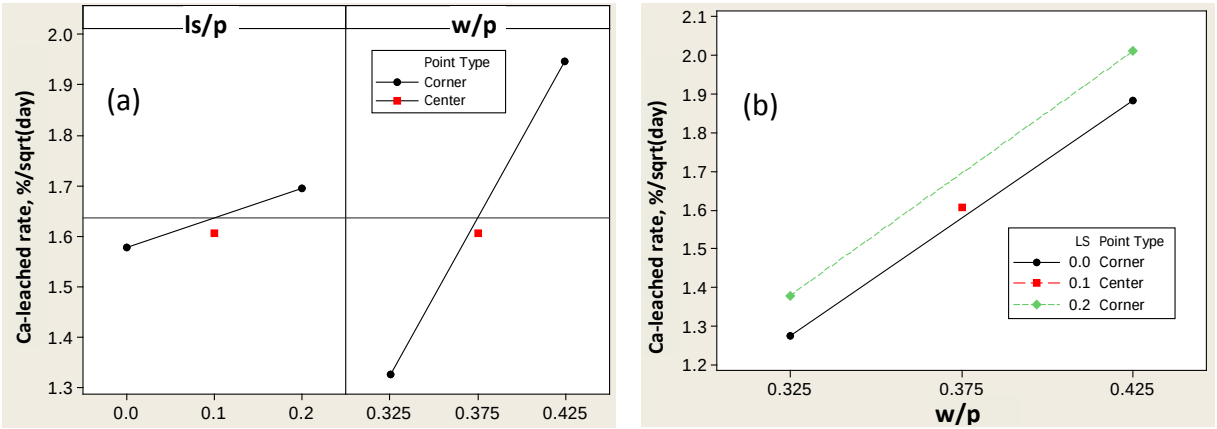

Figure 7.8. Main effects plot (a) and interaction plot (b) for Ca-leached rate

The interaction plot (Figure 7.8b) enables to visualize the interaction effect of w/p ratio and limestone filler replacement on the Ca-leached rate. As the connected lines of factor levels are parallel to each other, there is no interaction present.

7.4.2. Mass change due to leaching

This section aims at investigating the loss of sample mass and giving a proof of C-S-H contribution to the mass loss due to leaching. In case of no C-S-H leaching, it is possible to calculate the decrease of sample weight from ion chromatography results by making assumption that the mass loss due to the leaching of other ions (K^+, Na^+, Mg^{++}) is negligible. This assumption was confirmed by IC results of sample S1L in which the concentrations of other ions were much smaller than the Ca ion concentration. The amount of portlandite leached out was calculated from the Ca ion concentration in the surrounding solution as follows:

$$CH = [Ca]V_a \frac{M_{CH}}{M_{Ca}} \tag{7.3}$$

where CH is portlandite content, [g]; $[Ca]$ is Ca ion concentration determined by IC, [g/l]; V_a is volume of NH_4NO_3 solution, [l]; M_{CH} is molar mass of $Ca(OH)_2$, 74 [g/mol]; and M_{Ca} is molar mass of Ca, 40 [g/mol]. The change in porosity due to portlandite dissolution is simply expressed as:

$$\Delta\phi = \frac{CH / M_{CH} \; V_{CH}}{V_s} 100\% \tag{7.4}$$

where V_{CH} is molar volume of $Ca(OH)_2$, 0.033 [l/mol] and V_s is sample volume, [l]. It is assumed that leaching of portlandite will create capillary pores which are completely filled by water during leaching. Therefore, the decrease of sample mass can be derived as follows:

$$\Delta m = \frac{CH - CH/M_{CH} \, V_{CH} \rho_w}{M_s} 100\% \tag{7.5}$$

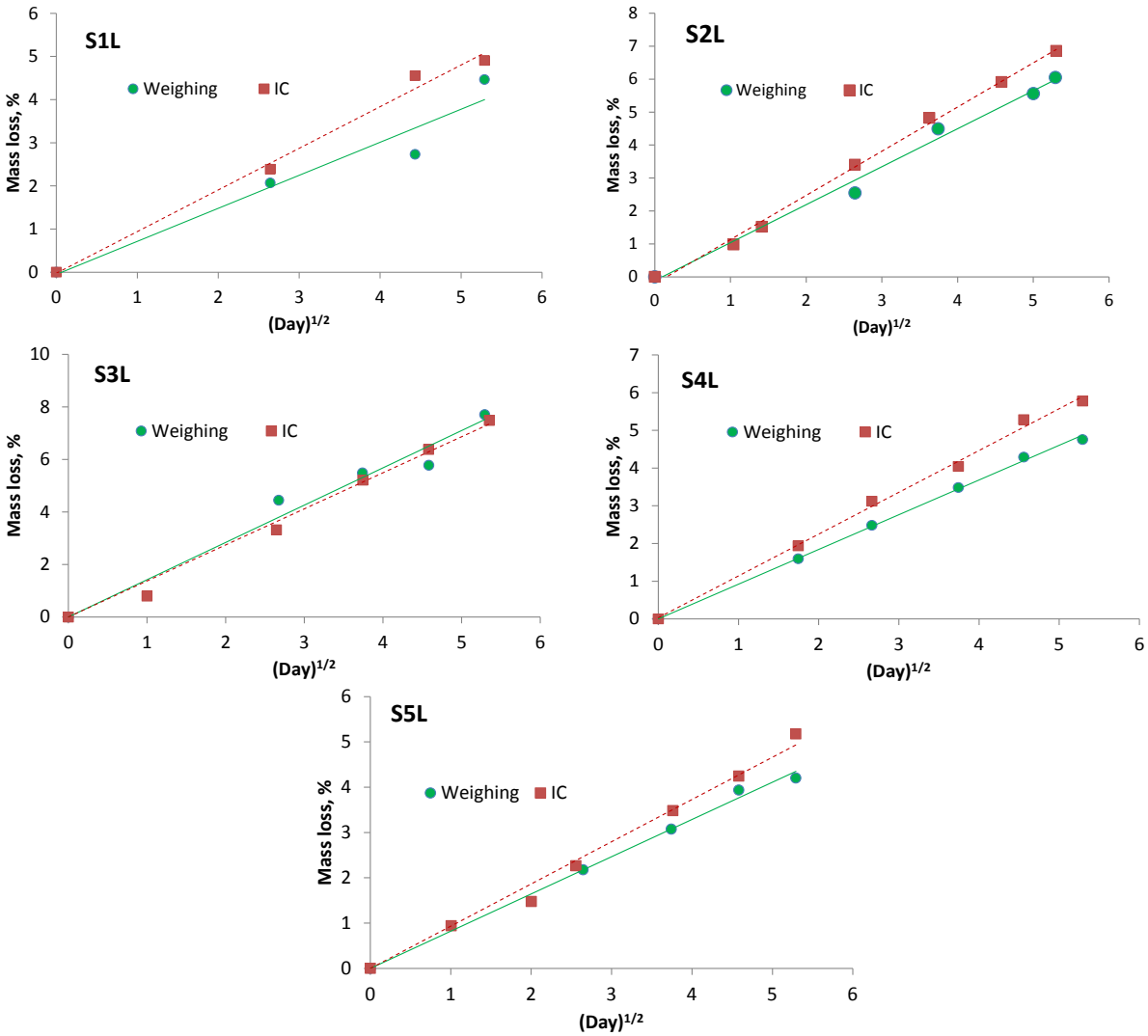

Figure 7.9. Comparisons of mass loss of leached samples during leaching determined by weighing method and ion chromatography method with assumption of no C-S-H decalcification

where Δm is percentage of mass loss, [%], M_s is sample mass, [g] and ρ_w is density of water, 1000 [g/l]. Figure 7.9 shows a comparison of the mass loss during leaching based on directly measuring the weight change of sample and the ion chromatography method (with assumption

of no C-S-H leaching). The mass of samples linearly decreased over the square root of immersed time. It can be seen that in most cases, the mass loss obtained from direct measurements of sample mass is smaller than IC method. The difference is attributed C-S-H leaching. The leaching of C-S-H creates extra pores including gel pores and small capillary pores. The gel pores are hardly accessible by water under normal condition, while the small capillary pores may still be filled by water during the experiment. Therefore, the mass loss due to calcium leached out is partially compensated by mass gain due to water filling.

7.5. Changes in porosity and pore size distribution

7.5.1. Nitrogen gas adsorption results

Figure 7.10 shows a comparison of nitrogen adsorption isotherms of leached and reference samples. The shape and size of the desorption hysteresis loop of the leached sample is characteristic for large ink-bottle shaped pores whereas the hysteresis loop of the reference sample is more characteristic for a slit-shaped or plate-like pore system [248]. Such a plate-like pore system corresponds to C-S-H gel which consists of very thin sheets [208]. The alteration towards ink-bottle shaped pores might indicate that part of the C-S-H has been dissolved during leaching. The surface areas determined by the BET method of the leached samples significantly increased (Table 7.1). The specific surface area of samples with high w/p ratios (S2L, S3L, S4L) increased 4-5 times after 28-day leaching in ammonium nitrate solution. For samples with lower w/p ratio (S1L, S5L), the specific surface area increased even more strongly - more than 7 times for S1L and 15 times for S5L. Such a large increase is not only attributed to the dissolution of portlandite but also the dissolution of C-S-H. The gel pores of C-S-H which have higher specific surface area compared to micro/mesopores made by the aggregation of the other cement components are more easily accessible by nitrogen after leaching.

Leaching seriously increased the porosity in mesopore region in all leached samples as shown in Table 7.1. The largest increase in porosity was for sample S5L of which the porosity increased almost 4 times. The samples with 20% limestone filler replacement (S2L, S4L) had similar porosity after leaching despite different initial porosities. Interestingly, the average pore diameter determined by BJH method of all leached samples relatively decreased after leaching. However, this observation should not be interpreted as the refinement of the pore structure of the leached materials. The reduction of the average pore diameter in the BET measurement range is because a considerable volume fraction of small pores, initially inaccessible, is opened up after leaching. The volume fraction of larger pores was indeed

increased but with smaller magnitude which will be shown in MIP results. Sample S1L and S5L (low w/p ratio) exhibited the largest decrease in average pore diameter, which could be the reason for obtaining the highest specific surface area increase due to leaching.

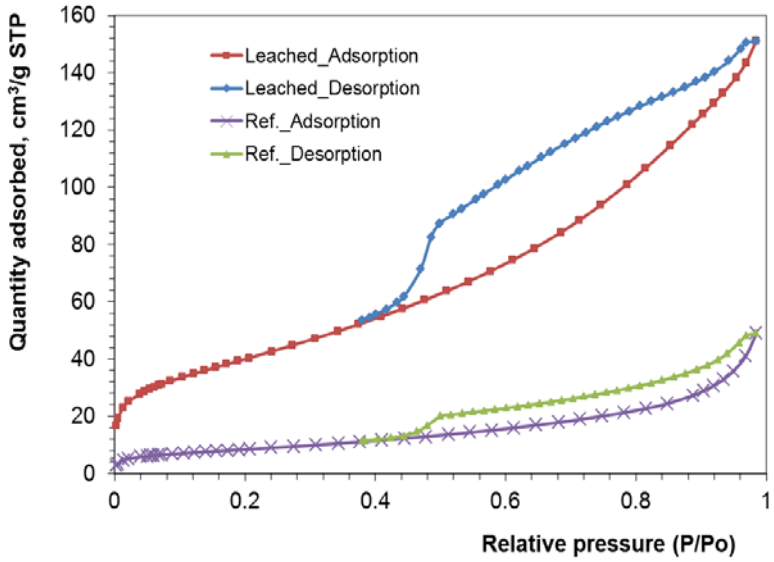

Figure 7.10. Adsorption isotherms of reference and 28-day leached sample S3L

Table 7.1. Summary of N_2-adsorption results of leached and reference samples – "L" denotes leached sample

Sample	S1	S1L	S2	S2L	S3	S3L	S4	S4L	S5	S5L
w/p	0.325	0.325	0.425	0.425	0.425	0.425	0.375	0.375	0.325	0.325
ls/p	0	0	0.2	0.2	0	0	0.1	0.1	0.2	0.2
BET surface area, m^2/g	9.9	73.1	33.3	130.9	30.6	145.8	34.8	182.3	5.5	86.7
Porosity (BJH), %	5.0	16.2	15.2	21.9	13.0	23.8	9.2	26.1	5.4	21.2
BJH adsorption average pore diameter (4V/A), nm	13.4	8.7	12.5	8.6	11.6	7.8	9.5	7.3	15.8	6.8

Table 7.2 presents the change in micropore structure of the leached materials. The micropores of all leached samples were strongly affected by leaching in ammonium nitrate solution, among them the highest alteration was again from the samples S1L and S5L. Both micropore surface area and micropore volume were significantly increased during accelerated leaching. The meso/micro volume ratio was reduced after leaching which can serve as an evidence for C-S-H decalcification which resulted in higher accessibility of gel pores.

Table 7.2. Micropore information of leached and reference samples determined using Dubinin-Astakhov model [242] – "L" denotes leached sample

Sample	S1	S1L	S2	S2L	S3	S3L	S4	S4L	S5	S5L
w/p	0.325	0.325	0.425	0.425	0.425	0.425	0.375	0.375	0.325	0.325
ls/p	0	0	0.2	0.2	0	0	0.1	0.1	0.2	0.2
Micropore spec. surface, m^2/g	8.1	58.6	27.6	95.7	23.7	131.6	26.4	165.4	4.2	67.9
Micropore volume, mm^3/g	4.0	27.9	13.5	47.5	11.6	65.0	12.8	82.2	2.1	32.5
Meso/micro volume ratio	6.5	4.2	6.5	4.2	6.9	3.3	3.9	2.8	12.1	4.6

Figure 7.11 to Figure 7.15 present the pore volume and pore size distribution of leached and reference samples determined by BJH method. Most leached samples exhibited a larger porosity compared to reference samples from the largest pore size which enables to be detected by N_2-adsorption method. Despite the difference in w/p ratios in composition (with/without limestone fillers) all leached samples showed a steeper slope of pore volume at pore diameters smaller than 20 nm which indicates a sudden increase in porosity beyond this pore size due to C-S-H leaching. The most frequently occurring pore size was in range of 4-5 nm which is fallen in the upper size of pores in the C-S-H structure.

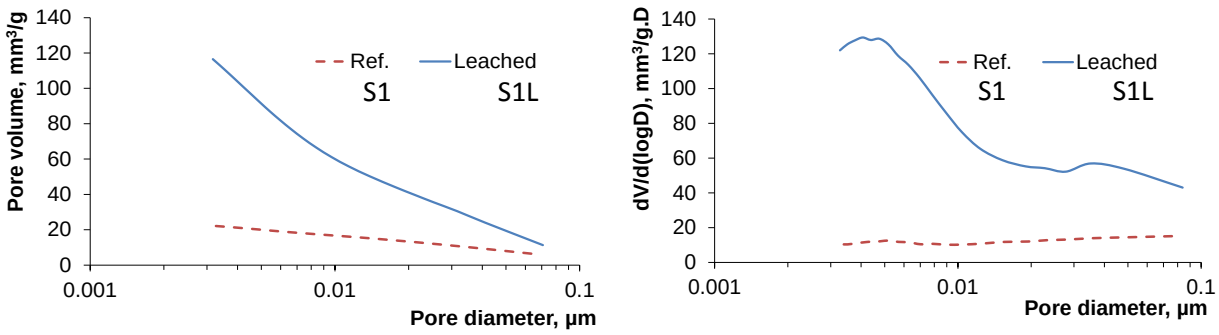

Figure 7.11. Changes in pore structure due to leaching accessed by N_2-adsorption: adsorbed volume vs. pore diameter (left) and differential pore size distribution (right) of leached and reference samples S1

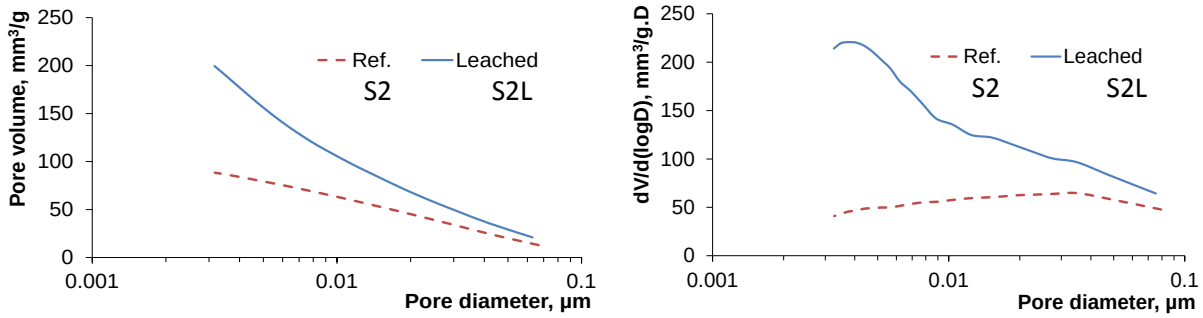

Figure 7.12. Changes in pore structure due to leaching accessed by N_2-adsorption: adsorbed volume vs. pore diameter (left) and differential pore size distribution (right) of leached and reference samples S2

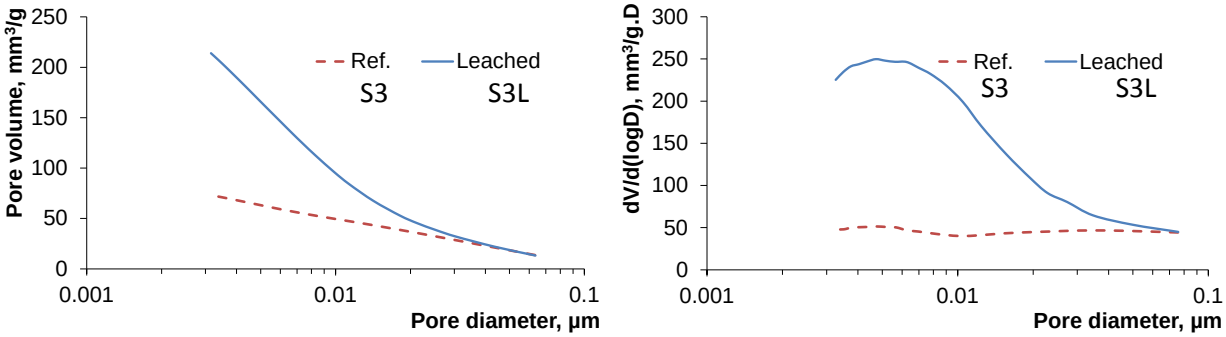

Figure 7.13. Changes in pore structure due to leaching accessed by N_2-adsorption: adsorbed volume vs. pore diameter (left) and differential pore size distribution (right) of leached and reference samples S3

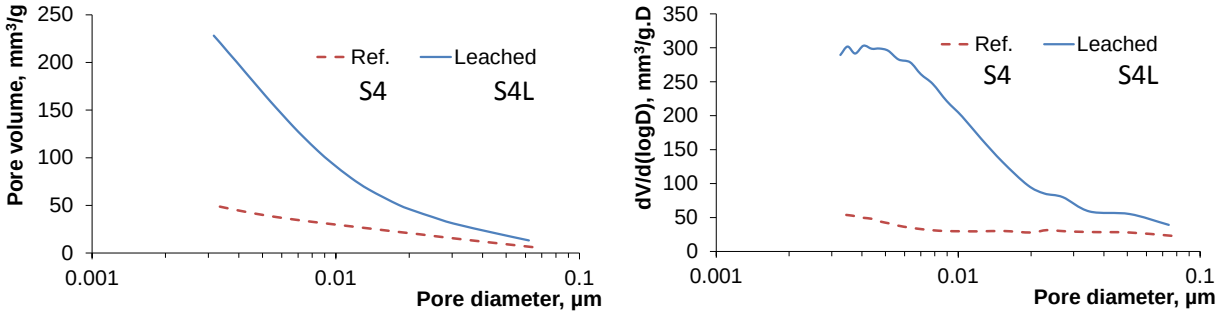

Figure 7.14. Changes in pore structure due to leaching accessed by N_2-adsorption: adsorbed volume vs. pore diameter (left) and differential pore size distribution (right) of leached and reference samples S4

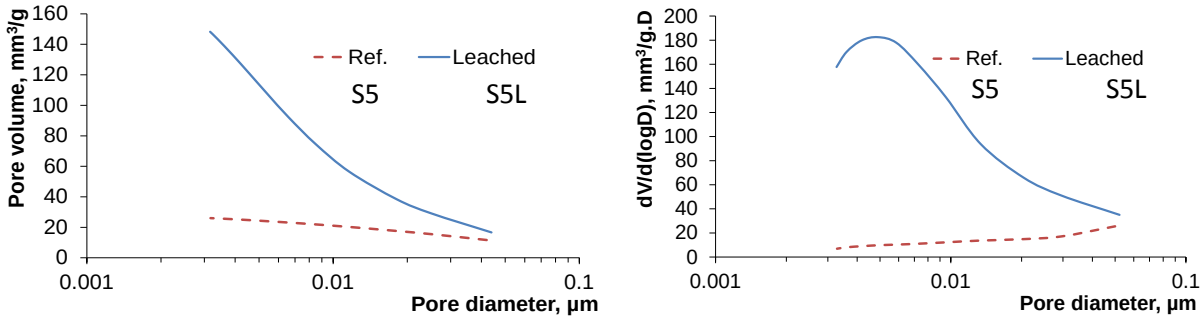

Figure 7.15. Changes in pore structure due to leaching accessed by N_2-adsorption: adsorbed volume vs. pore diameter (left) and differential pore size distribution (right) of leached and reference samples S5

7.5.2. Combined MIP and N_2-adsorption results

Due to significant loss of mechanical properties, more attention is needed during measurements and interpretation of MIP results. The complete dissolution of portlandite and partial decalcification of C-S-H can induce a strong loss of elasticity. As a result, the ductility of the leached material will be higher. The deformation at failure of leached samples can increase with a factor of 5 in tension and 2 in uniaxial compression [249]. Obviously, during the mercury intrusion process, the sample is under isotropic compression. Therefore, the deformation must be higher than that reported in [249]. In this study, the leached samples were checked after finishing the MIP tests to make sure that the samples were not broken during the test. No broken sample was observed. Therefore, it is needed to take into account the compression effect in the interpretation.

The porosimeter interprets sample compression as the occurrence of pores. Thus, in order to account for the deformation of the sample, the measurement needs to be corrected by subtracting the volume of sample compression as follows [250]:

$$v_c = v_i - \left(\frac{1}{\rho_b} - \frac{1}{\rho_a} \right) \tag{7.6}$$

where v_c is specific compression volume [m^3/kg]; v_i is specific intruded volume [m^3/kg]; ρ_b is bulk density [kg/m^3]; and ρ_a is apparent density which is defined as unit weight of sample at the end of the filling process [kg/m^3]:

$$\rho_a = \frac{m_s}{V_b - V_i^{cor}} \tag{7.7}$$

where m_s is sample mass [kg]; V_b is sample volume (including pores) [m^3]; V_i^{cor} is corrected intruded volume [m^3] and can be calculated as follows:

$$V_i^{cor} = (v_i - v_c) m_s \tag{7.8}$$

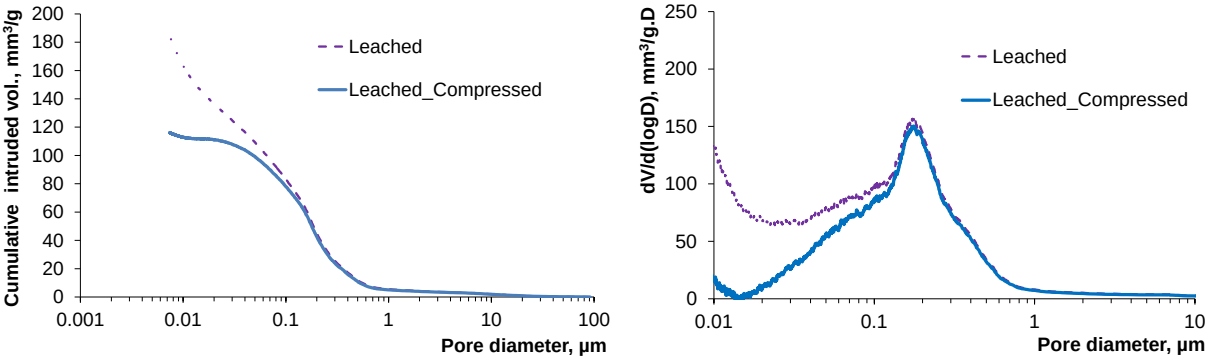

Figure 7.16. Influence of deformation of leached sample on MIP results: sample S1L – the blue curves are the corrected curves.

As an example, Figure 7.16 presents the cumulative intrusion curves and differential pore size distributions of leached sample S1L before and after correcting for the compression effect. It can be seen that the pore volume is compressed by 33%. Such a quite high value cannot be disregarded. However, even with compression correction, the MIP corrected results cannot be considered as the complete pore structure of the tested sample because the pore volume of the sample is always higher than the mercury intruded volume due to pore volume compression under pressure. The difference is larger when the pressure increases. In the context of this study, the corrected and uncorrected curves started diverging more and more at pressure of approximately 30 MPa (corresponding to a pore diameter of 0.05 µm). Furthermore, N_2-adsorption enables to measure the pores up to 0.07 µm. For these reasons, the combination of MIP and gas adsorption measurements will give a better understanding of the pore structure of cementitious materials, especially for leached pastes. The MIP gives reasonable results for pore size larger than 0.05 µm while N_2-adsorption provides information on the smaller pores. In this way, pore structure information is obtained in a broader pore size range and compression effect is reduced. For reference samples, the pores with diameter larger than 0.007 µm was determined by MIP and smaller pores was determined by N_2-adsorption. Note that the pore information obtained by MIP and N_2-adsorption is not identical because different methods/models are applied to calculate the porosity and pore size distribution. The porosity

calculated by N_2-adsoption was shifted at the combined pore dimameter (i.e. 0.05 µm) in order to obtain a continuous curve.

Figure 7.17 to Figure 7.21 compare the porosity and pore size distribution of leached and reference samples determined by the combined MIP and N_2-adsorption method. In the range of 3 nm - 100 µm, the porosity of leached samples hugely increased, from 68% up to 159% compared to the porosity of reference samples. Such a large porosity increase is not only due to the decalcification of portlandite but also due to (partial) decalcification of the C-S-H system because the maximum change in porosity obtained by completely dissolving portlandite is about 12.8% (see modelling chapter). Sample S1L had the smallest porosity after leaching, while sample S2L appeared as a material with the largest porosity after leaching. This may be attributed to its different initial porosities (before leaching) originating from different w/p ratio and limestone filler replacements. However, samples S3L, S4L and S5L exhibited a similar final porosity after leaching despite its difference in w/p ratio and limestone filler replacement (Figure 7.22).

In all leached samples, the cumulative pore volume curves exhibited two stages of significant porosity increase. The first stage was in range of about 60 nm – 500 nm pore sizes of which corresponds to portlandite dissolution. The second stage was in range of pore size smaller than 10 nm which corresponds to C-S-H (and other phases) dissolution. In contrast, reference samples exhibited only one significant pore volume increase stage. The differential pore size distribution plots show two (S1L, S5L) or three (S2L, S3L, S4L) peaks for leached samples while only one peak for reference samples. The critical pore size (which was determined from the average of two peaks with large pore sizes for S2L, S3L and S4L; while the peak with large pore size for S1L and S5L) was significantly shifted to bigger pore size range. The threshold pore diameter tended to increase in most leached samples, except for S3L and S5L of which the threshold pore diameters remained almost unchanged. In most cases, the bulk densities of the leached samples largely decreased after leaching (Table 7.3). Sample S4L was the sample with the largest bulk density decrease caused by the largest Ca removal as shown in Section 7.3.1.

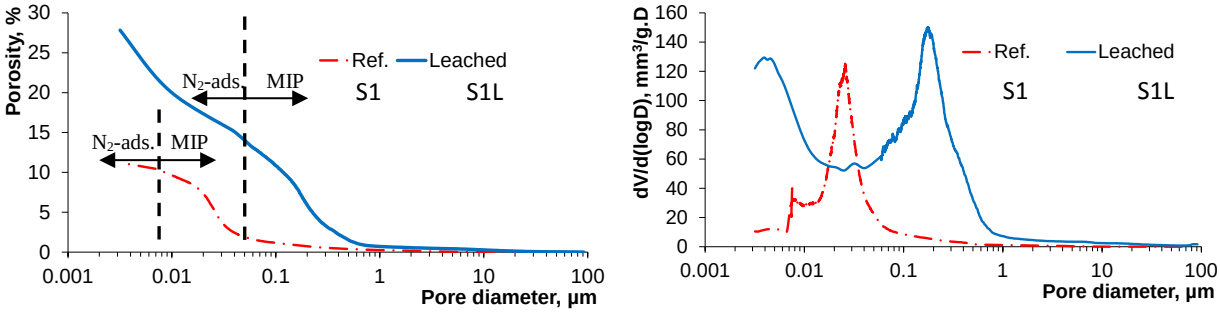

Figure 7.17. Changes in pore structure due to leaching assessed by combining MIP and N_2-adsorption: porosity vs. pore diameter (left) and differential pore size distribution (right) of leached and reference samples S1

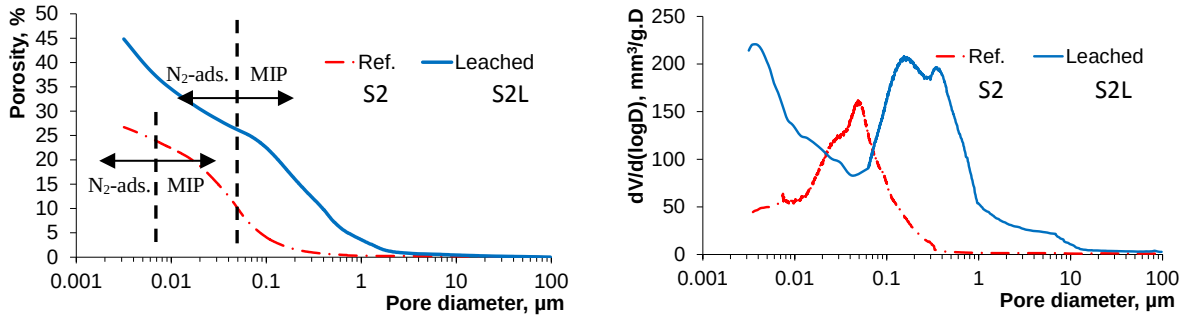

Figure 7.18. Changes in pore structure due to leaching assessed by combining MIP and N_2-adsorption: porosity vs. pore diameter (left) and differential pore size distribution (right) of leached and reference samples S2

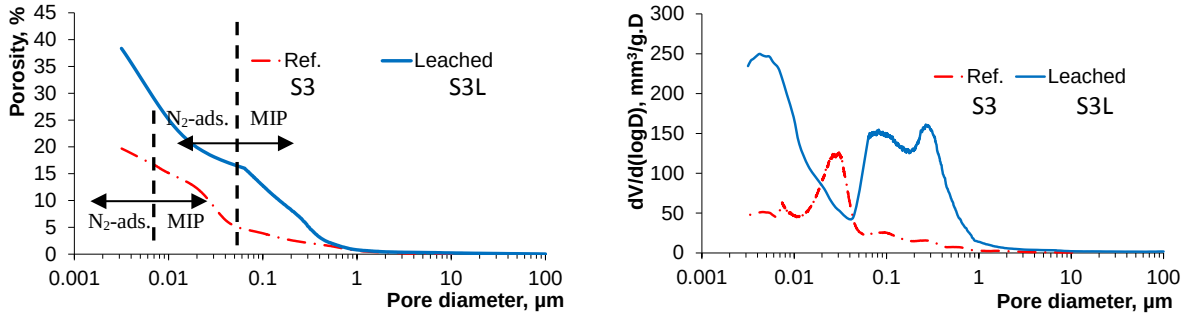

Figure 7.19. Changes in pore structure due to leaching assessed by combining MIP and N_2-adsorption: porosity vs. pore diameter (left) and differential pore size distribution (right) of leached and reference samples S3

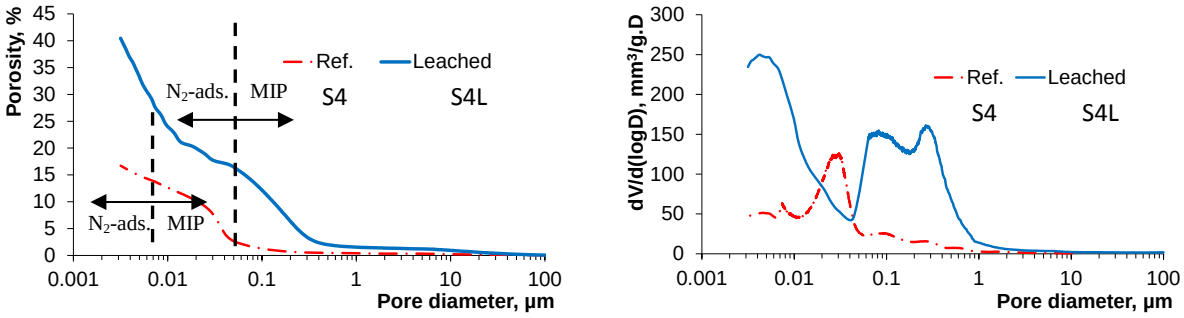

Figure 7.20. Changes in pore structure due to leaching assessed by combining MIP and N_2-adsorption: porosity vs. pore diameter (left) and differential pore size distribution (right) of leached and reference samples S4

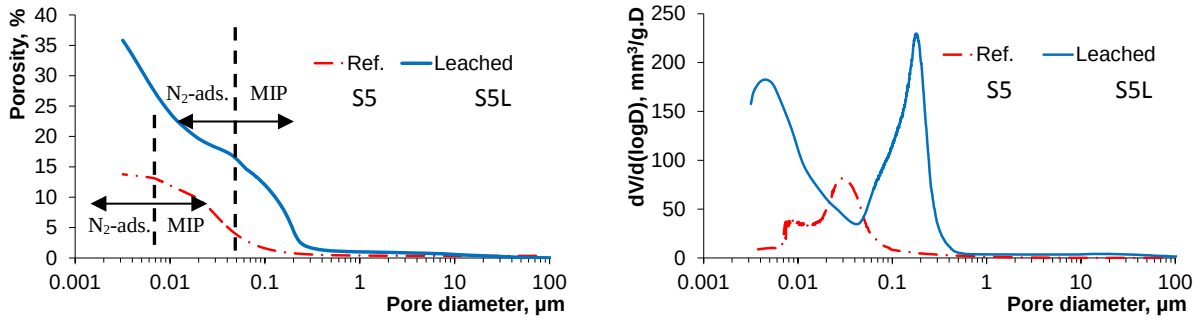

Figure 7.21. Changes in pore structure due to leaching assessed by combining MIP and N_2-adsorption: porosity vs. pore diameter (left) and differential pore size distribution (right) of leached and reference samples S5

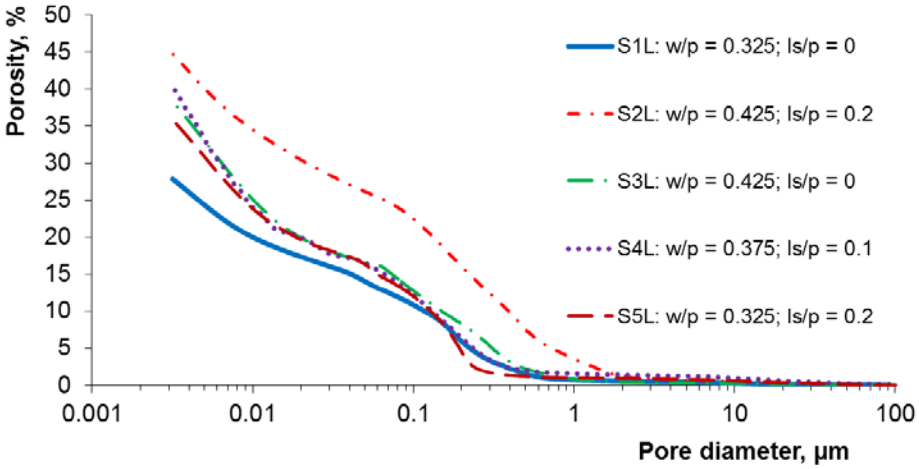

Figure 7.22. Comparison of porosity increases due to leaching of samples with different w/p ratios and limestone filler replacements

Table 7.3. Changes in porosity, critical and threshold pore diameters and bulk density due to leaching determined by N_2-adsorption and MIP combination – "L" denotes leached sample

Sample	S1	S1L	S2	S2L	S3	S3L	S4	S4L	S5	S5L
w/p	0.325	0.325	0.425	0.425	0.425	0.425	0.375	0.375	0.325	0.325
ls/p	0	0	0.2	0.2	0	0	0.1	0.1	0.2	0.2
Accessible porosity, %	11.2	27.8	26.7	44.8	19.7	38.4	16.8	40.5	13.8	35.8
Critical pore diameter, nm	25.7	180	49.9	150	32.0	110	36.4	170	29.0	180
Threshold pore diameter, nm	60	800	300	2000	1000	900	200	800	300	450
Bulk density, g/cm³	1.89	1.39	1.72	1.10	1.78	1.11	1.85	1.14	2.06	1.43

7.6. Phase changes via XRD/QXRD

Figure 7.23 presents the XRD patterns for leached and reference samples. Note that "leached sample" refers to a subsample taken from the leached zone (pH < 9) of the sample. It is clearly observable that portlandite was completely dissolved in all leached samples. There are two intense peaks of portlandite at 2θ = 17.9 and 34.2^o for the reference samples which totally disappear in the leached samples. Except for C-S-H, which cannot be detected (amorphous phase), the most visible phases in the XRD patterns of the leached samples are calcite, ettringite and unhydrated cement which indicates that they are hardly degraded by the NH_4NO_3 solution. Note that the intense peaks for calcite in reference and leached samples S2L, S4L and S5L are due to added limestone fillers. No new crystalline phases were observed as for leaching in deionized water. This underpins the statement that leaching in ammonium nitrate results in same end-products (same mechanism), as obtained for "natural" leaching processes.

The quantitative XRD results of 28-day leached and reference samples S3, S4 and S5 are shown in Table 7.4. Among 15 quantified phases, portlandite and calcite were the most occurring phases in the mixtures. The results showed that unhydrated phases, mainly alite, were still present in both leached and intact materials. There was no portlandite detected within 6 mm depth from the reactive surface which is consistent with the degraded depth determined by phenolphthalein spraying. However, beyond the phenolphthalein degraded depth (9.25, 7.5 and 5.9 mm for S3L, S4L and S5L, respectively), the amount of portlandite was smaller than the one in reference as shown in Figure 7.24. As an example, the degraded depth of S5L was 5.9 mm, while the amount of portlandite in the interval 6-9 mm was 4.7% which is much lower than one in reference sample, 15.3%. In the interval 9-12 mm, the portlandite amount was still slightly reduced (1.5%) compared to reference sample. This

indicates that leaching does not result in a sharp degraded front. Portlandite is still dissolved beyond the phenolphthalein degraded depth.

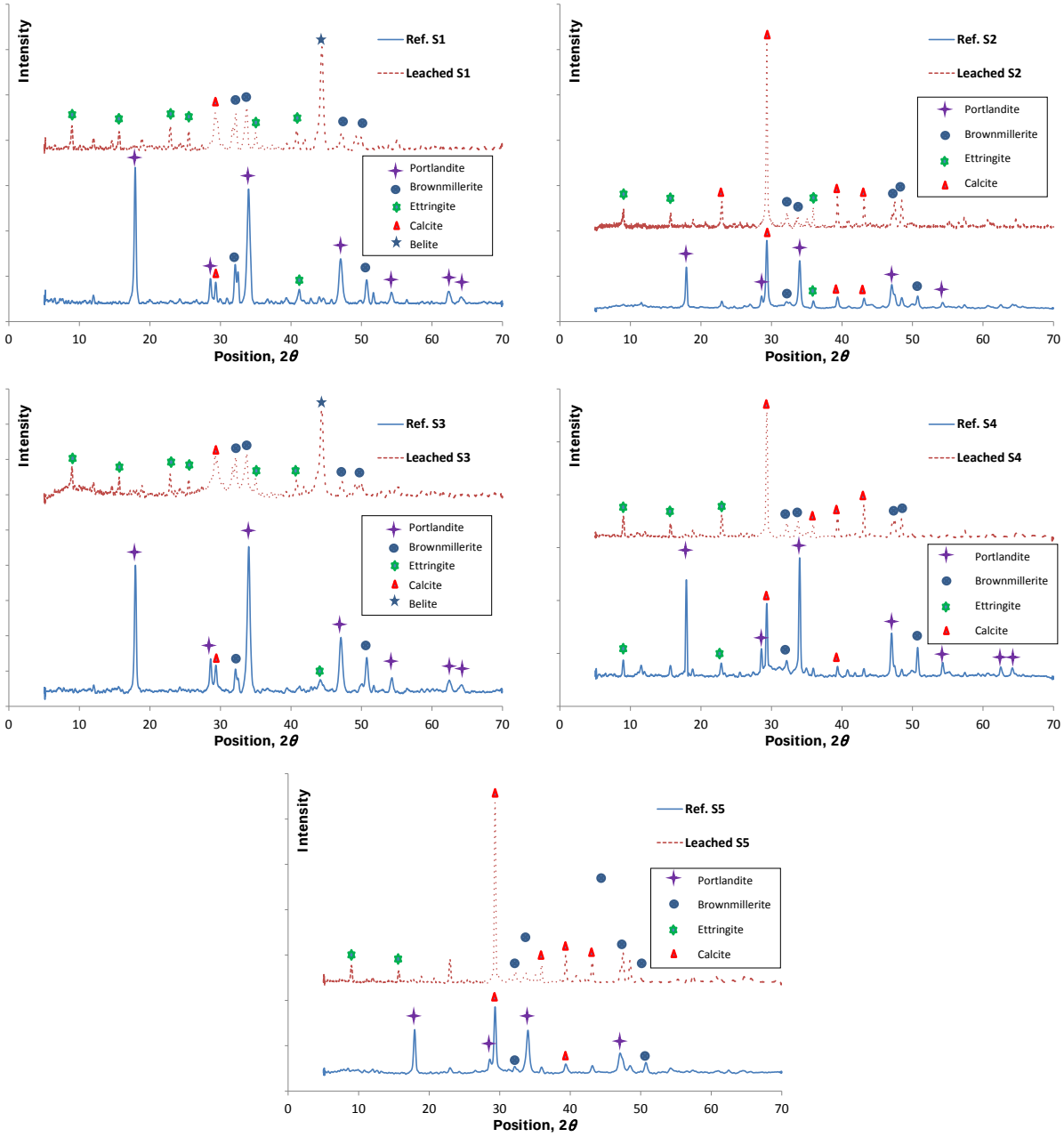

Figure 7.23. XRD patterns of reference and leached samples taken in the first 3 mm depth from the reactive surface

Table 7.4. Quantitative XRD results of leached and reference samples S3, S4 and S5 – 10% internal standard ZnO was added to the mixtures

Sample	Depth interval, mm	Portlandite	Calcite	Ettringite	Belite	Alite	Tricalcium aluminate	Brownmillerite	Calcium monocarboaluminate	Tobermorite	Clinotobermorite	Jennite	Stratlingite	Thaumasite	Anhydrite
S3	Ref.	16.7	2.4	0.2	0.0	1.4	0.0	0.4	0.8	0.1	0.9	0.2	0.0	0.5	0.1
S3L	0-3	0.0	5.0	0.5	0.6	1.2	0.0	0.5	0.5	0.1	1.3	0.2	0.0	0.9	0.1
	3-6	0.0	2.6	0.8	0.8	1.2	0.0	0.3	0.3	0.2	1.2	0.3	0.0	1.1	0.2
	6-9	0.6	1.9	0.6	2.0	2.3	0.0	0.3	0.4	0.1	0.9	0.1	0.0	2.8	0.7
	9-12	12.3	1.4	0.5	0.9	1.5	0.0	1.5	0.7	0.2	0.8	0.3	0.0	2.2	0.5
S4	Ref.	17.7	6.7	0.3	0.0	1.4	0.4	0.4	1.2	0.1	1.4	0.2	0.0	0.4	0.0
S4L	0-3	0.0	17.1	0.7	0.0	1.2	0.0	0.4	0.0	0.1	0.7	0.2	0.0	0.3	0.0
	3-6	0.0	13.4	1.0	0.5	1.4	0.0	0.2	0.2	0.1	1.2	0.5	0.0	0.6	0.0
	6-9	1.0	11.0	0.6	0.0	2.7	0.0	0.2	1.3	0.0	0.9	0.1	0.1	3.1	0.0
	9-12	9.9	8.2	0.5	0.5	3.1	0.0	0.3	1.1	0.2	1.0	0.3	0.2	1.5	0.4
S5	Ref.	15.3	13.1	0.5	0.2	1.0	0.0	1.0	0.0	0.2	0.1	0.2	0.0	0.1	0.0
S5L	0-3	0.0	21.8	0.6	0.8	1.1	0.1	0.5	0.7	0.1	0.9	0.2	0.0	0.2	0.4
	3-6	0.0	19.9	0.7	0.4	0.6	0.0	0.2	0.2	0.1	0.7	0.1	0.0	0.2	0.1
	6-9	4.7	15.6	0.5	0.4	2.3	0.0	1.2	0.7	0.2	1.3	0.2	0.0	0.5	0.1
	9-12	13.8	12.2	0.8	0.0	3.4	0.0	0.8	0.7	0.1	1.5	0.1	0.0	0.7	0.0

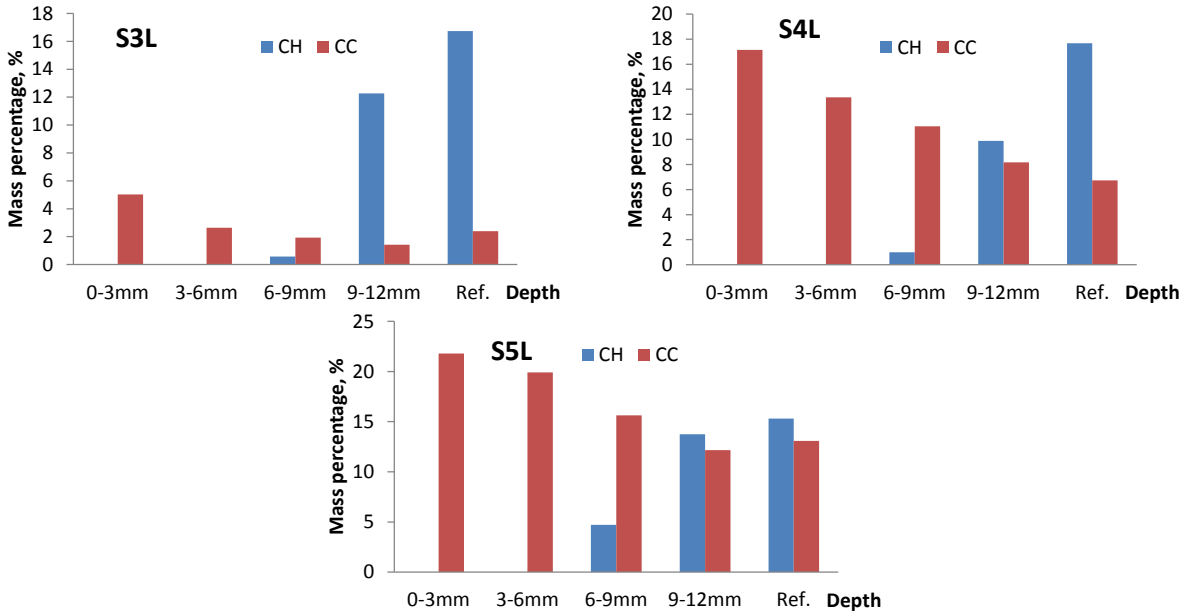

Figure 7.24. Changes in portlandite (CH) and calcite (CC) contents over the depth of leached samples S3L, S4L and S5L after 28 days of leaching in ammonium nitrate solution

The absolute amount of calcite should remain constant (or slightly decreased) because the leaching of CC is negligible. However, Figure 7.24 shows that the calcite amount decreases over the depth. This can be attributed to a reduction in mass of other solid phases which results in a decrease in bulk density of the leached materials. The following derivations enable to understand the variation of bulk density of leached sample over the depth. The mass fractions of calcite in reference, CC_{ref} [-], and in leached, CC_l [-], materials are expressed as in Equations (7.9) and (7.10):

$$CC_{ref} = \frac{m_{CC}}{m_{ref}^{solid} - m_{ref}^{a}} \tag{7.9}$$

$$CC_{l} = \frac{m_{CC}}{m_{l}^{solid} - m_{l}^{a}} \tag{7.10}$$

where m_{CC} is the absolute mass of calcite [kg]; m_{ref}^{solid} and m_{l}^{solid} are the total mass of solid phases in reference and leached materials, respectively [kg]; and m_{ref}^{a} and m_{l}^{a} are the mass of amorphous phases in reference and leached materials, respectively [kg]. Note that XRD only detects crystalline phases; therefore the denominators of Equations (7.9) and (7.10) are the mass of crystalline phases instead of the total mass of solid phases. With the assumption that there is no shrinkage during leaching, the total volumes of material before and after leaching are identical. Thus, the ratio between the mass fractions of calcite in reference and leached materials is related to the bulk densities and amorphous fractions of the reference and leached materials as expressed in Equation (7.11):

$$\frac{CC_{ref}}{CC_{l}} = \frac{m_{l}^{solid} - m_{l}^{a}}{m_{ref}^{solid} - m_{ref}^{a}} = \frac{1 - \frac{m_{l}^{a}}{m_{l}^{solid}}}{1 - \frac{m_{ref}^{a}}{m_{ref}^{solid}}} \times \frac{m_{l}^{solid}}{m_{ref}^{solid}}$$
$$\frac{CC_{ref}}{CC_{l}} = \frac{1 - A_{l}}{1 - A_{ref}} \times \frac{\rho_{l} \times (V_{l}^{solid} + V_{l}^{pore})}{\rho_{ref} \times (V_{ref}^{solid} + V_{ref}^{pore})} = \frac{1 - A_{l}}{1 - A_{ref}} \times \frac{\rho_{l}}{\rho_{ref}} \tag{7.11}$$

where A_l and A_{ref} are the mass fractions of amorphous phases in leached and reference materials, respectively [-]; V_{ref}^{solid} and V_{l}^{solid} are the volumes of solid phases in reference and leached materials, respectively [m^3]; V_{ref}^{pore} and V_{l}^{pore} are the pore volumes in reference and leached materials, respectively [m^3]; and ρ_{ref} and ρ_l are the bulk densities of reference and

leached materials, respectively [kg/m^3]. The reduction in bulk density due to leaching can be written as follows:

$$\Delta\rho = \frac{\rho_{ref} - \rho_l}{\rho_{ref}} 100\% = \left(1 - \frac{CC_{ref}(1 - A_{ref})}{CC_l(1 - A_l)}\right) 100\% \quad (7.12)$$

Figure 7.25 presents the changes in bulk density over the depth of leached samples S4L and S5L. The amount of calcite in sample S3 was small (without limestone fillers), therefore the quantified results of calcite in S3 was not reliable enough to be used for bulk density estimation. In the interval 0-3 mm, the bulk density was reduced 43% and 30% for samples S4L and S5L, respectively. These reductions are comparable with the decrease of bulk density determined by MIP: 38% and 31% for S4L and S5L, respectively. The bulk density gradually increased over the depth of the sample. Beyond the phenolphthalein degraded depth the bulk density of S5L still decreased 5%, while S4L exhibited a larger reduction (13%).

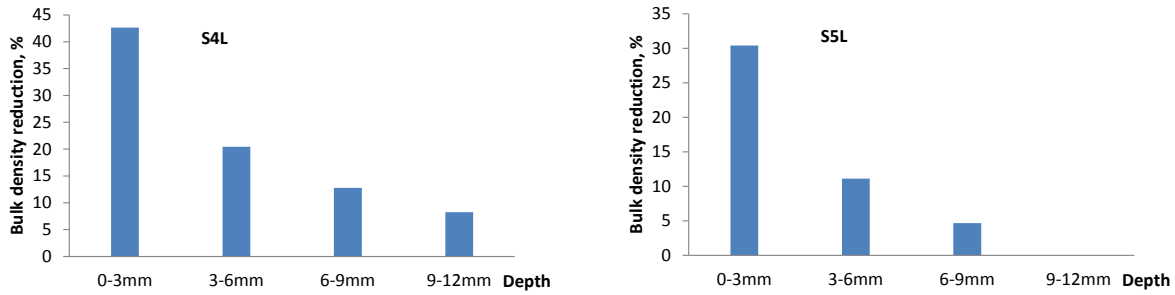

Figure 7.25. Changes in bulk density over the depth of leached samples S4L and S5L after 28 days of leaching in ammonium nitrate solution

7.7. SEM results

7.7.1. Microstructural alterations

Figure 7.26 to Figure 7.30 compare the microstructures of reference samples and 28-day leached samples in ammonium nitrate solution. Leaching clearly increased the pore sizes and total porosity which is in line with the results obtained by MIP and N_2-adsorption. Some big pores with diameter up to about 10 µm were observed in most leached samples. These pores are mainly resulted from portlandite leaching. The dissolution of C-S-H mainly contributes to the increase of pore volume in the micropore to low mesopore range which is difficult to detect by SEM. Micro cracks were observed in all leached samples. The observation of micro cracks is attributed to the decalcification shrinkage of the leached materials. Leaching of C-S-H induces polymerization shrinkage, especially in the region where the Ca/Si ratio is lower

than 1.2 [180]. In addition, leaching induces a significant loss of mechanical properties. Therefore, the decalcification shrinkage could generate tensile stresses surrounding rigid particles (e.g. limestone fillers, unhydrated cements) which results in cracking. The decalcification shrinkage even can generate differential stresses in the region where a gradient of Ca/Si ratio exists [180]. As seen in the SEM images, cracks are more pronounced around the limestone fillers (S2L, S4L, S5L) and unhydrated cements.

The leaching of Ca and other leachable elements creates connected pathways which can increase the percolation of the pore system and as a result, transport properties can be enhanced. There is an increased connectivity between the pores in the XY direction as observed at the bottom-rights of Figure 7.26 to Figure 7.30.

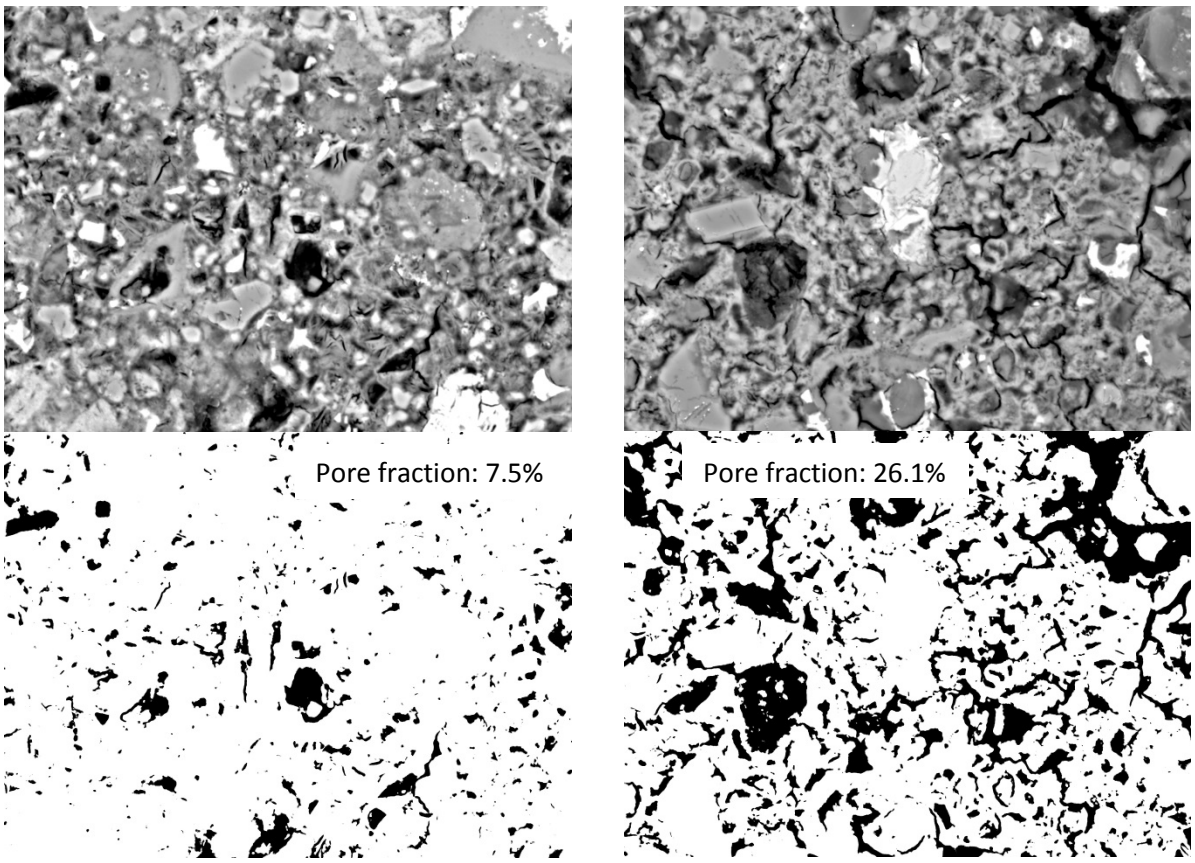

Figure 7.26. SEM backscattered electrons images of reference (top-left) and leached (top-right) samples S1L; and increases in porosity (in black), pore size and percolation due to leaching (bottom) - field width of 128 µm

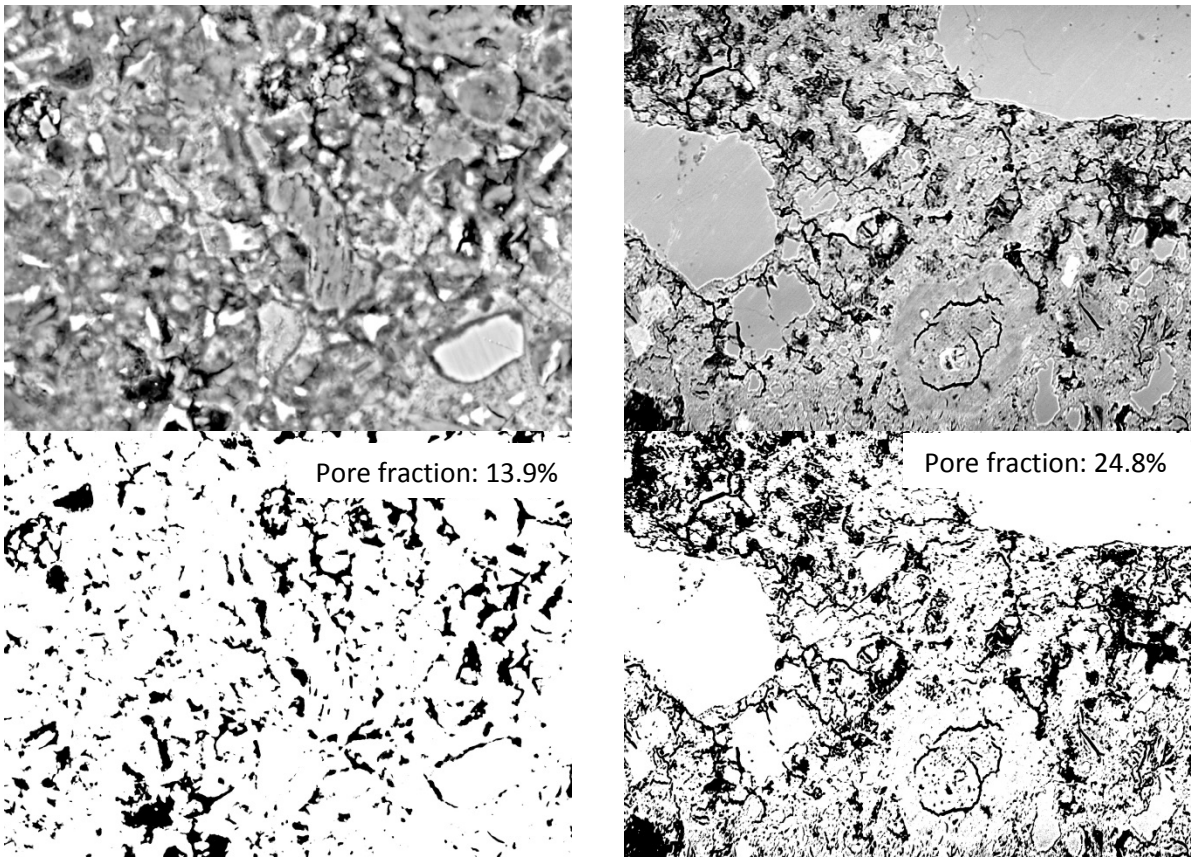

Figure 7.27. SEM backscattered electrons images of reference (top-left) and leached (top-right) samples S2L; and increases in porosity (in black), pore size and percolation due to leaching (bottom) - field width of 128 µm

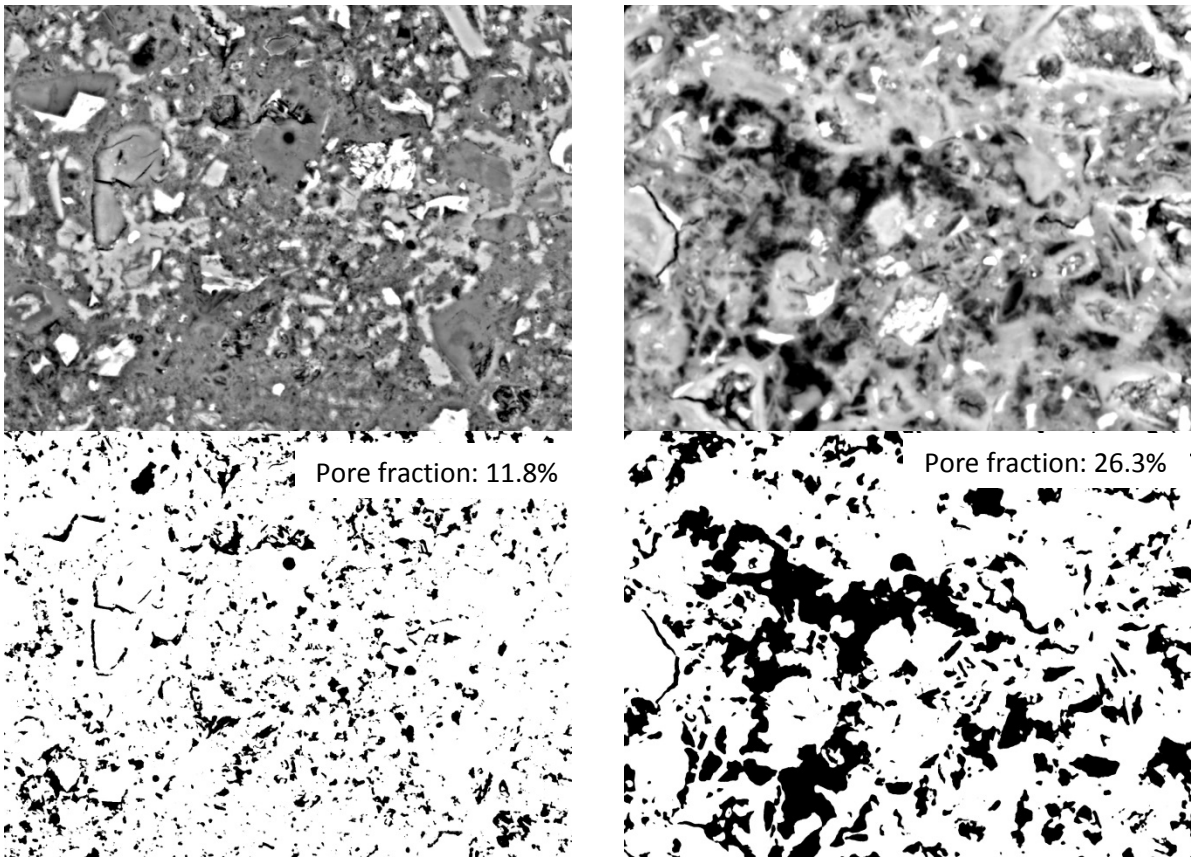

Figure 7.28. SEM backscattered electrons images of reference (top-left) and leached (top-right) samples S3L; and increases in porosity (in black), pore size and percolation due to leaching (bottom) - field width of 128 µm

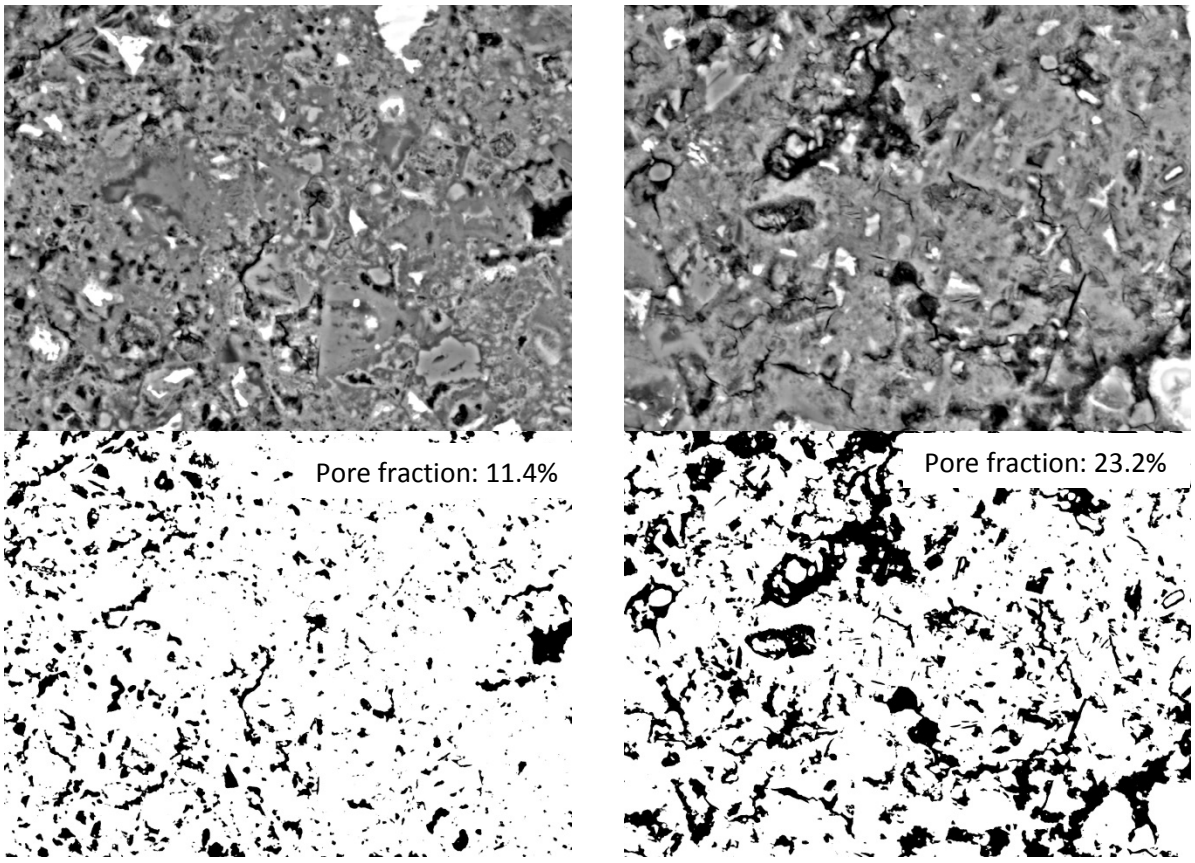

Figure 7.29. SEM backscattered electrons images of reference (top-left) and leached (top-right) samples S4L; and increases in porosity (in black), pore size and percolation due to leaching (bottom) - field width of 128 µm

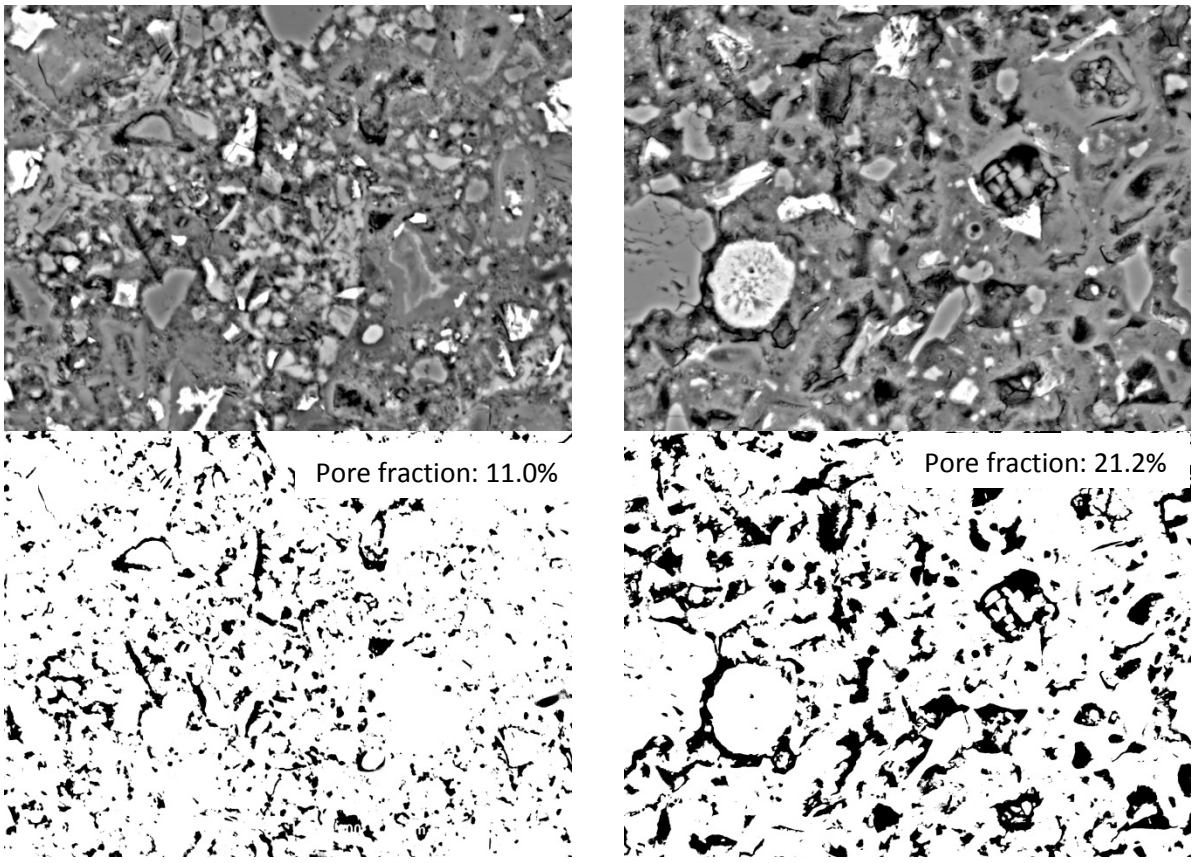

Figure 7.30. SEM backscattered electrons images of reference (top-left) and leached (top-right) samples S5L; and increases in porosity (in black), pore size and percolation due to leaching (bottom) - field width of 128 µm

7.7.2. Modification in atomic Ca/Si ratio

An EDX measurement was performed crossing a transition zone of leached sample S1L indicated by the red arrow in Figure 7.31 (top-left) to quantify the Ca and Si amount. The atomic Ca/Si ratio was converted from normalized mass percentage of Si and Ca and plotted in Figure 7.31 (bottom-left). It was found that the average Ca/Si ratio was approximately double in the intact area compared to the degraded area. There was a sudden jump in Ca/Si ratio at distance of about 220 µm because of the fact that it was scanned through Ca-rich region.

Figure 7.31 (top-right) shows the spatial distribution of Ca while Figure 7.31 (bottom-right) shows the combined spatial distribution of four main elements (Si, Ca, Al and Fe) in the transition zone. The intensity of the green colour is a measure for the Ca content. The intact area clearly indicates higher amount of Ca. Other elements (Si, Al, Fe) seemed to be equally distributed which indicates that those elements did not undergo significant leaching. Micro

cracking was indeed observed in the degraded part in both SEM image (top-left) and mapping figure (bottom-right).

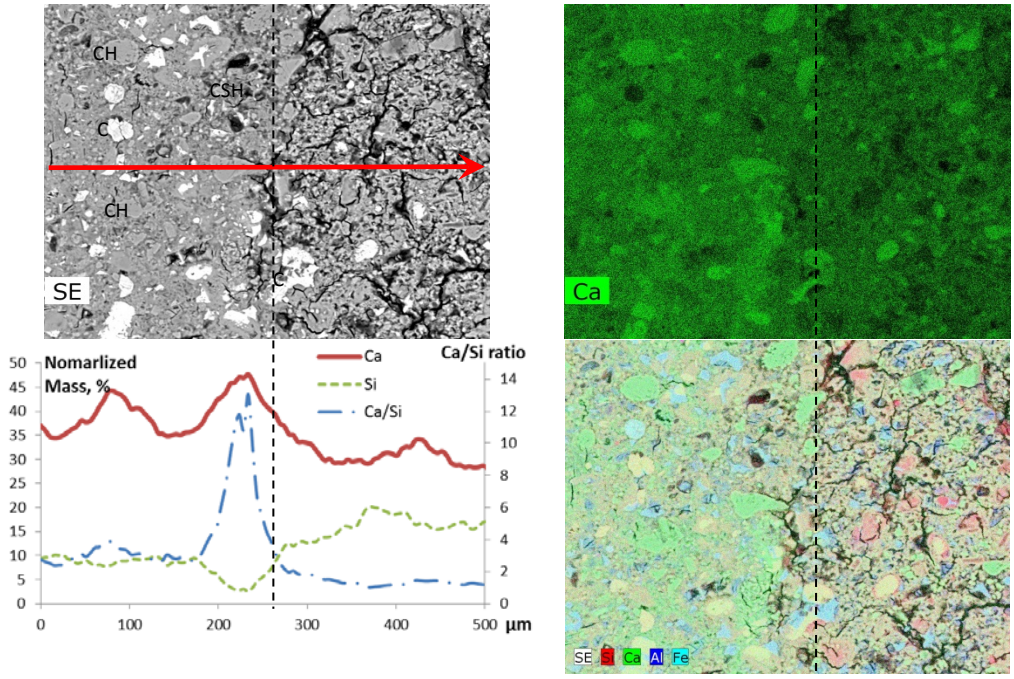

Figure 7.31. SEM BE image of transition zone of leached sample S1L: CH = portlandite, CSH = C-S-H phase, C = residual cement clinkers (top-left); Ca/Si ratio along the red arrow (bottom-left); spatial distribution of Ca (right-top) and element (Si, Ca, Al, Fe) mapping generated by x-ray imaging – field width of 500 µm

Figure 7.32 and Figure 7.33 compare the element mapping of leached and reference samples S4 and S5, respectively. Ca was indeed much more pronounced in the reference sample compared to the leached sample. Other element distributions were not changed due to leaching. It seems that more micro cracks were generated in leached S4L compared to S5L. This may indicate either less decalcification shrinkage or less loss of tensile strength in sample S5L compared to S4L.

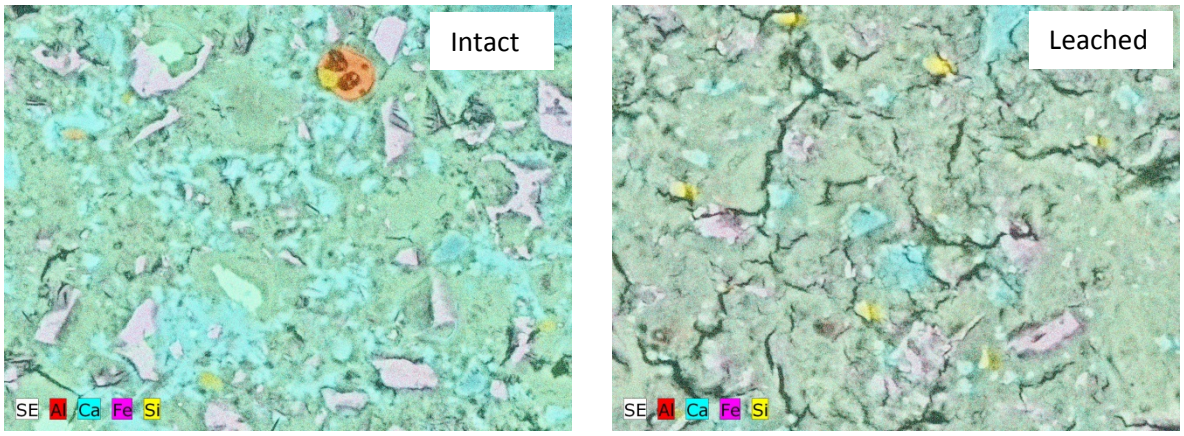

Figure 7.32. Element distribution before and after leaching of sample S4L - SE is referred to SEM backscattered electron image

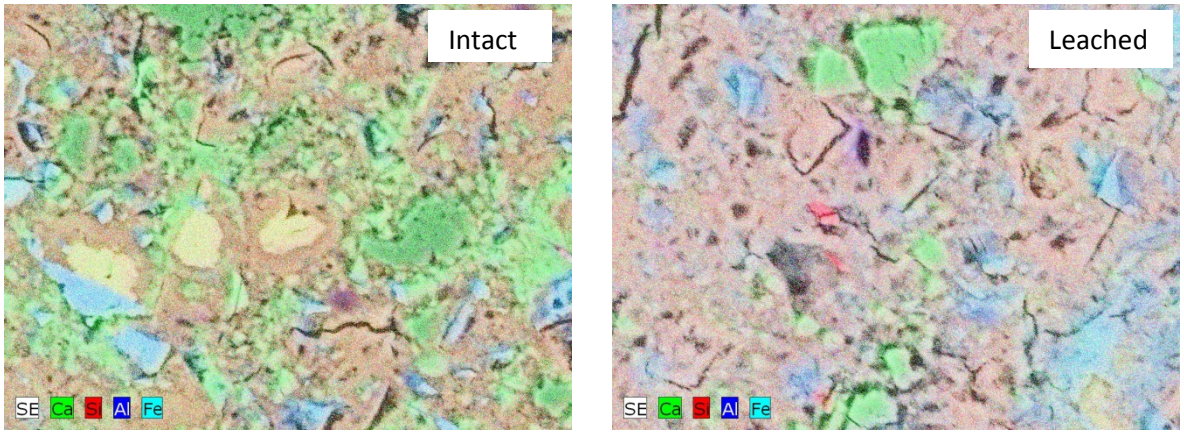

Figure 7.33. Element distribution before and after leaching of sample S5L – SE is referred to SEM backscattered electron image

In order to see the change of Ca/Si ratio over the depth, element line scans were performed on 28-day leached samples with different scan intervals: 9.9, 6.1 and 0.5 µm for S3L, S4L and S5L, respectively. The smaller scan interval, the noisier results are as seen in Figure 7.34 to Figure 7.36. However, the scan results may be better with low scan interval, especially in the transition zones. The atomic Ca/Si ratios were not identical in the degraded area (determined by phenolphthalein spraying) for all cases, but slightly increased over the depth. The average atomic Ca/Si ratio reached the lowest value of about 1, 1.1 and 1.2 for S3L, S4L and S5L, respectively. These Ca/Si ratios dropped in the range of which high decalcification shrinkage occurs. As a result, micro cracking was observed in SEM images. In transition zones (about 1 mm), the Ca/Si ratios rapidly increases along the depth towards the intact area. Beyond the transition zones, the Ca/Si ratio still increases slightly which is in line which quantitative

XRD results in which it was noticed that portlandite amount still decreases beyond the degraded zone.

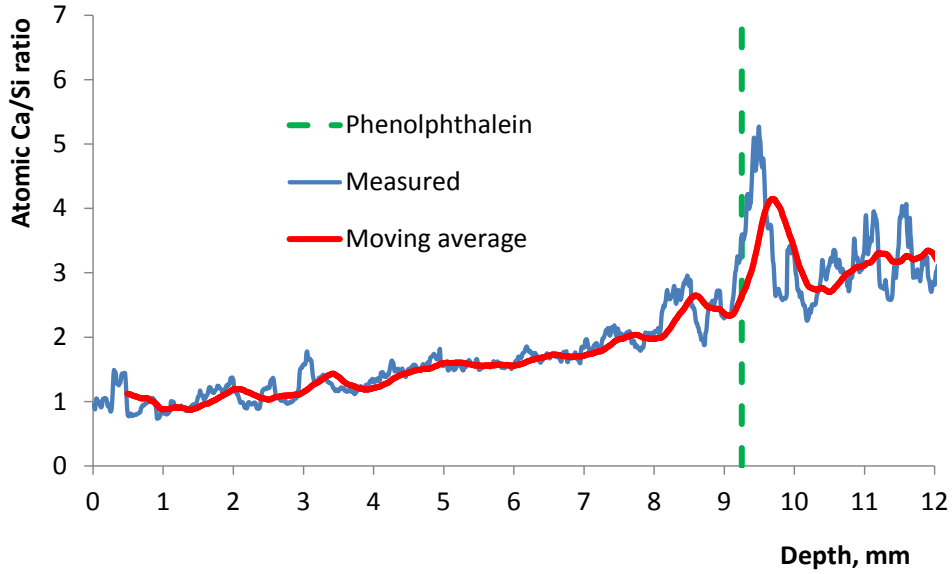

Figure 7.34. Decrease in atomic Ca/Si ratio of sample S3L due to leaching - scan interval was 9.9 µm

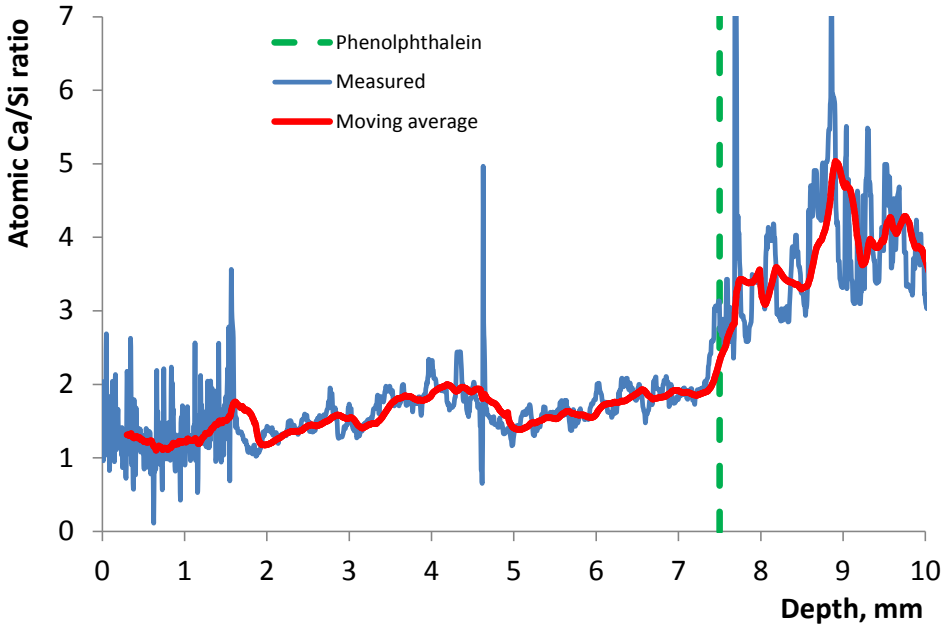

Figure 7.35. Decrease in atomic Ca/Si ratio of sample S4L due to leaching - scan interval was 6.1 µm

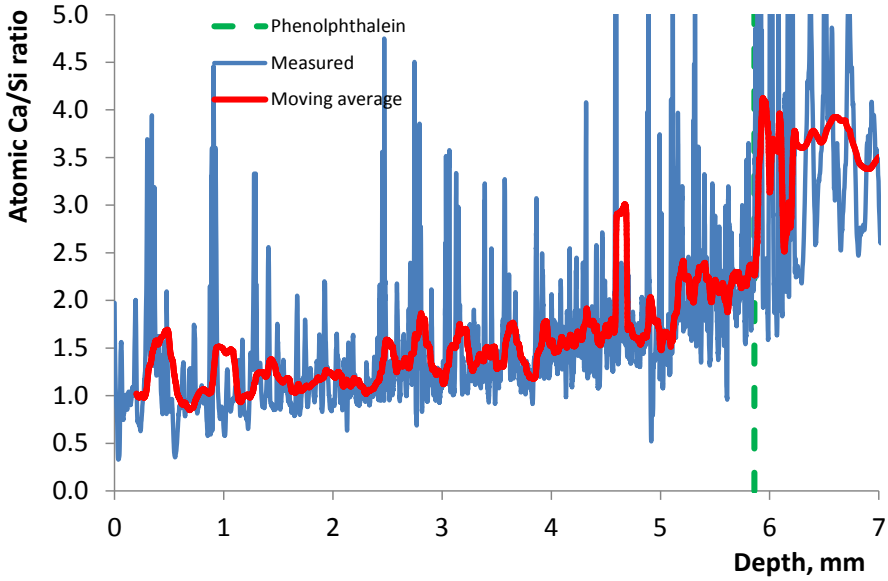

Figure 7.36. Decrease in atomic Ca/Si ratio of sample S5L due to leaching – scan interval was 0.5 µm

7.8. Change in water permeability

The increase of intrinsic permeability of leached sample S3L as a function of immersion time in ammonium nitrate solution is shown in Figure 7.37. Note that in the permeability setup, the applied pressure was perpendicular to leached surface. The permeability increased with proceeding leaching time, hence progressing leaching depth. After one week of NH_4NO_3 immersion, the permeability coefficient increased 6 times, from 2.3×10^{-20} to 1.4×10^{-19} m^2. It continued increasing up to 3.2×10^{-19} m^2 and 1.4×10^{-18} m^2 after 2 weeks and 8 weeks NH_4NO_3 immersion, respectively. As with carbonation, the decalcification of the sample was not uniform with depth and thus, the permeability represents a composite permeability.

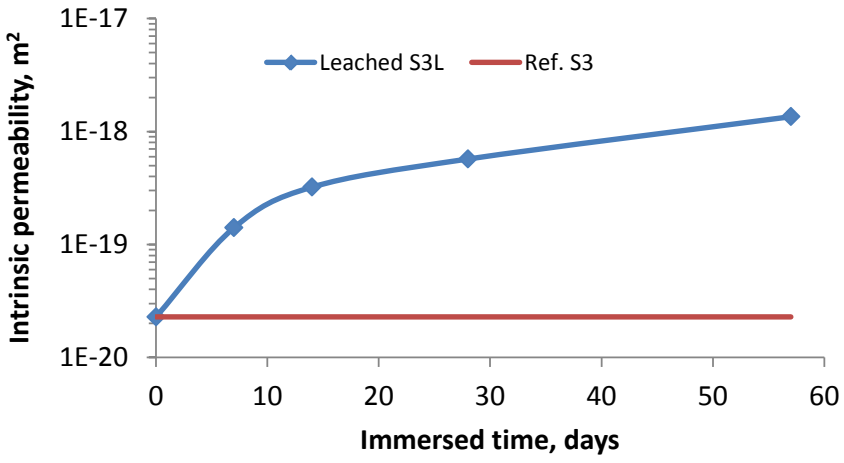

Figure 7.37. Change in intrinsic permeability of leached sample S3L due to leaching in 6 mol/l NH_4NO_3 as a function of immersed time

Table 7.5 summarizes the permeability of leached samples after 28-day immersion in ammonium nitrate solution 6 mol/l. The intrinsic permeability of leached samples increased one to two orders of magnitude depending on w/p ratio and composition. Sample S1L with the lowest w/c ratio (0.325) exhibited an increase in permeability by a factor of 6, while sample S2L with the highest w/c ratio (0.531) showed a more significant increase by a factor of 235. The extent of permeability increase is correlated with the porosity and pore size distribution after leaching. As seen in Figure 7.22, the porosity is the largest and pore size distribution is the coarsest for sample S2L and vice versa for sample S1L. Leached samples S3L, S4L and S5L had a quite similar final porosity and pore size distribution, however the degree of permeability increase was different because of its different degraded depth. After 28-day leaching, sample S3L obtained a degraded depth of 9.25 mm which resulted in 25-time permeability increase, while a lower permeability increase by a factor of 18 for sample S4L with degraded depth of 7.5 mm. Sample S5L (degraded depth of 5.9 mm) exhibited an increase in permeability by 8 times after 28-day leaching. However, the permeability was significantly increased by a factor of 592 when immersed in ammonium nitrate solution for 142 days. The degraded depth in this case was 25 mm which equaled to the sample depth (fully leached).

The permeability change is not limited to the zone where the pH is larger than 9 (phenolphthalein indicator). When applying the series model to compute the intrinsic permeability of the leached zone, the computed permeability turned negative. In these calculations, the permeability of the “unaltered” zone was taken from the permeability of the reference sample. Therefore, it is assumed that there exists a relatively thick transition zone over which the permeability is increased to a value somewhere between that of the degraded zone and the reference sample. As seen in Figure 7.34 to Figure 7.36, the Ca/Si ratio still decreases beyond the degraded depth which results in a change in microstructure, thereby permeability. In this contribution, a numerical model is needed to confirm this assumption and to quantify the depth of the transition zone.

The increase in permeability of the degraded material is due to the larger amount of capillary pores (see MIP results and SEM images) which is the result of portlandite dissolution. In general, mass transport properties are mainly affected by capillary and large pores [185]. However, calcium leaching is a process where Ca is not only leached from portlandite but

also from other phases (C-S-H), and as a result the created pathways can increase the connectivity of pores at the different levels: gel, micro and mesopores. Furthermore, the C-S-H leaching leads to a polymerization of C-S-H due to lower Ca/Si ratio which induce the decalcification shrinkage. As a result, the potential of crack generation in leached sample is increased as seen in SEM images. The author suggests that the dissolution of C-S-H (and probably other less leachable phases) considerably contributes to the change in permeability during accelerated leaching. The study of [190] also confirms the contribution of C-S-H leaching to permeability increase. When the sample is completely degraded (complete decalcification of portlandite), and further immersed in NH_4NO_3 solution (for an extra 8 days), the intrinsic permeability slightly increases.

Table 7.5. Increase in intrinsic permeability of cement pastes after leaching – sample S5L full was measured after 142-day leaching when the sample was fully decalcified (determined by phenolphthalein), the others were measured after 28-day leaching.

Sample	**S1**	**S1L**	**S2**	**S2L**	**S3**	**S3L**
Permeability, m^2	1.5×10^{-21}	9.1×10^{-21}	1.1×10^{-19}	2.6×10^{-17}	2.3×10^{-20}	5.7×10^{-19}
Sample	**S4**	**S4L**	**S5**	**S5L**	**S5L full**	
Permeability, m^2	1.4×10^{-20}	2.5×10^{-19}	2.0×10^{-20}	1.6×10^{-19}	1.2×10^{-17}	

7.9. Change in diffusivity

The diffusion experiments were performed on a 28-day leached sample S3L. The average porosity of the leached sample was calculated by weighted average method as the approach for carbonation (using Equation (6.5)). The retardation factor R_e was again set at one. Both diffusivities of He and Xe were able to determine for leached sample S3L despite shorter experimental time compared to reference sample S3. Figure 7.38 shows the fitted and measured partial pressure profiles of He and Xe at the outlet for the leached sample S3L. A good correlation was obtained for both gases. The He effective diffusion coefficient of S3L was 9.48×10^{-11} m^2/s, which is 4.1 times higher than the effective diffusion coefficient of the reference sample S3. Compared to the increase of permeability, the increase in diffusion due to leaching is much lower. Like permeability, the effective diffusion coefficient of the leached sample should be treated as the composite (overall) effective diffusion coefficient.

The Xe effective diffusion coefficient of the leached sample S3L was 8.58×10^{-12} m^2/s which is much smaller than the one of He. The effective diffusion coefficient of Xe for S3L was

almost double compared to the estimated effective diffusivity of intact material (the measured effective Xe diffusivity for the reference sample S3 was not obtained due to very long time experiment). It is surprising that the diffusivity evolution of He and Xe is not identical. One of possible explanations for this observation is the difference in molecular pore size of He (0.26 nm) and Xe (0.46 nm). Leaching can modify the microstructure of cement paste from micrometer scale down to sub nanometer scale as observed by MIP and N_2-adsorption experiments. Therefore, the change of pores with smaller diameter likely affects the diffusion of He (with bigger molecular size) rather than the diffusion of Xe.

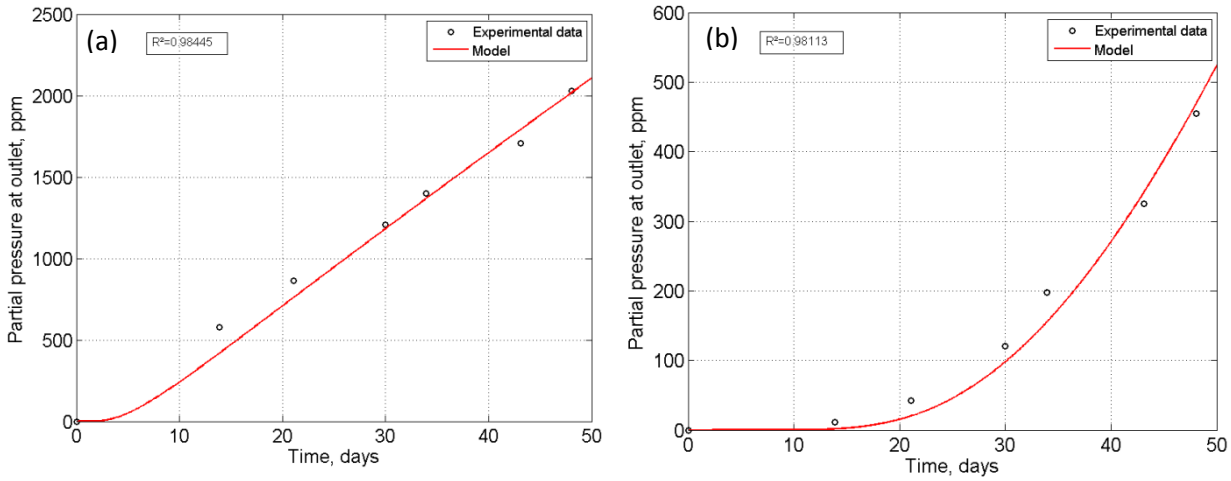

Figure 7.38. Comparison of the He (a) and Xe (b) partial pressure at the outlet obtained from experiment and model for carbonated sample S3L after 28 days of leaching in ammonium nitrate solution

7.10. Summary and conclusions

In the present work, an ammonium nitrate solution of 6M was used to accelerate the decalcification kinetics of hardened cement paste samples and to examine the changes in the microstructure and transport properties of leached materials. A variety of techniques including SEM/SEM-EDX, IC, XRD and quantitative XRD, MIP, N_2-adsorption and phenolphthalein spraying were used to characterize the microstructural and mineralogical changes and the degraded depth. The effect of accelerated leaching on transport behaviour was studied by measuring changes in the water permeability and diffusivity of dissolved gases.

Results showed that NH_4NO_3 solution was a reactive agent which can be used to accelerate leaching kinetics while still keeping the “nature” of the leaching process. The mineralogical changes under leaching in ammonium nitrate solution were quite similar to leaching in pure

water as no new phase was formed during leaching in ammonium nitrate solution. In this way, it enables to imitate long-term naturally degraded cementitious materials by accelerated leaching using ammonium nitrate solution. However, deeper investigations in the changes of mineralogy are still needed, especially when Ca/Si is lower than 1. The square-root-time law of propagation of the leaching front and leached Ca amount was applicable under accelerated conditions indicating diffusive transport conditions. The higher the w/p ratio and limestone filler replacement, the larger the rate of propagation of leaching (degraded depth). However, the effects of w/p ratio were more significant than limestone filler replacement. The comparison of mass change calculated from IC results and direct measurements (weighing) proved that C-S-H leaching contributes to the mass loss of the sample.

A combination of MIP – nitrogen adsorption analysis was used to obtain information on the porosity and pore size distribution changes. The accelerated leaching highly altered the microstructure of the cement paste to a more porous material which is evidenced by the increase of specific surface area, increase of total porosity and by the creation of a coarser pore size. The total accessible porosity of the leached samples highly depended on w/c ratio. Both meso- and micropore volumes were increased, but interesting is the micropore volume which was altered much more than the mesopore volume. Probably the leaching of C-S-H, of which the volume fraction is more than portlandite, results in a significant modification of the micropore structure. The bulk density was significantly reduced due to Ca removal (up to 42%) and not uniform over the depth. It increased with the depth of the leached zone which indicates a gradual alteration in mineralogy. Quantitative XRD indicates that portlandite was completely degraded in the leached zone while C-S-H was partially dissolved as evidenced from microstructural analysis. Beyond the leached front, part of the portlandite was also dissolved as confirmed by quantitative XRD and SEM-EDX.

SEM image analysis showed a significant increase in porosity and pore size for the leached materials. Some big pores (up to 10 µm) were observed. The decalcification shrinkage resulted in formation of micro cracks. More micro cracks were observed in samples with limestone filler. The leaching of Ca created connected pathways resulting in an increase of the percolation of the pore system. In the leached zone, the atomic Ca/Si ratio was gradually increased towards the degraded front with a jump in Ca/Si ratio indicative for the transition zone.

The changes in microstructures and mineralogy led to a significant increase in transport properties. The permeability increased by one to two orders of magnitude depending on the

immersion time in NH_4NO_3 and w/c ratio. For similar w/c ratio, the addition of limestone helps to reduce the permeability alteration. The extent of permeability increase is correlated to the porosity and pore size distribution after leaching. The permeability of the non-invasion zone (determined by phenolphthalein) was probably altered as the Ca/Si ratio still decreased beyond the degraded depth. The diffusivity also significantly increased after leaching, but with smaller magnitude compared to the change in permeability (e.g. factor of 24 for water permeability compared to factor 4 for He diffusivity of sample S3L).

This page is intentionally left blank!

CHAPTER 8: MODELLING OF CHEMICAL DEGRADATION UNDER LABORATORY CONDITIONS

8.1. Modelling of carbonation of cementitious materials under controlled CO_2 pressure conditions

8.1.1. Introduction

A number of models have been proposed based on Fick's law for diffusion [123, 251-253]. Almost all models relate the carbonation depth, *dep* [mm], (determined by phenolphthalein spraying method) with square root of time *t* [day]:

$$dep = C_{car}\sqrt{t} \tag{8.1}$$

where C_{car} [mm/day$^{0.5}$] is a lumped coefficient considered as the rate of carbonation and it depends on the surrounding conditions and the properties of concrete. The estimation of carbonation depth is very useful in the investigation of the service life of reinforced concrete structures. It can help designers to determine the thickness of the concrete cover to protect reinforcement bars from corrosion. However, a sharp front is not always observed. Instead of giving an explicit formula to predict the carbonation depth, a large number of models have been developed in order to solve the carbonation problem numerically [252, 254, 255]. These approaches are based on conservation laws and can capture most important factors influencing the carbonation process. However, identification of parameters for complex models may require several experiments and is not an easy task, for example to parameterize a constitutive relation between relative humidity, porosity changes and diffusivity of CO_2 during carbonation.

As mentioned in Chapter 3, carbonation of cement-based materials under atmospheric conditions is a slow process; therefore accelerated carbonation methods have been conventionally used to study carbonation. A common way is to put concrete samples in a controlled chamber with a specific CO_2 partial pressure and an optimized relative humidity (50-70%) to speed up carbonation. A new method has been proposed in Section 4.4.1 in which a high pressure gradient of pure CO_2 is applied to samples at controlled initial internal relative humidity. Interpretation of such accelerated carbonation experiment requires a one-dimensional reactive transport model accounting for advective flow as a consequence of the applied CO_2 pressure gradients. Contrary to the models previously mentioned, the proposed model accounted for both advective and diffusive transport mechanisms. Besides the

prediction of the carbonation depth, portlandite content, pH profile and CO_2 uptake, the model also enabled to predict the change in permeability, diffusivity, RH and porosity due to carbonation.

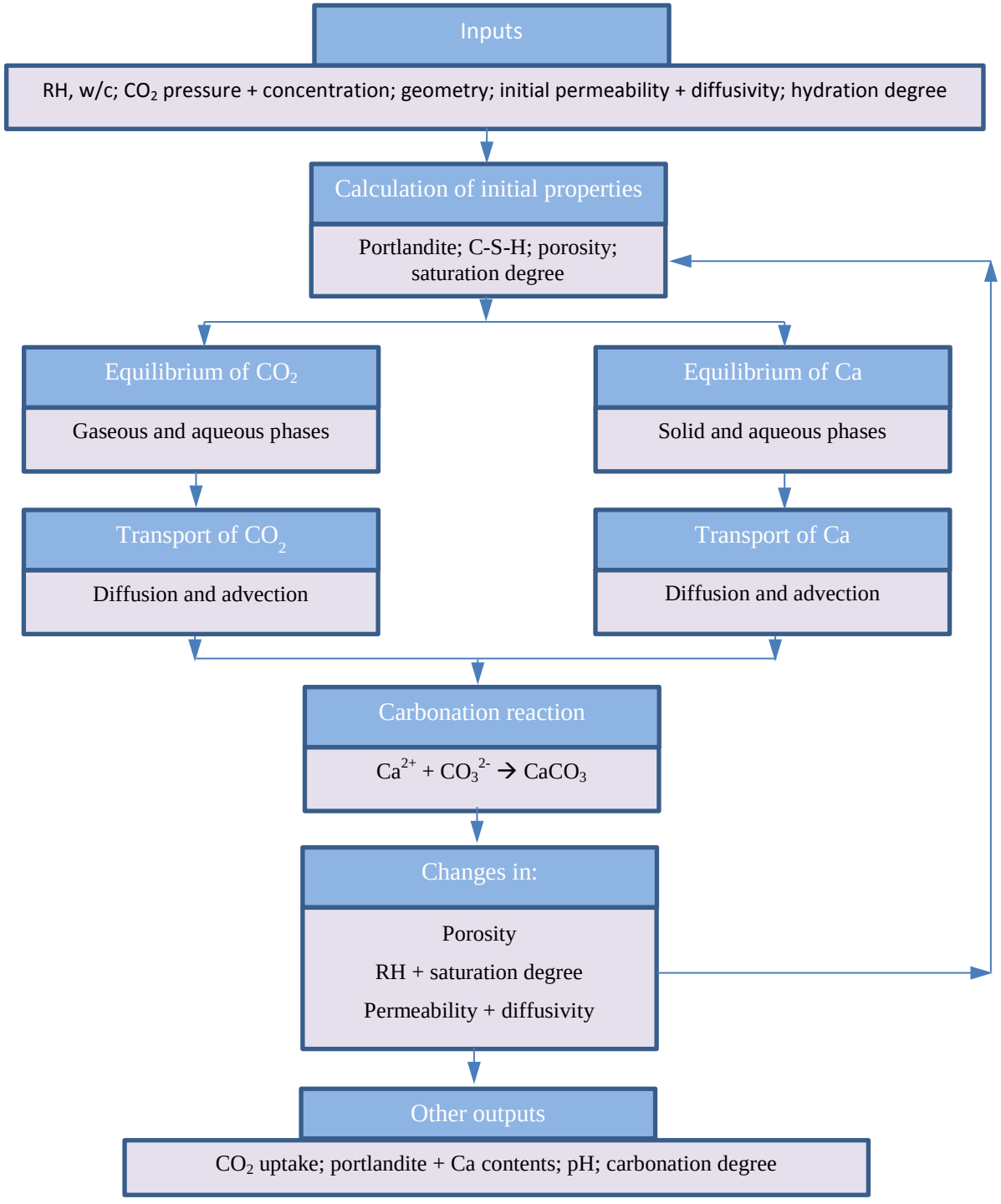

Figure 8.1. Overall scheme of carbonation model

The outline of the proposed model is shown in Figure 8.1. The model was based on a macroscopic mass balance for carbon dioxide in gaseous and aqueous phases. A simplified solid-liquid equilibrium curve was used to relate the Ca contents in the aqueous and solid phases. The model only considers the carbonation of portlandite and calcium silicate hydrates which are the main hydrated phases in typical CEM I Ordinary portlandite cement paste. Note that also other minor phases, such as the primary phases as ettringite and thaumasite or newly formed phases as strätlingite, eventually become carbonated [256]. Initial hygrothermal conditions were accounted for and their evolutions during carbonation are also considered. It is assumed that the hydration of concrete is not changed when the carbonation process starts, because verified experiments were conducted on 28 day-old samples and the time for carbonation was quite limited.

8.1.2. Theory

8.1.2.1. Mass conservation of CO_2

The mass balance equation for CO_2 is given as:

$$\frac{\partial c}{\partial t}+\frac{\partial J}{\partial x}=-Q \tag{8.2}$$

where c is the total concentration of CO_2 in the porous media [kg/m^3]; J is the total flux of CO_2 [kg/m^2.s]; Q is the reaction rate of CO_2 [kg/m^3.s], t is time [s] and x is the spatial distance [m].

Phase equilibrium of CO_2

The total concentration of CO_2 in the porous media is the sum of the amounts of CO_2 in the gaseous and aqueous phases:

$$c=\phi(1-S)c_g+\phi S c_l \tag{8.3}$$

where ϕ is porosity [-]; S is water saturation degree [-]; c_g and c_l are the concentrations of gaseous and dissolved carbon dioxide [kg/m^3], respectively. Henry's law is applied to relate the gaseous and aqueous concentrations of CO_2 as:

$$P=K_H\frac{c_l}{M_{CO_2}} \tag{8.4}$$

where P denotes the pressure of CO_2 gas [Pa]; M_{CO_2} denotes molar mass of CO_2 [kg/mol]; and K_H denotes the Henry constant [Pa/m^3.mol] (values of parameters and variables used in

this study are listed in the Appendix 1). Taking into account the Clapeyron equation for an ideal gas:

$$c_g = P\frac{M_{CO_2}}{RT} \tag{8.5}$$

It is finally obtained:

$$c_g = c_l\frac{K_H}{RT} \tag{8.6}$$

where R is universal gas constant [J/mol.K]; T is absolute temperature [K]. It is worth noting that this relation is only valid when the time needed to reach equilibrium between the gaseous and aqueous phase is very short. Because the rate of CO_2 absorption per unit surface of water is fast compared to the transport processes which govern the carbonation [257]. It is assumed that the equilibrium between the two phases will be reached instantaneously.

Two- phase transport of CO_2 in unsaturated cementitious materials

The total flux of CO_2 includes both the CO_2 fluxes in the gaseous and aqueous phase. Accounting for diffusion and advection results in following set of equations:

$$\begin{aligned} J &= J_g + J_l \\ J_g &= -\left[c_g v_g + D_g\frac{\partial c_g}{\partial x}\right] \\ J_l &= -\left[c_l v_l + D_l\frac{\partial c_l}{\partial x}\right] \end{aligned} \tag{8.7}$$

where J_g and J_l are the fluxes of gaseous and aqueous phase, respectively. D_g and D_l are effective diffusion coefficients of gaseous and aqueous phase, respectively [m^2/s]; v_g and v_l are the volumetric flux densities (i.e. Darcy flux) [m/s] of gaseous and aqueous phases due to a pressure gradient, respectively, which are obtained via Darcy's law for the aqueous phase:

$$\begin{aligned} v_l &= -\frac{k_l(\phi,S)}{\mu_{H_2O}}\frac{\partial P_l}{\partial x} \\ k_l(\phi,S) &= k_{l0}(\phi)k_l(S) \end{aligned} \tag{8.8}$$

and gaseous phase:

$$v_g = -\frac{k_g(\phi,S)\beta(P_a)}{\mu_{CO_2}}\frac{\partial P_g}{\partial x} \qquad (8.9)$$
$$k_g(\phi,S) = k_{g0}(\phi)k_g(S)$$

where μ_{H_2O} and μ_{CO_2} denote the dynamic viscosity of water and CO_2 gas, respectively [Pa.s]. These viscosity coefficients are supposed to be constant at a certain temperature. $k_{g0/l0}(\phi)$ is intrinsic permeability [m^2] which depends on porosity (detailed later) and $k_{g/l}(S)$ is the function accounting for the effect of saturation degree on the permeability of gaseous/aqueous phase, respectively.

The relationships between permeability and saturation degree are expressed by invoking the relation of van Genuchten [198] and Wardeh [258] for the aqueous and gaseous phases, respectively:

$$k_l(S) = S^p\left[1-(1-S^{1/q})^q\right]^2 \qquad (8.10)$$

$$k_g(S) = (1-S)^p\left(1-S^{1/q}\right)^{2q} \qquad (8.11)$$

where p [-] and q [-] are empirical coefficients.

Permeability is generally assumed to depend on porosity, but it is not easy to propose a direct relationship between permeability and porosity. Other pore structural parameters would affect the permeability, including pore size, tortuosity and connectivity. A relationship between permeability and pore structural parameters determined by MIP has been proposed in Chapter 5 for sound cement pastes. This relation may not be applicable for carbonated materials because carbonation alters the pore structures not only at meso scale (determined by MIP) but also at gel pore scale. For carbonated materials, the author explored a well-known relation proposed by Kozeny [54] and later modified by Carman [53] known as Kozeny-Carman (KC) equation. The KC equation was actually derived by comparing Poiseuille's law and Darcy's law [62].

$$k = \chi\frac{\phi^3}{(1-\phi)^2} \qquad (8.12)$$

where χ [m^2] is a function of tortuosity, τ [-]; specific surface of pores, S_a [m^2/m^3]; and shape factor, F_s [-] as follows:

$$\chi = \frac{1}{\tau^2 S_a^2 F_s} \tag{8.13}$$

The specific surface of pores of sound and carbonated materials can be obtained from BET nitrogen gas adsorption measurements and bulk density obtained from MIP measurements ($S_a = S_{BET} \times \rho$). In the transient stage, the specific surface of pores is assumed to be linearly varying with the carbonation degree. τ is the tortuosity and theoretically defined as the ratio between the effective channel length l_e and the length l of the porous material, $\tau = l_e/l$. The shape factor F_s characterizes for the shape of pores. Both parameters τ and F_s are very difficult to quantify because of the complex pore system of hardened cement paste. However, the lumped term $\Omega = \frac{1}{\tau^2 F_s}$ [-] can be determined with the knowledge of intrinsic permeability, total porosity and specific surface of pores. Numerical calculation of Ω was performed on carbonated and reference samples S3, S4 and S5 with the data presented in Chapter 6. The results show that the average value of Ω for sound materials is one order of magnitude higher than one for carbonated materials. Therefore, the author assumes that the lumped term Ω linearly decreases as a function of carbonation degree as follows:

$$\Omega = \Omega_0 - (\Omega_0 - \Omega_c) d_c = \Omega_0 (1 - 0.9 d_c) \tag{8.14}$$

where subscript 0 and c denote sound and carbonated materials; Ω_0 can be calculated from porosity, specific surface area and intrinsic permeability of reference sample; d_c is the carbonation degree (see Section 8.1.3.1). The KC relation works well for relatively homogeneous porous media. For more complex materials as hardened cement paste, the relation has some drawbacks because of the complex microstructure of cement hydrates and non-uniform pore sizes as stated elsewhere [63, 64]. Nevertheless, the KC equation has been used in concrete literature [20, 65, 66]. The current study, as a first approximation, also applies KC relation to consider the effect of variation in pore structures due to carbonation on permeability, i.e. $k_{g0/l0}(\phi)$ in Equations (8.8) and (8.9).

The $\beta(P_a)$ [-] function is introduced to account for the slip effect on gas permeability known as the Klinkenberg effect [69] and is written as:

$$\beta(P_a) = \left(1 + \frac{\lambda}{P_a}\right) \tag{8.15}$$

where λ is a saturation dependent parameter [259] $\lambda = 3.37 - 0.036S$ [atm] and P_a denotes the mean pressure ($P_a = (P_{in} + P_{out})/2$) [atm]. P_g and P_l denote the pressure of gaseous phase and pore solution, respectively. The gas pressure is assumed to be equal to the CO_2 gas pressure because the model is developed for carbonation studies under pure CO_2 at high pressure. The relationship between P_g and P_l is established through the capillary pressure, P_{cap} [Pa]:

$$P_{cap} = P_g - P_l \approx P - P_l \tag{8.16}$$

where the capillary pressure is related to saturation degree. Recently, Zhou [260] proposed the following model which is applicable for cement-based materials:

$$P_{cap} = \frac{1}{\kappa_1} \ln\left(\frac{\kappa_2 - 1 + S^{-1}}{\kappa_2}\right) g\gamma_w \tag{8.17}$$

κ_1 [1/m] and κ_2 [-] are fitting parameters; g [m/s^2] is gravitational acceleration; γ_w is unit weight of water [kg/m^3]. This assumption allows deriving the pressure gradient of the aqueous phase as:

$$\frac{\partial P_l}{\partial x} = \frac{\partial P}{\partial x} + \frac{g\gamma_w}{\kappa_1 S(\kappa_2 S - S + 1)} \frac{\partial S}{\partial x} \tag{8.18}$$

The pressure distribution inside the concrete sample depends on porosity, tortuosity, saturation level and applied pressure gradient. Therefore, the slope of pressure decrease in the carbonated zone should be steeper than in uncarbonated zone. To the knowledge of the author, this complicated relationship has not been established in literature. However, the gas pressure gradient can be linked to the concentration gradient of dissolved CO_2 by recalling Henry's law:

$$\frac{\partial P_g}{\partial x} = \frac{\partial P}{\partial x} = \frac{K_H}{M_{CO_2}} \frac{\partial c_l}{\partial x} \tag{8.19}$$

Equations (8.16) to (8.19) are only valid for unsaturated media. When part of the sample (from 0 to distance x) becomes saturated during carbonation, P_g equals zero and

$$\frac{\partial P_l}{\partial x} = \frac{P_{in} - P_{out}}{x} \tag{8.20}$$

where P_{in} and P_{out} are applied pressure at inlet and outlet, respectively [Pa]. In porous media, the effective diffusion coefficient generally depends on pore structure characteristics as follows:

$$D_{g/l} = \frac{\delta}{\tau^2}\phi D_{g0/l0} \tag{8.21}$$

where $D_{g0/l0}$ denotes the diffusivity of CO_2 in the air/water; τ accounts for the effects of tortuosity on diffusion which is not well defined in concrete materials as mentioned above. The tortuosity may be related to porosity by applying Millington-Quirk model [261], which is originally developed for sand, not for concrete [255, 262]. However, it seems that using Millington-Quirk model results in an overestimate of one order of magnitude in diffusion coefficient (based on the comparison of Millington-Quirk model and experimental data of [77]). In this study, the author uses the empirical formula proposed by Papadakis [77] to calculate the diffusivity of gaseous CO_2:

$$D_g = D_0\phi^{1.8}\left(1-RH\right)^{2.2} \tag{8.22}$$

where D_0 is suggested to be 1.64×10^{-6} [m^2/s]. The effective diffusivity calculated in Equation (8.22) is actually applied for large pores (molecular diffusion). However, in carbonated/carbonating material, of which the pore size range is shifted to smaller size, Knudsen diffusion should be considered together with molecular diffusion. In this case, the (bulk) effective diffusivity is smaller as reported by Houst [263]. In a simplified approach, the author takes into account this effect by changing D_0 to $10^{-d_c}D_0$, and $\phi^{1.8}$ to $\phi^{1.8+k_1 d_c}$, where d_c is the carbonation degree; and k_1 is in range 0.5 – 1. The value of k_1 may be determined if the gas diffusivity of carbonated cement paste is known (d_c = 1 for carbonated materials). For dissolved CO_2, the author accounts for the effects of porosity, tortuosity, and saturation degree as the proposed following equation to estimate effective diffusivity of dissolved CO_2:

$$D_l = D_{l0}\times k_D(\phi,\tau)\times k_D(S) \tag{8.23}$$

where $k_D(\phi,\tau)$ [-] (also known as relative diffusivity) accounts for the contributions of porosity and tortuosity. This relation was proposed Garboczi and Bentz based on image analysis in which the capillary porosity, ϕ_c, is the only factor captured in $k_D(\phi,\tau)$ [55].

$$k_D(\phi,\tau) = 0.001 + 0.07\phi_c^{\,2} + 1.8H(\phi_c - 0.18)(\phi_c - 0.18)^2 \tag{8.24}$$

where and H(ψ) is the Heaviside function (H(ψ) equals one if ψ is larger than one; and zero otherwise). $k_D(S)$ [-] accounts for the effect of saturation degree [264]:

$$k_D(S) = \frac{1}{1+625(1-S)^4} \tag{8.25}$$

Equation (8.24) was originally developed for sound materials. As carbonation proceeded, the precipitation of calcium carbonate does not only reduce the porosity but also increase the tortuosity. Therefore, with the same porosity drop, the reduction of diffusivity is expected to be faster for carbonation compared to hydration as presented in Figure 8.2. The relative diffusivity of carbonated zone of sample S3C is 6.45×10^{-4}, which is 70% smaller than the relative diffusivity of sound material (21.65×10^{-4}) with the sample capillary porosity (calculated from Equation (8.24)). Therefore, as a first estimation, Equation (8.24) is adapted for carbonating materials as follows:

$$k_D^*(\phi,\tau) = \left(1-0.7d_c\right)k_D(\phi,\tau) \tag{8.26}$$

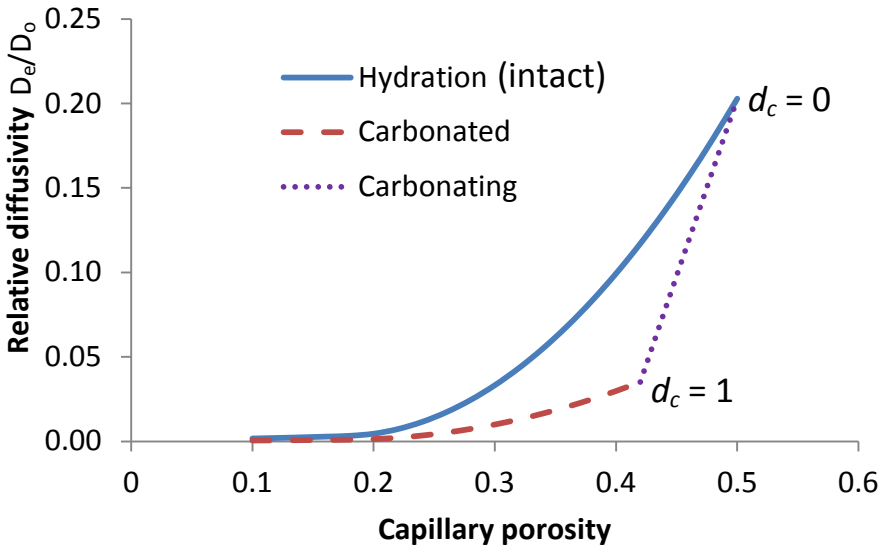

Figure 8.2. Relative diffusivity as a function of capillary porosity resulted from hydration (solid line) and carbonation (dashed line) – Dotted line represents the change of relative diffusivity as carbonation degree d_c increases from 0 to 1.

The saturation degree is related to the internal relative humidity by combining Kelvin-Laplace equation and van Genuchtens relation [198]:

$$S = \left[1+\left(-\alpha\ln(RH)\right)^{\frac{1}{1-\beta}}\right]^{-\beta} \tag{8.27}$$

where α and β are experimental fitting parameters. Equations (8.3) and (8.7) now can be rewritten as:

$$c = \left[\phi(1-S)\frac{K_H}{RT} + \phi S \right] c_l \tag{8.28}$$

$$J = -\left[\left(\frac{K_H}{RT} v_g + v_l \right) c_l + \left(\frac{K_H}{RT} D_g + D_l \right) \frac{\partial c_l}{\partial x} \right] \tag{8.29}$$

Evolution of porosity due to carbonation

The change in porosity is estimated by comparing the volume of new products (solid) produced by the carbonation of portlandite and C-S-H with the initial solid volume.

$Ca(OH)_2 + CO_2 = CaCO_3 + H_2O$

$$\Delta\phi_{CH} = \frac{\left(C_{CH0} - C_{CH}\right)}{M_{CH}} \left(V_{CH} - V_{CC}\right) \tag{8.30}$$

$y_0CaO{\bullet}SiO_2{\bullet}z_0H_2O + (y_0\text{-}y)CO_2 = yCaO{\bullet}SiO_2{\bullet}zH_2O + (y_0\text{-}y)CaCO_3 + (z_0\text{-}z)H_2O$

$$\Delta\phi_{CSH} = \frac{C_{CSH0}}{M_{CSH0}} \left[\left(y_0 - y\right) V_{CC} - \left(V_{CSH0} - V_{CSH}\right) \right] \tag{8.31}$$

where $\Delta\phi_{CH}$ and $\Delta\phi_{CSH}$ are porosity changes [-] due to portlandite and C-S-H carbonation, respectively; y and z are the average Ca/Si ratio and stoichiometric ratio of H_2O in C-S-H, respectively; C_{CH} and C_{CSH} are portlandite and C-S-H contents [kg/m^3], respectively; M_{CH} and M_{CSH} [kg/mol] are molar masses of portlandite and C-S-H, respectively; V_{CH}, V_{CC} and V_{CSH} [m^3/mol] are molar volumes of portlandite, calcite and C-S-H, respectively. Subscript 0 denotes initial condition. The molar volumes of the first 2 species are well defined in literature. However, data for molar volume of C-S-H is still scarce and it is supposed to be stoichiometry-dependent parameter. Recent experimental study [130] showed that the molar volume of C-S-H is in direct proportion to Ca/Si ratio as

$$V_{CSH0} - V_{CSH} = \omega\left(1 - y / y_0\right) \tag{8.32}$$

where $0.02 < \omega < 0.04$ [l/mol]. By comparing the porosity of carbonated and uncarbonated samples, the author finds that $\omega = 0.04$ [l/mol] gives the best fit. The total porosity of sample during carbonation is simply expressed as follows:

$$\phi = \phi_0 + \Delta\phi_{CH} + \Delta\phi_{CSH} \tag{8.33}$$

where ϕ_0 is initial total porosity which is determined experimentally or can be calculated as follows [265]:

$$\phi_0 = \frac{w/c - 0.17m}{w/c + 0.32} \tag{8.34}$$

in which *m* denotes the degree of hydration. The change in capillary porosity is mainly due to the carbonation of portlandite. However, C-S-H carbonation might partially contribute to the capillary porosity change, especially in accelerated conditions which is expressed by coefficient υ ($0 \le \upsilon \le 1$) as follows. The value of υ is set to be 0.5 in this study, which gives a good fit with capillary porosity change determined by MIP.

$$\phi_c = \phi_{c0} + \Delta\phi_{CH} + \upsilon\Delta\phi_{CSH} \tag{8.35}$$

where ϕ_{c0} is initial capillary porosity which is either determined by experiment or calculated as follows [40]:

$$\phi_{c0} = \frac{w/c - 0.36m}{w/c + 0.32} \tag{8.36}$$

Reaction kinetics

As mentioned before, the author only takes into account the carbonation of portlandite and calcium silicate hydrate. The overall processes of CH and C-S-H carbonation is described in section 3.2. Instead of separately modelling the carbonation reactions of CH and C-S-H, the author combines both reactions as a single reaction between Ca^{2+} (dissolved from CH and C-S-H) and CO_3^{2-} ions:

$$Ca^{2+}(total) + CO_3^{2-} \rightarrow CaCO_3 \tag{8.37}$$

The author considers that the reaction (8.37) is of the first order with respect to Ca^{2+} and CO_3^2. The rate of the combined carbonation reaction, *r* [mol/s.m^3], is written as follows:

$$r = -\frac{\partial[CH]}{\partial t} - \frac{\partial[C-S-H]}{\partial t} = k_C f(S) k_r \frac{C_{Ca}}{M_{Ca}} \frac{C_{CO_3}}{M_{CO_3}} \tag{8.38}$$

where k_C [m^3/mol.s] is the reaction rate coefficient, which is temperature dependent, expressed via the Arrhenius' equation:

$$k_C = \psi.\exp(-E_0/RT) \tag{8.39}$$

in which ψ is prefactor [m^3/mol.s] and E_0 is activation energy [J/mol]. C_{Ca} and C_{CO_3} [kg/m^3] are total concentration of Ca^{2+} in solution and concentration of CO_3^{2-}, respectively. M_{Ca} and M_{CO3} [kg/mol] are molar masses of Ca^{2+} and CO_3^{2-}, respectively. The concentration of CO_3^{2-} can be related to the concentration of dissolved CO_2 by considering the equilibrium of CO_2 in solution as shown later in Equation (8.52).

The factor *f(S)* is introduced in Equation (8.38) (following the approach of Papadakis [116]) in order to account for the effect of saturation degree on the carbonation reaction rate. The function is introduced because of the fact that kinetic carbonation reaction rate coefficient is established in the bulk aqueous solution instead of within the two phase medium of the concrete pore network.

$$f(S) = S^n \tag{8.40}$$

where parameter *n* is suggested to be 3.7 [116]. The carbonation products are mainly formed surrounding CH/C-S-H which will reduce the reaction rate because CO_2 has to diffuse through the product layer. Therefore, a retardant factor is added into Equation (8.38) as follows:

$$k_r = \left(\frac{C_{Ca}^s}{C_{Ca0}^s} \right)^2 \tag{8.41}$$

where C_{Ca}^s [mol/m^3] is total concentration of solid Ca except for Ca in calcium carbonate, subscript 0 denotes the initial concentration. The sink term in Equation (8.2) can be now expanded as:

$$Q_{CO_2} = Q_{CH} + Q_{C-S-H} = -\phi r M_{CO_2} = -f(S)\phi k_C k_r \frac{C_{Ca}}{M_{Ca}} \frac{C_{CO_3}}{M_{CO_3}} M_{CO_2} \tag{8.42}$$

Mass balance of aqueous CO_2

By substituting Equations (8.28), (8.29) and (8.42) into Equation (8.2), the author obtains the following expression of the mass balance of dissolved CO_2:

$$\frac{\partial\left(\left[\phi(1-S)\frac{K_{CO_2}^H}{RT}+\phi S\right]c_l\right)}{\partial t}-\frac{\partial\left(\left[\frac{K_{CO_2}^H}{RT}v_g+v_l\right]c_l\right)}{\partial x}$$
$$-\frac{\partial\left(\left[\frac{K_{CO_2}^H}{RT}D_g+D_l\right]\frac{\partial c_l}{\partial x}\right)}{\partial x}=-f(S)\phi k_C k_r\frac{C_{Ca}}{M_{Ca}}\frac{C_{CO_3}}{M_{CO_3}}M_{CO_2} \tag{8.43}$$

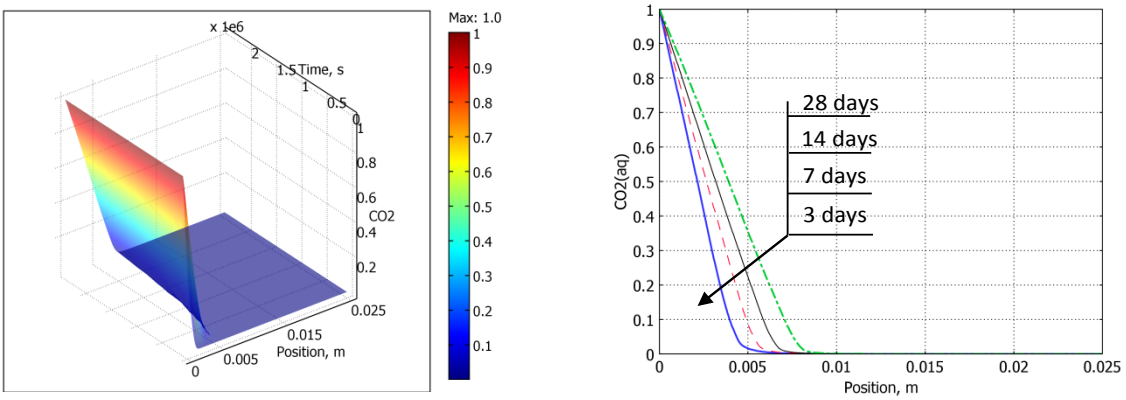

Figure 8.3. Distribution of normalized aqueous CO_2 concentration over space and experimental time: applied pressure of 6 bar pure CO_2, cement paste with w/c of 0.6, RH of 65% and sample thickness of 25 mm.

The partial differential Equation (8.43) describes the one-dimensional reaction-transport phenomenon in cement-based materials. Each term in Equation (8.43) corresponds to a different mechanism. The first term on the left hand side describes the exchange rate of CO_2 concentration in aqueous phase. The second term is called the advection term and obeys Darcy's law. The last term involves the diffusion, following Fick's law. The right hand side of Equation (8.43) is responsible for chemical reaction of CO_2 in which the total concentration of Ca^{2+} is determined by solving a separate reaction-transport equation of Ca^{2+} (Section 8.1.2.2). The initial and boundary conditions are:

$$\begin{cases} c_l(x,0)=c_{l0} & x\geq 0 \\ c_l(0,t)=c_l^{in} & t>0 \\ c_l(L,t)=c_l^{out} & t>0 \end{cases} \tag{8.44}$$

where c_l^{in} and c_l^{out} are the concentration of dissolved CO_2 at inlet and outlet, respectively; c_{l0} are the initial concentration of dissolved CO_2; L is the length of the sample [m]; x is space

direction [m] and t is time [s]. The problem is numerically solved by using the COMSOL Multiphysics program. The typical profile of aqueous CO_2 concentration is shown in Figure 8.3.

8.1.2.2. Mass conservation of calcium ion

In the same way as CO_2, the mass balance equation for total Ca^{2+} is given as:

$$\frac{\partial(\phi S C_{Ca})}{\partial t} - \frac{\partial(v_l C_{Ca})}{\partial x} - \frac{\partial\left(D_{Ca}\frac{\partial C_{Ca}}{\partial x}\right)}{\partial x} = -\phi r \frac{M_{Ca}}{M_{CO_2}} + r_d \tag{8.45}$$

where D_{Ca} [m^2/s] is the effective diffusivity of calcium ion in the porous media (cement/concrete) which is determined using Equation (8.23); r_d is the dissolution rate of CH and C-S-H [kg/m^3.s] which is calculated from the mass balance equation of total amount of Ca in solid CH and C-S-H as follows:

$$\frac{\partial C_{Ca}^s}{\partial t} M_{Ca} = -r_d \tag{8.46}$$

Note that in Equation (8.46) the releasing rate of Ca due to hydration is diminished. In order to establish a relation between concentration of calcium ion in solution and concentration of Ca in solid phases, the author proposes a solid-liquid equilibrium curve of Ca based on the experimental data collected by Berner [266] as shown in Figure 8.4 and mathematically expressed in Equation (8.47). The author assumes that there is a discretization of the decalcification of CH and C–S–H. The region AB corresponds to the fast portlandite dissolution. When CH is completely dissolved (point B), C-S-H starts progressively dissolving down to point C which is the starting point of a quicker decalcification of C-S-H to form silica gel.

$$C_{Ca}^s = \begin{cases} \frac{d}{a} C_{Ca} & C_{Ca} \le a \\ d + \frac{e-d}{b-a}(C_{Ca} - a) & a < C_{Ca} \le b \\ e + \frac{f-e}{c-b}(C_{Ca} - b) & b < C_{Ca} \le c \end{cases} \tag{8.47}$$

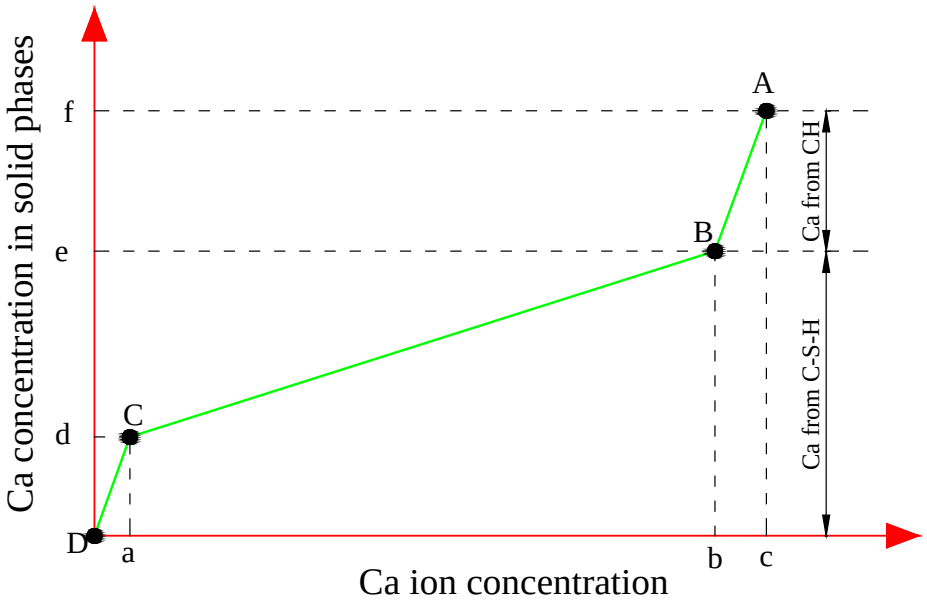

Figure 8.4. Solid-liquid equilibrium curve of calcium

The values of a, b and c are well-defined in literature. Therefore, the author uses fixed values: a = 2 [mol/m^3], b = 19 [mol/m^3] and c = 22 [mol/m^3] for numerical modelling. The Ca fraction in CH and C-S-H can be estimated from the hydration of minerals (C_2S, C_3S) in cement which can be estimated by the Bouge calculation. Whereas the critical value d where C-S-H starts sharply decalcifying is determined by multiplying the amount of SiO_2 in C-S-H with the Ca/Si ratio at point C which is around 0.85 [266].

By substituting Equations (8.46) and (8.47) to partially differential (8.45), with initial and boundary (Neumann) conditions (8.48) it is possible to determine the concentration of calcium in solution which is needed for the sink term of Equation (8.43).

$$\begin{cases} C_{Ca}(x,0) = c & x \geq 0 \\ \dfrac{\partial C_{Ca}(0,t)}{\partial x} = 0 & t > 0 \\ \dfrac{\partial C_{Ca}(L,t)}{\partial x} = 0 & t > 0 \end{cases} \tag{8.48}$$

8.1.3. Derivation of auxiliary variables

8.1.3.1. Carbonation degree definition and pH evolution

The term "carbonation depth" is commonly used to quantify the carbonation of concrete. It is experimentally determined by the de-colouring of phenolphthalein indicator in carbonated zone as presented in Section 6.1. The question is how to mathematically define the carbonation depth? Most available definitions of carbonation depth are based on the amount of calcite released [267] or portlandite consumed [268, 269] during carbonation process. While Peter *et al*. [268] defined the carbonation front position at the point where 90% of total portlandite is consumed; Park *et al*. [269], on the other hand, proposed a ratio of 50%. These assumptions are somehow unclear and need to be checked by the experiments. In the present study, the author combines the carbonation reaction of CH and C-S-H. Therefore, it is logical to relate the carbonation depth to total concentration of Ca in the solid phases. Here the author defines the carbonation depth as the position at which X_{Ca} percentage of total Ca is carbonated. By comparing with carbonation depth determined by phenolphthalein, it is found that X_{Ca} is roughly 20%. The carbonation degree, d_c, is then formulated as:

$$d_c = \begin{cases} 1 & C_{Ca}^s < X_{Ca} f \\ \dfrac{f - C_{Ca}^s}{(1 - X_{Ca}/100) f} & C_{Ca}^s \geq X_{Ca} f \end{cases} \tag{8.49}$$

In order to estimate the pH, the author simply calculates hydroxyl concentration in pore solution. With consideration that $Ca(OH)_2$ is a strong base, the ionization reaction of $Ca(OH)_2$ is given as:

$$Ca(OH)_2(aq) \leftrightarrow Ca^{2+} + 2OH^- \tag{8.50}$$

The hydroxyl concentration [mol/m^3] is double the concentration of Ca ion: [OH] = $2C_{Ca}$. Note that in this estimation the contributions of other alkalis (NaOH, KOH, etc.) are not included because of their low amount. The pH is modelled as follows:

$$pH = -\log(k_w \gamma_H/(2C_{Ca*})) = 14 + \log(2C_{Ca*}/\gamma_H) \tag{8.51}$$

where γ_H [-] is the activity coefficient of H^+ which is computed using Davies equation [270]; k_w is the dissociation constant of water, $k_w = 10^{-14}$ at 25^{o}C; and C_{Ca*} is the concentration of Ca in unit [mol/l].

Table 8.1. Equilibrium of CO_2 in pore solution

No.	Equilibrium
1.	$CO_2(g) \leftrightarrow CO_2(aq)$
2.	$CO_2(aq) + H_2O \leftrightarrow H_2CO_3$
3.	$H_2CO_3 \leftrightarrow HCO_3^- + H^+$
4.	$HCO_3^- \leftrightarrow CO_3^{2-} + H^+$

When considering the dissolution of CO_2 in water, attention must be paid to the second reaction in Table 8.1. There is only a small amount of dissolved CO_2 converted to carbonic acid (H_2CO_3) which is quantified by hydration equilibrium constant, K_{Hyd}, whereas the majority of dissolved CO_2 remains as solvated molecular CO_2. Therefore, almost all carbonic acid dissociation constants reported in literature are apparent dissociation constants, in which carbonic acid is defined as a mixture of H_2CO_3 and solvated CO_2:

$$K_a = \frac{[H^+][HCO_3^-]}{[CO_{2(aq)}]} = \frac{[H^+][HCO_3^-]}{[H_2CO_3]+[CO_{2(sol)}]} \tag{8.52}$$

The mass action law for the dissociation of HCO_3^- is:

$$K_b = \frac{[H^+][CO_3^{2-}]}{[HCO_3^-]} \tag{8.53}$$

where K_a, K_b are the temperature-dependent equilibrium constants of carbonic acid and bicarbonate, respectively. The total dissolved CO_2 in pore solution is derived from mass balance law:

$$[CO_{2(total)}] \equiv c_l = [CO_3^{2-}] + [HCO_3^-] + [H_2CO_3] + [CO_{2(sol)}] \tag{8.54}$$

It is worth noting that in the equilibrium of CO_2, Henry's law is not applied to calculate the total concentration of dissolved CO_2 but for the concentration of solvated molecular CO_2 which is in equilibrium with CO_2 gaseous phase. However, because the hydration equilibrium constant is very small ($K_{hyd} = 1.7\times10^{-3}$ at 25°C), Henry's law can be applied for total dissolved CO_2 with a good approximation. Substituting Equations (8.52) and (8.53) to Equation (8.54),

it enables to determine the concentrations of HCO_3^-, CO_3^{2-} and $CO_{2(aq)}$ species in pore solution:

$$\begin{aligned}
[HCO_3^-] &= \frac{K_a[H^+]}{[H^+]^2 + K_a[H^+] + K_aK_b} c_l \\
[CO_3^{2-}] &= \frac{K_aK_b}{[H^+]^2 + K_a[H^+] + K_aK_b} c_l \\
[CO_{2(aq)}] &= \frac{[H^+]^2}{[H^+]^2 + K_a[H^+] + K_aK_b} c_l
\end{aligned} \tag{8.55}$$

8.1.3.2. Portlandite content

It is evidenced from experiments (see Section 6.3.2) that in carbonated zone, there remains still up to 20% of portlandite. Therefore, in combination with Equation (8.47), the portlandite content, C_{CH} [mol/m^3] can be defined if the total amount of Ca in solid phases is known:

$$\begin{cases}
C_{CH} = \dfrac{0.2C_{Ca}^s}{e} & C_{Ca}^s \le e \\
C_{CH} = \dfrac{C_{Ca}^s - e}{f - e} + 0.2\dfrac{f - C_{Ca}^s}{f - e} & C_{Ca}^s > e
\end{cases} \tag{8.56}$$

8.1.3.3. CO_2 uptake

One of the new points of this model is that it can simulate the total CO_2 uptake due to the carbonation reactions of portlandite and C-S-H. Considering Equation (8.37), the number of moles of solid Ca consumed equals the number of moles of CO_2 uptake. Therefore, the CO_2 uptake (normalized to cement content in sample) due to carbonation can be expressed as:

$$Uptake_{CO_2} = \int_0^L \frac{\left[\left(f - C_{Ca}^s\right) + \left(C_{Ca}^0\phi_0 - C_{Ca}\phi\right)\right] M_{CO_2} F dx}{cem} 100\% \tag{8.57}$$

where $Uptake_{CO_2}$ is the CO_2 uptake with respect to cement mass in the sample [%]; F is the cross section of the sample [m^2]; m_{sam} is the mass of sample [kg]. The first and second groups in the numerator correspond to changes of Ca in solid and aqueous phase, respectively. A typical result of mass gain is shown in Figure 8.5. The CO_2 uptake dramatically increases at the beginning of carbonation. The uptake rate is then getting lower and almost stable after 5 years of carbonation. This can be explained because of the increase of RH, the decrease of porosity and the reduction of available Ca for carbonation over time.

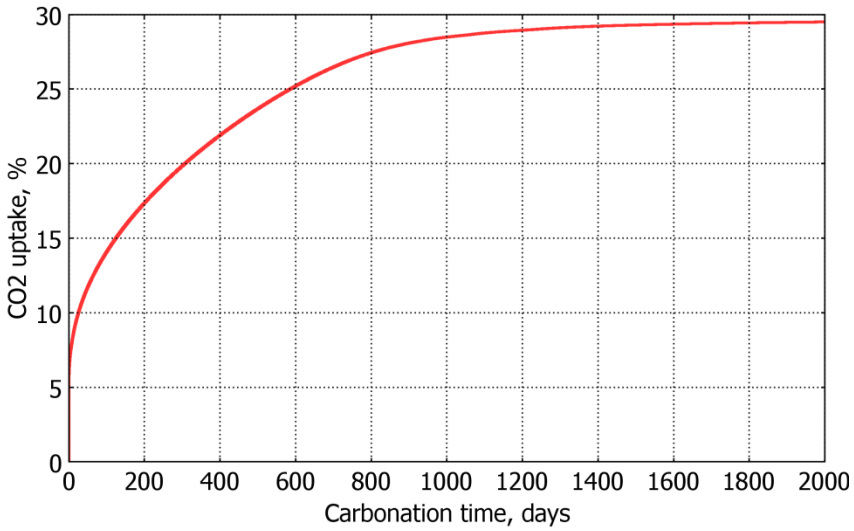

Figure 8.5. Simulation of CO_2 uptake (%) up to 2000 days of carbonation: applied pressure of 6 bar pure CO_2, cement paste with w/c of 0.6, RH of 65% and sample thickness of 25 mm.

8.1.3.4. Evolution of saturation degree during carbonation

As mentioned, the carbonation reactions release water. Therefore, the saturation degree (thereby RH) will change during carbonation. This change can be estimated based on the reactions of CH and C-S-H with CO_2 shown in Equations (8.30) and (8.31). The calculation of released water for CH carbonation is straightforward, i.e. 1 mol of Ca in CH will release 1 mol of H_2O. However, for C-S-H carbonation y mol of Ca in C-S-H will release z mol H_2O. The stoichiometry values of y and z are only slightly different [271]. Therefore, the author assumes that ratio y/z = 1. With this assumption, it is possible to calculate the amount of released water, m_{wr} [kg], based on the change of total Ca in solid phase.

$$m_{wr} = \left(f - C_{Ca}^{s} \right) M_w F dx \tag{8.58}$$

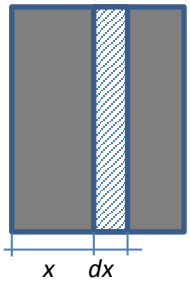

Figure 8.6. Schematic domain *Fdx* for calculation of saturation degree during carbonation

where M_w is molar weight of water [kg/mol], F denotes surface area of sample [m^2]. The total water in domain Fdx (Figure 8.6) can be computed as follows:

$$m_w = \left(f - C_{Ca}^s \right) M_w F dx + S_0 \phi_0 \gamma_w F dx \tag{8.59}$$

The second term in the above equation corresponds to initial water in the sample. Finally, the saturation degree can be calculated as:

$$S = \frac{V_w}{V_p} = \frac{\left(f - C_{Ca}^s \right) M_w / \gamma_w F dx + S_0 \phi_0 F dx}{\phi F dx} = \frac{\left(f - C_{Ca}^s \right) M_w / \gamma_w + S_0 \phi_0}{\phi} \tag{8.60}$$

where V_w and V_p [m^3] are volumes of water and pore in domain Fdx, respectively.

8.1.3.5. Changes in permeability and diffusivity under saturated condition

The permeability of carbonating material varies along the depth of sample. In order to calculate the composite (or overall) permeability coefficient of the sample, the sample depth is divided into small layer Δl. The permeability of each layer is assumed to be constant. The series model introduced in Section 6.6 is recalled. The fluxes in each layer and the overall flux must be the same because each layer is connected together in series.

$$J_1 = J_2 = ... = J_n = \frac{k_n}{\eta} \frac{\Delta p_n}{\Delta x} = \frac{k_{com}}{\eta} \frac{P}{L} \tag{8.61}$$

where J_n, k_n, Δx and Δp_n denote the flux, intrinsic permeability, thickness and pressure gradient of layer n, respectively; k_{com} denotes the composite intrinsic permeability coefficient of the sample. Additionally, the total pressure drop on each layer must be equal to gradient pressure applied on the sample:

$$\sum_{i=1}^{n} \Delta p_i = P \tag{8.62}$$

Therefore, the overall permeability coefficient can be derived as:

$$k_{com} = \frac{L}{\sum_{i=1}^{n} \frac{\Delta x}{k_i}} \approx \frac{L}{\int_0^L \frac{dx}{k(x)}} \tag{8.63}$$

where $k(\phi, x)$ is intrinsic permeability at distance x and can be estimated by Equation (8.8). Note that k(S) in Equation (8.8) now becomes unit because the permeability of saturated materials is being predicted and the effect of porosity on permeability is not expressed in

Equations (8.61) and (8.63) for a simplified expression (i.e. k_i instead of $k_i(\phi)$). With the same approach, the composite diffusivity, D_{com} [m^2/s], of carbonated materials is written as:

$$D_{com} = \frac{L}{\sum_{i=1}^{n} \frac{\Delta x}{D_i}} \approx \frac{L}{\int_0^L \frac{dx}{D(x)}} \tag{8.64}$$

where $D(x)$ [m^2/s] is effective diffusion coefficient at distance x and can be estimated by Equation (8.23).

8.1.4. Significant contribution of advection in accelerated carbonation

In order to study the contribution of advection to the carbonation process, the author did simulations considering different values of permeability and applied pressure. Figure 8.7 shows the profile of CO_2 dissolved in pore solution with and without contribution of advection term. It can be seen that dissolved CO_2 concentration is higher when considering advection, which results in a difference in porosity reduction as shown in Figure 8.7b. Despite the same porosity reduction in the first layer contacted directly with CO_2, the porosity reduction propagates more deeply in case of advection compared to the case without advection. The importance of advection is also more prominent for longer carbonation time. As carbonation proceeds, the saturation is increasing which limits the diffusion through gaseous phase (diffusion via aqueous phases is negligible compared to via gaseous phase). However, in case of applying a gradient pressure, the transport of CO_2 is compensated by the increase of permeation via aqueous phase.

Furthermore, the contribution of advection is much more important when sample has higher permeability. In Figure 8.7b, there is a transition zone in which porosity exhibits a nearly linear drop. If the experiment is long enough, the sample can be divided into 3 zones: well-carbonated and uncarbonated zone in which porosity is slightly changed, and partly-carbonated (transition) zone with a significant porosity drop. The transition zone is widened when permeability increases.

Advection highly affects the carbonation process and depends on the applied pressure as shown in Figure 8.8 and Figure 8.9. The pressure is increased from 2 bar to 6 bar, whereas other parameters are kept unchanged. The figures clearly show that higher pressure gradient helps dissolved CO_2 to quickly distribute in the sample which promotes the carbonation process. As a result, porosity (Figure 8.8b) and total calcium in CH and C-S-H (Figure 8.9a) are decreased faster. The 3 zones of carbonation are well defined in case of high applied

pressure. At a 2 bar applied pressure after 28 days of carbonation, the well-carbonated zone (defined as carbonation degree d_c = 1) increases from 3 to 7.7 mm when considering advection, whereas the increase is much higher at 6 bar applied pressure, from 4.3 to 14.7 mm, as illustrated in Figure 8.9b.

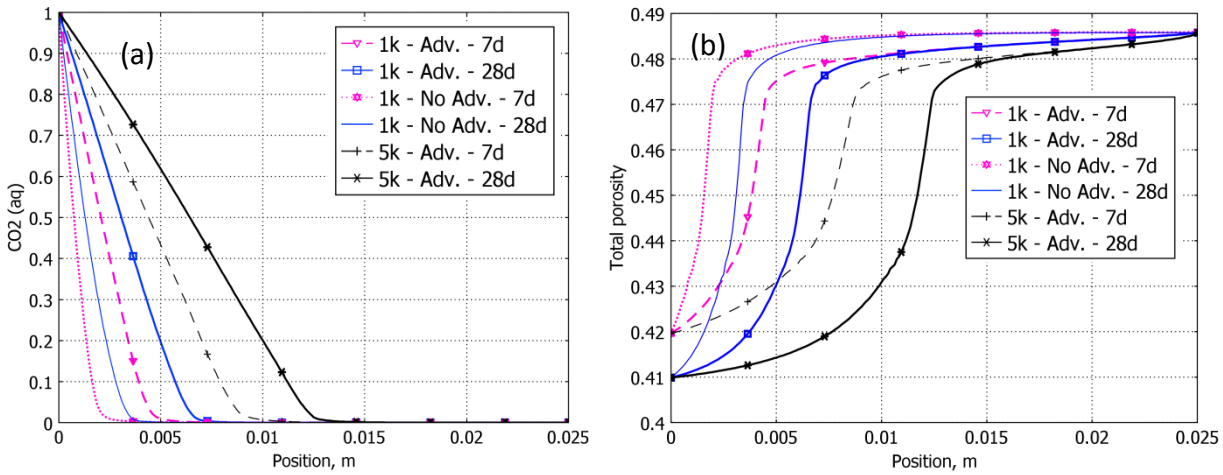

Figure 8.7. Contribution of advection to (normalized) dissolved CO_2 concentration (a) and porosity change (b): applied pressure of 6 bar pure CO_2, cement paste with w/c of 0.6, RH of 65% and sample thickness of 25 mm; simulations with gas permeability 20×10^{-19} m^2, water permeability 1×10^{-19} m^2 (1k) and gas permeability 1×10^{-17} m^2, water permeability 5×10^{-19} m^2 (5k) with (Adv.) and without advection effect (No Adv.) at 7 days (7d) and 28 days (28d).

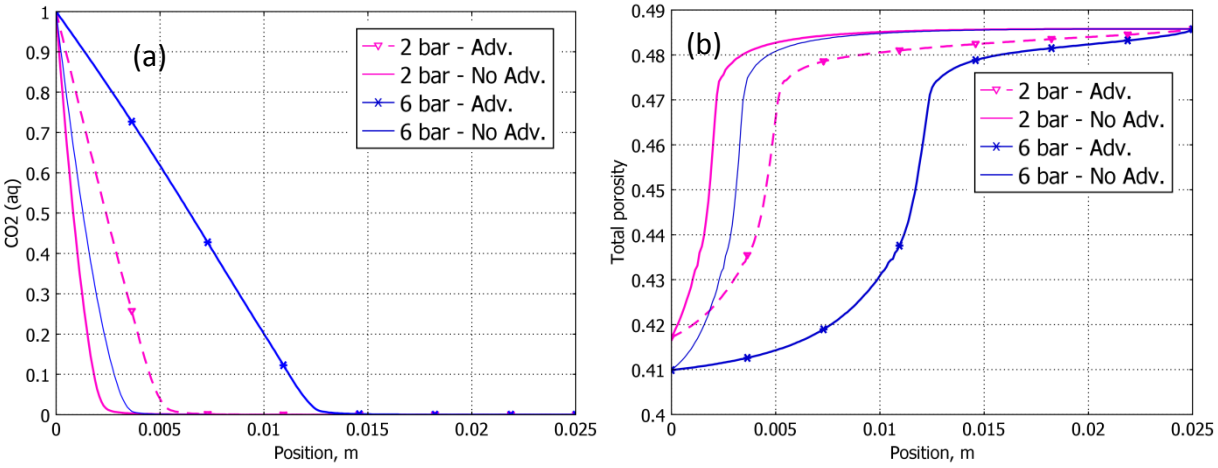

Figure 8.8. Contribution of advection to (normalized) dissolved CO_2 concentration (a) and porosity change (b) under different applied pressure: cement paste with w/c of 0.6, RH of 65% and sample thickness of 25 mm; simulations in 28 days with 2 bar and 6 bar applied pressure with (Adv.) and without advection effect (No Adv.).

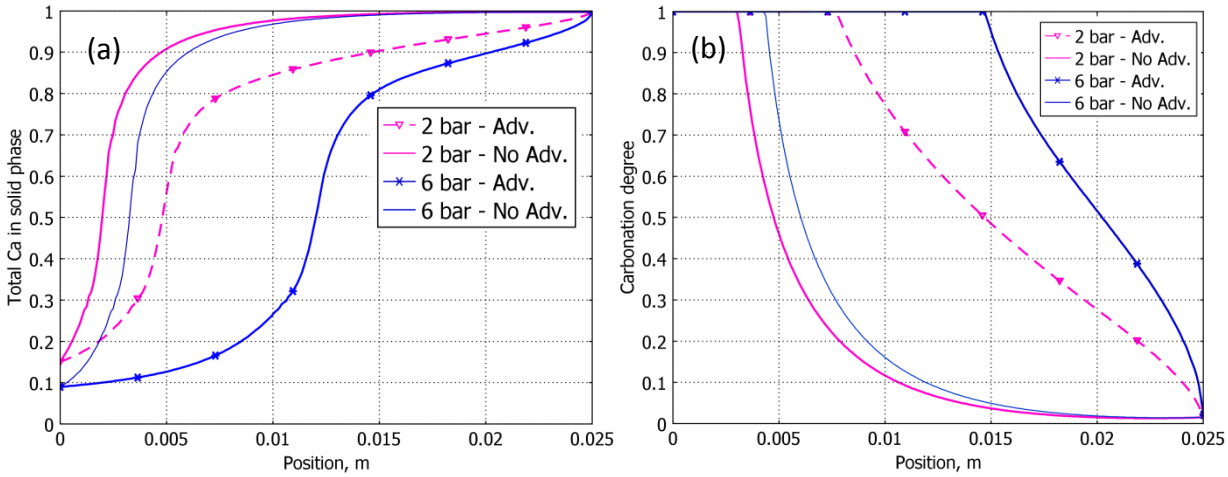

Figure 8.9. Contribution of advection to total (normalized) calcium concentration in solid phases (a) and degree of carbonation (b) under different applied pressure: cement paste with w/c of 0.6, RH of 65% and sample thickness of 25 mm; simulations in 28 days with 2 bar and 6 bar applied pressure with (Adv.) and without advection effect (No Adv.).

8.1.5. Modelling results and verifications

The model has been initially developed for OPC cement paste (without limestone filler addition). However, this section will compare modelling and experimental results for a sample without limestone filler (S3) and sample with 10% limestone filler replacement (S4). The dilution effect is taken into account for sample S4 by converting w/p ratio to w/c ratio in the simulation. However, the other effects (e.g. chemical interaction, ITZ effect) are not included at this stage. All parameters used for simulations are listed in the Appendix 1.

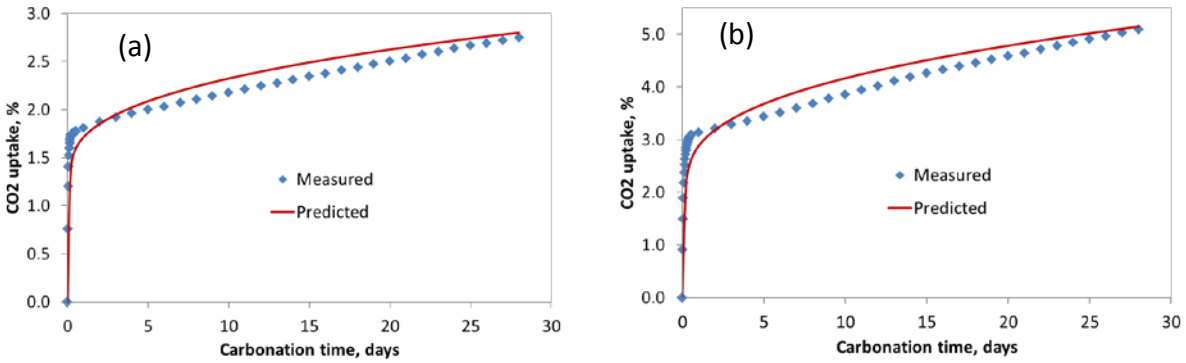

Figure 8.10. Comparison of predicted CO_2 uptakes of samples S3C (a) and S4C (b) with CO_2 uptakes obtained mass flow meters

Figure 8.10 compares the predicted CO_2 uptakes with the measurements. Except for a slight difference at the transition between initial and residual stages, the predicted CO_2 uptakes are in good agreement with the measured ones for both samples S3C and S4C. In the initial stage, CO_2 uptake rapidly increases but the uptake rate is significantly decreased in the residual stage because of porosity decrease and saturation degree increase.

Figure 8.11 shows the increase of internal relative humidity and saturation degree of sample due to carbonation. The relative humidity (and saturation degree) is significantly increased in the layer in contact with pure CO_2, from an initial RH of 65% to more than 90% for sample S3C after 12-week carbonation. The high RH prevents CO_2 transport which results in a significant drop of CO_2 uptake rate as seen in Figure 8.10. The increase of RH at the surface in contact with CO_2 for sample S4C is lower than for sample S3C which contributes to the higher CO_2 uptake of sample S4C compared to S3C.

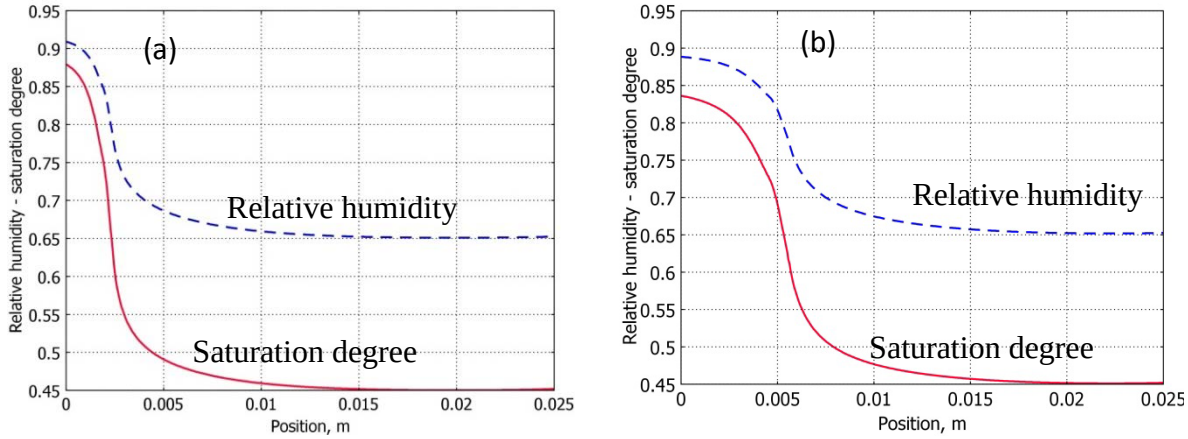

Figure 8.11. Simulation of increase of relative humidity and saturation degree of samples S3C (a) and S4C (b) after 12-week carbonation

The portlandite and total solid Ca (CH + C-S-H) profiles at different carbonation time are shown in Figure 8.12. The longer the experimental time, the higher the portlandite and total Ca content are decreased, but the difference among 4-week, 8-week and 12-week carbonation is not significant. It can be seen that under an applied pressure gradient, the carbonation front is not sharp as the portlandite and Ca content is gradually increased in the transition zone. This is in line with the observation of gradual front determined by phenolphthalein spraying. The transition zone is longer for sample S4C compared to S3C (without limestone filler). The portlandite content is still slightly decreased beyond the carbonation front. Figure 8.13 shows the comparison of predicted portlandite profiles with the ones obtained by TGA

measurements on the powder. The predicted values are in line with the measured ones, especially for sample S3C. The measured portlandite content of S4C at the downstream (not in contact with pure CO_2) is relatively smaller than the predicted value. The difference is attributed to the atmospheric carbonation which could occur during sample preparation for carbonation test or/and TGA measurements.

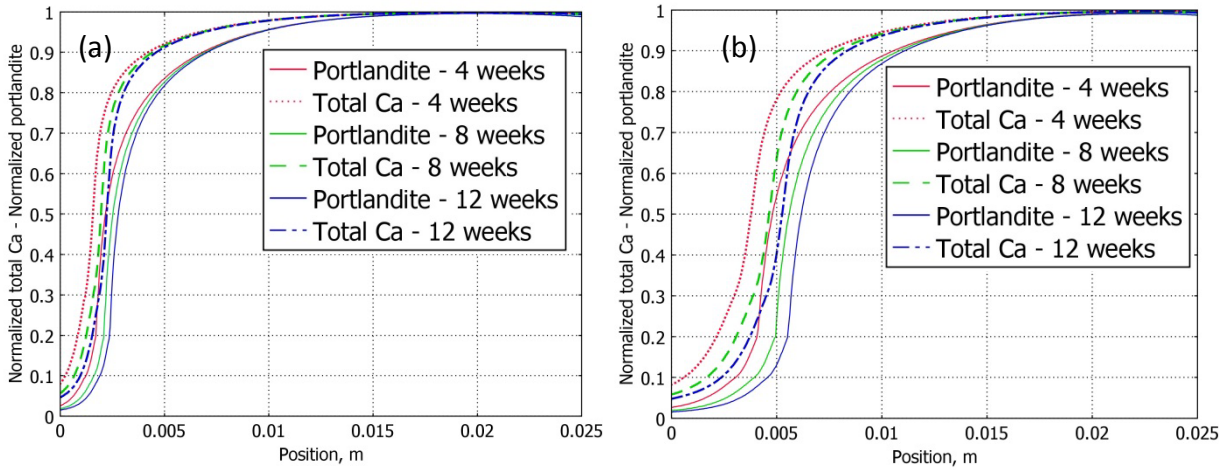

Figure 8.12. Simulated portlandite and solid Ca (in CH and C-S-H) profiles of samples S3C (a) and S4C (b) at different carbonation time

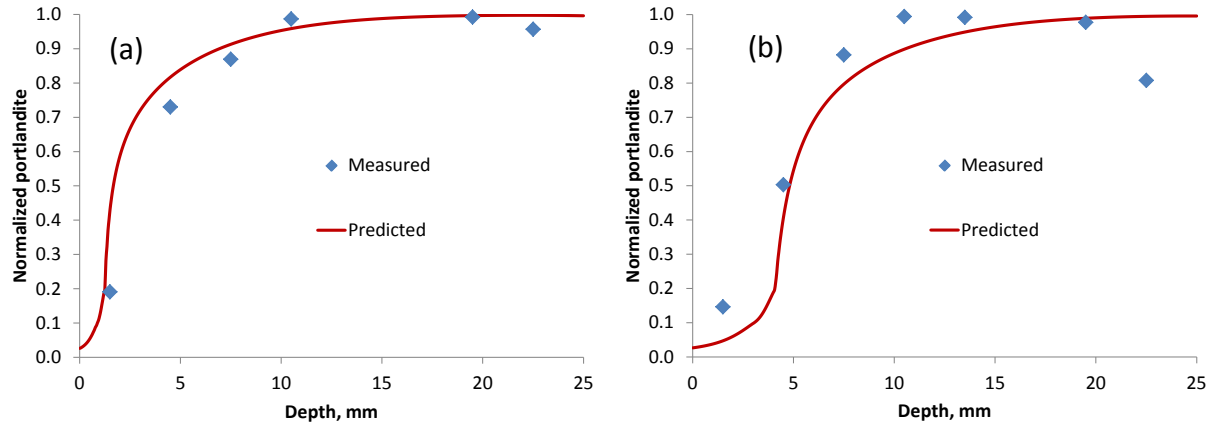

Figure 8.13. Comparison of predicted portlandite profiles of samples S3C (a) and S4C (b) with portlandite profiles obtained by TGA after 28-day carbonation

The capillary and total porosities relatively decrease due to carbonation as shown in Figure 8.14. The decrease in total porosity can mainly be attributed to the portlandite carbonation. However, in well-carbonated zone (near reacted surface), C-S-H carbonation may contribute up to 45% of total porosity reduction. The effect of C-S-H carbonation on porosity decrease is

higher for sample without limestone filler S3C compared to sample with limestone filler S4C. This confirms the hypothesis that limestone filler can play as a nucleation site for calcite precipitation which favours the portlandite carbonation. The average capillary porosity change, determined by MIP up to a depth of 3 mm from the exposed surface, compares well with the predicted capillary porosity change for sample S3C. However, the measured porosity change (2.4%) is smaller than the predicted one (4.4%) for sample S4C.

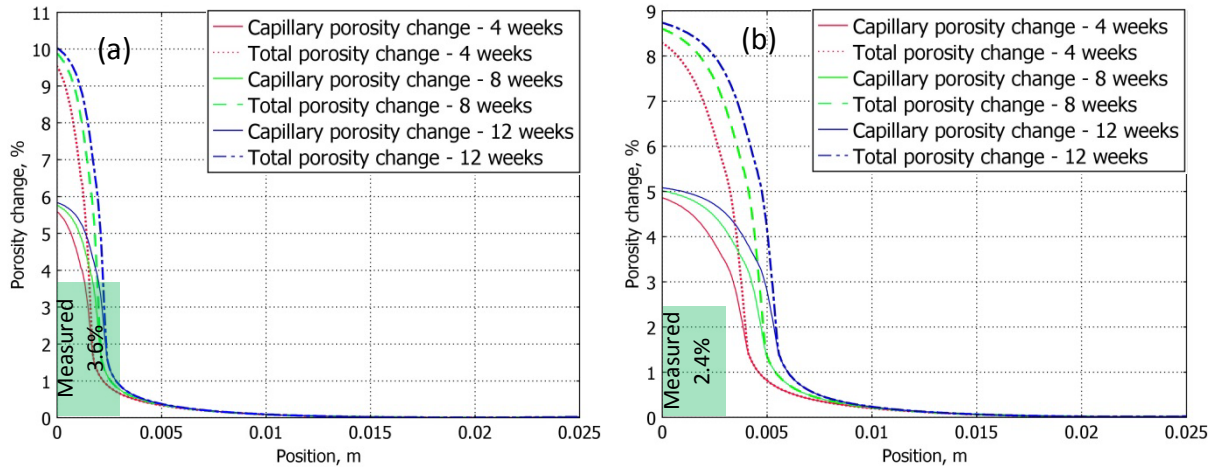

Figure 8.14. Reduction of capillary and total porosity of samples S3C (a) and S4C (b) at different carbonation time – measured capillary porosity is determined by MIP down to the pore sizes of 7 nm.

Permeability of carbonated zone significantly decreases as shown in Figure 8.15. After 4-week carbonation, the alteration in permeability is not significant when carbonation proceeds further. The permeability coefficient decreases 2 orders of magnitude in the zone near the exposed surface for sample S3C. Sample S4C shows a slower decrease in permeability, but the altered zone is deeper than sample S3C. The average predicted permeability of carbonated zone is 5.7×10^{-22} m^2 and 9.7×10^{-22} m^2 for samples S3C and S4C, respectively. These values are a bit higher than those estimated from experimental results for samples S3C (4.5×10^{-22} m^2) and S4C (6.9×10^{-22} m^2). The difference is attributed to the change of permeability in transition zone which is not captured in the estimation from experimental results.

The composite permeability is dominated by the permeability of the carbonated zone despite its limited depth compared to the sample length. Therefore, a significant decrease in composite permeability is also observed as presented in Figure 8.16. The composite

permeability rapidly decreases in the first few days of carbonation. The composite permeability is then slightly reduced as carbonation proceeds. The drop of composite permeability of sample S3C is more pronounced than sample S4C (with limestone filler). After 28-day carbonation, the predicted composite permeability of sample S4C is 4.6×10^{-21} m^2 which is pretty comparable with the measurement (4.8×10^{-21} m^2). However, the comparison between predicted and measure values of sample S3C is less satisfactory (i.e. 2.5×10^{-21} m^2 compared to 3.6×10^{-21} m^2). The differences may be attributed to the changes in tortuosity and shape factor (in Equation (8.13)) which are not well captured in the model.

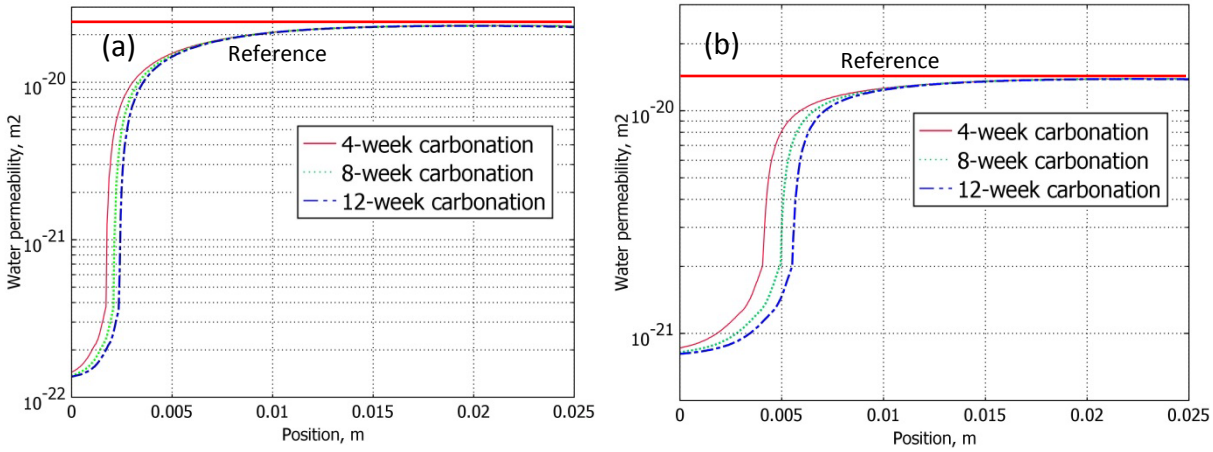

Figure 8.15. Prediction of change in intrinsic water permeability over the depth of samples S3C (a) and S4C (b) at different carbonation time – red line represents permeability of reference sample.

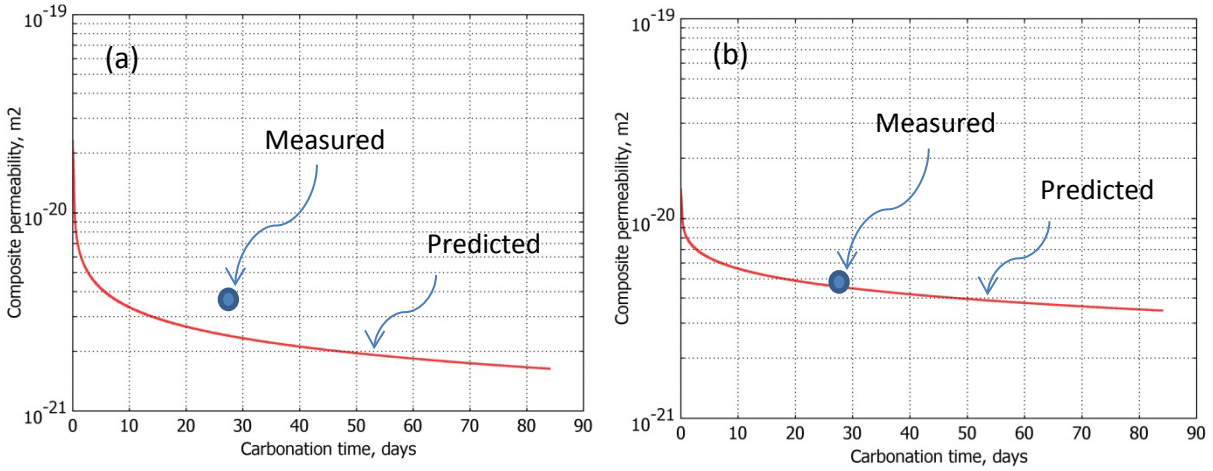

Figure 8.16. Composite permeability decrease as a function of carbonation time of samples S3C (a) and S4C (b) – measured permeability was only obtained for 28-day carbonation.

The modification of diffusivity over the depth of sample due to carbonation is shown in Figure 8.17. The diffusivity of the carbonated zone is significantly decreased similar to the decrease in permeability. However, the magnitude of the reduction is less pronounced than for permeability. After 4 weeks of carbonation, the saturated Ca diffusivity of sample S3C decreases by a factor of 5 for the zone near the exposed surface which is consistent with the estimation from experimental results (Section 6.6). The change in diffusivity due to carbonation of sample S4C is slightly less in magnitude, but the altered zone is deeper compared to sample S3C.

The evolution of composite diffusivity during leaching is shown in Figure 8.18. As permeability, the composite diffusivity rapidly decreases in the first few days of carbonation. In the later stage, the diffusivity is slightly decreased over carbonation time. As shown in Section 6.6, the composite diffusivity of dissolved He is decreased by 30% after 28-day carbonation for sample S3C, which is quite similar to the predicted Ca diffusivity decrease (27%). Note that the change in diffusion property of Ca and He due to carbonation may be differed from each other because of its difference in molecular size, electrical force and binding effect.

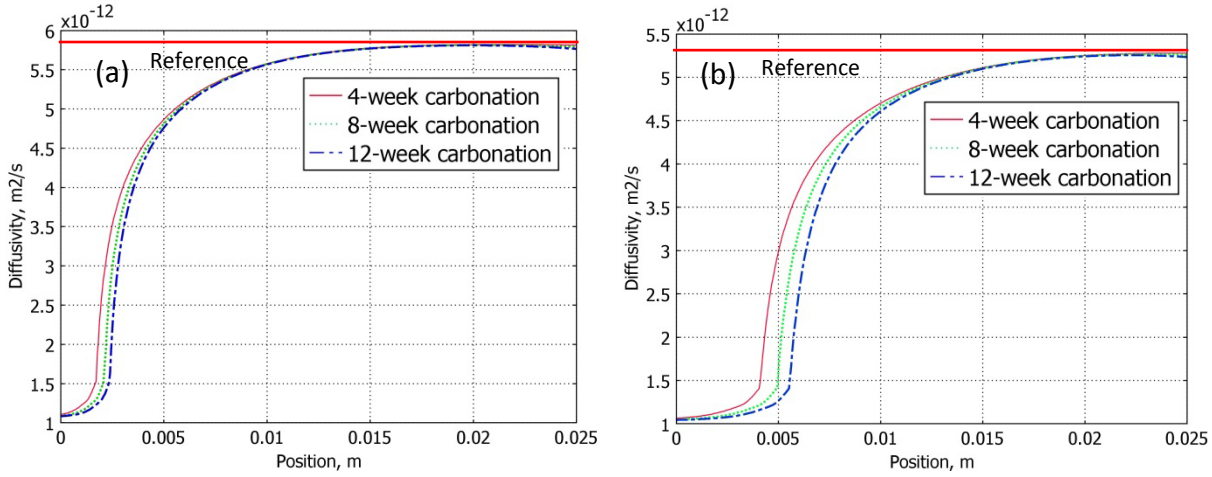

Figure 8.17. Prediction of change in (saturated) diffusivity of Ca over the depth of samples S3C (a) and S4C (b) at different carbonation time - red line represents diffusivity of reference sample.

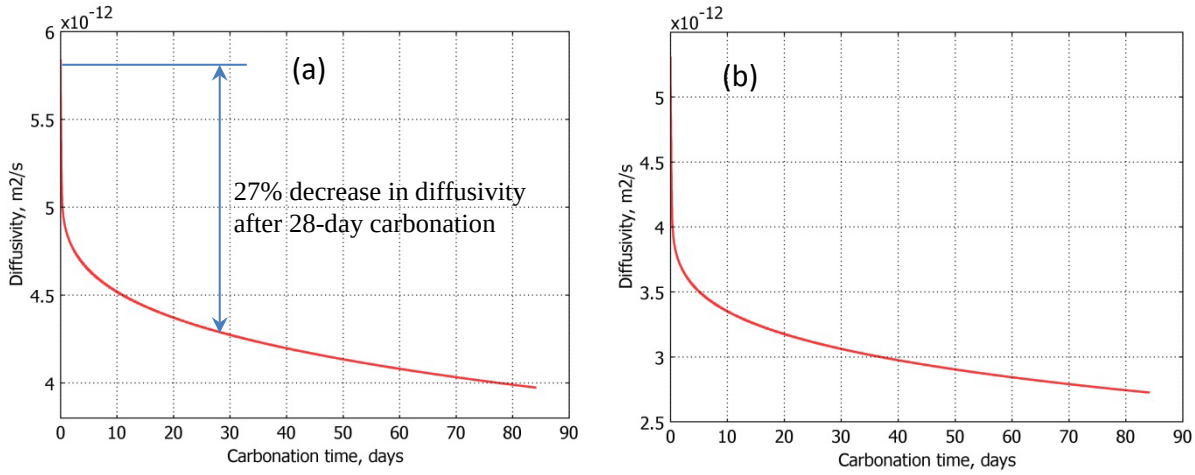

Figure 8.18. Prediction of composite Ca diffusivity decrease as a function of carbonation time of samples S3C (a) and S4C (b)

8.1.6. Conclusions on carbonation modelling

A one-dimensional reactive transport model coupled advection and diffusion to simulate the carbonation under controlled CO_2 pressure has been developed. The model enables to predict the carbonation degree, CO_2 uptake, portlandite content, porosity change and variation of transport properties over time and space. Parametric study confirms that advection term plays an important role in the transport of CO_2 in cases of carbonation under high applied pressure gradient on relatively permeable cement-based materials. The longer the carbonation experiment runs, the larger the contribution of advection on carbonation process. The model helps to better interpret the experimental observations and understand the phenomena behind such as the formation of a gradual carbonation front, the increase of saturation degree at the reacted surface. Primary verification with accelerated carbonation experiments gives a good agreement even though more experimental data is still required to validate and improve the model, especially to better predict the changes in transport properties.

The proposed model enables to further extend for the carbonation under natural conditions. In that case, only diffusive transport will be taken into account; and the concentration of CO_2 will equal the CO_2 concentration in atmosphere. However, the transport of moisture in the sample is needed to further simulate as there is a moisture exchange between the sample and surrounding environment, which is not considered in the present model.

8.2. Modelling of accelerated leaching using ammonium nitrate solution

8.2.1. Introduction

Ca-leaching is relevant for the long-term durability of cement based materials. This process is extremely slow under environmental conditions. Many accelerated methods have been proposed to experimentally study leaching because of the extremely slow nature of the degradation process under ambient condition. Modelling of the leaching process has also been pursued by many researchers to interpret the experimental results and predict the properties of leached materials, which is hard to be obtained by experimental study. Nguyen *et al*. [272] modelled the effects of Ca-leaching on the mechanical properties of concrete, while Bentz *et al*. [273] considered the influence on the microstructure and diffusivity. A 2D model was developed by Mainguy *et al*. [274] to predict the degraded depth and the variation of leached calcium flux with time. Jacques *et al*. [275] developed a thermodynamic model to calculate the geochemical changes of concrete during leaching with rain and soil water types, while Yokozeki *et al*. [169] modelled the long-term behaviour of cementitious materials used in an underground environment. Most of these models are based on the assumption of thermodynamic equilibrium of calcium in the solid and liquid phases in pure/deionized water which was first studied by Berner [170, 266]. Recently, Wan *et al*. developed a solid-liquid equilibrium curve of calcium in ammonium nitrate solution [276] which was later used in his model [277].

Many studies focus on the prediction of the degraded depth of leached materials and characterize its mechanical behaviour [181, 182]. However, there are only a few studies which discuss the modification of the microstructure after leaching [183, 184] and the effects of leaching on transport properties [185, 186]. This study aims at strengthening and bridging the relationship between leaching degradation of cement paste; changes in transport properties; and microstructural modification by a modelling tool. The outcomes of the model are then verified with experiments presented in Chapter 7.

8.2.2. Model development

The proposed model is a one-dimensional diffusion-based transport model which aims to simulate leaching of saturated hardened cement paste in contact with an aggressive NH_4NO_3 solution of 6 mol/l (see experimental setup in Chapter 4). This model is based on a macroscopic mass balance for Ca in aqueous and solid phases. The model only considers the leaching of portlandite and calcium silicate hydrates which are the main hydrated phases in

typical CEM I Ordinary Portlandite cement [278]. The outline of the proposed model is shown in Figure 8.19.

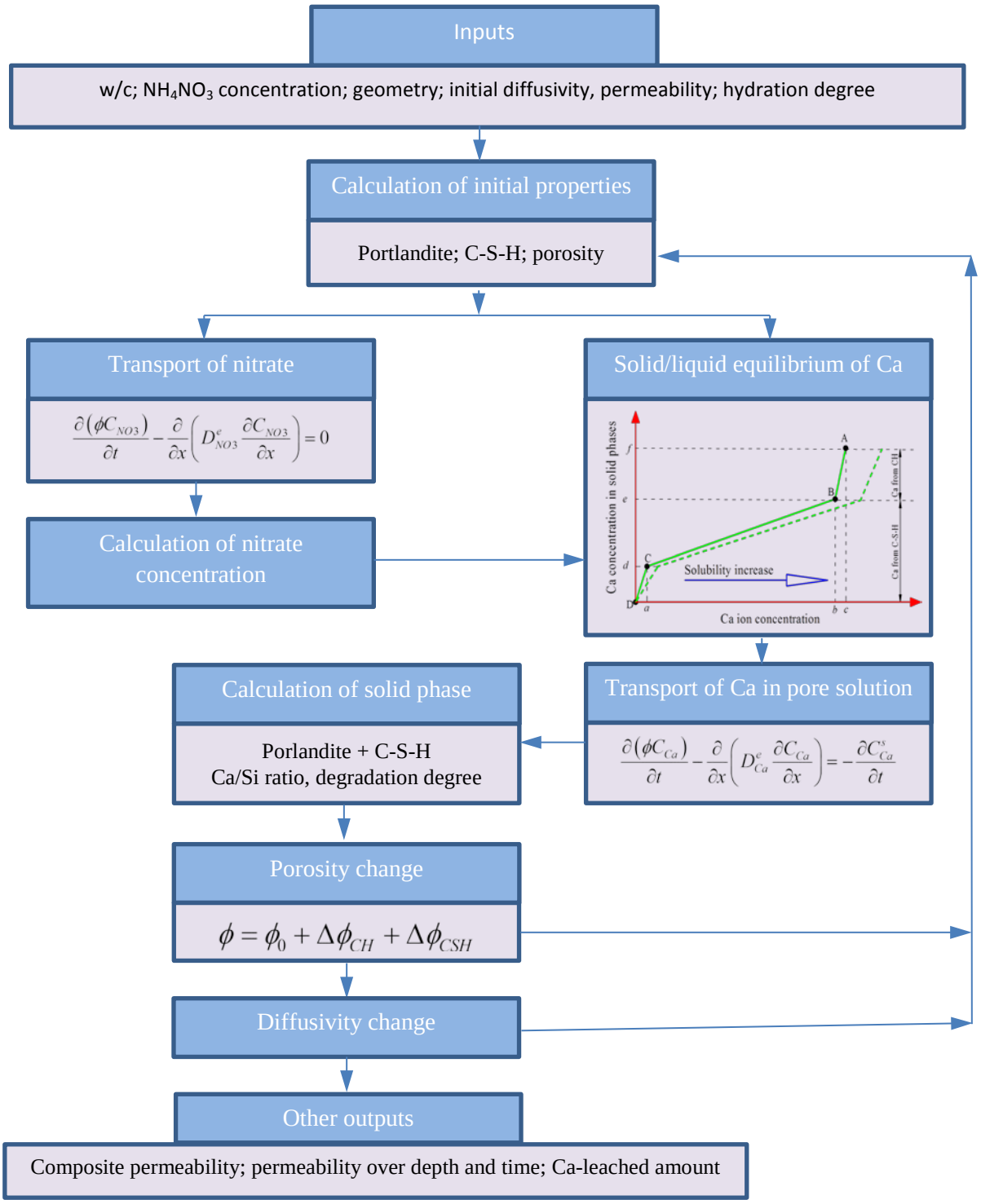

Figure 8.19. Overall scheme of leaching model – notations are explained in the text.

The mass balance equation for Ca in pore solution is given as:

$$\frac{\partial(\phi C_{Ca})}{\partial t}-\frac{\partial}{\partial x}\left(D_{Ca}^{e}\frac{\partial C_{Ca}}{\partial x}\right)=-\frac{\partial C_{Ca}^{s}}{\partial t} \tag{8.65}$$

where ϕ is porosity [-]; C_{Ca} is concentration of Ca ion in pore solution [mol/m^3]; C_{Ca}^{s} is total concentration of Ca in solid phases [mol/m^3]; D_{Ca}^{e} is effective diffusivity of Ca ion [m^2/s]; t is time [s] and x is spatial distance [m]. As carbonation, the total porosity increase of sample during leaching is simply expressed as follows (Note that the derivation of porosity change due to leaching is almost similar to the one for carbonation. Some equations are the same, but still listed hereafter for convenient tracking):

$$\phi=\phi_0+\Delta\phi_{CH}+\Delta\phi_{CSH} \tag{8.66}$$

where ϕ_0 is initial total porosity which is experimentally determined or calculated as follows [265]:

$$\phi_0=\frac{w/c-0.17m}{w/c+0.32} \tag{8.67}$$

in which m denotes the degree of hydration and w/c is water/cement ratio. $\Delta\phi_{CH}$ is the porosity increase due to portlandite dissolution:

$$\Delta\phi_{CH}=V_{CH}\left(C_{CH0}-C_{CH}\right) \tag{8.68}$$

where V_{CH} is molar volume of portlandite (33 cm^3/mol [279]), C_{CH0} and C_{CH} are, respectively, the initial and current portlandite concentration [mol/m^3]. $\Delta\phi_{CSH}$ is the porosity increase due to C-S-H dissolution. The decrease in the Ca/Si ratio of C-S-H results in a reduction of molar volume of C-S-H.

$$\Delta\phi_{CSH}=C_{CSH}\left(V_{CSH0}-V_{CSH}\right) \tag{8.69}$$

where C_{CSH} is the concentration of C-S-H [mol/m^3], and V_{CSH0} and V_{CSH} are the molar volume of the initial and current C-S-H, respectively. Data for molar volume of C-S-H is still scarce and it is supposed to be a stoichiometry-dependent parameter. A recent experimental study [130] showed that the molar volume of C-S-H is proportional to the Ca/Si ratio, y, as:

$$V_{CSH0}-V_{CSH}=\omega\left(1-y/y_0\right) \tag{8.70}$$

where y_0 is the initial Ca/Si ratio of C-S-H, y_0 = 1.7 [271], and 0.02 < ω < 0.04 l/mol. By comparing the porosity of leached and intact samples, however, the author finds that ω = 0.04 l/mol gives the best fit. The Ca/Si ratio is calculated from the solid-liquid equilibrium curve (described later).

The effective diffusion model proposed by Garboczi [55] and adapted for leaching condition by Jain [280] is used to simulate the evolution of effective diffusivity of Ca ion in this model. The modification of Garboczi's model actually comes from the fact that with the same porosity increase, the increase of diffusion due to leaching is faster than the increase of diffusion resulted from hydration.

$$D_{Ca}^{e} = D_{Ca}^{0}\begin{bmatrix} 0.001 - 0.07\phi_{c0}^{2} - 1.8H\left(\phi_{c0} - 0.18\right)\left(\phi_{c0} - 0.18\right)^{2} \\ +3.6H\left(\phi_{c} - 0.16\right)\left(\phi_{c} - 0.16\right)^{2} + 0.14\phi_{c}^{2} \end{bmatrix} \tag{8.71}$$

where D_{Ca}^{0} is the diffusivity of Ca ion in water; $H()$ is the Heaviside function; ϕ_c is capillary porosity (excluded gel pores) and ϕ_{c0} denotes initial capillary porosity which can be calculated as [265]:

$$\phi_{c0} = \frac{w/c - 0.36m}{w/c + 0.32} \tag{8.72}$$

Dissolution of portlandite results in an increase in capillary porosity. Although the C-S-H phase mainly consists of gel pores (less than 2 nm), decalcification of C-S-H may also contribute to the increase of capillary porosity due to the connection of gel pores of space. Therefore, the author assumes that 50% of the porosity increase by C-S-H decalcification (Equation (8.73)) results in an increase in ϕ_c:

$$\phi_{c} = \phi_{c0} + \Delta\phi_{CH} + 0.5\Delta\phi_{CSH} \tag{8.73}$$

The right side of Equation (8.65) can be rewritten as:

$$-\frac{\partial C_{Ca}^{s}}{\partial t} = -\left(\frac{C_{Ca}^{s}}{C_{Ca}}\frac{\partial C_{Ca}}{\partial t} + \frac{\partial}{\partial t}\left(\frac{C_{Ca}^{s}}{C_{Ca}}\right)C_{Ca}\right) \tag{8.74}$$

The term $\partial C_{Ca}^{s} / \partial C_{Ca}$ is derived from the Ca solid-liquid equilibrium curve. Wan *et al.* [276] showed that the Ca solid-liquid equilibrium curve in a 6 mol/l NH_4NO_3 solution has a similar three-stage dissolution pattern as in water, but with higher aqueous Ca concentrations. In this study, the Ca solid-liquid equilibrium curve is expressed as Equation (8.75) and visualized in Figure 8.20 (same approach as carbonation model in Section 8.1). Solid-liquid equilibrium is divided into discrete decalcification of portlandite and C-S-H. The region AB corresponds to the portlandite dissolution. When portlandite is completely dissolved (point B), C-S-H starts progressively dissolving down to the point C which is the starting point of a steeper decalcification of C-S-H which finally results in silica gel.

$$C_{Ca}^{s} = \begin{cases} \dfrac{d}{a} C_{Ca} & C_{Ca} \le a \\ d + \dfrac{e-d}{b-a}(C_{Ca} - a) & a < C_{Ca} \le b \\ e + \dfrac{f-e}{c-b}(C_{Ca} - b) & b < C_{Ca} \le c \end{cases} \tag{8.75}$$

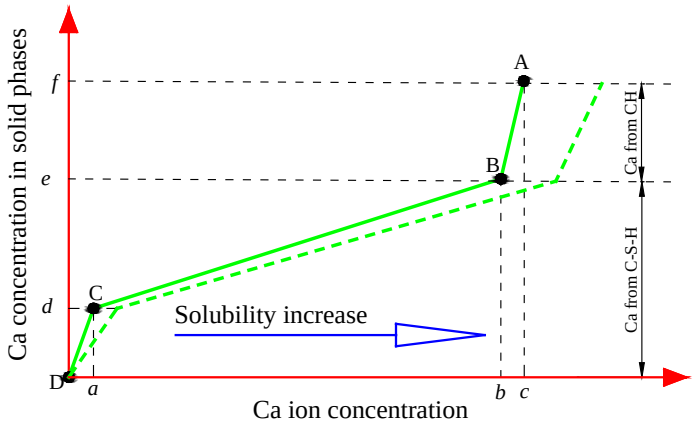

Figure 8.20. Solid-liquid equilibrium curve of calcium – dashed green line schematically shows the curve shift due to Ca solubility increase.

The values of *a*, *b* and *c* are kept constant during leaching in the existing literature. For example, Wan *et al*. [276] identified *a* = 273 mol/m^3, *b* = 2320 mol/m^3 and *c* = 2730 mol/m^3 for leaching in NH_4NO_3 solution of 6 mol/l. While Gerard *et al*. [281] still used the values as leaching in deionized water (i.e. *a* = 2 mol/m^3, *b* = 20 mol/m^3 and *c* = 22 mol/m^3). These simplified approaches do not fully describe the real solid-liquid equilibrium under ammonium nitrate attack. As Ca concentration depends also on the nitrate concentration [281], values of *a*, *b* and *c* should depends on the spatial-temporal variation of nitrate concentrations. In this study, this dependence on the nitrate concentration, C_{NO3}, is expressed as:

$$\begin{cases} a = 2 + \dfrac{C_{NO3}}{C_{NO3}^{0}}(273 - 2) \\ b = 20 + \dfrac{C_{NO3}}{C_{NO3}^{0}}(2320 - 20) \\ c = 22 + \dfrac{C_{NO3}}{C_{NO3}^{0}}(2730 - 22) \end{cases} \tag{8.76}$$

where C_{NO3}^{0} is the concentration of nitrate in surrounding solution, 6000 mol/m^3. The transport equation for nitrate is given as:

$$\frac{\partial(\phi C_{NO3})}{\partial t} - \frac{\partial}{\partial x}\left(D^e_{NO3}\frac{\partial C_{NO3}}{\partial x}\right) = 0 \tag{8.77}$$

where D^e_{NO3} is the effective diffusivity of nitrate ion in the sample which is also assumed to follow the effective diffusion model of Garboczi [55]. The diffusivity of nitrate ion in water is 1.7×10^{-9} m^2/s [282].

The initial Ca fraction in CH and C-S-H (values *e* and *f* [mol/m^3]) can be estimated from the hydration cement clinkers (C_2S, C_3S) by the Bouge calculation. The critical value *d* [mol/m^3]) at which C-S-H sharply decalcifies is determined by multiplying the amount of SiO_2 in C-S-H with the Ca/Si ratio at point C (about 0.85 following [266]). Finally, Equations (8.65) and (8.77) are recast as follows:

$$\left(\phi + \frac{C^s_{Ca}}{C_{Ca}}\right)\frac{\partial C_{Ca}}{\partial t} - \frac{\partial}{\partial x}\left(D^e_{Ca}\frac{\partial C_{Ca}}{\partial x}\right) + \frac{\partial}{\partial t}\left(\phi + \frac{C^s_{Ca}}{C_{Ca}}\right)C_{Ca} = 0 \tag{8.78}$$

$$\phi\frac{\partial C_{NO3}}{\partial t} - \frac{\partial}{\partial x}\left(D^e_{NO3}\frac{\partial C_{NO3}}{\partial x}\right) + \frac{\partial \phi}{\partial t}C_{NO3} = 0 \tag{8.79}$$

Because the changes in concentrations of Ca and nitrate at the boundaries are unknown, it is difficult to set the boundary conditions for Equations (8.78) and (8.79). The author extends the model for the sample itself to the whole system, i.e. the model composes 3 domains: solution domain 1 – sample domain – solution domain 2 as shown in Figure 8.21 (see **Figure 4.14**b for experimental setup).

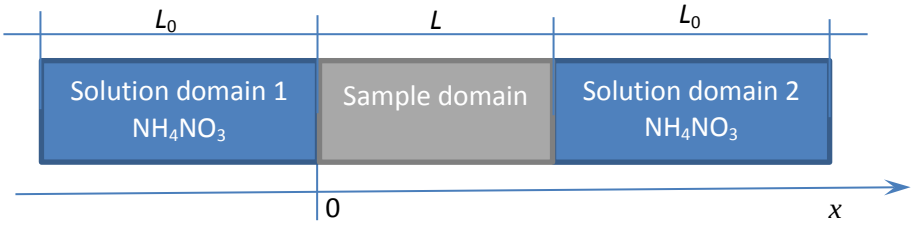

Figure 8.21. Model configuration with extended solution domains

The length of the extended domain, L_0 [m], is determined based on the total ammonium nitrate solution in the chamber:

$$L_0 = \frac{V}{2F} \tag{8.80}$$

where V [m^3] is the volume of the aqueous solution in the chamber (1.2 litre in the experimental setup), F is the cross section of the sample, [m^2], L [m] is the length of the sample (25 mm). The transport problem in solution domains is simply written as:

$$\frac{\partial C_{Ca}}{\partial t} - \frac{\partial}{\partial x}\left(D_{Ca}^{mix} \frac{\partial C_{Ca}}{\partial x} \right) = 0 \tag{8.81}$$

$$\frac{\partial C_{NO3}}{\partial t} - \frac{\partial}{\partial x}\left(D_{NO3}^{mix} \frac{\partial C_{NO3}}{\partial x} \right) = 0 \tag{8.82}$$

where D_{Ca}^{mix} and D_{NO3}^{mix} [m^2/s] are the mixed diffusion coefficients of Ca and nitrate in solution domains, respectively. The surrounding solution was mixed during experiment. Therefore D_{Ca}^{mix} and D_{NO3}^{mix} are expected to be very high. The author sets D_{Ca}^{mix} = D_{NO3}^{mix} =10^{-3} m^2/s for numerical simulation. In fact, the variation of mixed diffusivities is not affecting the modelling results as long as its values are much larger than the diffusivities of Ca and nitrate in the sample. Initial conditions for the specific experimental setup in this study are:

For calcium

$$\begin{cases} C_{Ca}(x,0) = C_{Ca}^0 & 0 \le x \le L \\ C_{Ca}(x,0) = 0 & -L_0 \le x < 0; L < x \le L + L_0 \end{cases} \tag{8.83}$$

For nitrate

$$\begin{cases} C_{NO3}(x,0) = 0 & 0 \le x \le L \\ C_{NO3}(x,0) = C_{NO3}^0 & -L_0 \le x < 0; L < x \le L + L_0 \end{cases} \tag{8.84}$$

For a closed system, the boundary conditions are simply expressed as:

$$\begin{cases} \dfrac{\partial C_{Ca}(-L_0,t)}{\partial x} = \dfrac{\partial C_{Ca}(L+L_0,t)}{\partial x} = 0 & t > 0 \\ \dfrac{\partial C_{NO3}(-L_0,t)}{\partial x} = \dfrac{\partial C_{NO3}(L+L_0,t)}{\partial x} = 0 & t > 0 \end{cases} \tag{8.85}$$

Because the dissolution rate is much faster than transport, transport is the rate-limiting step. Therefore, in literature, it is hypothesized that there exists a local chemically immediate equilibrium of Ca, and in context of simplification an “artificial” equivalent initial condition for calcium is used corresponding to a fixed solid-liquid equilibrium curve in NH_4NO_3 6 mol/l (i.e. values a, b and c are constant, C_{Ca}^0 = 2730 mol/m^3 [220, 277]). This approach is acceptable as long as the diffusivity of nitrate is much faster than the one of Ca (see Appendix 2). However, the Ca concentration in pore solution cannot be modelled correctly. In this study, by considering the dependence of solid-liquid equilibrium curve on the nitrate

concentration and modelling transport of both Ca and nitrate, the author enables to use the real initial Ca concentration, C_{Ca}^{0} = 22 mol/m^3. The problem is numerically solved by using the COMSOL Multiphysics program.

8.2.3. Derivation of auxiliary variables

8.2.3.1. Portlandite content and degraded depth

Based on Equation (8.38), the portlandite content, C_{CH} [mol/m^3] can be simply defined if the total amount of Ca in solid phases is known:

$$\begin{cases} C_{CH} = 0 & C_{Ca}^{s} \le e \\ C_{CH} = C_{Ca}^{s} - e & C_{Ca}^{s} > e \end{cases} \tag{8.86}$$

As no portlandite was present in the degraded zone as seen in experimental Chapter 7, the author defines the degraded depth as the position at which portlandite is totally dissolved. The degradation degree, d_l, is then formulated as:

$$d_l = \begin{cases} 1 & C_{Ca}^{s} < e \\ \dfrac{f - C_{Ca}^{s}}{f - e} & C_{Ca}^{s} \ge e \end{cases} \tag{8.87}$$

8.2.3.2. Ca-leached amount

The amount of Ca leached out of the sample can be calculated by considering the changes in concentrations of Ca in pore solution and solid phase:

$$\Delta Ca = \int_0^L \left[\left(f - C_{Ca}^{s} \right) F - \left(C_{Ca}\phi - C_{Ca}^{0}\phi_0 \right) F \right] dx \tag{8.88}$$

where ΔCa is Ca-leached amount [mol], and C_{Ca}^{0} is the initial equilibrium concentration of calcium (22 mol/m^3). The first and second terms in bracket on the right side stand for the changes of Ca content in solid phase and pore solution, respectively.

8.2.3.3. Change in water permeability and diffusivity

As carbonation, the Kozeny-Carman relation is used to compute the intrinsic permeability of leached materials. Trial simulation shows that the lumped term $\Omega = \dfrac{1}{\tau^2 F_s}$ is related to the square of the degradation degree. Therefore it is adapted for leaching materials as follows:

$$\Omega = \Omega_0 - \left(\Omega_0 - \Omega_l \right) d_l^2 \tag{8.89}$$

where subscript 0 and l denote for sound and leached materials; Ω_0 can be calculated from porosity, specific surface area and intrinsic permeability of reference sample; d_l is the degradation degree (see Equation (8.87)). Numerical calculation of Ω_l on fully leached sample S5L shows that the average value of Ω_l for leached materials is about 3 orders of magnitude higher than the one for sound materials. More experimental data are needed to make a relationship between Ω_l and Ω_0, however as a first estimation, the author assumes that $\Omega_0 = 10^{-3}\Omega_l$.

The permeability and diffusivity of leached material varies along the depth of the sample as the case for carbonation. Therefore, the series model is again applied to predict the composite permeability and diffusivity of leached materials.

8.2.4. Modelling results and verifications

The experimental results of samples S1L and S3L which are samples without limestone filler are used to verify the model. All parameters used for simulations are listed in the Appendix 2. Figure 8.22 compares the simulated leached depths (a) and the amount of calcium leached out the samples (b) with the measurements. Both the predicted degraded depth and Ca-leached amount are in good agreement with the measured ones. The modelling results show that within investigated duration (28 days), the propagation rates of degraded depth and Ca-leached amount are almost in direct proportion to the square root of time. However, if the experiment lasts for a longer time, the rates are slightly decreasing because the amount of leached Ca is not taken away from the system (solution replacement).

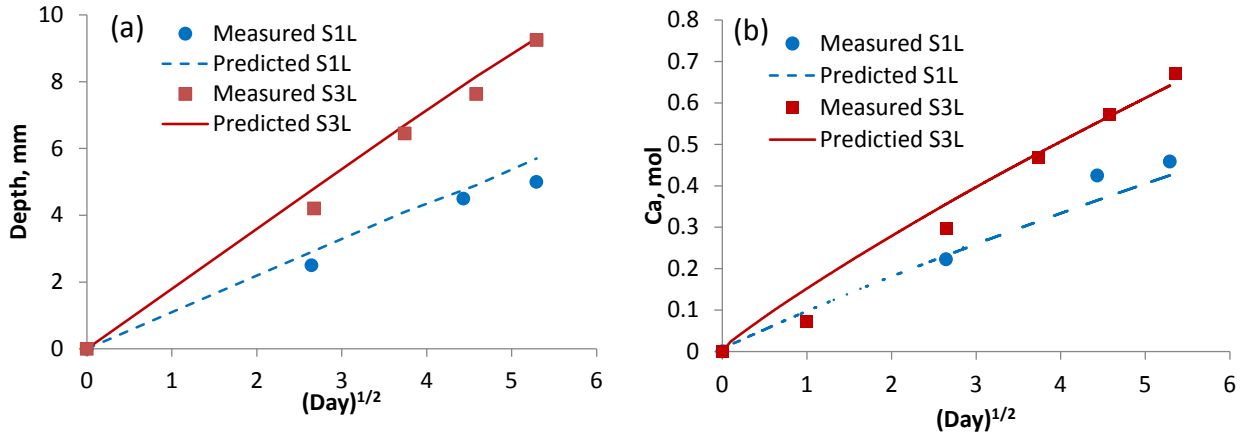

Figure 8.22. Comparisons of experimental and modelling results: leached depth (a) and leached calcium amount (b)

The portlandite profiles after 28-day immersion in ammonium nitrate 6 mol/l are shown in Figure 8.23a and Figure 8.24a for samples S1L and S3L, respectively. The portlandite content is suddenly increased after the degraded front. Sample S1L with low w/c ratio exhibits a steeper jump of portlandite content at the front compared to sample S3L with higher w/c ratio. Both samples show a slight decrease of portlandite content beyond the degraded front. Figure 8.24a also shows the comparison of portlandite profile for sample S3L. The predicted values are in line with the measured ones which are determined by quantitative X-ray diffraction on the powder. Figure 8.23b and Figure 8.24b present the variation of total Ca content in solid phases (CH + C-S-H). In the zone A-B, the total Ca content decreases sharply near the portlandite dissolution front. In the portlandite depleted zone (B-C), further decalcification is due to the leaching of C-S-H phase. As the change of portlandite content, the drop in slope of Ca content is also steeper for sample with low w/c ratio.

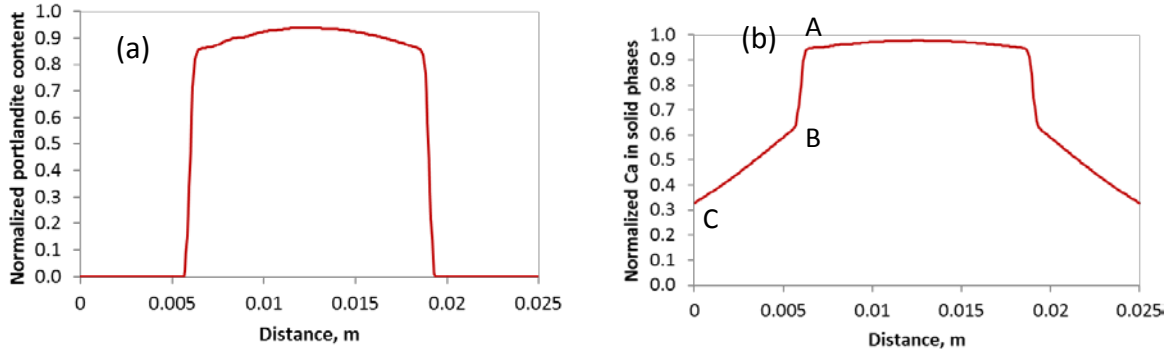

Figure 8.23. Prediction of normalized portlandite content (a) and solid Ca (in CH and C-S-H) (b) profiles of sample S1L after 28-day leaching in ammonium nitrate solution

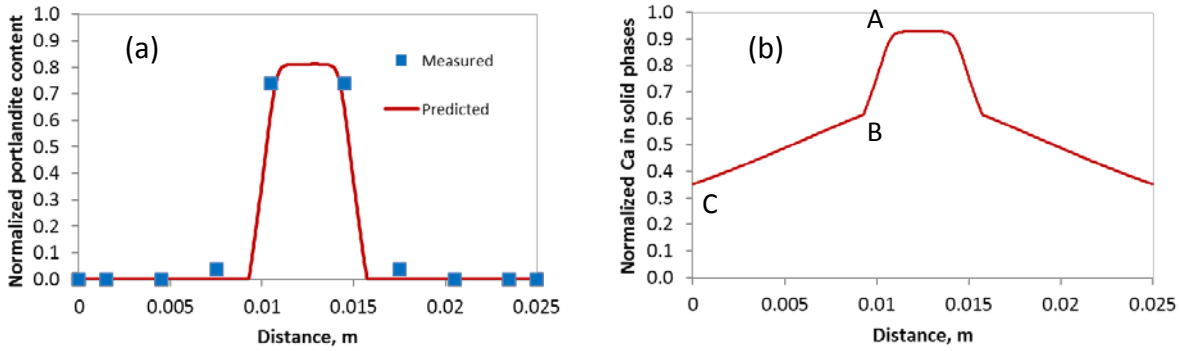

Figure 8.24. Normalized portlandite content (a) and solid Ca (in CH and C-S-H) (b) profiles of sample S3L after 28-day leaching in ammonium nitrate solution – The portlandite content is compared with quantitative XRD results.

The capillary and total porosities increase significantly due to leaching as shown in Figure 8.25. There also exist two zones with different slopes of increase in porosity corresponding to the leaching of portlandite and C-S-H. The increase in total porosity can mainly be attributed to portlandite dissolution. After 28-day leaching, the portlandite dissolution contributes about 13% to the total porosity increase, while C-S-H leaching only contributes about 5% regardless of different w/c ratio. The average porosity change, determined by a combination of mercury intrusion porosimetry and N_2-adsorption, up to a depth of 3 mm from the exposed surface compares well with the predicted total porosity change, but a bit higher than predicted capillary porosity change. Note that the combined MIP – N_2-adsorption method enables to determine pores with diameters down to 3 nm which may include some gel pores from C-S-H.

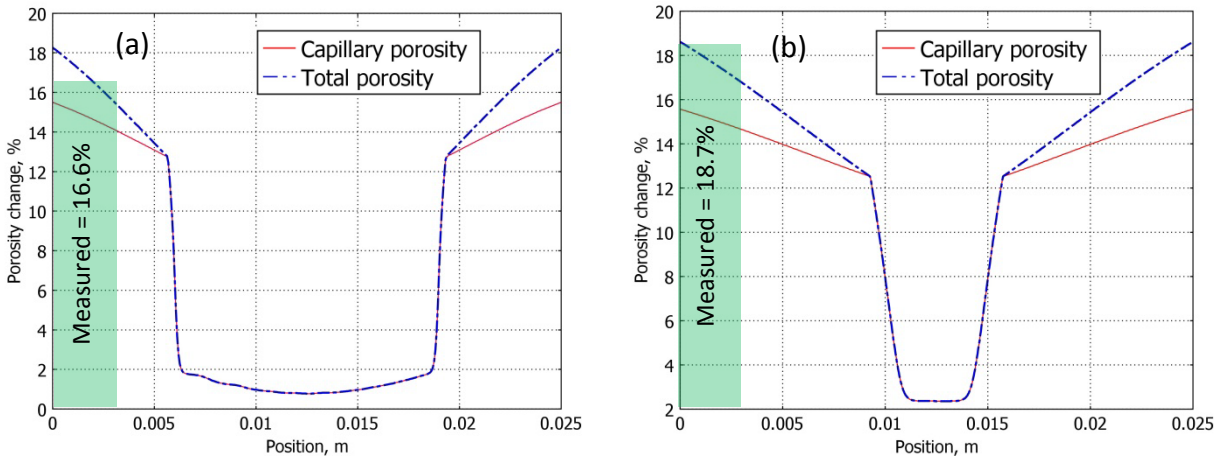

Figure 8.25. Reduction of capillary and total porosity of samples S1L (a) and S3L (b) after 28-day leaching in ammonium nitrate solution

Permeability significantly increases after leaching as shown in Figure 8.26 and Figure 8.27 (for samples S1L and S3L, respectively). After 4 weeks of NH_4NO_3 immersion, the permeability coefficient increases more than two orders of magnitude for the zone near the exposed surface. The composite permeability which is dominated by the permeability of "sound" zone also significantly increases but only by one order of magnitude after 28-day leaching (Figure 8.26b and Figure 8.27b). The change in permeability due to leaching of sample S3L (higher w/c ratio) is more significant than sample S1L.

The evolution of composite permeability during leaching is shown in Figure 8.26b and Figure 8.27b for samples S1L and S3L, respectively. The longer the immersion time in ammonium nitrate solution, the larger the permeability coefficient. The composite permeability rapidly

increases in the first leaching stage when portlandite is still present in the sample. In the second leaching stage, the rate of permeability increase is slower because C-S-H decalcification has a smaller effect on the porosity increase. Figure 8.26b and Figure 8.27b also compare the measured and predicted composite permeability for samples S1L (only at 28-day leaching) and S3L, respectively. The predicted values are quite comparable with the measured ones in the first leaching stage, but there is less agreement at later stage. The differences may be attributed to the changes in tortuosity and shape factor which are not well captured in the model.

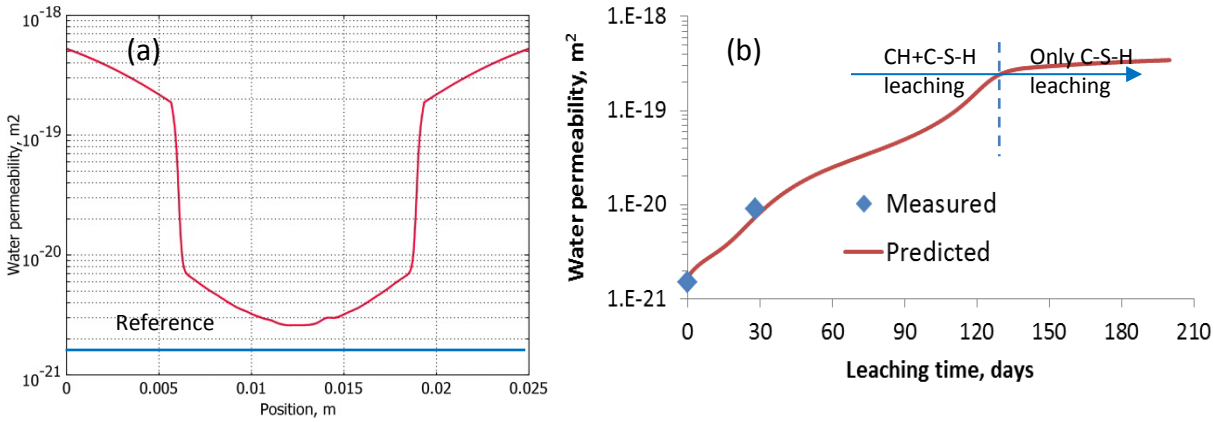

Figure 8.26. Prediction of water permeability profile of sample S1L after 28-day immersion in NH_4NO_3 (a) and time evolution of composite permeability over time (b)

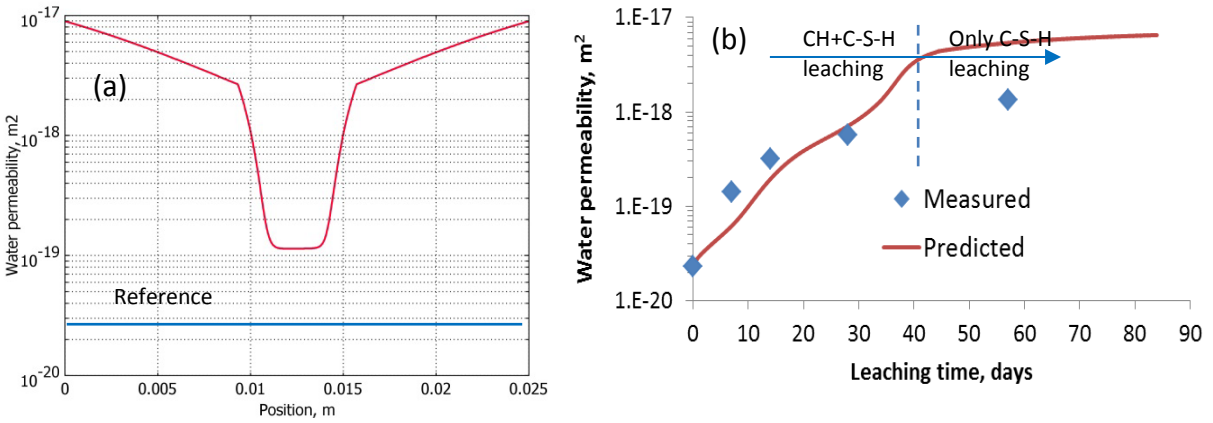

Figure 8.27. Prediction of water permeability profile of sample S3L after 28-day immersion in NH_4NO_3 (a) and time evolution of composite permeability over time (b)

The modification of diffusivity due to leaching is shown in Figure 8.28 and Figure 8.29 for samples S1L and S3L, respectively. As permeability, diffusivity is also significantly increased after leaching but less pronounced than permeability. After 4 weeks of NH_4NO_3 immersion, the diffusion coefficient of calcium (under saturated condition) increases one order of magnitude for the zone near the exposed surface. The change in diffusivity due to leaching of sample S3L (higher w/c ratio) is higher than sample S1L.

The evolution of composite diffusivity during leaching is shown in Figure 8.28b and Figure 8.29b for samples S1L and S3L, respectively. As composite permeability, the composite diffusivity rapidly increases in the portlandite dissolution stage. In the C-S-H leaching stage, the diffusivity is slightly increased over immersion time. As shown in Section 7.8, the composite diffusivity of dissolved He is increased 4.1 times after 28-day leaching in ammonium nitrate solution for sample S3L, which is smaller than the predicted Ca diffusivity increase (11.5 times). The diversion may be attributed the differences in characteristics (molecular size, weight, electrical charging, interaction with pore walls, etc.) of those diffusive species. Furthermore, the changes in tortuosity may be not well captured in the model.

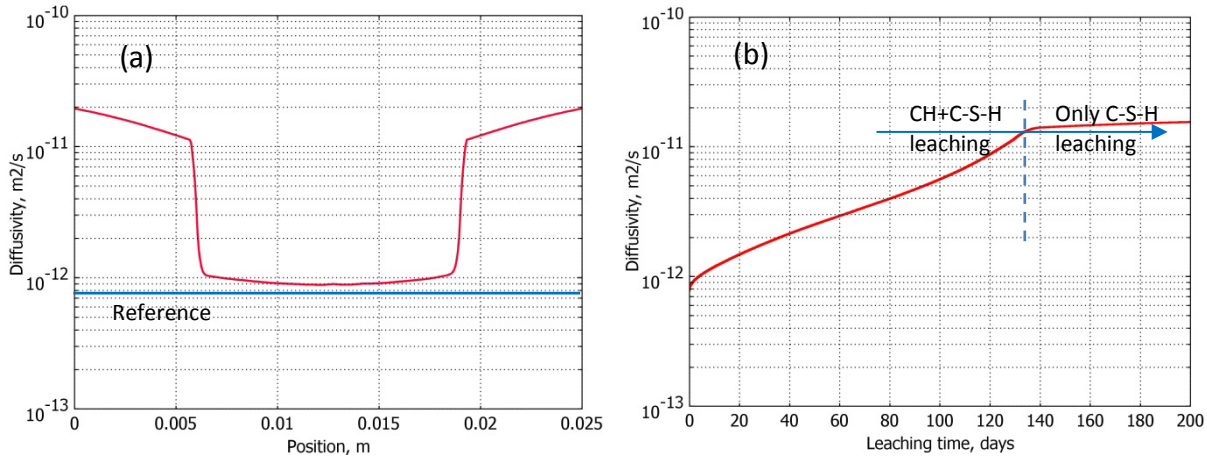

Figure 8.28. Prediction of change in (saturated) diffusivity of Ca over the depth after 28-day immersion in NH_4NO_3 (a) and composite diffusivity increase as a function of leaching time of samples S1L

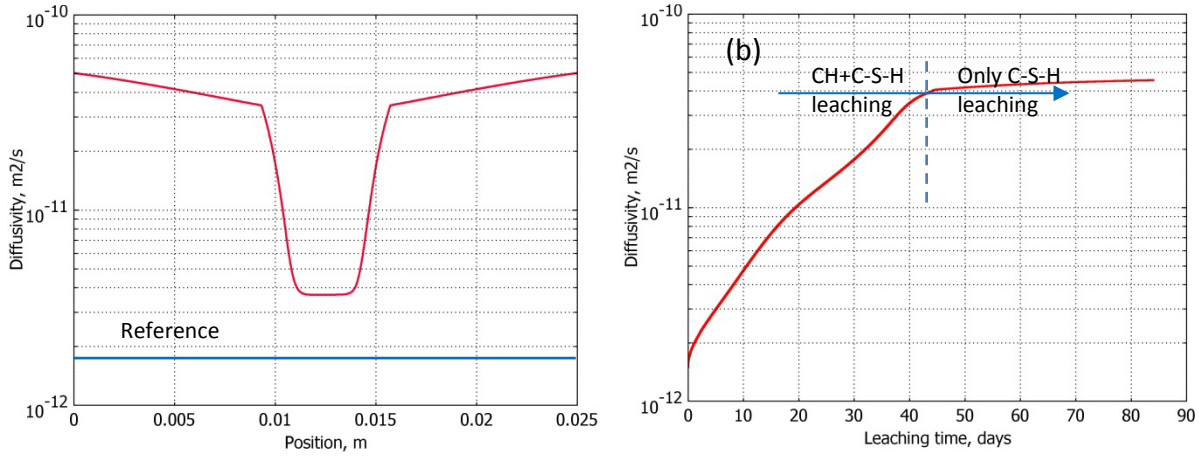

Figure 8.29. Prediction of change in (saturated) diffusivity of Ca over the depth after 28-day immersion in NH_4NO_3 (a) and composite diffusivity increase as a function of leaching time of samples S3L

8.2.5. Conclusions on Ca-leaching modelling

A one-dimensional model for Ca-leaching in ammonium nitrate solution based on the solid-liquid equilibrium of Ca is developed. The transport of both calcium and nitrate are considered because Ca-solubility strongly depends on the nitrate content. The model enables to predict the leaching depth, Ca-leached amount, portlandite content, solid Ca content, porosity, diffusivity and permeability changes over time and space. By introducing a direct relation between the solubility and nitrate concentration, the solid-liquid equilibrium curve describes better the phase equilibrium in NH_4NO_3 solution. Modelling results show that the accelerated leaching in ammonium nitrate solution significantly increases the porosity and decreases the Ca/Si ratio, which both lead to a significant increase in permeability and diffusivity. More importantly, the transport properties of the zone beyond the degradation front are also significantly increased as portlandite dissolution. The contribution of C-S-H to changes in microstructure and transport properties is clearly seen by modelling which helps to better explain the experimental observations. Verifications with accelerated leaching experiments gave a good agreement even though more experimental data are still required to validate and improve the model, especially to improve the prediction of transport properties.

This page is intentionally left blank!

CHAPTER 9: DISCUSSION, CONCLUSIONS AND FUTURE WORK

9.1. Discussion

9.1.1. Key microstructural parameters governing transport properties of degraded cement-based materials

Through this discussion, the author would like to stress that the existing models, which relate the microstructure to the transport properties (diffusivity, permeability) exhibit numerous errors when applied to degraded materials. Most of the models consider porosity as the key parameter affecting the transport properties, while the other microstructural parameters (tortuosity, constrictivity, pore size distribution, specific surface area) are not taken into account. The predictions are acceptable for the intact cement-based materials with a conventional w/c ratio (0.35 – 0.5) as the unaccounted parameters may not be significantly varied during hydration. However, the limitations are magnified under chemical degradation.

Carbonation results in a small porosity decrease, but induces a significant reduction in permeability and diffusivity. Such a large alteration cannot be the consequence of the porosity decrease alone, but rather the tortuosity increase could be the main reason of the decrease in transport properties. Note that the tortuosity is not a unique function of porosity as materials with a similar porosity can have a different tortuosity. Furthermore, carbonation exhibits a decrease or increase in specific surface area depending on the mix compositions. This inconsistent variation results in different changes in transport properties as the specific surface area could relatively affect the transport properties by changing the friction between transported species and pore wall. Despite a similar critical pore diameter the pore size distribution of carbonated materials becomes broader towards the finer pore sizes compared to intact materials, which contributes to the reduction of transport properties.

In a similar manner, Ca-leaching not only results in a large porosity increase, but also in a significant shift in the pore size distribution towards larger pore sizes. More importantly, the tortuosity of the leached materials must be significantly decreased as results of porosity increase and newly created pathways during leaching. However, the significant increase in specific surface area reduces the magnitude of the increase of transport properties, especially for diffusivity as a major fraction of specific surface area increase comes from the C-S-H leaching, opening up micro porosity. All of the mentioned microstructural parameters should be taken into account in order to understand the alteration of transport properties of the degraded materials.

9.1.2. Relevance of accelerated degradation experiments to long-term durability assessments of cementitious materials

Accelerated experiments are widely used in research and industry in an attempt to derive information about long-term behaviour of materials subjected to particular working environments. The expected lifetime of important concrete structures varies considerably corresponding to its application but can be up to hundreds or even thousands of years (e.g. in waste disposal systems). With such time scales it becomes virtually impossible to understand their long-term performance under service conditions without relying on accelerated tests. It becomes even more important for extremely slow degradation processes such as carbonation and Ca-leaching. However, there is still on-going discussion regarding whether the degradation mechanism under accelerated conditions is the same as in natural conditions. If it is, it is still not generally validated how to extrapolate the accelerated testing conditions to real performance.

In this study, ammonium nitrate solution was used to accelerate the Ca-leaching process. The results showed that leaching kinetics was significantly increased while still keeping the "nature" of the leaching process. The square-root-time law of propagation of the leaching front and leached Ca amount was applicable under accelerated conditions indicating diffusive transport conditions. The mineralogical changes under leaching in ammonium nitrate solution were quite similar to leaching in pure water and no new phases were formed during leaching in ammonium nitrate solution. In order to extrapolate the accelerated test results to the natural environments in which concretes undergo leaching, one may define the degradation stages in terms of the changes in mineralogy (portlandite content, Ca/Si ratio) or microstructure (porosity, pore size distribution). It is then possible to predict the other properties (diffusivity, permeability, pH) at the same or similar degradation stages for leaching under normal conditions. In this sense, the combination of accelerated experiments and phenomenological models, for which inputs are obtained from accelerated tests, could be very useful to identify the comparative parameters and to predict the long-term behaviour of leached materials. In this way, it is able to imitate long-term naturally degraded cementitious materials by accelerated leaching using ammonium nitrate solution.

For carbonation, an elevated CO_2 pressure was applied to accelerate the carbonation process. This condition partially simulates what happens in some special underground structures. Therefore, the carbonation mechanism differs from natural carbonation process, in which advection does not exist, in terms of the carbonation rate, propagation of the carbonation

front, and the competition of CH and C-S-H carbonation. However, both accelerated and natural carbonation lead to the same end-products (calcium carbonate (with minor difference in morphology), lower Ca/Si ratio of C-S-H) and result in a lower pH, porosity decrease, refined pore size distribution, and thereby a decrease in transport properties. Those parameters are important indicators for concrete durability. Therefore, with the same approach as for accelerated leaching, one may still obtain meaningful prediction of long-term concrete performance by combining modelling and accelerated experiments.

Strictly speaking, accelerated experiments cannot be expected to mimic all possible exposures and boundary conditions. One important thing that cannot be captured in accelerated tests is the continuous hydration of cement-based materials. Under natural conditions there is still evolution of the hydrated cement matrix structure, while under accelerated conditions the continuous hydration is not taken into account due to short experimental time. Furthermore, service environments change in time, which is not captured in the accelerated tests. It is generally assumed that accelerated tests can be used for the characterization of degraded materials and its resistance to chemical degradation as long as the limitations of accelerated techniques are fully considered. However, it is not fully recommended to use accelerated testing for the kinetic study in term of predicting the degradation rate under natural conditions.

9.2. Summary and Conclusions

This study was motivated by the needs of understanding and predicting the chemical degradation of concrete structures in the (very) long-term (e.g. nuclear waste disposal, important civil infrastructure). A clear understanding of the potential degradation, of which carbonation and Ca-leaching are the most important concerns, is useful for the design of materials, operation, maintenance of concrete structures, and prediction of lifetime of the structures. Diffusivity and permeability as macroscopic properties of concrete determine how fast aggressive substances penetrate into concrete and are considered as fundamental parameters for characterizing long-term performance of concrete. The knowledge of the alteration of transport properties of concrete under working conditions is thus of utmost importance. The scientific community agrees that carbonation/leaching changes the transport properties of cement-based materials; however, to what extent is still questionable. This study, by deeper investigations of the modifications of mineralogy and microstructure, allows for a better understanding of the alteration degree of transport properties due to chemical degradation.

This work may be divided into three main parts. In the first part, new methods were developed/adapted in order to study the changes in microstructure, mineralogy and transport properties of cement-based materials due to chemical degradation. In the second part, the proposed methodologies were successfully applied on cement pastes to qualitatively and quantitatively study the carbonation and leaching under accelerated conditions. Finally, phenomenological models were developed to improve the understanding of experimental results and predict other properties of the degraded materials, which are out of reach from experimental work.

9.2.1. Developments of methodologies

Within this study, the author did not aim at developing single methods, but the efforts were spent on the development of integrated techniques, which allow for handling a series of experiments to achieve the goals of this study. In this experimental sequence, a single test method/setup was able to provide/receive information of the testing sample, which had been subjected to degradation or permeability/diffusivity determination. The developed methods, however, are not limited for this study.

- A new technique was optimized to measure water permeability of cement-based materials using a controlled constant flow method. The method allows determination of water permeability with high accuracy at relatively short experimental time.
- A method to measure the diffusivity of dissolved gases was proposed, which enabled determination of the effective diffusion coefficients of two gases in a single experiment.
- A new carbonation method has been developed in which a high (pure) CO_2 pressure gradient was applied to accelerate the carbonation process. The proposed method allows for an accurate quantification of CO_2 uptake, good control of initial conditions and examination of the effect of carbonation on the permeability and diffusivity changes of carbonated cement-based materials. Two carbonation procedures were proposed: continuous and cyclic carbonation. The cyclic carbonation seems to be a relevant method to increase the carbonation degree compared to the continuous carbonation, but may initiate micro-cracking during drying cycles. The continuous carbonation allows studying the contribution of advection to the carbonation of cement-based materials and provides useful inputs for modelling due to its good monitoring of the initial and boundary conditions.
- The leaching process was accelerated by using 6M ammonium nitrate solution. The changes in permeability and diffusivity due to chemical degradation could be easily

investigated in a testing series thanks to the compatibility of the proposed methods. Results showed that NH_4NO_3 solution was a reactive agent, which can be used to accelerate leaching kinetics while still keeping the "nature" of the leaching process.

- A variety of complementary post-analysis techniques including SEM/SEM-EDX, MIP, TGA, IC, N_2-adsorption, XRD/QXRD were used to qualitatively and quantitatively examine the intact and degraded materials. Comprehensive information obtained from these techniques provides a full picture of how transport properties of cement-based materials are changed due to leaching and carbonation via the evolution of the mineralogy and the microstructure.

9.2.2. Application of proposed methods on cement pastes

Intact cement pastes

The effects of limestone filler replacement and w/p ratio on microstructure and water permeability were investigated by a factorial experimental program. It was observed that both limestone filler and w/p ratio had significant influences on water permeability. Permeability was increased with the increase of w/p ratio and limestone filler replacement. However, there was no interaction (or combined) effect between w/p ratio and limestone filler replacement in the testing range. If the comparison is based on a given w/c ratio instead of w/p ratio, the limestone filler replacement reduced the permeability of cement pastes.

At a given w/p ratio, adding limestone filler made the microstructure coarser, especially for high w/p ratio. However, at a given w/c ratio, the limestone filler replacement refined the microstructure of the cement pastes. The water permeability was highly correlated to key pore structure parameters obtained from MIP experiments: accessible porosity and critical pore diameter. A good correlation of intrinsic water permeability and $d_{cr}^2 \frac{\phi^{2.5}}{(1-\phi)}$ was found.

Gas diffusion experiments were carried out on 2 selected samples (with and without limestone filler, similar w/c ratio) for comparison. The same trend of the effects of w/p ratio and limestone filler replacement was observed for dissolved gas diffusion. However the effects were less significant than for water permeability.

Carbonated cement pastes

Continuous vs. cyclic carbonation resulted in a different mechanism compared to carbonation under normal conditions in terms of the transport of CO_2, the propagation of carbonation front and the contribution of cementitious phases (CH, C-S-H) to carbonation. The square-root-time

law of carbonation was not applicable under the studied conditions due to the contribution of advective transport. The evolution of relative humidity during continuous carbonation significantly decreased the carbonation rate.

Microstructural analysis confirmed a relative reduction in porosity of the carbonated materials. The pore size distribution of most carbonated samples was broader and slightly shifted to smaller pore sizes. TGA results showed that portlandite was still present in the carbonated zone detected by phenolphthalein spraying. More importantly, the portlandite content was gradually decreasing over the depth of sample, which indicates that the carbonation front is not sharp under the experimental conditions of coupled advection and diffusion. Portlandite was the main phase that was carbonated but also C-S-H was carbonated under the testing conditions, especially in the sample without limestone filler.

Limestone filler replacement showed some interesting results. With the similar w/c ratio, addition of limestone filler increased the CO_2 uptake. Limestone fillers can partially serve as nucleation sites for precipitation of calcium carbonates, which promotes portlandite carbonation. The micropore volume and specific surface area were decreased for carbonated sample with limestone fillers, but increased for carbonated sample without limestone filler as a consequence of C-S-H carbonation.

Due to carbonation, the samples exhibited a significant decrease in permeability and diffusivity resulting from the changes in microstructure and mineralogy. The permeability decrease could be mainly attributed to the portlandite carbonation and partially to C-S-H carbonation. The changes in diffusion might be mainly due to C-S-H carbonation, which could explain the lower reduction in diffusion compared to permeability. A series model was also proposed to estimate the permeability and diffusivity of the carbonated zone.

Leached cement pastes

A factorial experimental program was used to study the effects of w/p ratio and limestone filler replacement on the degradation depth and Ca-leaching rate. The higher the w/p ratio and limestone filler replacement, the larger the leaching rate. However, the effects of w/p ratio were more significant than the effects of limestone filler replacement. The comparison of mass change calculated from IC results and direct measurements proved that C-S-H leaching contributes to the mass loss of the sample.

Accelerated leaching highly alters the microstructure of the cement paste to a more porous material, which is evidenced by the increase of specific surface area, total porosity and by a

coarser pore size. The total accessible porosity of the leached samples highly depended on w/c ratio. Both meso- and micropore volumes were increased, but interesting is the micropore volume, which was altered much more than the mesopore volume. Probably the leaching of C-S-H whose volume fraction is higher than that of portlandite in the cement matrix results in a significant modification of the micropore structure. The bulk density increased towards the intact zone which indicates a gradual alteration in mineralogy. Portlandite was completely degraded in the leached zone while C-S-H was partially dissolved. Beyond the leached front, portlandite was partly dissolved.

SEM image analysis showed a significant increase in porosity and pore size for the leached materials. The decalcification shrinkage resulted in the formation of micro cracks. More micro cracks were observed in samples with limestone filler addition. The leaching of Ca created connected pathways resulting in an increase of the percolation of the pore system. In the leached zone, the atomic Ca/Si ratio was gradually increased towards the degraded front with a jump in Ca/Si ratio indicative for the transition zone.

The changes in microstructure and mineralogy led to a significant increase in transport properties. The permeability increased by one to two orders of magnitude depending on immersion time in NH_4NO_3 and w/c ratio. For similar w/c ratio, the addition of limestone filler helps to reduce the permeability alteration. The extent of permeability increase is correlated to the porosity and pore size distribution after leaching. The permeability of the pristine zone (determined by phenolphthalein) was probably altered as the Ca/Si ratio still decreased beyond the degraded depth. The diffusion was also significantly increased by leaching in ammonium nitrate solution, but not as significant as the change in permeability (factor of 4 for composite He diffusivity of sample S3L).

9.2.3. Phenomenological models

Accelerated carbonation and Ca-leaching experiments in combination with phenomenological modelling provides us insights in the evolution of the microstructure and related transport properties of cementitious materials on the long-term. The models were developed and verified based on the experimental results within this study. However, the prediction for other cases is possible by changing the input parameters (e.g. material properties (w/c ratio, cement type, hydration degree), and boundary conditions (concentration, pressure)).

A one-dimensional reactive transport model coupling advection and diffusion to simulate the carbonation under controlled CO_2 pressure conditions has been developed. The model enables

prediction of a variety of important parameters including the carbonation degree, CO_2 uptake, portlandite content, porosity change and variation of transport properties over time and space. A parametric study confirms that the advection term plays an important role in the transport of CO_2 in case of carbonation under a high pressure gradient on relatively permeable cement-based materials. The model helps to better interpret the experimental observations and understand the on-going phenomena, such as the formation of the gradual carbonation front, and the increase of the saturation degree at the reacted surface. Preliminary verification with accelerated carbonation experiments gives a good agreement.

For Ca-leaching in an ammonium nitrate solution, a one-dimensional model based on the solid-liquid equilibrium of Ca is developed. What is new in the model is that the transport of both calcium and nitrate are considered because of the dependence of Ca-solubility on the nitrate concentration. By introducing a direct relation between the solubility and nitrate concentration, the solid-liquid equilibrium curve describes better the phase equilibrium in NH_4NO_3 solution. The model enables prediction of the leaching depth, Ca-leached amount, portlandite content, solid Ca content, porosity, diffusivity and permeability changes over time and space. The modelling results show that the accelerated leaching in ammonium nitrate solution significantly increases the porosity and decreases the Ca/Si ratio, which both lead to a significant increase in permeability and diffusivity. More importantly, the transport properties of the zone beyond the degradation front are also significantly increased, which confirmed the experimental results. The contribution of C-S-H to changes in microstructure and transport properties is clearly seen by modelling, which helps in explaining the experimental observations. Verifications with accelerated leaching experiments were in good agreement.

9.3. Suggestions for future research

Despite the fact that more insights on how microstructure and transport properties change under chemical degradation processes have been gained, this study has revealed some interesting problems that should be considered in further study.

- More experimental data on the changes in transport properties of degraded materials at different degradation time is still required to validate and better predict the changes in transport properties due to chemical degradation.
- The change in microstructure is partially attributed to C-S-H leaching/carbonation as proved in this study by indirect integrated techniques. The degradation of C-S-H at nanometer level could be better captured by applying advanced techniques such as Focus

ion beam - Scanning electron microscopy (FIB-SEM). 3D imaging analysis could offer a great potential in fully characterizing the pore network of degraded materials.

- The effect of temperature on Ca-leaching and carbonation should be considered as it significantly affects the reaction rate and the transport of aggressive species.
- Combined carbonation and leaching is also important to study as they (often) occur simultaneously. Knowledge of such combined process is important to understand how much each process contributes to the combined process in terms of changes in microstructure and transport properties.
- The proposed test methods are applicable not only to cement paste but also to mortar or concrete. The extension of this study to more "real" materials used in structures is meaningful and provides the knowledge of the contribution of interfacial transition zone (ITZ) to the degradation processes.
- The multi-purpose cell (also called permeability, diffusion or carbonation cell) can be slightly adapted by replacing the non-flexible resin by a rubber ring. This adaption will prevent cracking that may occur due to the shrinkage of testing materials, especially during drying cycles of the cyclic carbonation experiment.
- Mechanical properties of degraded materials should be investigated in future research as most service conditions involve some type of mechanical loading.
- Long-term degradation experiments simulating the working conditions (on the same materials as under accelerated conditions) are costly and time consuming, but will provide useful information on how far the accelerated tests can be used for the predictions of long-term concrete durability. It could also help for kinetic studies in which the lifetime of real concrete structure can be predicted.

APPENDIXES

Appendix 1. Numerical parameters used for carbonation simulation

Parameter	Notation	Value	Reference/note
Temperature	T	298 K	
Molar mass Ca	M_{Ca}	0.040 kg/mol	
Molar mass CO_2	M_{CO_2}	0.044 kg/mol	
Molar mass $Ca(OH)_2$	M_{CH}	0.074 kg/mol	
Molar mass water	M_w	0.018 kg/mol	
Henry constant	$K_{CO_2}^H$	2941 m^3.Pa/mol	At 298 K
Universal gas constant	R	8.314 J/mol.K	
Viscosity coefficient of water	η_{H_2O}	0.89×10^{-3} Pa.s	At 298 K
Viscosity coefficient of CO_2 gas	η_{CO_2}	1.5×10^{-5} Pa.s	At 298 K
Intrinsic permeability of aqueous phase	k_0^l	2.3×10^{-20} m^2	For sample S3
		1.4×10^{-20} m^2	For sample S4
Intrinsic permeability of gaseous phase	k_0^g	1.6×10^{-19} m^2	For sample S3
		2.8×10^{-19} m^2	For sample S4
Empirical coefficients in Eq. (8.10)	p	5.5	[258]
	q	0.56	
Volume fraction of CO_2 in atmosphere		0.03%	Needed to calculate C_l^{out}
Diffusivity of Ca ion in water	D_{l0}^{Ca}	4.5×10^{-10} m^2/s	[277]
Diffusivity of CO_2 in water	$D_{l0}^{CO_2}$	1.94×10^{-9} m^2/s	[283]
Experimental fitting parameters in Eq. (8.27)	α	5.72	[284]
	β	0.444	
Hydration degree	m	0.83	For sample S3
		0.82	For sample S4
Prefactor in Arrhenius' equation	ψ	1.69 m^3/mol.s	Deduced from reaction rate constant proposed by [285]
Activation energy	E_0	16700 J/mol	[286]
Sample dimension: diameter	d	0.0975 m	
length	L	0.025 m	

Parameter	Notation	Value	Reference/note
Equilibrium constant of H_2CO_3	K_a	$10^{-6.347}$ mol/l	At 298 K [287]
Equilibrium constant of HCO_3^-	K_b	$10^{-10.32}$ mol/l	At 298 K [287]
Unit weight of water	γ_w	1000 kg/m^3	
Molar volume of $Ca(OH)_2$	V_{CH}	33×10^{-6} m^3/mol	
Molar volume of $CaCO_3$	V_{CC}	36.85×10^{-6} m^3/mol	
Molar volume of CSH(1.7)	$V_{CSH(1.7)}$	72×10^{-6} m^3/mol	
Lumped parameter in Eq. (8.14)	Ω_0	4.38×10^{-4}	For sample S3
		4.25×10^{-4}	For sample S4
Initial Ca/Si ratio	y_0	1.7	[271]
BET specific surface area	S_{BET}	30.6 m^2/g	Intact S3
		38.0 m^2/g	Carbonated S3
		34.8 m^2/g	Intact S4
		23.2 m^2/g	Carbonated S4
Bulk density	ρ	1780 kg/m^3	Intact S3
		2140 kg/m^3	Carbonated S3
		1850 kg/m^3	Intact S4
		1860 kg/m^3	Carbonated S4

Appendix 2. Numerical parameters used for Ca-leaching simulation

Parameter	Notation	Value	Reference/note
Initial concentration of nitrate	C^0_{NO3}	6 mol/l	
Volume of NH_4NO_3 6 mol/l	V	1.2 l	
Diffusivity of Ca ion in water	D^0_{Ca}	4.5×10^{-10} m^2/s	[277]
Diffusivity of NO_3^- in water	D^0_{NO3}	1.94×10^{-9} m^2/s	[283]
Experimental fitting parameters in Eq. (8.70)	ω	0.04 l/mol	
Sample dimension: diameter	d	0.0975 m	
length	L	0.025 m	
Molar volume of portlandite	V_{CH}	33×10^{-6} m^3/mol	[279]
Initial Ca/Si ratio	y_0	1.7	[271]
Hydration degree	m	0.72	For sample S1
		0.83	For sample S3
Parameters in Eq. (8.75)	d	3280 mol/m^3	For sample S1
		2972 mol/m^3	For sample S3
	e	6559 mol/m^3	For sample S1
		5943 mol/m^3	For sample S3
	f	10417 mol/m^3	For sample S1
		9667 mol/m^3	For sample S3
			Bouge calculation
Lumped parameter in Eq. (8.89)	Ω_0	7.89×10^{-6}	For sample S1
		4.38×10^{-4}	For sample S3
BET specific surface area	S_{BET}	9.9 m^2/g	Intact S1
		73.1 m^2/g	Leached S1
		30.6 m^2/g	Intact S3
		145.8 m^2/g	Leached S3
Bulk density	ρ	1890 kg/m^3	Intact S1
		1390 kg/m^3	Leached S1
		1780 kg/m^3	Intact S3
		1110 kg/m^3	Leached S3

CURRICULUM VITAE

Quoc Tri Phung

Magnel Laboratory for Concrete Research, Ghent University
Technologiepark Zwijnaarde 904, 9052 Ghent, Belgium

R&D Disposal, Institute of Health, Environment and Safety
Belgian Nuclear Research Centre (SCK•CEN)
Boeretang 200, 2400 Mol, Belgium
Telephone: (32) 14 33 31 20
Email: qphung@sckcen.be

PERSONAL INFORMATION

Name:	Quoc Tri Phung
Date of Birth:	October 16, 1983
Citizenship:	Vietnamese
Gender:	Male
Marital Status:	Married
Current address:	Boeretang 204/13, 2400 Mol, Belgium

EDUCATION

03/2011 – present:	PhD candidate at Ghent University & Belgian Nuclear Research Centre Major: Concrete materials
03/2008 – 01/2010:	M.Sc, Civil & Environmental Engineering, MyongJi University, Korea Major: Concrete materials
09/2001 – 06/2006:	B.Eng, Civil Engineering, University of Civil Engineering, Vietnam Major: Technology of Building Materials

TEACHING EXPERIENCE

10/2006 – 03/2008: Assistant Lecturer, Faculty of Bridge & Road Engineering, Da Nang University of Technology, Vietnam

03/2008 – 03/2010: Tutorial Assistant, Department of Civil & Environmental Engineering, MyongJi University, Korea.

03/2010 – 03/2011: Lecturer, Faculty of Bridge & Road Engineering, Da Nang University of Technology, Vietnam

RESEARCH EXPERIENCE

03/2008 – 03/2010: Assistant, Concrete Lab MyongJi University, Korea.

03/2011 – present: PhD research student at R&D Disposal, SCK•CEN and Magnel Laboratory for Concrete Research, Ghent University

RESEARCH INTERESTS

- Degradation of cement-based materials
- Transport properties cement-based materials
- Microstructure of cement-based materials
- Self-compacting concrete, High strength concrete
- Formwork pressure of concrete
- Creep and Shrinkage in concrete
- Fracture mechanics of concrete

PROFESSIONAL MEMBERSHIPS

- American Concrete Institute (ACI). Member, since 2011
- The International Union of Laboratories and Experts in Construction Materials, Systems and Structures Member (RILEM). Member, since 2011
- Active member of RILEM Technical Committee MCT: Multi-component transport and chemical equilibrium in cement based materials, since 2012

SKILLS AND QUALIFICATIONS

- Computer skills: Microsoft Office, AutoCAD, Minitab
  Data analysis software: XRD, TGA, MIP, SEM images
  Programming: Matlab, Maple, Mathematica
  FEM analysis: COMSOL, SAP 2000

- Languages: Vietnamese (mother language), English, Dutch (beginner)

SCIENTIFIC OUTPUT

- **Q.T. Phung**, N. Maes, D. Jacques, E. Bruneel, I.V. Driessche, G. Ye, G.D. Schutter, **Effect of limestone fillers on microstructure and permeability due to carbonation of cement pastes under controlled CO_2 pressure conditions**, Constr Build Mater, (DOI: 10.1016/j.conbuildmat.2015.02.093).
- **Q.T. Phung**, N. Maes, D. Jacques, E. Jacop, A. Grade, G.D. Schutter, G. Ye, **Determination of diffusivities of dissolved gases in saturated cement-based materials**, in: International Conference on Concrete Repair, Rehabilitation and Retrofitting, ICCRRR 2015, Leipzig, Germany, (submitted).
- **Q.T. Phung**, N. Maes, D. Jacques, G.D. Schutter, G. Ye, **Decalcification of cement paste in NH4NO3 solution: Microstructural alterations and its influence on the transport properties**, in: J. Bastien, N. Rouleau, M. Fiset, M. Thomassin (Eds.) 10th fib International PhD Symposium in Civil Engineering, Québec, Canada., 2014 pp. 179 - 187.
- **Q.T. Phung**, N. Maes, D. Jacques, G.D. Schutter, G. Ye, **Microstructural and permeability changes due to accelerated Ca leaching in ammonium nitrate solution**, in: M. Grantham, P.A.M. Basheer, B. Magee, M. Soutsos (Eds.) Concrete Solutions - 5th International Conference on Concrete Repair, CRC Press, 2014 pp. 431-438.
- **Q.T. Phung**, N. Maes, D. Jacques, J. Perko, G.D. Schutter, G. Ye, **Modeling the decalcification of cement paste in ammonium nitrate solution**, in: 3rd internatinal conference on Service Life design for Infrastructure: Keynote speech, Zhuhai, China, 2014 pp. 27-40.

- **Q.T. Phung, Changes in microstructure and transport properties of cement paste due to carbonation and leaching – from experiments to phenomenological models**, Day of the PhD's, Belgian Nuclear Research Centre, Belgium, 2014 (presentation)
- **Q.T. Phung, Long-term Chemical Degradation of Cement-Based Materials and Its Impact on Transport Properties**, in: 3rd Magnel Research Seminar, Ghent University, Belgium, 2013, pp. 44-45.
- **Q.T. Phung**, R. Patel, A. Soto, S. Seetharam, J. Perko, N. Maes, D. Jacques, Y. Guang, K.v. Breugel, G.D. Schutter, **Long term degradation processes on concrete: An overview**, in: Ageing Centre Launch Event, Delft, The Netherlands, 2013 (poster).
- **Q.T. Phung, Effect of Chemical Degradation on Microstructural Changes and Transport Properties of Concrete - Phenomenological Study,** in: 14th FEA PhD Symposium, Ghent University, Belgium, 2013 (poster).
- **Q.T. Phung,** N. Maes, D. Jacques, G. De Schutter, G. Ye, **Effects of Accelerated Ca-leaching on Microstructure and Permeability of Hardened Cement Paste**, Day of the PhD's, Belgian Nuclear Research Centre, Belgium, 2013 (poster)
- **Q.T. Phung**, N. Maes, D. Jacques, G.D. Schutter, G. Ye, **A Model to Predict Carbonation of Cementitious Materials under a High CO_2 Pressure Condition**, in: 3rd International Workshop Mechanisms and Modelling of Waste/Cement Interactions, Ghent, Belgium 2013 (presentation).
- **Q.T. Phung**, N. Maes, G. De Schutter, D. Jacques, G. Ye, **Determination of water permeability of cementitious materials using a controlled constant flow method**, Constr Build Mater, 47 (2013) 1488-1496.
- D. Jacques, N. Maes, J. Perko, S.C. Seetharam, **Q.T. Phung**, R. Patel, A. Soto, S. Liu, L. Wang, G.D. Schutter, G. Ye, K.v. Breugel, **Concrete in engineered barriers for radioactive waste disposal facilities - phenomenological study and assessment of long term performance**, in: 15th International Conference on Environmental Remediation and Radioactive Waste Management - ICEM2013, Brussels, Belgium, 2013, pp. 1-10.
- **Q.T. Phung, Chemical Degradation of Cement-Based Materials and Its Impact on Transport Properties**, Day of the PhD's, Belgian Nuclear Research Centre, Belgium, 2012 (presentation)

- **Q.T. Phung**, G.D. Schutter, N. Maes, D. Jacques, G. Ye, **Measuring permeability of cementitious materials**, in: M.G. Alexander, H.-D. Beushausen, F. Dehn, P. Moyo (Eds.) Concrete Repair, Rehabilitation and Retrofitting III, CRC Press, 2012, pp. 287-295.
- **Q.T. Phung,** N. Maes, D. Jacques, G. De Schutter, G. Ye, **Measuring Hydraulic Conductivity of Cement-Based Materials**, Day of the PhD's, Belgian Nuclear Research Centre, Belgium, 2011 (poster)
- S.H. Kwon, **Q.T. Phung**, H.Y. Park, J.H. Kim, S.P. Shah, **Effect of wall friction on variation of formwork pressure over time in self-consolidating concrete**, Cement and Concrete Research, 41 (2011) 90-101.
- S.H. Kwon, S.P. Shah, **Q.T. Phung**, J.H. Kim, Y. Lee, **Intrinsic Model to Predict Formwork Pressure**, ACI Mater J, 107 (2010) 20-26.
- S.H. Kwon, **Q.T. Phung**, H.Y. Park, J.H. Kim, S.P. Shah, **Experimental study on Effect of Wall Friction on Formwork Pressure of Self-Consolidating Concrete**, in: 6th International RILEM Symposium on Self-Compacting Concrete (SCC-2010), Canada, 2010.
- S.H. Kwon, **Q.T. Phung**, J.H. Kim, **Experiment for Verification of Prediction model for SCC Formwork pressure**, in: Proceedings of the Korea Concrete Institute (KCI). Vol. 21 No. 1, pp. 217 – 218, May 2009.
- **Q.T. Phung**, S.H. H.Y. Park, **Experimental Study on Effect of Wall Friction on Formwork Pressure Exerted by Self-Consolidating Concrete**, in: Proceedings of the Korea Concrete Institute (KCI). Vol. 21 No. 2, pp. 473 – 474, November, 2009.

REFERENCES

[1] NIRAS, Synthese van het veiligheidsrapport voor de oppervlaktebergingsinrichting van categorie A-afval in Dessel, in: NIROND-TR 2012–17 N 2012, pp. 174.

[2] NIRAS, Afvalplan voor het langetermijnbeheer van geconditioneerd hoogradioactief en/of langlevend afval en overzicht van verwante vragen, in: NIROND 2011-02 N, 2011, pp. 269.

[3] K.L. Scrivener, J.F. Young, Mechanisms of Chemical Degradation of Cement-based Systems, Taylor & Francis, 1997.

[4] P. Faucon, F. Adenot, J.F. Jacquinot, J.C. Petit, R. Cabrillac, M. Jorda, Long-term behaviour of cement pastes used for nuclear waste disposal: Review of physico-chemical mechanisms of water degradation, Cement and Concrete Research, 28 (1998) 847-857.

[5] C. Galle, H. Peycelon, P. Le Bescop, S. Bejaoui, V. L'Hostis, B. Bary, P. Bouniol, C. Richet, Concrete long-term behaviour in the context of nuclear waste management: Experimental and modelling research strategy, J Phys Iv, 136 (2006) 25-38.

[6] B. Craeye, G. De Schutter, H. Van Humbeeck, A. Van Cotthem, Early age behaviour of concrete supercontainers for radioactive waste disposal, Nucl Eng Des, 239 (2009) 23-35.

[7] J.L.G. Calvo, A. Hidalgo, C. Alonso, L.F. Luco, Development of low-pH cementitious materials for HLRW repositories Resistance against ground waters aggression, Cement and Concrete Research, 40 (2010) 1290-1297.

[8] NIRAS, Evolution of the Near-Field of the ONDRAF/NIRAS Repository Concept for category B and C wastes, in: NIROND-TR 2007-07 E, 2007, pp. 154.

[9] S. Talukdar, N. Banthia, J.R. Grace, Carbonation in concrete infrastructure in the context of global climate change – Part 1: Experimental results and model development, Cement and Concrete Composites, 34 (2012) 924-930.

[10] F.P. Glasser, J. Marchand, E. Samson, Durability of concrete - Degradation phenomena involving detrimental chemical reactions, Cement and Concrete Research, 38 (2008) 226-246.

[11] R.T. Pabalan, F.P. Glasser, D.A. Pickett, G.R. Walter, S. Biswas, M.R. Juckett, L.M. Sabido, J.L. Myers, Review of Literature and Assessment of Factors Relevant to Performance of Grouted Systems for Radioactive Waste Disposal, in: CNWRA 2009-001, Center for Nuclear Waste Regulatory Analyses, San Antonio, Texas, 2009, pp. 359.

[12] F.A.L. Dullien, Porous media : fluid transport and pore structure, Academic Press, San Diego, 1992.

[13] A.P.S. Selvadurai, P. Carnaffan, A transient pressure pulse method for the measurement of permeability of a cement grout, Can J Civil Eng, 24 (1997) 489-502.

[14] H. Loosveldt, Z. Lafhaj, F. Skoczylas, Experimental study of gas and liquid permeability of a mortar, Cement and Concrete Research, 32 (2002) 1357-1363.

[15] W. Vichit-Vadakan, G.W. Scherer, Measuring permeability of rigid materials by a beam-bending method: III, cement paste, J Am Ceram Soc, 85 (2002) 1537-1544.

[16] A. Bhargava, N. Banthia, Measurement of concrete permeability under stress, Exp Techniques, 30 (2006) 28-31.

[17] G.W. Scherer, Dynamic pressurization method for measuring permeability and modulus: I. theory, Mater Struct, 39 (2006) 1041-1057.

[18] Z.C. Grasley, G.W. Scherer, D.A. Lange, J.J. Valenza, Dynamic pressurization method for measuring permeability and modulus: II. cementitious materials, Mater Struct, 40 (2007) 711-721.

[19] G.W. Scherer, J.J. Valenza, G. Simmons, New methods to measure liquid permeability in porous materials, Cement and Concrete Research, 37 (2007) 386-397.

[20] V. Picandet, D. Rangeard, A. Perrot, T. Lecompte, Permeability measurement of fresh cement paste, Cement and Concrete Research, 41 (2011) 330-338.

[21] D. Ludirdja, R.L. Berger, J.F. Young, Simple Method for Measuring Water Permeability of Concrete, Aci Mater J, 86 (1989) 433-439.

[22] C.A. Jones, Z.C. Grasley, Correlation of Radial Flow-Through and Hollow Cylinder Dynamic Pressurization Test for Measuring Permeability, J Mater Civil Eng, 21 (2009) 594-600.

[23] A.S. Eldieb, R.D. Hooton, A High-Pressure Triaxial Cell with Improved Measurement Sensitivity for Saturated Water Permeability of High-Performance Concrete, Cement and Concrete Research, 24 (1994) 854-862.

[24] A.S. Eldieb, R.D. Hooton, Water-Permeability Measurement of High-Performance Concrete Using a High-Pressure Triaxial Cell, Cement and Concrete Research, 25 (1995) 1199-1208.

[25] J.R. Nimmo, Experimental Testing of Transient Unsaturated Flow Theory at Low Water-Content in a Centrifugal Field, Water Resour Res, 26 (1990) 1951-1960.

[26] J.R. Nimmo, J. Rubin, D.P. Hammermeister, Unsaturated Flow in a Centrifugal Field - Measurement of Hydraulic Conductivity and Testing of Darcy Law, Water Resour Res, 23 (1987) 124-134.

[27] ASTM Standard D6527 - 00(2008), "Standard Test Method for Determining Unsaturated and Saturated Hydraulic Conductivity in Porous Media by Steady-State Centrifugation", in, ASTM International, West Conshohocken, PA, 2008, pp. 10.

[28] J.L. Conca, J. Wright, Diffusion And Flow In Gravel, Soil, And Whole Rock, Applied Hydrogeology, 1 (1992) 5-24.

[29] W.F. Brace, J.B. Walsh, W.T. Frangos, Permeability of Granite under High Pressure, J Geophys Res, 73 (1968) 2225-2236.

[30] H. Meziani, Gas permeability measurements of cement-based materials under hydrostatic test conditions using a low-transient method, Magazine of Concrete Research, 58 (2006) 489-503.

[31] G.W. Scherer, Measuring permeability of rigid materials by a beam-bending method: I, theory, J Am Ceram Soc, 83 (2000) 2231-2239.

[32] G.W. Scherer, Bending of Gel Beams - Method for Characterizing Elastic Properties and Permeability, J Non-Cryst Solids, 142 (1992) 18-35.

[33] W. Vichit-Vadakan, G.W. Scherer, Measuring permeability of rigid materials by a beam-bending method: II, porous glass, J Am Ceram Soc, 83 (2000) 2240-2245.

[34] W. Vichit-Vadakan, G.W. Scherer, Measuring permeability and stress relaxation of young cement paste by beam bending, Cement and Concrete Research, 33 (2003) 1925-1932.

[35] G.W. Scherer, H. Hdach, J. Phalippou, Thermal Expansion of Gels: A Novel Method for Measuring Permeability, J Non-Cryst Solids, 130 (1991) 157-170.

[36] G.W. Scherer, Measuring permeability by the thermal expansion method for rigid or highly permeable gels, Journal of Sol-Gel Science and Technology, 3 (1994) 31-40.

[37] G.W. Scherer, Thermal expansion kinetics: Method to measure permeability of cementitious materials: I, theory, J Am Ceram Soc, 83 (2000) 2753-2761.

[38] H. Ai, J.F. Young, G.W. Scherer, Thermal expansion kinetics: Method to measure permeability of cementitious materials: II, application to hardened cement pastes, J Am Ceram Soc, 84 (2001) 385-391.

[39] C.A. Jones, Z.C. Grasley, Correlation of hollow and solid cylinder dynamic pressurization tests for measuring permeability, Cement and Concrete Research, 39 (2009) 345-352.

[40] L. Alarcon-Ruiz, M. Brocato, S. Dal Pont, A. Feraille, Size Effect in Concrete Intrinsic Permeability Measurements, Transport Porous Med, 85 (2010) 541-564.

[41] N. Hearn, Self-sealing, autogenous healing and continued hydration: What is the difference?, Mater Struct, 31 (1998) 563-567.

[42] N. Hearn, C.T. Morley, Self-sealing property of concrete - Experimental evidence, Mater Struct, 30 (1997) 404-411.

[43] C. Edvardsen, Water permeability and autogenous healing of cracks in concrete, Aci Mater J, 96 (1999) 448-454.

[44] V. Picandet, A. Khelidj, H. Bellegou, Crack effects on gas and water permeability of concretes, Cement and Concrete Research, 39 (2009) 537-547.

[45] J.-P. Charron, E. Denarié, E. Brühwiler, Transport properties of water and glycol in an ultra high performance fiber reinforced concrete (UHPFRC) under high tensile deformation, Cement and Concrete Research, 38 (2008) 689-698.

[46] B.J. Christensen, T.O. Mason, H.M. Jennings, Comparison of measured and calculated permeabilities for hardened cement pastes, Cement and Concrete Research, 26 (1996) 1325-1334.

[47] S. Goto, D.M. Roy, The Effect of W-C Ratio and Curing Temperature on the Permeability of Hardened Cement Paste, Cement and Concrete Research, 11 (1981) 575-579.

[48] P. Soongswang, M. Tia, D. Bloomquist, Factors Affecting the Strength and Permeability of Concrete Made with Porous Limestone, Aci Mater J, 88 (1991) 400-406.

[49] H.S. Wong, R.W. Zimmerman, N.R. Buenfeld, Estimating the permeability of cement pastes and mortars using image analysis and effective medium theory, Cement and Concrete Research, 42 (2012) 476-483.

[50] Z. Lafhaj, M. Goueygou, A. Djerbi, M. Kaczmarek, Correlation between porosity, permeability and ultrasonic parameters of mortar with variable water/cement ratio and water content, Cement and Concrete Research, 36 (2006) 625-633.

[51] A.J. Katz, A.H. Thompson, Quantitative Prediction of Permeability in Porous Rock, Phys Rev B, 34 (1986) 8179-8181.

[52] B.B. Das, B. Kondraivendhan, Implication of pore size distribution parameters on compressive strength, permeability and hydraulic diffusivity of concrete, Constr Build Mater, 28 (2012) 382-386.

[53] P.C. Carman, Fluid flow through granular beds, T I Chem Eng-Lond, 15 (1937) 150-166.

[54] J. Kozeny, Über kapillare Leitung des Wassers im Boden, Akad Wiss Wien, 136 (1927) 271-306.

[55] E.J. Garboczi, D.P. Bentz, Computer simulation of the diffusivity of cement-based materials, J Mater Sci, 27 (1992) 2083-2092.

[56] X.Y. Lu, Application of the Nernst-Einstein equation to concrete, Cement and Concrete Research, 27 (1997) 293-302.

[57] E.J. Garboczi, Permeability, Diffusivity, and Microstructural Parameters - a Critical-Review, Cement and Concrete Research, 20 (1990) 591-601.

[58] A.S. Eldieb, R.D. Hooton, Evaluation of the Katz-Thompson Model for Estimating the Water Permeability of Cement-Based Materials from Mercury Intrusion Porosimetry Data, Cement and Concrete Research, 24 (1994) 443-455.

[59] B. Pradhan, M. Nagesh, B. Bhattacharjee, Prediction of the hydraulic diffusivity from pore size distribution of concrete, Cement and Concrete Research, 35 (2005) 1724-1733.

[60] P. Xu, B. Yu, Developing a new form of permeability and Kozeny–Carman constant for homogeneous porous media by means of fractal geometry, Adv Water Resour, 31 (2008) 74-81.

[61] H.A. Nooruddin, M.E. Hossain, Modified Kozeny–Carmen correlation for enhanced hydraulic flow unit characterization, J Petrol Sci Eng, 80 (2011) 107-115.

[62] I. Pop, D.B. Ingham, Transport Phenomena in Porous Media II, Elsevier Science, 2002.

[63] S. Benbow, C. Watson, D. Savage, Investigating Conceptual Models for Physical Property Couplings in Solid Solution Models of Cement, in: SKI report 2005:64, Statens kärnkraftinspektion, 2005, pp. 137.

[64] J.P. Ollivier, M. Massat, Permeability and Microstructure of Concrete - a Review of Modeling, Cement and Concrete Research, 22 (1992) 503-514.

[65] N. Neithalath, J. Weiss, J. Olek, Characterizing Enhanced Porosity Concrete using electrical impedance to predict acoustic and hydraulic performance, Cement and Concrete Research, 36 (2006) 2074-2085.

[66] X.J. Wang, K.V. Subramaniam, Ultrasonic monitoring of capillary porosity and elastic properties in hydrating cement paste, Cement Concrete Comp, 33 (2011) 389-401.

[67] G. Ye, P. Lura, K. van Breugel, Modelling of water permeability in cementitious materials, Mater Struct, 39 (2006) 877-885.

[68] M. Zalzale, P.J. McDonald, K.L. Scrivener, A 3D lattice Boltzmann effective media study: understanding the role of C-S-H and water saturation on the permeability of cement paste, Model Simul Mater Sc, 21 (2013) 085016.

[69] L.J. Klinkenberg, The Permeability of Porous Media to Liquids and Gases, in: Drilling and Production Practice, American Petroleum Institute, 1941, pp. 14.

[70] B.V. Iversen, P. Moldrup, P. Schjonning, O.H. Jacobsen, Field Application of a Portable Air Permeameter to Characterize Spatial Variability in Air and Water Permeability, Vadose Zone J, 2 (2003) 618-626.

[71] P. Loll, P. Moldrup, P. Schjonning, H. Riley, Predicting saturated hydraulic conductivity from air permeability: Application in stochastic water infiltration modeling, Water Resour Res, 35 (1999) 2387-2400.

[72] M. García-Gutiérrez, J.L. Cormenzana, T. Missana, M. Mingarro, J. Molinero, Overview of laboratory methods employed for obtaining diffusion coefficients in FEBEX compacted bentonite, Journal of Iberian Geology, 32 (2006) 37-53.

[73] J. Sercombe, R. Vidal, C. Galle, F. Adenot, Experimental study of gas diffusion in cement paste, Cement and Concrete Research, 37 (2007) 579-588.

[74] G.J.G. Gluth, W. Zhang, M. Gaggl, B. Hillemeier, F. Behrendt, Multicomponent gas diffusion in hardened cement paste at temperatures up to 350°C, Cement and Concrete Research, 42 (2012) 656-664.

[75] M. Daimon, T. Akiba, R. Kondo, Through Pore Size Distribution and Kinetics of the Carbonation Reaction of Portland Cement Mortars, J Am Ceram Soc, 54 (1971) 423-428.

[76] L.C. Chen, D.L. Katz, Diffusion of Methane Through Concrete, ACI Journal 75 (1978) 673-679.

[77] V.G. Papadakis, C.G. Vayenas, M.N. Fardis, Physical and Chemical Characteristics Affecting the Durability of Concrete, Aci Mater J, 88 (1991) 186-196.

[78] F. Tittarelli, Oxygen diffusion through hydrophobic cement-based materials, Cement and Concrete Research, 39 (2009) 924-928.

[79] S.W. Yu, C.L. Page, Diffusion in cementitious materials: 1. Comparative study of chloride and oxygen diffusion in hydrated cement pastes, Cement and Concrete Research, 21 (1991) 581-588.

[80] M. Castellote, C. Alonso, C. Andrade, G.A. Chadbourn, C.L. Page, Oxygen and chloride diffusion in cement pastes as a validation of chloride diffusion coefficients obtained by steady-state migration tests, Cement and Concrete Research, 31 (2001) 621-625.

[81] J. Crank, The mathematics of diffusion, Clarendon Press, 1975.

[82] J.O.M. Bockris, A.K.N. Reddy, Modern Electrochemistry: An Introduction to an Interdisciplinary Area, Plenum Press, 1974.

[83] T. Luping, L.-O. Nilsson, Rapid Determination of the Chloride Diffusivity in Concrete by Applying an Electric Field, Aci Mater J, 89 (1993) 49-53.

[84] M. Castellote, C. Andrade, C. Alonso, Measurement of the steady and non-steady-state chloride diffusion coefficients in a migration test by means of monitoring the conductivity in the anolyte chamber - Comparison with natural diffusion tests, Cement and Concrete Research, 31 (2001) 1411-1420.

[85] B. Park, S.Y. Jang, J.-Y. Cho, J.Y. Kim, A novel short-term immersion test to determine the chloride ion diffusion coefficient of cementitious materials, Constr Build Mater, 57 (2014) 169-178.

[86] ASTM, ASTM Standard Test Method for Determining the Apparent Chloride Diffusion Coefficient of Cementitious Mixtures by Bulk Diffusion (C 1556-04), in, 2004.

[87] Nordtest, Concrete, hardened: Accelerated chloride penetration (NT BUILD 443), in, 1995.

[88] T. Luping, J. Gulikers, On the mathematics of time-dependent apparent chloride diffusion coefficient in concrete, Cement and Concrete Research, 37 (2007) 589-595.

[89] M. Aguayo, P. Yang, K. Vance, G. Sant, N. Neithalath, Electrically driven chloride ion transport in blended binder concretes: Insights from experiments and numerical simulations, Cement and Concrete Research, 66 (2014) 1-10.

[90] C.C. Yang, S.C. Chiang, L.C. Wang, Estimation of the chloride diffusion from migration test using electrical current, Constr Build Mater, 21 (2007) 1560-1567.

[91] O. Truc, J.P. Ollivier, M. Carcasses, A new way for determining the chloride diffusion coefficient in concrete from steady state migration test, Cement and Concrete Research, 30 (2000) 217-226.

[92] ASTM, Standard Test Method for Electrical Indication of Concrete's Ability to Resist Chloride Ion Penetration (C1202-97), in, 1997.

[93] NT BUILD 492: Concrete, mortar and cement-based repair materials: Chloride migration coefficient from non-steady-state migration experiments in, Nordtest, Finland, 1999.

[94] C. Andrade, M.A. Sanjuán, A. Recuero, O. Río, Calculation of chloride diffusivity in concrete from migration experiments, in non steady-state conditions, Cement and Concrete Research, 24 (1994) 1214-1228.

[95] N. Olsson, V. Baroghel-Bouny, L.-O. Nilsson, M. Thiery, Non-saturated ion diffusion in concrete – A new approach to evaluate conductivity measurements, Cement and Concrete Composites, 40 (2013) 40-47.

[96] A.T.C. Guimaraes, M.A. Climent, G. de Vera, F.J. Vicente, F.T. Rodrigues, C. Andrade, Determination of chloride diffusivity through partially saturated Portland cement concrete by a simplified procedure, Constr Build Mater, 25 (2011) 785-790.

[97] C. Sun, J. Chen, J. Zhu, M. Zhang, J. Ye, A new diffusion model of sulfate ions in concrete, Constr Build Mater, 39 (2013) 39-45.

[98] H.-Y. Moon, S.-T. Lee, H.-S. Kim, S.-S. Kims, Experimental Study on the Sulfate Resistance of Concrete Blended Ground Granulated Blast-furnace Slag for Recycling, Geosystem Engineering, 5 (2002) 67-73.

[99] P.J. Tumidajski, I. Turc, A rapid test for sulfate ingress into concrete, Cement and Concrete Research, 25 (1995) 924-928.

[100] J. Condor, K. Asghari, D. Unatrakarn, Experimental Results of Diffusion Coefficient of Sulfate Ions in Cement Type 10 and Class G, 10th International Conference on Greenhouse Gas Control Technologies, 4 (2011) 5267-5274.

[101] P.F. McGrath, R.D. Hooton, Influence of voltage on chloride diffusion coefficients from chloride migration tests, Cement and Concrete Research, 26 (1996) 1239-1244.

[102] G.A. Narsillo, R. Li, P. Pivonka, D.W. Smith, Comparative study of methods used to estimate ionic diffusion coefficients using migration tests, Cement and Concrete Research, 37 (2007) 1152-1163.

[103] L. Tong, O.E. Gjørv, Chloride diffusivity based on migration testing, Cement and Concrete Research, 31 (2001) 973-982.

[104] G.E. Archie, The Electrical Resistivity Log as an Aid in Determining Some Reservoir Characteristics.

[105] P.J. Tumidajski, A.S. Schumacher, S. Perron, P. Gu, J.J. Beaudoin, On the relationship between porosity and electrical resistivity in cementitious systems, Cement and Concrete Research, 26 (1996) 539-544.

[106] M.R. Nokken, R.D. Hooton, Using pore parameters to estimate permeability or conductivity of concrete, Mater Struct, 41 (2008) 1-16.

[107] B.H. Oh, S.Y. Jang, Prediction of diffusivity of concrete based on simple analytic equations, Cement and Concrete Research, 34 (2004) 463-480.

[108] S. Bejaoui, B. Bary, Modeling of the link between microstructure and effective diffusivity of cement pastes using a simplified composite model, Cement and Concrete Research, 37 (2007) 469-480.

[109] P. Halamickova, R.J. Detwiler, D.P. Bentz, E.J. Garboczi, Water Permeability and Chloride-Ion Diffusion in Portland-Cement Mortars - Relationship to Sand Content and Critical Pore Diameter, Cement and Concrete Research, 25 (1995) 790-802.

[110] L. Liu, H.S. Chen, W. Sun, G. Ye, Microstructure-based modeling of the diffusivity of cement paste with micro-cracks, Constr Build Mater, 38 (2013) 1107-1116.

[111] M.Z. Zhang, G.A. Ye, K. van Breugel, Microstructure-based modeling of water diffusivity in cement paste, Constr Build Mater, 25 (2011) 2046-2052.

[112] M. Zhang, Y. He, G. Ye, D.A. Lange, K.v. Breugel, Computational investigation on mass diffusivity in Portland cement paste based on X-ray computed microtomography (μCT) image, Constr Build Mater, 27 (2012) 472-481.

[113] Y.F. Houst, Carbonation Shrinkage of Hydrated Cement Paste, in: Proc 4th CANMET/ACI International Conference on Durability of Concrete, CANMET, Ottawa, Canada, 1997, pp. 481-491.

[114] E.G. Swenson, P.J. Sereda, Mechanism of the carbonatation shrinkage of lime and hydrated cement, Journal of Applied Chemistry, 18 (1968) 111-117.

[115] A. Hidalgo, C. Domingo, C. Garcia, S. Petit, C. Andrade, C. Alonso, Microstructural changes induced in Portland cement-based materials due to natural and supercritical carbonation, J Mater Sci, 43 (2008) 3101-3111.

[116] V.G. Papadakis, C.G. Vayenas, M.N. Fardis, Experimental Investigation and Mathematical-Modeling of the Concrete Carbonation Problem, Chem Eng Sci, 46 (1991) 1333-1338.

[117] V.G. Papadakis, C.G. Vayenas, M.N. Fardis, Fundamental Modeling and Experimental Investigation of Concrete Carbonation, Aci Mater J, 88 (1991) 363-373.

[118] E.J. Reardon, B.R. James, J. Abouchar, High Pressure Carbonation of Cementitious Grout, Cement and Concrete Research, 19 (1989) 385-399.

[119] M. Fernandez Bertos, S.J.R. Simons, C.D. Hills, P.J. Carey, A review of accelerated carbonation technology in the treatment of cement-based materials and sequestration of CO(2), J Hazard Mater, 112 (2004) 193-205.

[120] B. Lagerblad, Carbon dioxide uptake during concrete life cycle: State of the art, Swedish Cement and Concrete Research Institute, 2005.

[121] J.J. Chen, J.J. Thomas, H.F.W. Taylor, H.M. Jennings, Solubility and structure of calcium silicate hydrate, Cement and Concrete Research, 34 (2004) 1499-1519.

[122] M.A. Venhuis, E.J. Reardon, Vacuum method for carbonation of cementitious wasteforms, Environ Sci Technol, 35 (2001) 4120-4125.

[123] V.G. Papadakis, M.N. Fardis, C.G. Vayenas, Fundamental Concrete Carbonation Model and Application to Durability of Reinforced Concrete, Durability of Building Materials and Components, (1991) 12.

[124] Š. Zdeněk, Carbonization of porous concrete and its main binding components, Cement and Concrete Research, 1 (1971) 645-662.

[125] A. Dauzeres, P. Le Bescop, P. Sardini, C. Cau Dit Coumes, Physico-chemical investigation of clayey/cement-based materials interaction in the context of geological waste disposal: Experimental approach and results, Cement and Concrete Research, 40 (2010) 1327-1340.

[126] M.D. Craen, L. Wang, M.V. Geet, H. Moors, Geochemistry of Boom Clay pore water at the Mol site, in: SCK•CEN-BLG-990 SCK•CEN, Mol, Belgium, 2004.

[127] C.D. Atis, Accelerated carbonation and testing of concrete made with fly ash, Constr Build Mater, 17 (2003) 147-152.

[128] L. Deceukelaire, D. Vannieuwenburg, Accelerated Carbonation of a Blast-Furnace Cement Concrete, Cement and Concrete Research, 23 (1993) 442-452.

[129] L. Fernández-Carrasco, D. Torréns-Martín, S. Martínez-Ramírez, Carbonation of ternary building cementing materials, Cement and Concrete Composites, 34 (2012) 1180-1186.

[130] A. Morandeau, M. Thiéry, P. Dangla, Investigation of the carbonation mechanism of CH and C-S-H in terms of kinetics, microstructure changes and moisture properties, Cement and Concrete Research, 56 (2014) 153-170.

[131] F. Lollini, E. Redaelli, L. Bertolini, Effects of portland cement replacement with limestone on the properties of hardened concrete, Cement and Concrete Composites, 46 (2014) 32-40.

[132] P.H.R. Borges, J.O. Costa, N.B. Milestone, C.J. Lynsdale, R.E. Streatfield, Carbonation of CH and C-S-H in composite cement pastes containing high amounts of BFS, Cement and Concrete Research, 40 (2010) 284-292.

[133] H. Kinoshita, C. Circhirillo, I. SanMartin, C.A. Utton, P.H.R. Borges, C.J. Lynsdale, N.B. Milestone, Carbonation of composite cements with high mineral admixture content used for radioactive waste encapsulation, Miner Eng, 59 (2014) 107-114.

[134] Y.-s. Ji, M. Wu, B. Ding, F. Liu, F. Gao, The experimental investigation of width of semi-carbonation zone in carbonated concrete, Constr Build Mater, 65 (2014) 67-75.

[135] A. Younsi, P. Turcry, A. Aït-Mokhtar, S. Staquet, Accelerated carbonation of concrete with high content of mineral additions: Effect of interactions between hydration and drying, Cement and Concrete Research, 43 (2013) 25-33.

[136] M. Castellote, C. Andrade, X. Turrillas, J. Campo, G.J. Cuello, Accelerated carbonation of cement pastes in situ monitored by neutron diffraction, Cement and Concrete Research, 38 (2008) 1365-1373.

[137] M. Castellote, L. Fernandez, C. Andrade, C. Alonso, Chemical changes and phase analysis of OPC pastes carbonated at different CO_2 concentrations, Mater Struct, 42 (2009) 515-525.

[138] D.N. Huntzinger, Carbon dioxide sequestration in cement kiln dust through mineral carbonation, in: Geological and Mining Engineering and Sciences, Michigan Technological University, 2006, pp. 178.

[139] D.N. Huntzinger, J.S. Gierke, S.K. Kawatra, T.C. Eisele, L.L. Sutter, Carbon Dioxide Sequestration in Cement Kiln Dust through Mineral Carbonation, Environ Sci Technol, 43 (2009) 1986-1992.

[140] E. Rendek, G. Ducom, P. Germain, Carbon dioxide sequestration in municipal solid waste incinerator (MSWI) bottom ash, J Hazard Mater, 128 (2006) 73-79.

[141] M.A. Venhuis, E.J. Reardon, Carbonation of cementitious wasteforms under supercritical and high pressure subcritical conditions, Environ Technol, 24 (2003) 877-887.

[142] T. Hartmann, P. Paviet-Hartmann, J.B. Rubin, M.R. Fitzsimmons, K.E. Sickafus, The effect of supercritical carbon dioxide treatment on the leachability and structure of cemented radioactive waste-forms, Waste Manage, 19 (1999) 355-361.

[143] V. Rostami, Y. Shao, A. Boyd, Carbonation Curing versus Steam Curing for Precast Concrete Production, J Mater Civil Eng, 24 (2012) 1221-1229.

[144] S. Kashef-Haghighi, S. Ghoshal, CO2 Sequestration in Concrete through Accelerated Carbonation Curing in a Flow-through Reactor, Ind Eng Chem Res, 49 (2009) 1143-1149.

[145] C.D. Hills, D.C. Johnson, C.L. MacLeod, P.J. Carey, Solidification of stainless steel slag by accelerated carbonation, Environ Technol, 24 (2003) 671-678.

[146] RILEM, CPC-18 Measurement of hardened concrete carbonation depth, Mater Struct, 21 (1988) 453-455.

[147] C.F. Chang, J.W. Chen, The experimental investigation of concrete carbonation depth, Cement and Concrete Research, 36 (2006) 1760-1767.

[148] G. Villain, G. Platret, Two experimental methods to determine carbonation profiles in concrete, Aci Mater J, 103 (2006) 265-271.

[149] G. Villain, M. Thiery, Gammadensimetry: A method to determine drying and carbonation profiles in concrete, Ndt&E Int, 39 (2006) 328-337.

[150] P.A. Slegers, P.G. Rouxhet, Carbonation of the hydration products of tricalcium silicate, Cement and Concrete Research, 6 (1976) 381-388.

[151] N.V. Vagenas, A. Gatsouli, C.G. Kontoyannis, Quantitative analysis of synthetic calcium carbonate polymorphs using FT-IR spectroscopy, Talanta, 59 (2003) 831-836.

[152] Q.T. Phung, N. Maes, G. De Schutter, D. Jacques, G. Ye, A methodology to study carbonation of cement paste and its effect on permeability, in: 4th International Conference

on Accelerated Carbonation for Environmental and Materials Engineering (ACEME-2013), 2013, pp. 459-463.

[153] E. Liteanu, C.J. Spiers, Fracture healing and transport properties of wellbore cement in the presence of supercritical CO2, Chem Geol, 281 (2011) 195-210.

[154] P.A. Claisse, H. El-Sayad, I.G. Shaaban, Permeability and pore volume of carbonated concrete, Aci Mater J, 96 (1999) 378-381.

[155] P. Borges, N. Milestone, J. Costa, C. Lynsdale, T. Panzera, A. Christophoro, Carbonation durability of blended cement pastes used for waste encapsulation, Mater Struct, (2011) 1-16.

[156] V.T. Ngala, C.L. Page, Effects of carbonation on pore structure and diffusional properties of hydrated cement pastes, Cement and Concrete Research, 27 (1997) 995-1007.

[157] S.E. Pihlajavaara, Some results of the effect of carbonation on the porosity and pore size distribution of cement paste, Mat Constr, 1 (1968) 521-527.

[158] L. Mo, D.K. Panesar, Effects of accelerated carbonation on the microstructure of Portland cement pastes containing reactive MgO, Cement and Concrete Research, 42 (2012) 769-777.

[159] J.J. Thomas, J. Hsieh, H.M. Jennings, Effect of carbonation on the nitrogen BET surface area of hardened portland cement paste, Advanced Cement Based Materials, 3 (1996) 76-80.

[160] Y.F. Houst, The role of moisture in the carbonation of cementitious materials, Internationale Zeitschrift für Bauinstandsetzen und Baudenkmalpflege, 2 (1996) 49-66.

[161] D. Chen, E. Sakai, M. Daimon, Y. Ohba, Carbonation of low heat portland cement paste precured in water for different time, Journal of University of Science and Technology Beijing, Mineral, Metallurgy, Material, 14 (2007) 178-184.

[162] B. Johannesson, P. Utgenannt, Microstructural changes caused by carbonation of cement mortar, Cement and Concrete Research, 31 (2001) 925-931.

[163] K.S. You, S.H. Lee, S.H. Hwang, J.W. Ahn, Effect of CO2 Carbonation on the Chemical Properties of Waste Cement: CEC and the Heavy Metal Adsorption Ability, Mater Trans, 52 (2011) 1679-1684.

[164] C.A. Rochelle, G. Purser, A.E. Milodowski, D. Noy, D. Wagner, A. Butcher, J. Harrington, CO2 migration and reaction in cementitious repositories : a summary of work conducted as part of the FORGE project, in, Nottingham, UK, 2013.

[165] P.J. Dewaele, E.J. Reardon, R. Dayal, Permeability and Porosity Changes Associated with Cement Grout Carbonation, Cement and Concrete Research, 21 (1991) 441-454.

[166] H.W. Song, S.J. Kwon, Permeability characteristics of carbonated concrete considering capillary pore structure, Cement and Concrete Research, 37 (2007) 909-915.

[167] M. Lesti, C. Tiemeyer, J. Plank, CO_2 stability of Portland cement based well cementing systems for use on carbon capture & storage (CCS) wells, Cement and Concrete Research, 45 (2013) 45-54.

[168] A. Fabbri, J. Corvisier, A. Schubnel, F. Brunet, B. Goffe, G. Rimmele, V. Barlet-Gouedard, Effect of carbonation on the hydro-mechanical properties of Portland cements, Cement and Concrete Research, 39 (2009) 1156-1163.

[169] K. Yokozeki, K. Watanabe, N. Sakata, N. Otsuki, Modeling of leaching from cementitious materials used in underground environment, Applied Clay Science, 26 (2004) 293-308.

[170] U.R. Berner, Modeling the Incongruent Dissolution of Hydrated Cement Minerals, Radiochim Acta, 44-5 (1988) 387-393.

[171] C. Pichler, A. Saxer, R. Lackner, Differential-scheme based dissolution/diffusion model for calcium leaching in cement-based materials accounting for mix design and binder composition, Cement and Concrete Research, 42 (2012) 686-699.

[172] F.H. Heukamp, Chemomechanics of calcium leaching of cement-based materials at different scales: the role of CH-dissolution and C-S-H degradation on strength and durability performance of materials and structures, in: Dept of Civil and Environmental Engineering, Massachusetts Institute of Technology, 2003.

[173] H. Saito, A. Deguchi, Leaching tests on different mortars using accelerated electrochemical method, Cement and Concrete Research, 30 (2000) 1815-1825.

[174] K. Haga, S. Sutou, M. Hironaga, S. Tanaka, S. Nagasaki, Effects of porosity on leaching of Ca from hardened ordinary Portland cement paste, Cement and Concrete Research, 35 (2005) 1764-1775.

[175] J. Jain, N. Neithalath, Analysis of calcium leaching behavior of plain and modified cement pastes in pure water, Cement and Concrete Composites, 31 (2009) 176-185.

[176] A. Bertron, J. Duchesne, G. Escadeillas, Accelerated tests of hardened cement pastes alteration by organic acids: analysis of the pH effect, Cement and Concrete Research, 35 (2005) 155-166.

[177] L. De Windt, P. Devillers, Modeling the degradation of Portland cement pastes by biogenic organic acids, Cement and Concrete Research, 40 (2010) 1165-1174.

[178] E.J. Butcher, J. Borwick, N. Collier, S.J. Williams, Long term leachate evolution during flow-through leaching of a vault backfill (NRVB), Mineralogical Magazine, 76 (2012) 3023-3031.

[179] C. Carde, G. Escadeillas, A.H. François, Use of ammonium nitrate solution to simulate and accelerate the leaching of cement pastes due to deionized water, Magazine of Concrete Research, 49 (1997) 295-301.

[180] J.J. Chen, J.J. Thomas, H.A. Jennings, Decalcification shrinkage of cement paste, Cement and Concrete Research, 36 (2006) 801-809.

[181] T. de Larrard, S. Poyet, M. Pierre, F. Benboudjema, P. Le Bescop, J.-B. Colliat, J.-M. Torrenti, Modelling the influence of temperature on accelerated leaching in ammonium nitrate, Eur J Environ Civ En, 16 (2012) 322-335.

[182] V.H. Nguyen, H. Colina, J.M. Torrenti, C. Boulay, B. Nedjar, Chemo-mechanical coupling behaviour of leached concrete: Part I: Experimental results, Nucl Eng Des, 237 (2007) 2083-2089.

[183] H. Yang, L. Jiang, Y. Zhang, Q. Pu, Y. Xu, Predicting the calcium leaching behavior of cement pastes in aggressive environments, Constr Build Mater, 29 (2012) 88-96.

[184] S. Poyet, P. Le Bescop, M. Pierre, L. Chomat, C. Blanc, Accelerated leaching of cementitious materials using ammonium nitrate (6M): influence of test conditions, Eur J Environ Civ En, 16 (2012) 336-351.

[185] C. Perlot, J. Verdier, M. Carcasses, Influence of cement type on transport properties and chemical degradation: Application to nuclear waste storage, Mater Struct, 39 (2006) 511-523.

[186] C. Gallé, H. Peycelon, P.L. Bescop, Effect of an accelerated chemical degradation on water permeability and pore structure of cementbased materials, Adv Cem Res, 16 (2004) 105-114.

[187] M. Berra, F. Carassiti, T. Mangialardi, A.E. Paolini, M. Sebastiani, Leaching behaviour of cement pastes containing nanosilica, in: Adv Cem Res, 2013, pp. 352-361.

[188] I. Segura, M. Molero, S. Aparicio, J.J. Anaya, A. Moragues, Decalcification of cement mortars: Characterisation and modelling, Cement and Concrete Composites, 35 (2013) 136-150.

[189] A. Cheng, S.J. Chao, W.T. Lin, Effects of Leaching Behavior of Calcium Ions on Compression and Durability of Cement-Based Materials with Mineral Admixtures, Materials, 6 (2013) 1851-1872.

[190] F. Agostini, Z. Lafhaj, F. Skoczylas, H. Loodsveldt, Experimental study of accelerated leaching on hollow cylinders of mortar, Cement and Concrete Research, 37 (2007) 71-78.

[191] I. Yurtdas, S.Y. Xie, N. Burlion, J.F. Shao, J. Saint-Marc, A. Garnier, Deformation and Permeability Evolution of Petroleum Cement Paste Subjected to Chemical Degradation Under Temperature, Transport Porous Med, 86 (2011) 719-736.

[192] K. Haga, M. Shibata, M. Hironaga, S. Tanaka, S. Nagasaki, Change in pore structure and composition of hardened cement paste during the process of dissolution, Cement and Concrete Research, 35 (2005) 943-950.

[193] J.J.P. Bel, S.M. Wickham, R.M.F. Gens, Development of the Supercontainer Design for Deep Geological Disposal of High-Level Heat Emitting Radioactive Waste in Belgium, MRS Online Proceedings Library, 932 (2006) null-null.

[194] B. Craeye, Early-age thermo-mechanical behaviour of concrete Supercontainers for radwaste disposal, in: Department of Structural engineering, Ghent University, Ghent, 2010, pp. 376.

[195] G.D. Schutter, J. Gibbs, P. Domone, P.J. Bartos, Self-compacting Concrete, Whittles Publishing, Dunbeath, Scotland, UK, 2008.

[196] I. Wemaere, J. Marivoet, S. Labat, R. Beaufays, T. Maes, Mol -1 borehole (April-May 1997). Core manipulations and determination of hydraulic conductivities in the laboratory, in, SCK•CEN report R-3590A, Mol, Belgium, 2002, pp. 61.

[197] E. Jacops, G. Volckaert, N. Maes, E. Weetjens, J. Govaerts, Determination of gas diffusion coefficients in saturated porous media: He and CH_4 diffusion in Boom Clay, Applied Clay Science, 83–84 (2013) 217-223.

[198] M.T. van Genuchten, A Closed-Form Equation for Predicting the Hydraulic Conductivity of Unsaturated Soils, Soil Sci Soc Am J, 44 (1980) 892-898.

[199] F.H. Heukamp, F.J. Ulm, J.T. Germaine, Mechanical properties of calcium-leached cement pastes: Triaxial stress states and the influence of the pore pressures, Cement and Concrete Research, 31 (2001) 767-774.

[200] N.B. Winter, Scanning Electron Microscopy of Cement and Concrete, WHD Microanalysis, 2012.

[201] H.N. Walker, D.S. Lane, P.E. Stutzman, Petrographic methods of examining hardened concrete: a petrographic manual, in, Federal Highway Administration, McLean, VA, 2006, pp. 351.

[202] N.C. Collier, J.H. Sharp, N.B. Milestone, J. Hill, I.H. Godfrey, The influence of water removal techniques on the composition and microstructure of hardened cement pastes, Cement and Concrete Research, 38 (2008) 737-744.

[203] P.E. Stutzman, J.R. Clifton, Specimen Preparation for Scanning Electron Microscopy, in: L. Jany, A. Nisperos (Eds.) Proceedings of the Twenty- First International Conference on Cement Microscopy, Las Vegas, 1999, pp. 10-22.

[204] E.W. Washburn, Note on a Method of Determining the Distribution of Pore Sizes in a Porous Material, P Natl Acad Sci USA, 7 (1921) 115-116.

[205] S. Diamond, Mercury porosimetry - An inappropriate method for the measurement of pore size distributions in cement-based materials, Cement and Concrete Research, 30 (2000) 1517-1525.

[206] K.K. Aligizaki, Pore Structure of Cement-Based Materials: Testing, Interpretation and Requirements, Taylor & Francis, 2005.

[207] C. Gallé, Effect of drying on cement-based materials pore structure as identified by mercury intrusion porosimetry: A comparative study between oven-, vacuum-, and freeze-drying, Cement and Concrete Research, 31 (2001) 1467-1477.

[208] T.C. Powers, T.L. Brownyard, Studies of the physical properties of hardened portland cement paste, Research Bulletin 22, Portland Cement Association, 1948.

[209] V. Rostami, Y. Shao, A.J. Boyd, Z. He, Microstructure of cement paste subject to early carbonation curing, Cement and Concrete Research, 42 (2012) 186-193.

[210] L. Alarcon-Ruiz, G. Platret, E. Massieu, A. Ehrlacher, The use of thermal analysis in assessing the effect of temperature on a cement paste, Cement and Concrete Research, 35 (2005) 609-613.

[211] A. Chaipanich, T. Nochaiya, Thermal analysis and microstructure of Portland cement-fly ash-silica fume pastes, J Therm Anal Calorim, 99 (2010) 487-493.

[212] R. Jenkins, J.L. De Vries, An Introduction to X-ray Powder Diffractometry, Wiley, 2012.

[213] A. Zürz, I. Odler, XRD studies of portlandite present in hydrated Portland cement paste, in: Adv Cem Res, 1987, pp. 27-30.

[214] K.L. Scrivener, A. Fullmann, E. Gallucci, G. Walenta, E. Bermejo, Quantitative study of Portland cement hydration by X-ray diffraction/Rietveld analysis and independent methods, Cement and Concrete Research, 34 (2004) 1541-1547.

[215] G. Walenta, T. Füllmann, Advances in quantitative XRD analysis for clinker, cements, and cementitious additions, Powder Diffr, 19 (2004) 40-44.

[216] G. Le Saoût, V. Kocaba, K. Scrivener, Application of the Rietveld method to the analysis of anhydrous cement, Cement and Concrete Research, 41 (2011) 133-148.

[217] R. Snellings, A. Salze, K.L. Scrivener, Use of X-ray diffraction to quantify amorphous supplementary cementitious materials in anhydrous and hydrated blended cements, Cement and Concrete Research, 64 (2014) 89-98.

[218] J. Zhang, G.W. Scherer, Comparison of methods for arresting hydration of cement, Cement and Concrete Research, 41 (2011) 1024-1036.

[219] R.T. Downs, M. Hall-Wallace, The American mineralogist crystal structure database, Am Mineral, 88 (2003) 247-250.

[220] T. de Larrard, F. Benboudjema, J.B. Colliat, J.M. Torrenti, F. Deleruyelle, Concrete calcium leaching at variable temperature: Experimental data and numerical model inverse identification, Comp Mater Sci, 49 (2010) 35-45.

[221] Y.F. Houst, F.H. Wittmann, Depth profiles of carbonates formed during natural carbonation, Cement and Concrete Research, 32 (2002) 1923-1930.

[222] H. Akima, A New Method of Interpolation and Smooth Curve Fitting Based on Local Procedures, J ACM, 17 (1970) 589-602.

[223] L. Cui, J.H. Cahyadi, Permeability and pore structure of OPC paste, Cement and Concrete Research, 31 (2001) 277-282.

[224] V. Boel, K. Audenaert, G. De Schutter, G. Heirman, L. Vandewalle, B. Desmet, J. Vantomme, Transport properties of self compacting concrete with limestone filler or fly ash, Mater Struct, 40 (2007) 507-516.

[225] P.K. Mehta, P.J.M. Monteiro, Concrete: microstructure, properties, and materials, McGraw-Hill, 2006.

[226] A.A. Ramezanianpour, E. Ghiasvand, I. Nickseresht, M. Mahdikhani, F. Moodi, Influence of various amounts of limestone powder on performance of Portland limestone cement concretes, Cement Concrete Comp, 31 (2009) 715-720.

[227] S. Tsivilis, E. Chaniotakis, G. Batis, C. Meletiou, V. Kasselouri, G. Kakali, A. Sakellariou, G. Pavlakis, C. Psimadas, The effect of clinker and limestone quality on the gas permeability, water absorption and pore structure of limestone cement concrete, Cement Concrete Comp, 21 (1999) 139-146.

[228] S. Tsivilis, J. Tsantilas, G. Kakali, E. Chaniotakis, A. Sakellariou, The permeability of Portland limestone cement concrete, Cement and Concrete Research, 33 (2003) 1465-1471.

[229] R. Dhir, R. Jones, Euro-Cements: Impact of ENV 197 on Concrete Construction, Taylor & Francis, 1994.

[230] G.K. Moir, S. Kelham, Developments in the Manufacture and Use of Portland Limestone Cement, ACI Special Publication, 172 (1999) 797-820.

[231] Q.T. Phung, N. Maes, G. De Schutter, D. Jacques, G. Ye, Determination of water permeability of cementitious materials using a controlled constant flow method, Constr Build Mater, 47 (2013) 1488-1496.

[232] T.C. Powers, L.E. Copeland, J.C. Hayes, H.M. Mann, Permeability of Portland Cement Paste, Jounal of The American Concrete Institute, 51-14 (1954) 285-298.

[233] G. Ye, Experimental Study & Numerical Simulation of the Development of the Microstructure and Permeability of Cementitious Materials, in, Technology University of Delft, The Netherlands, 2003, pp. 208.

[234] D.P. Bentz, Three-dimensional computer simulation of portland cement hydration and microstructure development, J Am Ceram Soc, 80 (1997) 3-21.

[235] Z.G. Xu, M.S. Tang, J.J. Beaudoin, Relationships between Composition, Structure and Mechanical-Properties of Very Low Porosity Cementitious Systems, Cement and Concrete Research, 23 (1993) 187-195.

[236] N. Banthia, S. Mindess, Water Permeability of Cement Paste, Cement and Concrete Research, 19 (1989) 727-736.

[237] V. Bonavetti, H. Donza, V. Rahhal, E. Irassar, Influence of initial curing on the properties of concrete containing limestone blended cement, Cement and Concrete Research, 30 (2000) 703-708.

[238] B. Jähne, G. Heinz, W. Dietrich, Measurement of the diffusion coefficients of sparingly soluble gases in water, Journal of Geophysical Research: Oceans, 92 (1987) 10767-10776.

[239] Y.S. Han, G. Hadiko, M. Fuji, M. Takahashi, Factors affecting the phase and morphology of $CaCO_3$ prepared by a bubbling method, J Eur Ceram Soc, 26 (2006) 843-847.

[240] V. Kocaba, Development and evaluation of methods to follow microstructural development of cementitious systems including slags, in, EPFL, 2009.

[241] S. Diamond, Reply to the discussion by S. Chatterji of the paper "Mercury porosimetry - an inappropriate method for the measurement of pore size distributions in cement-based materials", Cement and Concrete Research, 31 (2001) 1659-1659.

[242] M. Dubinin M, A. Astakhov V, Description of Adsorption Equilibria of Vapors on Zeolites over Wide Ranges of Temperature and Pressure, in: Molecular Sieve Zeolites-II, AMERICAN CHEMICAL SOCIETY, 1971, pp. 69-85.

[243] M. Arandigoyen, B. Bicer-Simsir, J.I. Alvarez, D.A. Lange, Variation of microstructure with carbonation in lime and blended pastes, Applied Surface Science, 252 (2006) 7562-7571.

[244] J.J. Thomas, J.J. Chen, A.J. Allen, H.M. Jennings, Effects of decalcification on the microstructure and surface area of cement and tricalcium silicate pastes, Cement and Concrete Research, 34 (2004) 2297-2307.

[245] J.J. Thomas, H.M. Jennings, A colloidal interpretation of chemical aging of the C-S-H gel and its effects on the properties of cement paste, Cement and Concrete Research, 36 (2006) 30-38.

[246] H.M. Jennings, Refinements to colloid model of C-S-H in cement: CM-II, Cement and Concrete Research, 38 (2008) 275-289.

[247] A.M. Ramezanianpour, R.D. Hooton, A study on hydration, compressive strength, and porosity of Portland-limestone cement mixes containing SCMs, Cement and Concrete Composites, 51 (2014) 1-13.

[248] S.J. Gregg, K.S.W. Sing, Adsorption, Surface Area and Porosity, 2nd ed., Academic Press, London, 1982.

[249] F. Heukamp, F. Ulm, J. Germaine, Does Calcium Leaching Increase Ductility of Cementitious Materials? Evidence from Direct Tensile Tests, J Mater Civil Eng, 17 (2005) 307-312.

[250] SO.L.I.D software manuals for PASCAL Series Mercury Porosimeters, (2011).

[251] H.S. Lee, X.Y. Wang, A model predicting carbonation depth of concrete containing silica fume, Mater Struct, 42 (2009) 691-704.

[252] A. Muntean, M. Bohm, J. Kropp, Moving carbonation fronts in concrete: A moving-sharp-interface approach, Chem Eng Sci, 66 (2011) 538-547.

[253] H.W. Song, S.J. Kwon, K.J. Byun, C.K. Park, Predicting carbonation in early-aged cracked concrete, Cement and Concrete Research, 36 (2006) 979-989.

[254] S.A. Meier, Modelling and simulation of concrete carbonation with internal layers, Zentrum für Technomathematik, Univ. Bremen, 2005.

[255] B. Bary, A. Sellier, Coupled moisture-carbon dioxide-calcium transfer model for carbonation of concrete, Cement and Concrete Research, 34 (2004) 1859-1872.

[256] J. Diederik, Benchmarking chemical concrete degradation simulations using a mass-action law and a Gibbs free energy minimization thermodynamic models, (in preparation).

[257] J.K. Stolaroff, D.W. Keith, G.V. Lowry, Carbon dioxide capture from atmospheric air using sodium hydroxide spray, Environ Sci Technol, 42 (2008) 2728-2735.

[258] G. Wardeh, B. Perrin, Relative permeabilities of cement-based materials: Influence of the tortuosity function, J Build Phys, 30 (2006) 39-57.

[259] A. Abbas, M. Carcasses, J.P. Ollivier, Gas permeability of concrete in relation to its degree of saturation, Mater Struct, 32 (1999) 3-8.

[260] C. Zhou, Predicting water permeability and relative gas permeability of unsaturated cement-based material from hydraulic diffusivity, Cement and Concrete Research, 58 (2014) 143-151.

[261] R.J. Millington, J.P. Quirk, Permeability of porous solids, Transactions of the Faraday Society, 57 (1961) 1200-1207.

[262] V. Baroghel-Bouny, Water vapour sorption experiments on hardened cementitious materials. Part II: Essential tool for assessment of transport properties and for durability prediction, Cement and Concrete Research, 37 (2007) 438-454.

[263] Y.F. Houst, F.H. Wittmann, Influence of porosity and water content on the diffusivity of CO2 and O2 through hydrated cement paste, Cement and Concrete Research, 24 (1994) 1165-1176.

[264] M. Thiéry, Modélisation de la carbonatation atmosphérique des matériaux cimentaires: prise en compte des effets cinétiques et des modifications microstructurales et hydriques, in, Laboratoire central des ponts et chaussées, Paris, 2005, pp. 347.

[265] T. Hansen, Physical structure of hardened cement paste. A classical approach, Mater Struct, 19 (1986) 423-436.

[266] U.R. Berner, Evolution of pore water chemistry during degradation of cement in a radioactive waste repository environment, Waste Manage, 12 (1992) 201-219.

[267] S.A. Meier, M.A. Peter, A. Muntean, M. Bohm, Dynamics of the internal reaction layer arising during carbonation of concrete, Chem Eng Sci, 62 (2007) 1125-1137.

[268] M.A. Peter, A. Muntean, S.A. Meier, M. Böhm, Competition of several carbonation reactions in concrete: A parametric study, Cement and Concrete Research, 38 (2008) 1385-1393.

[269] D.C. Park, Carbonation of concrete in relation to CO2 permeability and degradation of coatings, Constr Build Mater, 22 (2008) 2260-2268.

[270] B. Lothenbach, Thermodynamic equilibrium calculations in cementitious systems, Mater Struct, 43 (2010) 1413-1433.

[271] A.J. Allen, J.J. Thomas, H.M. Jennings, Composition and density of nanoscale calcium-silicate-hydrate in cement, Nat Mater, 6 (2007) 311-316.

[272] V.H. Nguyen, B. Nedjar, J.M. Torrenti, Chemo-mechanical coupling behaviour of leached concrete: Part II: Modelling, Nucl Eng Des, 237 (2007) 2090-2097.

[273] D.P. Bentz, E.J. Garboczi, Modelling the leaching of calcium hydroxide from cement paste: effects on pore space percolation and diffusivity, Mater Struct, 25 (1992) 523-533.

[274] M. Mainguy, C. Tognazzi, J.-M. Torrenti, F. Adenot, Modelling of leaching in pure cement paste and mortar, Cement and Concrete Research, 30 (2000) 83-90.

[275] D. Jacques, L. Wang, E. Martens, D. Mallants, Modelling chemical degradation of concrete during leaching with rain and soil water types, Cement and Concrete Research, 40 (2010) 1306-1313.

[276] K. Wan, L. Li, W. Sun, Solid–liquid equilibrium curve of calcium in 6 mol/L ammonium nitrate solution, Cement and Concrete Research, 53 (2013) 44-50.

[277] K.S. Wan, Y. Li, W. Sun, Experimental and modelling research of the accelerated calcium leaching of cement paste in ammonium nitrate solution, Constr Build Mater, 40 (2013) 832-846.

[278] H.F.W. Taylor, Cement chemistry, 2nd ed., T. Telford, London, 1997.

[279] B. Lothenbach, T. Matschei, G. Möschner, F.P. Glasser, Thermodynamic modelling of the effect of temperature on the hydration and porosity of Portland cement, Cement and Concrete Research, 38 (2008) 1-18.

[280] J. Jain, N. Neithalath, Analysis of calcium leaching behavior of plain and modified cement pastes in pure water, Cement Concrete Comp, 31 (2009) 176-185.

[281] B. Gerard, C. Le Bellego, O. Bernard, Simplified modelling of calcium leaching of concrete in various environments, Mater Struct, 35 (2002) 632-640.

[282] C. Picioreanu, M.C.M. van Loosdrecht, J.J. Heijnen, Modelling the effect of oxygen concentration on nitrite accumulation in a biofilm airlift suspension reactor, Water Science and Technology, 36 (1997) 147-156.

[283] A. Tamimi, E.B. Rinker, O.C. Sandall, Diffusion-Coefficients for Hydrogen-Sulfide, Carbon-Dioxide, and Nitrous-Oxide in Water over the Temperature-Range 293-368-K, J Chem Eng Data, 39 (1994) 330-332.

[284] E. Stora, C. Conrardy, R. Barbarulo, J. Chen, F. Thoue, A Reactive Transport Model Based on Thermodynamic Computations to Estimate the Atmospheric Carbonation of Cementitious Materials, Rilem Workshop on Long-Term Performance of Cementitious Barriers and Reinforced Concrete in Nuclear Power Plants and Waste Management, 64 (2009) 193-202.

[285] K. Maekawa, Multi-scale Modelling of Structural Concrete, Taylor & Francis, 2009.

[286] D.R. Trainer, A Study of Calcium Carbonate Crystal Growth in the Presence of a Calcium Complexing Agent, in, Lawrence University, 1981, pp. 77.

[287] L.N. Plummer, E. Busenberg, The Solubilities of Calcite, Aragonite and Vaterite in CO_2-H_2O Solutions between 0^oC and 90^oC, and an Evaluation of the Aqueous Model for the System $CaCO_3$-CO_2-H_2O, Geochim Cosmochim Ac, 46 (1982) 1011-1040.